

**SHEAR FLOWS IN 2D STRONGLY COUPLED FLUIDS
- A THEORETICAL AND COMPUTATIONAL STUDY**

By

Akanksha Gupta

PHYS06201104006

Institute For Plasma Research, Bhat

Gandhinagar 382428, India

A thesis submitted to the
Board of Studies in Physical Sciences

In partial fulfillment of requirements
for the degree of

DOCTOR OF PHILOSOPHY

of

HOMI BHABHA NATIONAL INSTITUTE

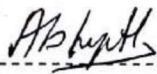


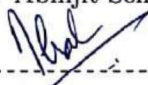
May 2017


Homi Bhabha National Institute

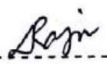
Recommendations of the Viva Voce Committee

As members of the Viva Voce Committee, we certify that we have read the dissertation prepared by **Akanksha Gupta** entitled "Shear flows in 2D strongly coupled fluids - A theoretical and computational study" and recommend that it may be accepted as fulfilling the thesis requirement for the award of Degree of Doctor of Philosophy.


----- Date : 18/ 09/ 2017
Chairman : Prof. Abhijit Sen


----- Date : 18/ 09/ 2017
Guide/ Convener : Prof. Rajaraman Ganesh



----- Date : 18/ 09/ 2017
Examiner : Prof. Mahendra Kumar Verma


----- Date : 18/ 09/ 2017
Member : Dr. D. Raju


----- Date : 18/ 09/ 2017
Member : Dr. R. Srinivasan

Final approval and acceptance of this thesis is contingent upon the candidate's submission of the final copies of the thesis to HBNI.

I hereby certify that I have read this thesis prepared under my direction and recommend that it may be accepted as fulfilling the thesis requirement.


----- Date : 18/ 09/ 2017
Guide : Prof. Rajaraman Ganesh Place: IPR, Gandhinagar

STATEMENT BY AUTHOR

This dissertation has been submitted in partial fulfillment of requirements for an advanced degree at Homi Bhabha National Institute (HBNI) and is deposited in the Library to be made available to borrowers under rules of the HBNI.

Brief quotations from this dissertation are allowable without special permission, provided that accurate acknowledgement of source is made. Requests for permission for extended quotation from or reproduction of this manuscript in whole or in part may be granted by the Competent Authority of HBNI when in his or her judgement the proposed use of the material is in the interests of scholarship. In all other instances, however, permission must be obtained from the author.



Akanksha Gupta

DECLARATION

I, hereby declare that the investigation presented in the thesis has been carried out by me. The work is original and the work has not been submitted earlier as a whole or in part for a degree/diploma at this or any other Institution/University.


Akanksha Gupta

List of Publications arising from the thesis

Publications in Peer Reviewed Journals:

1. **Kolmogorov flow in two dimensional strongly coupled dusty plasma**
[Akanksha Gupta](#), R. Ganesh and A. Joy. *Byys. Blazmas* **21**, 073707, (2014).
2. **Kolmogorov flow in two dimensional strongly coupled Yukawa liquid: A molecular dynamics study**
[Akanksha Gupta](#), R. Ganesh and A. Joy. *Byys. Blazmas* **22**, 103706, (2015).
3. **Molecular shear heating and vortex dynamics in thermostated two dimensional Yukawa liquids**
[Akanksha Gupta](#), R. Ganesh and A. Joy. *Byys. Blazmas* **23**, 073706 (2016).
4. **Compressibility effects on shear flow in strongly coupled dusty plasma: A study using computational fluid dynamics-Part I**
[Akanksha Gupta](#) and R. Ganesh. “*To be submitted*” (2017)
5. **Compressible Kolmogorov flow in strongly coupled dusty plasma using Molecular dynamics and Computational fluid dynamics: A comparative study-Part II**
[Akanksha Gupta](#), R. Ganesh and A. Joy. “*To be submitted*” (2017)
6. **Observation of elastic waves in strongly correlated liquids using molecular dynamics**
[Akanksha Gupta](#), R. Ganesh and A. Joy. “*To be submitted*” (2017)

International Conferences:

1. **Compressible Kolmogorov Flow in Strongly Coupled Dusty Plasma: A Study Using Molecular Dynamics and Computational Fluid Dynamics** [[Oral presentation](#)]

[Akanksha Gupta](#), Rajaraman Ganesh and Ashwin Joy. *8th International Conference on the Physics of Dusty Plasmas (8ICBDB)*, 20–25, May, 2017, Prague, Czech Republic

2. **Emergence and propagation of elastic wave from a vortex source in strongly correlated dusty plasma using molecular dynamics** [[Poster presentation](#)]

[Akanksha Gupta](#), Rajaraman Ganesh and Ashwin Joy. *8th International Conference on the Physics of Dusty Plasmas (8ICBDB)*, 20–25, May, 2017, Prague, Czech Republic

3. **Unstable shear flows in two dimensional strongly correlated liquids- A hydrodynamic and molecular dynamics study** [[Oral presentation](#)]

[Akanksha Gupta](#), Rajaraman Ganesh and Ashwin Joy. *69th Annual meeting of the ABS division of fluid dynamics*, 20–22, Nov, 2016, Portland, U.S.A

4. **A comparative study of Molecular Dynamics simulation and a viscoelastic fluid model for two dimensional shear flows** [[Poster presentation](#)]

[Akanksha Gupta](#), Rajaraman Ganesh and Ashwin Joy. *7th International Conference on the Physics of dusty Plasmas (ICBDB-2014)*, 3–7 Marcy, 2014, Delhi, India.

5. **Shear flows in two dimensional strongly coupled complex plasma : A comparative study using molecular and fluid simulations** [[Poster presentation](#)]

[Akanksha Gupta](#), Rajaraman Ganesh and Ashwin Joy. *7th International Conference on the Frontiers of plasma physics and technology (FPPT – 7)*, 13–17 April, 2015, Kochi (former Cochin), India

6. Kolmogorov flow in 2D strongly coupled dusty plasma :: A comparative study using Molecular dynamics and fluid simulations [Poster presentation]

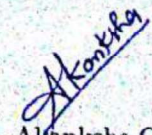
Akanksha Gupta, Rajaraman Ganesh and Ashwin Joy. *Diagnostics and simulation of Dusty Plasmas (DSDP-2015)*, 9 – 11, Sept, 2015, Kiel, Germany

7. As a participant

Akanksha Gupta, 10th Asia Plasma and Fusion Association (APFA), 14 – 18 Dec, 2015, Gandhinagar, India

National Conferences/Schools:

1. 1st PSSI-Plasma Scholars Colloquium (PPSC – 2012), Institute for Plasma Research, Gandhinagar, Gujarat, India 3-4 July 2012
2. Nonlinear theory and Simulation program, NIT Durgapur, Kolkata, India 14 – 18 Jan, 2013.
3. DST SERC School on Tokamaks & Magnetized Plasma Fusion, Institute for plasma research, Gandhinagar, Gujarat, India 25-Feb to 15-Mar 2013
4. The 28th National Conference on Plasma Science and Technology, KIIT university, Bhubaneswar, India 3 – 6Dec, 2013.
5. 8th Conference on Nonlinear Systems and Dynamics, IIT, Indore, India 11 – 14 Dec, 2013.
6. The 29th National Symposium on Plasma Science and Technology and the International Conference on Plasma and Nanotechnology Kottayam, Kerala, India 8 – 11 Dec, 2014.
7. Hands-on School on Nonlinear Dynamics, Institute for Plasma Research, Gandhinagar, Gujarat, India 16 – 22 Feb, 2015.


Akanksha Gupta

DEDICATIONS

*To my teachers, family and
friends.*

ACKNOWLEDGEMENTS

First and foremost, I would like to thank the omnipresent and almighty God, the One who has always guided me to work on the right path of life. I am fortunate to have Prof. Rajaraman Ganesh as my Ph.D supervisor, who patiently taught me numerical simulation and computational methods. I have greatly benefited from his keen scientific insight, his knack for solving seemingly intractable numerical difficulties, and his ability to put complex ideas into simple terms. I gained a lot from his vast physics and computational knowledge and scientific curiosity. In addition to regular discussions, I exchanged several emails, chats, phone calls during the tenure of my Thesis to understand various physics problems, which I had attempted and some of them I had finished and presented in this Thesis. In future, if I get a chance to be a supervisor, I would prefer to be like “YOU” Ganesh !!!.

I am particularly indebted to my doctoral committee Chairman Prof. Abhijit Sen and members Dr. D. Raju and Dr. R. Srinivasan, for their insightful comments and content recommendations. My most profound thanks are to Dr. Ashwin Joy, for his stimulating discussions with me on molecular dynamics simulation and providing me the MPMD and basic fluid dynamics code. I appreciate Rupak and Harish for the valuable discussion with me about concept of configurational temperature.

I would like to thank Prof. Sudip Sengupta, Prof. Amita Das, Prof. S. Mukherjee, Dr. M Kundu, Dr. Joydeep Ghosh, Prof. R. Ganesh, Dr. Devendra Sharma, Dr. Nirmal Bisai, Dr. Debasis Chandra, Dr. Mukesh Ranjan, Dr. C. Balasubramanian, Dr. P. Bharathi, Dr. G. Ravi, Dr. Suryakant Pathak, Dr. Shantanu Karkari for teaching me first year course work. I would also like to convey my sincere thanks to IPR library, IPR administration and computer center staff and HPC-team for their kind support during my thesis period.

I would like to take this opportunity to say warm thanks to my friends Vidhi, Vara, Prassi, Deepa and Samir who have been so supportive all along, through my thesis. I warmly thank them for being with me in good and bad times of life

during my Ph.D. tenure.

I really enjoyed my course work and hostel time with my batchmates Vidhi, Deepa, Vara, Samir, Bibhu, Neeraj, Mangilal, Rupendra, Chandrasekhar, Meghraj, Upendra and Harish. I am thankful to my seniors and postdoctoral fellow Vikrant, Maya, Sharad, Satya, Shekar, Jugal, Kshitish, Deepak, Ujjwal, Gurudatt, Vikram, Prabal, Ashwin, Sita, Swati, Bhawana, Sanjay, Rameswar, Sushil, Sanat, Pravesh, Sayak, Manjit, Aditya, Soumen for giving me guidance and encouragement for completing Ph.D. I would also like to convey my best wishes to my younger friends Sonu, Debraj, Ratan, Narayan, Arghya, Umesh, Modhu, Amit, Bhumika, Sagar, Chetan, Atul, Deepak Verma, Alam, Prabhakar, Jervis, Sandeep, Pallavi, Minakshi, Harshita, Arun, Rupak, Shivam, Avnish, Subroto, Neeraj, Srimanto, Dipshikha, Garima and other scholars. I really enjoyed our discussion at tea time, I personally called it “Chay Pe Charcha”.

I am thankful to my dear friends Shalini, Pragya, Suchita, Neelam, Ashish, Deepak and Rishikesh. I thank my parents Mr. Ramesh Chandra and Mrs. Manorama for giving me constant love, support, strength and patience. I express love and best wishes for my younger brother Amber. I express my love and respect for Mr. Govind Kumar for having full faith, trust in me and being the source of emotional, inspirational strength and source of encouragement.

Last but not least, deepest thanks goes to all people who took part in making this thesis real.

Akanksha Gupta

Date:18/09/2017

Contents

Synopsis	v
List of Figures	xiii
List of Tables	xxv
1 Introduction	1
1.1 Overview of dusty or Complex plasma	3
1.2 Motivation	5
1.3 Organization of the thesis	11
2 Molecular and computational fluid dynamics	15
2.1 Fluid simulation : Pseudo Spectral method	16
2.1.0.1 Anti-aliasing or de-aliasing	19
2.1.0.2 Nordsieck-Gear predictor-corrector method	21
2.1.0.3 Courant-Friedrichs-Lewy (CFL) condition	22
2.1.1 Dusty plasma as a continuum medium	23
2.1.1.1 Advanced Generalised SPECTral Code (AG-Spect)	
.	26
2.2 Dusty plasma as molecular medium	28
2.2.1 MPMD code	30
2.2.2 Leap-frog integration	30
3 Shear flow in a Yukawa liquid: A Molecular dynamics study	33
3.1 Introduction	33
3.2 Parallel Shear flow: Kolmogorov flow	36
3.2.1 Kolmogorov flow	36
3.2.2 Particle or molecular dynamics studies	39
3.2.3 Kolmogorov flow as an initial value problem in Yukawa liquid	43
3.2.4 Molecular heating due to shear flow	47
3.3 Rotational shear flow	56

3.3.1	Rankine Vortex	56
3.3.2	Study of non-linear elastic wave	59
3.3.3	Onset of the nonlinear wave structure	69
3.4	Summary	71
4	Molecular shear heating and vortex dynamics in thermostatted two dimensional Yukawa liquids	75
4.1	Introduction	75
4.2	Configurational Temperature	77
4.2.0.1	Kinetic and configurational temperatures	78
4.3	Configurational Thermostat	80
4.4	Kolmogorov Flow as an initial value problem in Yukawa liquid with and without molecular heat generation	84
4.5	Rotational shear flow	96
4.6	Summary	99
5	Compressible and incompressible shear flow in strongly coupled liquids: A computational fluid dynamics study	101
5.1	Introduction	101
5.2	Generalized Hydrodynamic model and Governing equations	103
5.3	Incompressible limit	104
5.3.1	Study of linear stability of viscoelastic Kolmogorov flow	106
5.3.2	Numerical results of linear stability analysis	107
5.3.3	Nonlinear study of Kolmogorov flow using incompressible viscoelastic model	113
5.3.3.1	Initial value problem	113
5.3.3.2	Numerical modeling and results	114
5.4	Compressible Limit	117
5.4.1	Generalized Hydrodynamic model and Governing equation	120
5.4.2	Linear stability analysis	121
5.4.3	Nonlinear Simulation	125

5.4.4	Rotational Shear flow: Nonlinear coherent structures in strongly coupled dusty plasma in the compressible limit using generalized fluid model	129
5.5	A comparative study of compressible parallel shear flow using MD and CFD simulations	133
5.5.1	Normalizations in MD and CFD studies	134
5.6	Results	135
5.7	Summary	141
6	Conclusion	145
6.1	Future scope	151
	Appendices	155
A	Complex viscosity and viscoelastic operator ($F_t \frac{h}{ht}$) based Modified Hydrodynamic model	155
A.1	Compressible hydrodynamic model and suitable normalization : Two velocity field formulation	160
A.2	Incompressible hydrodynamic model : Vorticity-Stream function formulation	164
B	Viscoelastic-Density Functional (VEDF) based hydrodynamic model	165
C	Fluctuation-dissipation theorem based hydrodynamic model	165
D	Parallelization of pseudo spectral code	166
E	Ewald sums	167
	Bibliography	167

SYNOPSIS

The contents of this synopsis provide a detailed analytical and numerical study of shear flows in strongly correlated liquids, considering strongly coupled dusty plasma as a prototype. Numerical methods consist of molecular and computational fluid dynamics.

Conventional low temperature plasma is often found embedded with large size grains or dust. Study of such plasma comprised of electrons, ions and grains has become a novel area of research because of its application to astrophysical (Solar nebula, planetary ring, white dwarfs, Supernova shells, molecular clouds, Saturn's rings, comet tails, lightning) [1, 2], industrial (microelectronics processing etc) [3], technological (fusion devices, deposition of nano size particles, ceramic deposition-composites) and in fundamental plasma physics studies as well. In general, these grains may have sizes ranging from few tens of nanometres to few hundreds of micrometers and may be composed of dielectric (e.g. PTO_2 or Al_2O_3) or conducting materials (Mn_2O_3) [2]. Grain attains high value of charge partly due to the size of the dust and partly due to the high relative mobility of electrons. Unlike electrons and ions of the background plasma, the ratio of potential energy to kinetic energy per grain (Γ) can be much greater than one leading to strong coupling effects in the grain medium. Thus, depending upon the temperature of the dust grain T_h , inter-grain spacing "a" and charge q_h per dust grain, the grain medium can be strongly coupled and can exhibit different phases of matter, such as solid-like (crystal) [4], liquid-like [5], gas-like phases. Strongly coupled dusty plasma is characterized by two dimensionless parameters, namely, coupling strength Γ , which is the ratio of average potential to average kinetic energy per particle $\Gamma = q_h^2/4\pi\epsilon_0 a k_B T_h$ and screening parameter $\kappa = a/\lambda_h$ (λ_h is Debye length of background plasma, where for 2D $a = 1/\sqrt{n\pi}$ and $a = (3/4\pi n)^{1/3}$ respectively). For a weakly coupled plasma $\Gamma \ll 1$, while for a strongly coupled plasma, the value of coupling parameter $\Gamma \geq 1$. The range of coupling strength and screening parameter can be controlled in the laboratory dusty plasma mainly by varying power and pressure of the gas. Due to their large mass, the dust grain dynamics occurs in much slower time scale as compared to electron and

ion time scales and hence unlike regular plasma components (electrons and ions) in laboratory, dust grains can be illuminated by laser light and the dynamics of dust grain can be recorded by CCD camera or other optical devices [6]. Grain medium in conventional plasma responds in two qualitatively different ways. [I] When $r_h < \lambda_h < a$, where r_h is the mean radius of single dust grain, in this case, dust grain number density is low and the interaction between the grains is weak. Such grain medium is called “dust-in-plasma” or “grain-in-plasma”. [II] When $r_h < a < \lambda_h$, in this case, dust number density is relatively high and grains interact via screening Coulomb potential (or Yukawa potential). The dust grain medium shows collective behavior on its own slow time and long length scales and is known as “dusty plasma”. In this thesis work, our primary interest is “dusty plasma”.

To understand physical phenomena in a range of time scales and length scales in strongly coupled dusty plasma experiments, typically, one or several of the following approaches is (are) used: Molecular Dynamics, Navier-Stokes Hydrodynamic models, phenomenological hydrodynamic models, multiscale particle in cell (PIC) simulation, Quasi-localized charge approximation and orbital motion limiter theory. The variety of interesting phenomena, including grain charging, interaction between charged particles, momentum exchange between different species, dust ion acoustic wave (DIAW), dust acoustic wave (DAW), phase transition, dust plasma crystal and other studies have been investigated in dusty plasma [2].

It has been found that the several phenomenon common to conventional hydrodynamic fluids, such as two stream instability (Kelvin Helmholtz instability), saturation in non-linear regime, vortex roll formation, inverse cascading, etc., are also found to happen in strongly coupled dusty plasma. For example, using Molecular dynamics method, it has been observed that a strongly correlated dusty plasma exhibits Kelvin Helmholtz instability [7]. Formation of coherent structures [8], such as dipole formation, has also been studied. In the same way, using phenomenological hydrodynamic model, shear waves, two stream instability (Kelvin-Helmholtz), non-linear saturation, vortex roll formation, etc., have been investigated [9, 10, 11, 12]. Far-from-equilibrium questions, such as transition from laminar to turbulent flows, vortex-vortex interactions, interaction of embedded co-

herent structures or rotational structures with the background turbulence etc - for these fundamental questions, even a qualitative comparative study of strongly correlated grain medium using fluid models and molecular dynamics simulations has not been attempted yet.

The transition from laminar to turbulent flows in liquids remains a problem of great interest despite decades of intensive research. Hydrodynamic like flows are generally studied to understand such transition and stability of flow. Conventionally, such shear flow related problem is mainly described by modelling the medium as a continuum. As Γ is increased, it is found that the dusty plasma in the liquid regime may also be understood as a viscoelastic fluid. Though Navier-Stokes equations are well known hydrodynamic equations, however, Navier-Stokes equation does not incorporate elastic effects. To understand the role of strong coupling, there are several phenomenological hydrodynamic models which tend to incorporate elastic effects arising out of strong correlation effects into N-S model. One of them is memory effect based model [Frenkel (1945)] which was applied to dusty plasma for $\Gamma \geq 1$ [Kaw and Sen (1998)]. In these models, viscoelastic response of strongly correlated fluid is incorporated by a non-local viscoelastic operator which incorporates memory effect and long range order, via a relaxation time E_t . Thus for $E_t = 0$ (memory-independent), these phenomenological models reduce to conventional Navier-Stokes fluid model. In 2015, Diaw and Murillo [13] described yet another hydrodynamic model for strongly coupled plasma system suggested called as the viscoelastic-density functional (VEDF) model using density functional method. More recently, Di Luo et.al [14] have introduced another hydrodynamic approach to simplify the calculation of dynamical structure factor of strongly coupled plasmas using fluctuation-dissipation theorem. In this thesis, to study shear flow dynamics in strongly coupled dusty plasma from continuum point of view, E_t based model has been used. In the concluding chapter, comments on the more recent fluids models are made and possible future work is indicated

Dusty plasma or strongly correlated liquids can also be treated as particle medium. As described earlier, the experiments allow direct observation of position and velocity of each dust grain. This unprecedented capability makes MD and com-

parison with experiments a very attractive possibility. In molecular dynamics study, classical Newton's second law of motion is solved for each particles. In this method force between dust-grain is calculated by interaction potential. From molecular dynamics study, data for individual particles to continuum data may be estimated. Thus fluid models and particle (or Molecular dynamics) models may be compared. Let alone for far-from-equilibrium phenomena described earlier, even for near-equilibrium phenomena such as onset of an instability, a detailed comparison between fluid and particle models has not been attempted.

In continuum models, whenever there is a shear in macroscopic velocity profile, it is well known that large scale fluid instabilities set in. However, in dusty plasma experiment, it is found that, whenever there is a shear in macroscopic velocity profiles, viscous shear heating occurs at the microscale because of collisions of grains near the shear layers [6]. This shear induced localized heating reduces the strong coupling effects. However, a detailed study of microscale shear heating and its effects on macroscopic flows in strongly coupled plasma has not yet been addressed. In present thesis, a well known macroscopic flow, namely, Kolmogorov flow as an initial shear flow has been considered. Kolmogorov flow is an unsteady, unbounded sinusoidal driven flow $\mathbf{U}_{initial}(x) = U_0 \cos(k_x x) \hat{y}$, where U_0 is magnitude of initial velocity of Kolmogorov flow and $k_x = 2\pi n_0 / L_x$, where n_0 , L_x are equilibrium mode number, size of the system along x direction respectively. For conventional fluids, Kolmogorov proposed a class of flows, which exhibits laminar to turbulence transition at low Reynolds number and is amenable to analytical methods. For example, Meshalkin and Sinai 1961 [15, 16] have performed the linear stability analysis of such flows in an unbounded domain, and obtained the critical value of Reynolds number $R_c = \sqrt{2}$, where R_c is laminar to turbulent transition point. Using Kolmogorov flow as initial shear flow, various fundamental processes including "Anti turbulence", metastability and vortex pairing study and nonlinear phenomena e.g bifurcation have been observed for Navier Stokes flow. In laboratory experiments, Kolmogorov flow has been studied in magnetized electrolyte fluid [16, 17] and also in driven soap film [18]. Due to its smooth (sinusoidal) flow profile, we believe it is possible to realize such flow Kolmogorov flow in laboratory dusty plasma experiments.

A. Particle or molecular dynamics studies

We consider parallel shear profile with sinusoidal perturbation has the form $\mathbf{U}(x, y) = U_0 \cos(k_x x)(1 + \delta \cos(k_y y))\hat{y}$ where U_0, δ are magnitude of initial velocity of Kolmogorov flow and magnitude of perturbation respectively and $k_x = 2\pi n_0/L_x$, $k_y = 2\pi m/L_y$ where n_0, m, L_x, L_y are equilibrium mode number, perturbation mode number, size of the system along x and y directions respectively. Using large scale non-equilibrium molecular dynamics, the early phase and late time dynamics of this parallel flow in strongly coupled plasma is addressed. A parametric study of stability of the flow with Reynolds number R has also been performed and found that below a critical value of Reynolds number R_c , flow exhibits a neutral stability. However, above $R > R_c$, a transition occurs from laminar to unstable state and eventually turning into a turbulent flow. It is found that the value of R_c decreases with increasing value of coupling strength. It is observed that for the given value of initial coupling parameter and screening parameter, molecular shear heating strongly reduces the magnitude of coupling parameter and its decay-rate is mainly found to be dependent upon the ratio of equilibrium shear velocity to thermal velocity. It is found that the magnitude of coupling parameter decays exponentially by the end of the growth phase, thus altering the state of “background grains” dramatically [19].

To understand the vortex dynamics of strongly coupled molecular fluids undergoing macroscale shear flows in the absence of molecular heat, MD simulation has also been performed, which allows the macroscopic vortex dynamics to evolve, while at the same time “removes” the microscopically generated heat without using the velocity degrees of freedom. It is demonstrated that by using a configurational thermostat (Profile Unbiased Thermostat or “PUT”) in a novel way, the microscale heat generated by shear flow can be thermostatted out efficiently without compromising the large scale vortex dynamics. In this work, using MD simulations, a comparative study of shear flow evolution in Yukawa liquids in the presence and absence of molecular or microscopic heating is presented [20]. However, when PUT is “ON” it is observed that the peaks of local temperature profile at the shear flow

location are much lesser in magnitude and global average temperature of the system is maintained as compared to the case with PUT “OFF”. Above mentioned study has also been done with rotational shear flow, wherein visco-elastic nonlinear wave evolution, nonlinear interaction have been observed.

B. Continuum or computational fluid dynamics studies

To study the behavior of parallel (Kolmogorov flow) and circular shear flow (Rankine, Gaussian, dipole etc.) using continuum model, a phenomenological fluid model [9, 10] has been adopted. In the fluid model, the effect of strong correlation is considered by using a visco-elastic relaxation time E_t , Thus for example, as $E_t \rightarrow 0$, the model becomes Navier-Stokes fluid model. For this purpose, a new two-dimensional fully parallized generalised hydrodynamic pseudo spectral code has been developed for incompressible ($M = 0$) [12], weakly ($M < 0.3$) and strongly compressible ($M > 0.3$) fluids. Using generalised compressible hydrodynamic model good agreement in linear growth rates obtained from eigen value solver and time dependent simulation has been observed [21].

In the incompressible limit of strongly correlated fluid, it is found that R_c is strongly reduced for increasing values of E_t . A critical E_t^c is found above which Kolmogorov flow is unconditionally unstable and becomes independent of Reynolds number. For $R < R_c$, the neutral stability regime found in Navier Stokes fluid ($E_t = 0$) is now found to be a damped regime in viscoelastic fluids, thus changing the fundamental nature of transition of Kolmogorov flow as function of Reynolds number R . Nonlinear states obtained from the pseudo spectral code exhibit cyclicity and pattern formation in vorticity and viscoelastic oscillations in energy.

The compressibility effects on the two-dimensional strongly coupled dusty plasma by means of computational fluid dynamics (CFD) simulations for various initial shear flow profiles has also been studied. Incorporation of compressibility effect allows dissipation of some amount of energy to drive longitudinal modes. Nonlinear compressible vortex flow dynamics and other linear and nonlinear properties of such flow in the presence of variable density, pressure and electrostatic potential are addressed. In CFD study, the suppression of instability, elongated vortex

structures, nonlinear saturation, viscoelastic oscillations and pattern formation have been observed.

Various linear and nonlinear properties of parallel and rotational shear flow, for example, laminar to turbulent transition, shear flow instability, macroscale vortex flow dynamics, microscopic shear heating, suppression of molecular heating (using “PUT”), compressibility effects over such shear flow instability have been addressed in this thesis. In the incompressible limit (Mach number $M \ll 1$) of the fluid, where transverse variation dominates, generation and propagation of transverse shear waves have been reported using CFD model and MD simulation as well.

A qualitative comparison between fluid and molecular dynamics studies has also been performed in this thesis.

Chapter-wise thesis plan is as follows-

Chapter-1: [*Introduction and outline of the problem*] Introduction about strongly coupled liquids, shear flow instabilities, coherent structure formation, shear heating phenomena, viscoelastic response and motivation behind doing this problem.

Chapter-2: [*A development of Pseudo spectral code and molecular dynamics methods*] Numerical and computation algorithms of computer fluid dynamics (CFD) and molecular dynamics (MD).

Chapter-3: [*Kolmogorov shear flow: Study of molecular shear heating*] The phenomena of heat generation at the strong shear in molecular dynamics study. Exponential decay in average or global Γ (inverse of temperature) value, destruction of vortex due to molecular heating, stable to unstable transition and its dependency crucially dependency on the Reynolds number values are important results observed. To do a comparative study between the fluid and molecular study, for example, fluid-like phenomena of K-flows, it is important to prevent molecular heating up to some extent.

Chapter-4: [*Kolmogorov shear flow in the absence molecular shear heating*] Uniqueness of configurational thermostat to control the temperature by using augmented equations of motions for the instantaneous particle positions without disturbing

the instantaneous velocity of particles. In this chapter, vortex evolution, nonlinear pattern formation, neutral to unstable flow transition, a parametric study of growth-rate of perturbed mode and their comparison with Profile Biased Thermostat (PBT) e.g Gaussian thermostat will be presented. Observation of elastic shear waves in presence of circular shear flow will also be presented.

Chapter-5: [*Viscoelastic response of shear flow in incompressible and compressible limits of fluids*] Using fluid simulation, the shear flow instability and other nonlinear properties of parallel and circular flows in strongly coupled liquids (viscoelastic liquids) will be addressed in the incompressible and compressible limit. A qualitative comparison between fluid and molecular dynamics studies.

Chapter-6: [*Conclusion and Future scope*] will conclude and summarize the thesis work. Future direction of this thesis and open questions that remain to be solved.

List of Figures

1.1	Phase transition of matter due to increasing temperature.	1
1.2	A typical experimental example to setup shear flow in a laboratory dusty plasma using laser [Figure adapted from Yan Feng et.al. PRE, 83 (2012)]	8
2.1	Figure shows the aliasing error: suppose as $k_1 + k_2$ arises out of a nonlinear interaction such that $k_1 + k_2$ lies “outside” $[-K_0, K_0]$. Hence, due to periodic boundaries, the information about $k_1 + k_2$ comes inside the simulation region wrongly.	21
2.2	Maxwell model: Stress relaxation behavior using a spring and dash- pot in series.	23
2.3	Scalability of the code for different grid sizes. Typical input param- eters are $E_l = 10$, $\nu = 2.0$, $dt = 1e - 4$ (in normalized unit) and total time=5.0 (in normalized unit).	27
2.4	Diagram showing the structure of the Leap-Frog method	31
3.1	Initial velocity profile of Kolmogorov flow. Red and blue coloured contour show the positive and negative direction of velocity respec- tively	38
3.2	Figure shows the viscous heating and thermal conduction at maxi- mum shear location.	38
3.3	Total energy vs time for initial coupling parameter $\Gamma_0 = 50$, screen- ing parameter $\kappa(t = 0) = 0.5$, spatial period number $n_0 = 3$ in canonical $[(0 - 300)\omega_0^{-1}]$ and micro-canonical $[(300 - 600)\omega_0^{-1}]$ runs. At $[(600 - 1600)\omega_0^{-1}]$ of shear flow profile over thermally equilibrated dust bed (micro-canonical Run). Superposition of shear flow in- creases the velocity of particles, hence the value of total energy changes from 1.147 to 1.3967 (for $U_0 = 1.0$) with $\delta E_{total}^{Nut\ erical} =$ 0.24 from Eq.3.4 it is $\delta E_{total}=0.25$. Similarly for $U_0 = 0.7$ with $\delta E_{total}^{Nut\ erical} = 0.12$, which is same as the value obtained from Eq.3.4 .	40

3.4	A plot of average coupling parameter $\bar{\Gamma}(t)$ vs time for initial coupling parameter $\Gamma_0 = 50$, screening parameter $\kappa = 0.5$ spatial period number $n_0 = 3$ and shear velocity $U_0=1$. (a) canonical run for time $(0 - 300)\omega_0^{-1}$, (b) micro-canonical run for time $(300 - 600)\omega_0^{-1}$, wherein peak to peak fluctuation 1.406%, (c) micro-canonical run for time $(600 - 1600)\omega_0^{-1}$ after superposition of shear flow profile over thermally equilibrated particles of the system	43
3.5	A plot of perturbed kinetic energy (left y-axis) and decay of coupling parameter (right y-axis) in a linear-log scale for number for perturbation mode $m_0 = 2$, initial coupling parameter $\Gamma_0(t = 0) = 50$, screening parameter $\kappa = 0.5$, spatial period number $n_0 = 3$ and shear velocity $U_0=1$. Calculated growth rate from simulation is 5.5×10^{-2} . The zero of time-axis shown in Fig.3.5 is after the superposition of shear flow	45
3.6	Shear viscosity vs coupling strength plot for different κ values. Here Γ is same as Γ_0 . After Ref: [22]	46
3.7	A plot of self-diffusion coefficient D^* obtained from equilibrium MD simulation vs reduced temperature $T^* = T/T_c$ or Γ_c/Γ (where T_c and Γ_c are melting temperature and coupling strength for low value of κ , where diffusion coefficient D^* are normalized by $\omega_E a^2$ with ω_E being the Einstein frequency. [After Ref: [23]]	47
3.8	Reduced thermal conductivity λ^* normalized by the Einstein frequency as a function of the reduced temperature $T^* = T/T_c$ or Γ_c/Γ for different κ values (equilibrium MD simulation). After Ref: [24]	48
3.9	A plot of perturbed kinetic energy in linear-log scale for number for perturbation mode $m_0 = 2$, initial coupling parameter $\Gamma_0(t = 0) = 10$, screening parameter $\kappa = 0.5$, spatial period number $n_0 = 3$ and shear velocity $U_0=1$. Calculated growth rate from simulation is 4.5×10^{-2} . Zero in Time-axis shown in Fig.3.9 is after the superposition of shear flow.	49

3.10	Contour plot of fluid vorticity ($\omega = \nabla \times \vec{U}$) obtained from molecular data. The grain velocity in the bins are fluidized through a 55×55 grid to construct vorticity. The horizontal color bar at the bottom show the magnitude of vorticity and blue and red strips show the opposite sign vorticity respectively. Perturbation mode $m = 2$, initial coupling parameter $\Gamma_0 = 50$, screening parameter $\kappa = 0.5$ equilibrium spatial period number is $n_0 = 3$, initial Reynolds number $R = 235.149$ and shear velocity $U_0=1$. Vorticity plots generated from microscopic velocity show Kolmogorov instability in Molecular Dynamics, the micro scale heating quickly destroy the vorticity structures.	50
3.11	Growth-Rate vs initial Reynolds number R for different initial value of Γ_0 with $\kappa = 0.5$	51
3.12	Growth-Rate vs initial Reynolds number R showing bifurcation for all the three initial Γ_0 values. R_c for various initial coupling strength $\Gamma_0 = 10, 50$ and 130 are $59, 47, 18$ respectively.	51
3.13	Figure shows the location of maximum shear and localized shear heating zones and the thermal conduction away from the shear heating zone. Vertical lines \updownarrow show the node points (shear heating zones) in velocity profile.	52
3.14	$\bar{T}(x_G) = \langle \bar{T}(x_G, 0, t) \rangle$, temporal evolution of temperature profile as a function of x_G for different time for $\Gamma_0 = 50$, equilibrium velocity magnitude $U_0 = 1$, screening parameter $\kappa = 0.5$	53
3.15	$v_y(x_G) = \langle v(x_G, 0, t) \rangle$, temporal evolution of velocity profile as a function of x_G for different time for $\Gamma_0 = 50$, equilibrium velocity magnitude $U_0 = 1$, screening parameter $\kappa = 0.5$	54
3.16	Spatial average coupling parameter Γ vs time plot for different value of initial Γ_0 for equilibrium velocity magnitude $U_0 = 1$, screening parameter $\kappa = 0.5$ at $y_G = 0$ axis.	54
3.17	Spatially averaged coupling parameter $\Gamma(t)$ as a function of time for three different values of initial Γ_0 , namely $\Gamma_0 = 50(*)$, $100(box)$ and $150(\circ)$. Colors correspond to the cases $\alpha = 0.5$ (red), 2 (green) and 6 (blue). . .	54

3.18	A plot of $\langle \Gamma \rangle_{xy}$ vs time plot for $\Gamma_0 = 50$, equilibrium velocity to thermal velocity ratio, say $\alpha = U_0/v_{th} = 5$. Fit line is $0.2[1 + 4.0 \exp(-\beta t)]$. Calculated decay rate is $\beta = 3.4 \times 10^{-3}$. Solid line shows the exponential fit.	55
3.19	Decay rate vs $\alpha = U_0/v_{th}$ plot for number of perturbation mode $m = 2$, coupling parameter $\Gamma_0 = 50$, screening parameter $\kappa = 0.5$ equilibrium spatial period number $n_0 = 3$	55
3.20	Rankine vortex profile ($\omega = \nabla \times V$) for $\Gamma_0 = 70$, $\kappa = 1.0$, $R = 10$ and $V_0 = 5$. The magnitude of vorticity inside the inner core $\omega = 2V_0 r/R = 1.0$. Black colored arrows show the direction of velocity field at $t = 400$, the time of superposition of Rankine vortex.	58
3.21	Total energy plot for $\Gamma_0 = 70$ and $\kappa = 1.0$. (a) in canonical run (b) in micro-canonical run (c) in micro-canonical run after superposition of rotational shear flow with various equilibrium velocity magnitudes, viz $V_0 = 5.0, 8.0$ and 10.0	59
3.22	Time evolution plots of Rankine vortex for $\Gamma_0 = 70$, $\kappa = 1.0$ and $V_0 = 5$. Black coloured arrows show the direction of velocity field.	61
3.23	Maximum amplitude of nonlinear waves along x and y directions for $\Gamma_0 = 70$, $\kappa = 1.0$, $R = 10$ and $V_0 = 5$	62
3.24	Time evolution of maximum value of spatially averaged density $\langle n(x, y, t) - n_0 \rangle_{xy}$ for $\Gamma_0 = 70$, $\kappa = 1.0$ and equilibrium velocity $U_0 = 5$. Initial density is $n_0 = 1/\pi$	63
3.25	Time evolution of maximum value of spatially averaged divergence of velocity $\langle \nabla \cdot U \rangle_{xy}$ for $\Gamma_0 = 70$, $\kappa = 1.0$ and equilibrium velocity $V_0 = 5$	63
3.26	Propagation of nonlinear wave for $\Gamma_0 = 70$, $\kappa = 1.0$ and different values of azimuthal equilibrium velocity (a) $V_0 = 5$, $C_x = 2.109$, $C_{NLW} = 2.98$ (b) $V_0 = 8$, $C_x = 2.687$, $C_{NLW} = 3.8$ and (c) $V_0 = 10$, $C_x = 2.833$, $C_{NLW} = 4.0$, where C_{NLW} is calculated by $\Delta x/\Delta t$. Similar structure is seen along y - axis.	64

3.27	Propagation of density wave (or compression wave) for $\Gamma_0 = 70$, $\kappa = 1.0$ and different values of azimuthal equilibrium velocity (a) $V_0 = 5$, $C_x = 2.2$, $C_{NLW} = 3.11$ (b) $V_0 = 8$, $C_x = 2.6$, $C_{NLW} = 3.68$ and (c) $V_0 = 10$, $C_x = 2.96$, $C_{NLW} = 4.18$, where C_{NLW} is calculated by $\Delta x/\Delta t$. Similar structure is seen along y - axis.	65
3.28	Effect of coupling strength over time evolution of Rankine vortex for $\kappa = 1.0$ and $V_0 = 10$. Black colored arrows show the direction of velocity field.	66
3.29	Effect of coupling strength on nonlinear wave speed for $\kappa = 1.0$ and $V_0 = 10$. Similar structure is seen along y - axis. Speed of nonlinear wave ($C_{NLW} = \sqrt{C_x^2 + C_y^2}$) are 4.6, 4.6, 4.45, 4.21, 4.32, 4.21, 4.21, 4.21, 4.21 for $\Gamma_0=1, 9, 15, 30, 50, 70, 90, 110, 130$ respectively. . . .	67
3.30	Speed of non-linear wave with various equilibrium coupling strength for $\kappa = 1.0$ and $V_0 = 10$	68
3.31	Speed of non-linear wave variation with equilibrium coupling strength for different values of azimuthal speed with screening parameter $\kappa = 1.0$	68
3.32	Longitudinal sound velocity $C_s/\omega_p a$ is same as C_L used in the text. The plot represents the C_L as a function of κ for $\Gamma = 10$ and 100. (After Ref.[25]). The values of C_L, C_T for $\kappa = 4$ are 0.289 and 0.12 respectively.	69
3.33	Propagation of nonlinear wave with various value of screening parameter κ for $V_0 = 0.75$, $\Gamma_0 = 50$	70
3.34	Speed of nonlinear wave (C_{NLW}) vs longitudinal Mach number (M_{CL}) for $V_0 = 0.75$, $\Gamma_0 = 50$ with various values of screening parameter κ	71
3.35	Speed of longitudinal sound C_L and nonlinear wave (C_{NLW}) vs screening parameter (κ) plot for $V_0 = 0.75$, $\Gamma_0 = 50$. Sound speeds are calculated from our MD simulation. As shown in Fig.3.30 as V_0 increases the value of C_{NLW} increases.	71

4.1	Thermalisation of particles using Gaussian thermostat for screening parameter $\kappa = 0.5$ and various desired coupling parameter Γ_0 value. From $0 - 300\omega_0^{-1}$ Gaussian thermostat is ON (canonical run) and after that for next $300\omega_0^{-1}$ thermostat is OFF (microcanonical run) for different $\Gamma_0 = 50, 100, 150$	79
4.2	Kinetic (blue) and configurational (red) $\Gamma(t)$ extracted under micro-canonical conditions for the Yukawa liquid previously equilibrated at $\Gamma = 50, 100, 150$ with $\kappa = 0.5$	80
4.3	Canonical run using B-T thermostat for desired coupling parameter $\Gamma_0 = 50$ with various effective mass Q_μ for $N = 2500, \kappa = 0.5$	84
4.4	Extended Hamiltonian of the system with time. Canonical run from $(0 - 250)\omega_0^{-1}$ and microcanonical run for next $250\omega_0^{-1}$ for various Q_μ values for $N = 2500, \kappa = 0.5$ and $\Gamma_0 = 50$	85
4.5	Kinetic (blue) and configurational (red) Γ vs time. Parameters used: $Q_\mu = 2 \times 10^6, N = 2500$ and $\kappa = 0.5$	85
4.6	Coupling parameter vs time. The system is evolved (a) coupled to Gaussian thermostat (b) under micro-canonical conditions (c) with PUT “ON” and flow superposed at $t = 600$ (d) with PUT “OFF”. A fit (red) to show that weakening of Γ is indeed exponential in time has been provided. Parameters used: $\Gamma_0 = 50$	87
4.7	Coupling parameter vs time plot with PUT always “ON”. Shear flow is superimposed at time $t = 1000$	87
4.8	“Fluid” vorticity ($\omega = \nabla \times \mathbf{U}$) contour plots. Color bars show the magnitude of local vorticity. Parameters used: perturbation mode $m = 2$, equilibrium spatial period number $n_0 = 3$, $\Gamma_0 = 50, \kappa = 0.5$, initial Reynolds number $R = 235.149$ and shear velocity $U_0=1$ with PUT “OFF”. The micro scale heating quickly destroy the vorticity structures when PUT is “OFF”.	89

4.9	“Fluid” vorticity ($\omega = \nabla \times \mathbf{U}$) contour plots. Color bars show the magnitude of local vorticity. Parameters used: perturbation mode $m = 2$, equilibrium spatial period number $n_0 = 3$, $\Gamma_0 = 50$, $\kappa = 0.5$, initial Reynolds number $R = 235.149$ and shear velocity $U_0=1$ with PUT “ON”. When PUT is “ON”, vortex structures sustain for longer time.	90
4.10	Spatial distribution of $\Gamma(x, y, t)$ -Contour plots of Coupling parameter Γ . Parameters used: perturbation mode $m = 2$, equilibrium spatial period number $n_0 = 3$, $\Gamma_0 = 50$, $\kappa = 0.5$, initial Reynolds number $R = 235.149$ and shear velocity $U_0=1$ with PUT “OFF”.	91
4.11	Contour plots of Coupling parameter. Parameters used: perturbation mode $m = 2$, equilibrium spatial period number $n_0 = 3$, $\Gamma_0 = 50$, $\kappa = 0.5$, initial Reynolds number $R = 235.149$ and shear velocity $U_0=1$, when PUT is “ON”.	92
4.12	y - averaged temperature profiles ($\bar{T}(x_G, y_G, t)$) at various times after the shear flow is superimposed. Parameters used are $\Gamma_0 = 50$, $U_0 = 1$ and $\kappa = 0.5$. Symbols show the temperature profile with PUT “OFF” and solid lines show temperature variation with PUT “ON”.	93
4.13	Temporal evolution of y averaged velocity $v_y(x_G)$ profile for $\Gamma_0 = 50$, equilibrium velocity magnitude $U_0 = 1$, screening parameter $\kappa = 0.5$, in the presence of heating (PUT “OFF”). Time t here are shown after superimposition of shear flow.	94
4.14	Temporal evolution of y averaged velocity $v_y(x_G)$ profile for $\Gamma_0 = 50$, equilibrium velocity magnitude $U_0 = 1$, screening parameter $\kappa = 0.5$, in the presence of heating (PUT “OFF”). Time t here are shown after superimposition of shear flow.	94
4.15	Perturbed kinetic energy in linear-log scale with and without PUT. Calculated growth rates from simulation are 5.5×10^{-2} and 6.0×10^{-2} for PUT “OFF” and “ON” case respectively.	94
4.16	Growth-Rate vs initial Reynolds number $\left(R = \frac{U_0 l \bar{n}}{\eta_0}\right)$ plot for screening parameter $\kappa = 0.5$	95

4.17	Growth-Rate vs initial Reynolds number $R^* = R - R_c$ plot showing trans-critical kind of bifurcation for screening parameter $\kappa = 0.5$, where $R_c = 47$ and 18.80 for $\Gamma_0 = 50$ and 130 respectively.	96
4.18	Time evolution plots of Rankine vortex for $\Gamma_0 = 70$, $\kappa = 1.0$ and $V_0 = 5$ with configurational thermostat. Black coloured arrows show the direction of velocity field.	97
4.19	Propagation of nonlinear wave for $\Gamma_0 = 70$, $\kappa = 1$ and $V_0 = 5$ [$C_x = \Delta x / \Delta t = 2.109$, $C_{NLW} = \sqrt{C_x^2 + C_y^2} = 2.98$] with configurational thermostat. Similar structure is seen along y - axis.	98
4.20	Propagation of density wave (or compression wave) for $\Gamma_0 = 70$, $\kappa = 1.0$ and $V_0 = 5$ with configurational thermostat. Similar structure is seen along y - axis. The nonlinear wave speed $C_x = \Delta x / \Delta t = 2.22$, $C_{NLW} = 3.1395$	98
5.1	Equilibrium vorticity contour plot showing the direction of velocity flow and shearing length	102
5.2	Growth rate vs Reynolds number plot with different value of N value for $F_t = 0$, Navier Stokes case. Notice that R_c is nearly independent of N	108
5.3	Growth rate vs Reynolds number plot with different value of k value for $F_t = 0$, Navier Stokes case	108
5.4	Growth rate vs Reynolds number plot with different value of N value for $F_t = 1$	108
5.5	Growth rate vs Reynolds number plot with different value of k value $F_t = 1$	108
5.6	Growth rate vs vs Reynolds number (R) for various values of viscoelastic coefficient F_t and perturbed mode number $k = 2$	109
5.7	Real frequency ω_r vs Reynolds number (R) for various values of viscoelastic coefficient F_t and perturbed mode number $k = 2$. For $F_t = 0$, ω_r is identical zero and not shown here.	109
5.8	Growth rate vs vs Reynolds number (R) for various values of viscoelastic coefficient F_t and perturbed mode number $k = 2$	110

5.9	Contour plot of growth rate of Kolmogorov flow with variation of N and R for $F_t = 0$ (Upper plot), $F_t = 1$ (middle Plot), $F_t = 10$ (lower Plot)	111
5.10	Contour plot of growth rate of Kolmogorov flow with variation of k and R for $F_t = 0$ (Upper plot), $F_t = 1$ (middle Plot), $F_t = 10$ (lower Plot)	111
5.11	Growth rate from simulation is 0.45 and from eigen value solver is 0.48 for Reynolds number $R=2$, Number for perturbation mode $k=2$, Maxwell's relaxation time $F_t = 10$, equilibrium wave number $N=3$ and shear velocity $U_0=0.5$	115
5.12	Damping rate from simulation is -0.07 and from eigen value solver is -0.0722 for Reynold number $R = 1 < R_c$, Number for perturbation mode $k=2$, Maxwell's relaxation time $F_t = 5$, equilibrium wave number $N=3$ and shear velocity $U_0=0.5$. Note that the real frequency of damping $2\omega_r$ is close to $\frac{2\pi}{\tau_m}$, which is corresponds to ω_r^{linear} , See Fig.5.7	116
5.13	Comparison of growth rate between eigen value solver and nonlinear pseudo spectral code for perturbation mode number $k=2$, Maxwell's relaxation time $F_t = 10$ (upper) and $F_t = 5$ (lower), equilibrium wave number $N=3$ and shear velocity $U_0=0.5$. For above given parameters, real frequency in this case is very small $\sim 10^{-4}$ [Not shown here, see fig.5.7]	117
5.14	Vorticity contour show a variety of pattern formation at different time with Kolmogorov initial condition for Reynold number $R=2$, Number for perturbation mode number $k=2$, Maxwell's relaxation time $F_t = 10$, equilibrium wave number $N=3$ and shear velocity $U_0=0.5$	118

5.15	Vorticity contour show a variety of pattern formation at different time with Kolmogorov initial condition for Reynold number $R=5000$, Number for perturbation mode number $k=2$, Maxwell's relaxation time $F_t = 0$ (Navier-Stokes fluid), equilibrium wave number $N=3$ and shear velocity $U_0=0.5$. The choice of such high Reynold number is just to show the laminar to turbulent transition, note that for $R=2$, Navier Stokes fluid is stable for our case, see Fig.5.3.	119
5.16	Growth rates (γ_g) vs Reynolds number (R) plot for various perturbation wave number k_y for equilibrium wave number $k_x = 3$, equilibrium velocity $U_0 = 1$, relaxation time $F_t = 5$ and Mach number= $U_0/C_s = 0.5$	123
5.17	Growth rates (γ_g) vs Reynolds number (R) plot for various equilibrium wave number k_x for perturbation wave number $k_y = 2$, equilibrium velocity $U_0 = 1$, relaxation time $F_t = 5$ and Mach number= $U_0/C_s = 0.5$	123
5.18	Growth rates (γ_g) vs Reynolds number (R) for various Mach number for equilibrium wave number $k_x = 3$ for perturbation wave number $k_y = 2$, equilibrium velocity $U_0 = 1$, relaxation time $F_t = 5$	124
5.19	Growth rates (γ_g) vs Reynolds number (R) for various relaxation time F_t for equilibrium wave number $k_x = 3$, equilibrium velocity $U_0 = 1$, perturbation wave number $k_y = 2$ and Mach number= $U_0/C_s = 0.5$	124
5.20	Perturbed kinetic energy vs time plot for perturbation wave number $k_y = 2$, equilibrium wave number $k_x = 3$, equilibrium velocity $U_0 = 1$, relaxation time $F_t = 5$, $\eta = 0.33$ and Mach number $M = 0.5$. . .	127
5.21	Growth-rate (γ_g) vs Reynolds number (R) plot for Mach number $M=0.5$, perturbation wave number $k_y = 2$, equilibrium wave number $k_x = 3$, equilibrium velocity $U_0 = 1$ and relaxation time $F_t = 5$. . .	127
5.22	Time evolution of vorticity for $U_0 = 1$, $\eta = 0.33$, $k_x = 3$, $F_t = 5$ and $k_y = 2$ and Mach number $M=0.5$	128
5.23	Time evolution of divergence of velocity ($\nabla \cdot U$) for $U_0 = 1, \eta = 0.33$, $k_x = 3$, $F_t = 5$ and $k_y = 2$ and Mach number $M=0.5$	128

5.24	Vortex evolution plots of Gaussian profile for $\omega_0 = 5.0$, $F_t = 5$, $\eta = 0.3$ and Mach number $M = 0.5$ (compressible limit).	130
5.25	Vortex evolution plots of co-rotating vortex of equal magnitude separated by a distance such that total circulation $C = \frac{\iint \omega dxdy}{\iint dxdy}$ is non-zero through out the simulation for $\omega_0 = 5.0$, $F_t = 5$, $\eta = 0.3$ and Mach number $M = 0.5$ (compressible limit).	131
5.26	Vortex evolution plots of co-rotating unlike profile for $\omega_0 = 5.0$, $F_t = 5$, $\eta = 0.3$ and Mach number $M = 0.5$ (compressible limit). Total circulation $C = \frac{\iint \omega dxdy}{\iint dxdy}$ is zero through out the simulation	131
5.27	Vortex evolution plots of elliptic profile for $\omega_0 = 3.0$, $F_t = 5$, $\eta = 0.3$ and Mach number $M = 0.5$ (compressible limit).	132
5.28	Contour plot of fluid vorticity ($\omega = \nabla \times \vec{U}$) obtained from molecular data. The grain velocity in the bins are fluidized through a 55×55 grid to construct vorticity. The horizontal color bar at the bottom show the magnitude of vorticity and blue and red strips show the opposite sign vorticity respectively. Perturbation mode $m = 2$, initial coupling parameter $\Gamma_0 = 50$, screening parameter $\kappa = 1.0$ equilibrium spatial period number is $n_0 = 3$ and shear velocity $U_0=1$. Vorticity plots generated from microscopic velocity show Kolmogorov instability in Molecular Dynamics, the micro scale heating quickly destroy the vorticity structures. The dimensionless parameters are initial Reynolds number $R = 235$ and Mach number $M = 1$. Simulation box is doubly periodic of size $L_x = L_y = 443$	137
5.29	Contour plot of fluid vorticity ($\omega = \nabla \times \vec{U}$) obtained from computational fluid dynamics simulation. Input parameters are: number for perturbation mode $m_0 = 2$, initial viscoelastic coefficient F_t ($\Gamma = 50, \kappa = 1.0$) $= 2.0$, spatial period number $n_0 = 3$ and shear velocity $U_0=0.028$ with system size $L_x = L_y = 4\pi$. The dimensionless parameters are initial Reynolds number $R = 235$ and Mach number $M = 1$	138

5.30	Perturbed kinetic energy in linear-log scale for number for perturbation mode $m_0 = 2$, initial coupling parameter $\Gamma_0(t = 0) = 50$, screening parameter $\kappa = 1.0$, spatial period number $n_0 = 3$ and shear velocity $U_0=1$, Reynolds number $R = 235$ and Mach number $M = 1.0$. Calculated growth rate (γ_g) from simulation is 0.01 with system size and number density $L_x = L_y = 443$ and $\bar{n} = 1/\pi$	139
5.31	Perturbed kinetic energy in linear-log scale for number for perturbation mode $m_0 = 2$, initial viscoelastic coefficient F_l ($\Gamma = 50, \kappa = 1.0$) = 2.0, spatial period number $n_0 = 3$ and Reynolds number $R = 235$ and Mach number $M = 1.0$. Calculated growth rate (γ_g) from simulation is 0.015. System size and number density are $L_x = L_y = 4\pi$ and $\bar{n} = 400$	139

List of Tables

5.1	Table for normalized quantities, here length $\lambda_{Dt\ ix}^2 = \frac{\epsilon_0 k_B T_i}{Z_d e^2 n_{d0}} \simeq \frac{\epsilon_0 k_B T_i}{e^2 n_{i0}} \simeq \lambda_{Di}^2 \simeq \lambda_D^2$, dust plasma frequency $\omega_{ph}^2 = (Q_h^2 n_{h0} / \epsilon_0 M_h)$, $Q_h = Z_h e$ and M_h are charge and mass of single dust particle. . .	121
5.2	Table for normalized quantities used in MD simulation	135
5.3	Table for normalized quantities, here length $\lambda_{Dt\ ix}^2 = \frac{\epsilon_0 k_B T_i}{Z_d e^2 n_{d0}} \simeq \frac{\epsilon_0 k_B T_i}{e^2 n_{i0}} \simeq \lambda_{Di}^2 \simeq \lambda_D^2$, dust plasma frequency $\omega_{ph}^2 = (Q_h^2 n_{h0} / \epsilon_0 M_h)$, $Q_h = Z_h e$ and M_h are charge and mass of single dust particle. . .	135
5.4	Table for values of parameters used in MD and CFD simulations. In above table table l is shearing length $l = L/n_0$	136
1	Table for normalized quantities. where length $\lambda_{Dt\ ix}^2 = \frac{\epsilon_0 k_B T_i}{Z_d e^2 n_{d0}} = \lambda_{Di}^2$, dust plasma frequency $\omega_{ph}^2 = (Q_h^2 n_{h0} / \epsilon_0 M_h)$. $Q_h = Z_h e$ and M_h are charge and mass of single dust particle.	163

Introduction

Gases, liquids and solids are all made up of a large number of atoms and molecules. They differ primarily from each other in two aspects: (a) the average distance between the particles which is decided largely by the Potential Energy (P.E) between particles and (b) the extent to which the ions or molecules move randomly which is governed by the Kinetic Energy (K.E) of the molecules. If the P.E per particle exceeds the K.E per particle [say $\Gamma = \text{P.E} / \text{K.E} > 1$], spatial correlations tend to increase near the vicinity of each particle. In general, the matter becomes more active when the temperature rises [see Fig.1.1]. The dimensionless parameter Γ , which decreases from left to right in Fig.1.1 decides whether the substance will be in solid, liquid, gas or plasma phase. In solids, particles only vibrate around their mean position. However, the atoms in fluids (Gases and Liquids) move around in all possible directions. Fluids have an inherent viscous property (or dissipation)

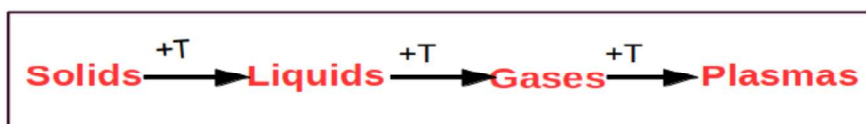


Figure 1.1: Phase transition of matter due to increasing temperature.

as particles transfer momentum across. Thus, in general, spatial correlation acts like a restoring force or has an elastic effect. Hence any fluid medium can be thought of as a “viscoelastic medium”, i.e as a medium which has both solid-like elastic properties and liquid-like viscous properties. Thus depending on the value of Γ , the viscous and elastic or viscoelastic properties can change, in a correlated medium. For example, synthetic polymers, human tissue, polymeric fluids (melts and solutions) used to make plastic articles, food systems such as dough used to make bread and pasta and biological fluids such as synovial fluids found in joints display significant viscoelastic effects [26].

Plasma is an ionized gas consisting of ions and electrons as well as neutrals. The Coupling parameter Γ for charged particle is

$$\Gamma = \frac{q^2}{4\pi\epsilon_0\bar{r}k_B T} \propto \frac{q^2 n^{1/3}}{T} \quad (1.1)$$

where \bar{r} , q , T and k_B are the mean inter-particle distance, particle charge, temperature and Boltzmann constant respectively. In a conventional plasma system, low density and high temperature make coupling parameter to be much less than one. Thus electrons and ions are very weakly correlated or behave like an ideal fluid. Let us now introduce large micron or sub-micron sized grains in this weakly correlated plasma. The grains tend to accumulate a large negative charge because of the relatively high mobility of electrons. This massive charged grain medium with very low density exhibits a strong correlation with $\Gamma_{grain} > 1$. Such plasmas are called “Complex plasma” or “Dusty plasma”. From Eq.1.1, it is clear that Γ can be made greater than one by increasing density or by reducing temperature or by increasing charge. For example, highly dense astrophysical plasma ($\approx 10^{26}/cm^3$) [27] and ultra cold plasma ($T_e \approx 100mk$), ($T_i \approx 10\mu K$) [28] also behave like strongly coupled plasmas.

1.1 Overview of dusty or Complex plasma

Micron-sized dust grains get highly charged when immersed in a conventional plasma because of relatively high mobility of electrons [1]. The average charge on a single dust grain is typically $\sim 10^3e - 10^4e$, where e is the absolute electronic charge. There are many examples of plasma in nature wherein large sized grains interact with an ambient plasma and play an important role, for example, comets, planetary rings, white dwarf, earth's atmosphere and in laboratory conditions such as plasma processing reactors, plasma torch and fusion devices [3].

These charged grains or dust particles interact via a shielded Coulomb interaction or as “Yukawa potential” as the ambient plasma shields the bare grain charge. Such plasmas can be characterized by two non-dimensional parameters $\kappa = a/\lambda_D$ (where a is average inter-grain spacing and $\lambda_D = \lambda_i\lambda_e/\sqrt{\lambda_i^2 + \lambda_e^2}$ is the Debye length of the background plasma and λ_i, λ_e are the Debye length of electron and ion respectively) and the coupling parameter $\Gamma = Q_h^2/(4\pi\epsilon_0ak_BT_h)$ wherein Q_h and T_h are charge and temperature of grains respectively. Γ and κ relation of dusty plasma with conventional plasma can be represented as follow $\Gamma = \frac{Q_d^2T_d}{3e^2N_DT_i\kappa} = \frac{Z_d^2T_d}{3N_DT_i\kappa}$, where $Q_h = Z_he$, T_i are total charge over dust and the temperature of ion. N_D is plasma parameter $N_D = 4\pi n\lambda_D^3/3$. It is found that in conventional plasma for densities of the order $10^{11} - 10^{16}cm^{-3}$, temperatures ranging $10^4 - 10^8K$ with $Z = 1$, the range of Γ parameter exists $10^{-7} - 10^{-3}$. Therefore, conventional plasmas are found to be in weak coupling limit.

For dust grain system, high charge over dust $Q_h = Z_he = 10^3 - 10^4e$ makes coupling parameter grater than unity. A system with $1 < \Gamma < \Gamma_c$, is in liquid state with strong correlation. It is found that crystallization occurs when Γ is grater than $\Gamma_c = 168 \pm 2$. In laboratory experiments, a grain medium can easily attain different states such as gaseous-like, liquid-like and crystal-like phases with varying density, charge, temperature and size of the dust particles which can be characterized by

Chapter 1. Introduction

κ and Γ values [1, 4, 5, 29, 30]. Grain medium in a conventional plasma responds in two qualitative by different ways: [I] When $r_h < \lambda_h < a$, where r_h is the mean radius of a single dust grains, in this case, dust grain number density is low and the interaction between the grains is weak. Such a grain medium is called “dust-in-plasma” or “grain-in-plasma”. [II] When $r_h < a < \lambda_h$, in this case dust number density is relatively high and grains interact via screening Coulomb potential (or Yukawa potential). The dust grain medium shows a collective behavior on its own slow time scale and long length scales and is known as “dusty plasma”.

To understand the physical phenomena in a range of time scales and length scales in strongly coupled dusty plasma experiments [6, 29, 31], typically, one of the following approaches is (are) used: Molecular Dynamics [7, 22, 32, 33, 34], phenomenological hydrodynamic models [9, 10, 11, 12], particle-in-cell Monte Carlo simulation [35], Quasi-localized charge approximation [36, 37] and orbital motion limiter theory [38]. In laboratory experiments, because of longer time scale and large spatial scale of dust grain dynamics, each dust grain can be visualized (by unaided eye) and tracked by simple optical cameras [29]. A variety of interesting phenomena, including grain charging [39], interaction between charged particles, momentum exchange between different species [40], dust ion acoustic wave (DIAW), dust acoustic wave (DAW) [37] and other studies have been investigated in dusty plasma. Our primary focus in this Thesis is in the liquid-like state which can sustain shear flows. To study shear flow instability in a strongly coupled dusty plasma a modified hydrodynamic model approach and a molecular dynamics approach have been considered.

It is well known that two-dimensional macroscale shear flows are susceptible to instabilities leading to macroscale vortical structures. The linear and nonlinear fate of such a macroscale flow in a strongly coupled medium is a fundamental problem.

1.2 Motivation

As described earlier, a massive grain in a plasma attains a large mean charge Q . Also, the electrons and ions behave as a massless medium and attain Boltzmann distribution on time scale of slow dust grain dynamics. Thus, Dusty plasma experiments allow direct observation of instantaneous position and instantaneous velocity of each dust grain. This unique capability makes Molecular Dynamics (MD) simulation and direct comparison with experiments a very attractive possibility. In a Molecular Dynamics study, classical Newton's second law of motion is solved for each particle. In this method, the force between the dust-grains is calculated by a grain-grain interaction potential. From Molecular Dynamics study, using data of individual grains, the continuum "fluid" quantities may be obtained by averaging. Thus, fluid models and particle (or Molecular Dynamics) models may be compared with experiments. Using a Molecular Dynamics simulation, many interesting features of dusty plasma, for example, phase transition[41], study of transport coefficients such as shear and bulk viscosities [32], Maxwell relaxation time [22], heat conduction, wave dispersion [42], self diffusion [33], fluid instability such as shear-driven Kelvin-Helmholtz instability [7] and grain crystallization [43], have been addressed in the past.

Hydrodynamic like flows and instabilities (Rayleigh Benard instability, Rayleigh Taylor instability, Kelvin-Helmholtz instability etc.) are generally studied to understand stability and transition of flows. In general, hydrodynamic flow related problems are addressed by modeling the system as continuum where the average number density (\bar{n}) of the medium is high enough (for example, for water $\bar{n} = 3.33 \times 10^{28} \text{ m}^{-3}$ and for ideal gas $\bar{n} = 2.5 \times 10^{25} \text{ m}^{-3}$) inspite of the range of the interaction between particles being very short. On the other hand, dusty plasma modelled as Yukawa liquids are very low density soft matter [44], for example, $\bar{n}_{\text{grain}} \sim 10^8 \text{ m}^{-3}$. In spite of relatively low number density of grain ($\bar{n} = 10^7 - 10^8 \text{ m}^{-3}$) as compared to conventional liquids ($\bar{n} = 3.33 \times 10^{28} \text{ m}^{-3}$),

Chapter 1. Introduction

grains form liquid phase. This “liquid phase” is often treated as a modified Navier-Stokes continuum. It is also modeled as particles system interacting via a modified Coloumb potential.

It is well known that whenever there is a shear in macroscopic velocity profiles, a viscous shear heating occurs at the microscale. For some fluids, it is not necessary that the shear heating lead to increase in the local temperature at the shear layer. This is because heat conduction can be so rapid at the location of the velocity shear where the heat is generated that as soon as heat is generated, it is carried away or transported away due to thermal conduction. In general, the effect of viscous shear heating and thermal conduction is measured by a dimensionless parameter, known as Brinkman number [45, 46] $B_r \approx \eta(\Delta V)^2/\lambda\Delta T$ (where η , λ are shear viscosity and thermal conductivity and ΔV , ΔT are difference in mean flow velocity and temperature respectively) [46]. (This number can also be represented by the product of two other non-dimensional number, viz. $B_r = P_r E_c$, where P_r and E_c are Prandlt and Eckert numbers. Prandlt number is the ratio of momentum diffusivity to thermal diffusivity and signifies how fast the thermal diffusion takes place in comparison to momentum diffusion [47]. Eckert number is the ratio of the kinetic energy to the enthalpy driving force for heat transfer). When the value of dimensionless number B_r is less than 1 i.e $B_r \ll 1$, the energy dissipation or shear heating can be neglected [48]. For example, for Navier-Stokes like fluids, B_r which is the ratio of viscous heating to thermal conduction, is much smaller than unity ($\approx (1 - 17) \times 10^{-8}$) [49] and hence shear heating does not alter the local transport properties in any significant way. Crucial to this discussion is the fact that thermal conduction λ is, typically, dependent on the average number density \bar{n} of the system. Thus for high \bar{n} , Brinkman number B_r can be expected to be much less than one and for low \bar{n} , B_r may be expected to be comparable to 1.

In Fig.1.2 a laboratory experiment used to set up a macroscale shear flow in a dusty plasma experiment is shown. As described earlier, the bare grain charge gets

electrostatically shielded by the background plasma interact via screened Coulomb potential or a Yukawa potential. Dusty plasma modeled as Yukawa liquids are very low density soft matter [44], for example, $\bar{n}_{grain} \sim 10^8 m^{-3}$. Hence these system in liquid state may be expected to have a relatively less thermal conductivity compared to higher density liquids such as water. If the thermal conductivity of the medium is relatively small. The generated heat may be accumulated in the shear zone. In the past, using classical molecular dynamics (MD) simulations, the development and propagation of a nonlinear heat front and shear heating in parallel shear flows of a strongly coupled Yukawa liquid was identified [8]. In laboratory experiments, macroscopic shear flows have been induced by an external laser-drive in Yukawa liquids [6, 31]. To study shear heating phenomena from an atomistic (or particle) level, we perform a classical first principle MD study considering Kolmogorov flow (continuous gradient in velocity profile), as the initial flow profile as continuous gradient in the shear flow profile would be relatively easily attainable in a laboratory dusty plasma experiments than sharp velocity gradient profiles [34]. A detailed study of shear heating in macroscopic flows in Yukawa liquids using a molecular dynamics simulation has not yet been addressed where the grains interact with each other through a shielded Coulomb potential, due to the screening provided by background free electrons and ions. Therefore, it is worthwhile to ask as to what would be the flow dynamics for large Brinkman number ($B_r \sim 1$) fluids system such as Yukawa liquids when the macroscale shear flow is initialized in a Yukawa liquid, where the viscous heat may be expected to alter the local transport coefficient of the medium in a non-trivial fashion? What would be the effect of shear heating over large scale (macro-scale) vortex dynamics due to small scale molecular heating (micro-scale)? How does average coupling strength (Γ) of the system change due to microscale heating and in turn alters the vortex dynamics? To address some of these questions, it becomes necessary to perform a classical first principle simulation such as molecular dynamics where no assumption or approximations regarding transport coefficients are introduced.

In parallel shear flows [7, 8, 19], the spatio-temporal evolution of instabilities as

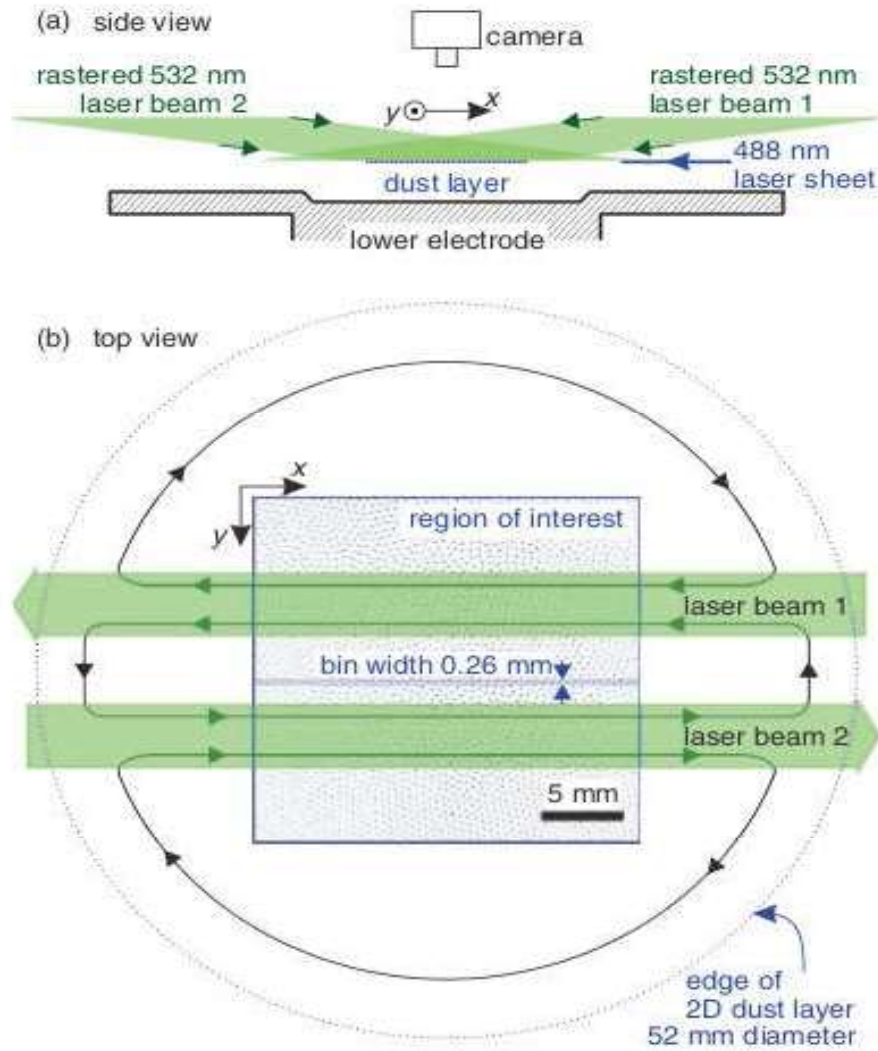


Figure 1.2: A typical experimental example to setup shear flow in a laboratory dusty plasma using laser [Figure adapted from [Yan Feng et.al. PRE, 83 \(2012\)](#)]

an initial value problem have been studied using molecular dynamics in a micro-canonical ensemble. As no attempt was made to control the temperature of the liquid during the simulation, the flow evolves under adiabatic conditions and the shear heat generated due to shear heating. An increase in overall temperature and also strong localized gradients eventually destroy large scale vortex structures. We investigate whether or not, at least in principle, it is possible to address macroscale vortex dynamics using MD simulation and at the same time maintain the grain bed at the desired temperature. For this purpose, using a thermostat based on configurational space degrees of freedom [50, 51, 52, 53], it is demonstrated that the average coupling strength can be controlled without compromising the effects of strong correlations on the macroscopic shear flow and vortex dynamics.

Unlike parallel shear flows discussed earlier, there is an important class of 2D coherent flows, namely, rotational or circular flows. Strong coupling effects of the Dusty plasma medium tend to couple the optical or transverse wave dynamics to the acoustic or compressional wave dynamics [54]. However, this initial condition with shear also may introduce strong shear heating. This important aspect is investigated here. The nonlinear structures found here resemble nonlinear elastic-like wave. Understanding of such wave propagation has many important applications in geophysics, petroleum engineering and mining, earthquakes and seismology [55] as well.

In general, the governing equations for Newtonian fluid dynamics is Navier-Stokes equations, have been known for over 150 years. As discussed earlier, strongly coupled dusty plasma can be often treated like a fluid and modeled by modified Navier-Stokes equations called as generalized hydrodynamics models [9, 10]. For example, a recently proposed generalized hydrodynamic model for strongly coupled plasma system referred as the viscoelastic-density functional (VEDF) model uses a density functional method [13]. In another work, yet another generalised hydrodynamic approach is used to simplify the calculation of dynamical structure factor of strongly coupled plasmas using fluctuation-dissipation theorem [14]. In

this Thesis, a generalized hydrodynamic model with a single relaxation E_t is used to model the “elastic” nature of strongly coupled dusty plasma. First an incompressible version is used to study linear and nonlinear properties of a parallel shear flow, namely, an undriven Kolmogorov flow as an initial value problem in strongly coupled dusty plasma has been addressed. The transition from stable to unstable flow has been found to occur at a critical value of Reynolds number R_c such that for $R < R_c$, growth rate is less than zero (i.e. or damped) and for $R > R_c$ growth rate greater than zero (i.e. or unstable). A novel observation is that unlike Kolmogorov flow in Navier Stokes hydrodynamics which is neutrally stable for $R < R_c$, Kolmogorov flow in strongly coupled dusty plasma is found to have no such neutral stability, however small the non zero value of E_t may be.

When density and temperature of the fluid element system spatio-temporal variations, one can not ignore the effect of compressibility. The compressibility effect on shear flow is an important problem in the field of hydrodynamic flows and has been addressed in the past using both atomistic [56, 57] (MD) and continuum (fluid) approaches [9, 10, 11, 12]. It was found that compressibility stabilizes the instability and changes the nature of stability from “exchange of instability” to “over-stability” [58]. Similarly in strongly coupled plasma, Kelvin-Helmholtz instability in the presence of compressibility with quasi-neutrality and mixed boundary (periodic along flow and bounded along the direction perpendicular to the flow) conditions [11] has also been shown to be relatively stable as compared to the incompressible limit. In this Thesis, the effect of compressibility on the onset of laminar to turbulent transition of Kolmogorov in strongly coupled plasma and on rotational shear flow such as monopolar, Rankine-like vortex and other structures for non-zero variation of mean density, pressure and electrostatic potential perturbations have been addressed. Finally, for non-zero variation of mean density, pressure and electrostatic potential perturbations using MD and CFD simulations, we perform a comparative study of compressible parallel shear flow using Molecular dynamics (MD) simulation and computational fluid dynamics (CFD) using

Kolmogorov flows as initial conditions.

1.3 Organization of the thesis

In this Thesis, detailed analytical and numerical studies of various linear and non-linear properties of shear flow in strongly coupled dusty plasma have been described. The Chapters of this thesis are organized in the following fashion:

Chapter-2: Dusty plasma can be treated as a continuum or discrete particle system depending upon the value of Γ and the phenomena studied. Typically, a Computational Fluid Dynamics (CFD) based generalized hydrodynamic model is used for continuum description at low Γ values and long wavelength and Molecular dynamics is used for capturing particle effects at arbitrary Γ values. In this Chapter, we present the basic model and algorithm of fluid and molecular dynamics simulation. As discussed, in general, fluid motion is governed by the well-known Navier-Stokes equations. However, strongly coupled dusty plasma can be modeled by modified Navier-Stokes equation where the effect of finite spatial correlation is incorporated via a memory effect (memory dependent fluid equations). A set of coupled and nonlinear partial differential equations is derived from the basic laws of conservation of mass, momentum and energy and phenomenological complex viscosity coefficient. Various numerical aspects of computational fluid dynamics and molecular dynamics simulation is presented in this Chapter. To understand shear flow instability from a continuum point of view a new CFD code has been developed based on a pseudo spectral method has been chosen. As strongly coupled dusty plasma is often modeled using Yukawa interaction between grains, a Molecular Dynamics procedure is used wherein Newton's second law of motion has been used to simulate the N-body problem.

Chapter-3: It is well known that, whenever there is a shear in macroscopic velocity profiles, viscous shear heating occurs at the microscale. Recently, laboratory

Chapter 1. Introduction

experiments [Fig.1.2] and MD studies of shear flows in strongly coupled Yukawa liquids have indicated occurrence of strong molecular shear heating. In dusty plasma experiments, to study shear flow generate laser driven has been shown to be effective [Fig.1.2]. The velocity profile thus obtained experimentally is continuous in space without sharp spatial changes. Therefore, to study shear heating phenomena from atomistic level, we consider Kolmogorov flow (continuous gradient in velocity profile) as an initial input profile because we believe it is relatively easily attainable in laboratory dusty plasma experiments. Rotational shear flows are addressed with monopolar coherent vortex for example, Rankine vortex source in strongly coupled Yukawa medium using MD simulation. The results thus obtained in our MD simulations may be directly comparable with experiments. The findings may have relevance to wave propagation in geophysics, petroleum engineering and mining, earthquakes and seismology [55]. In this Chapter, the emergence of non-linear elastic waves from monopolar coherent vortex source in strongly correlated Yukawa medium using Molecular dynamics simulation has been also studied.

Chapter-4: To understand the vortex dynamics of strongly coupled molecular fluids undergoing macroscale shear flows and molecular shear heating, MD simulation has been performed, which allows the macroscopic vortex dynamics to evolve while at the same time, “removes” the microscopically generated heat without using the velocity degrees of freedom. We demonstrate that by using a configurational thermostat in a novel way, the microscale heat generated by shear flow can be thermostatted out efficiently without compromising the large scale vortex dynamics. In present work, using MD simulations, a comparative study of shear flow evolution in Yukawa liquids in presence and absence of molecular or microscopic heating is presented for a prototype shear flow namely, Kolmogorov flow and a rotational shear flow namely, monopole and Rankine-like vortex are considered.

Chapter-5: It was found that several phenomena common to conventional hydrodynamic fluids, such as shear waves, [10] shear flow instability (Kelvin-Helmholz)

[11, 59], nonlinear saturation, vortex roll formation etc have been investigated in the field of strongly coupled dusty plasma using generalized hydrodynamic model. In this chapter, transition of stable Kolmogorov flow to unstable regime is demonstrated for strongly coupled dusty plasma using a generalized hydrodynamic fluid model where in strong coupling effects are incorporated via viscoelastic relaxation time F_t in the incompressible limit using a linear stability analysis and nonlinear pseudo spectral simulation.

In the above studies, in the incompressible, compressible limit, density and potential variations have not been considered. Fluids sustaining flow speeds with a good fraction of sound speed in the medium are found to be compressible. Thus, density and temperature of the fluid element have spatio-temporal variation, which leads to effects of compressibility. In second section of this Chapter, linear and nonlinear properties of Parallel (Kolmogorov flow) and Rotational flow in the presence of variable density, pressure and electrostatic potential are addressed using generalized compressible hydrodynamic model. A comparative study has been performed between computational fluid dynamics and molecular dynamics for compressible Kolmogorov flow. While the MD considers the interaction of grains using a screened Coulomb or Yukawa potential, the compressible fluid model includes the effect of non-uniformity in density and the consequent non- zero divergence of velocity, the effect of electrostatic potential and pressure while the effect of correlations is included phenomenologically using a visco-elastic relaxation time.

Finally, comparative study between CFD and MD results for parallel shear flow namely K-flows is also reported.

Chapter-6: A summary and conclusion of this thesis work is presented. The important problems that remain unsolved are also discussed point wise which could be interesting for further research.

2

Molecular and computational fluid dynamics

Classical molecular dynamics (MD) and computational fluid dynamics (CFD) allow one to study large-scale hydrodynamic phenomena from two very different viewpoints viz microscopic or MD and macroscopic or CFD respectively. Classical molecular dynamics provides the system behavior in terms of the dynamics of individual atoms or molecules, using Newton's law. In MD simulation, Newton's second law of motion is used to simulate the N-body problem. The mean or average behavior is then extracted using the principle of equilibrium statistical mechanics or non-equilibrium statistical mechanics which ever is applicable to the problem of interest. No assumptions are made as to the transport coefficients, for example, viscosity, diffusion, thermal conductivity etc are all self consistently obtained. In contrast, CFD describes the motion of a fluid element from a macroscopic level in terms of the transport of mass, momentum, and energy of a system and a set of assumed transport coefficients.

Depending upon the problem of interest, a dusty plasma system may be treated as a fluid medium or as a collection of interacting particles. In this Chapter, we

present the basic model and algorithm of fluid and molecular dynamics simulation to be used in this Thesis work.

Fluid motion is governed by a set of coupled, nonlinear partial differential equations derived from the basic laws of conservation of mass, momentum and energy and assumed transport coefficient which may be phenomenological. There are several ways to solve a set of the fluid equations in time. For example, Adams-Bashforth method [60], Crank-Nicolson method [61], fourth Runge-Kutta method [62] and Rahman midpoint predictor/corrector. In the Section, we present the development of a pseudo-spectral code. In space, spectral or Fourier synthesis is used. In the following, we present the structure of the CFD code developed using the example of the Navier-Stokes equation. The actual equation used for dusty plasma as a visco-elastic fluid is presented in Appendix-A.

2.1 Fluid simulation : Pseudo Spectral method

In 1822 Claude Navier and in 1845 George Stokes formulated the famous Navier-Stokes equation that describes the dynamics of fluids. Besides the Navier-Stokes equation which describes conservation of momentum, two additional equations namely continuity equation describes mass conservation and a state equation describes energy conservation are needed to simulate fluids. In general, these are partial differential equations. In the following, we give the outline of how pseudo spectral method, which is used to solve Navier-Stokes equation. As indicated earlier, our fluids equation [see Appendix-A] is for viscoelastic fluids.

Spectral methods are a class of techniques used in applied Mathematics and scientific computing to numerically solve the partial differential equations (PDEs). A popular method is Fourier Spectral Method, which is based on Fourier Transform [63]. Fourier spectral methods (e.g pseudo spectral method, Galerkin method) have emerged as powerful computational techniques for the simulation of complex

continuum problem have been addressed using a pseudo-spectral method. Since 1970 spectral methods have been extensively used in fluid dynamics. For example, several interesting phenomena such as turbulent flow, vortex dynamics, fluid instabilities, geomagnetism, aerodynamic and astrophysical related phenomena. In 1972 Orszag [64] developed a Fourier series based method for the solution of isotropic turbulence, which he termed as a pseudo-spectral method. Since then many variants have been developed.

To demonstrate how pseudo spectral method works, a non-dimensional (velocity and space are normalized by characteristic velocity V and characteristic length L and density ρ is normalized to some equilibrium density). Continuity and Navier-Stokes momentum equations have been considered:

$$\frac{\partial \rho}{\partial t} + \vec{\nabla} \cdot (\rho \vec{U}) = 0 \quad (2.1)$$

$$\frac{\partial \rho}{\partial t} + \rho \vec{\nabla} \cdot \vec{U} + \vec{U} \cdot \vec{\nabla} \rho = 0 \quad (2.2)$$

where $\vec{U} = u\hat{i} + v\hat{j}$. When the density of fluid does not vary with space and time then $\frac{\partial \rho}{\partial t} + \vec{U} \cdot \vec{\nabla} \rho = 0$ or $\frac{h\rho}{ht} = 0$. Then Eq.2.2 with $\frac{h\rho}{ht} = 0$ may be described as $\vec{\nabla} \cdot \vec{U} = 0$ and the medium is said to be in the incompressible limit. For incompressible, two dimensional fluid in a $(x-y)$ plane, a scalar function ψ , called the stream function and can be defined in such a way that the incompressibility is automatically satisfied. For example, stream function ψ can be represented conventionally in the following way $\vec{U} = \hat{z} \times \nabla \psi$ or $u = \partial \psi / \partial y$ and $v = -\partial \psi / \partial x$, where \hat{z} is a unit vector, normal to the $x - y$ plane. Poisson's equation can be obtained by substituting velocity component in the stream function form in vorticity definition $\omega = (\vec{\nabla} \times \vec{U}) \cdot \hat{z}$ as

$$\omega = -\nabla^2 \psi \quad (2.3)$$

Chapter 2. Molecular and computational fluid dynamics

Navier-Stokes equation in velocity form is-

$$\frac{\partial \vec{U}}{\partial t} + \vec{U} \cdot \nabla \vec{U} = \frac{1}{R} \nabla^2 \vec{U} - \frac{\nabla P}{\rho} \quad (2.4)$$

where ρ , \vec{U} , P , R are density, fluid flow velocity, pressure and Reynolds number ($R = UL/\nu$) and ν is kinematic viscosity. Curl of Eq.2.4 gives the Navier-Stokes equation in vorticity form, which is as follows

$$\frac{\partial \omega}{\partial t} + \vec{U} \cdot \nabla \omega = \frac{1}{R} \nabla^2 \omega \quad (2.5)$$

where $\nabla^2 = \frac{\partial^2}{\partial x^2} + \frac{\partial^2}{\partial y^2}$ and $\omega = \vec{\nabla} \times \vec{U}$. Now Eq.2.5 becomes

$$\frac{\partial \omega}{\partial t} + u \frac{\partial \omega}{\partial x} + v \frac{\partial \omega}{\partial y} = \frac{1}{R} \left(\frac{\partial^2}{\partial x^2} + \frac{\partial^2}{\partial y^2} \right) \omega \quad (2.6)$$

To describe the pseudo-spectral method, we recall that the discrete Fourier transform of a periodic function, say vorticity in one-dimensional space $\omega(x)$:

$$\omega_k = \frac{1}{N} \sum_{j=-N}^{N+1} \omega(x_j) e^{-ikx_j} \quad (2.7)$$

The inversion formula

$$\omega(x_j) = \frac{1}{N} \sum_{k=-N}^{N+1} \omega(k) e^{+ikx_j} \quad (2.8)$$

Taking the Fourier transform of Eq.2.3 in \mathbf{K} -space (k_x, k_y) , we get.

$$\frac{\omega_k}{(k_x^2 + k_y^2)} = \psi_k, \quad (2.9a)$$

$$u_k = -\mathcal{T}_y \psi_k, \quad (2.9b)$$

$$v_k = \mathcal{T}_x \psi_k \quad (2.9c)$$

Using Eq.2.8, derivatives may be transformed as:

$$\frac{\partial \omega}{\partial x} = -\mathcal{T}_x \omega_k \quad (2.10a)$$

$$\frac{\partial \omega}{\partial y} = -\mathcal{T}_y \omega_k \quad (2.10b)$$

K-space Eq.2.5 becomes:

$$\frac{\partial \omega_k}{\partial t} + FFT[NLT] = -\frac{1}{R} (k_x^2 + k_y^2) \omega_k \quad (2.11)$$

where NLT implies Non-Linear Terms ($\vec{U} \cdot \vec{\nabla} \omega$) and FFT implies Fast Fourier Transform, a discrete Fourier transform algorithm which reduces the amount of computational time, for N points, from $2N^2$ [from discrete Fourier transform (DFTs)] to $2N \log_2 N$ [from fast Fourier transform (FFTs)]. Fourier transform of non-linear terms ($u \frac{\partial \omega}{\partial x} + v \frac{\partial \omega}{\partial y}$) is obtained in the following fashion, using FFTW-library [65].

$$NLT = \left(u \frac{\partial \omega}{\partial x} + v \frac{\partial \omega}{\partial y} \right) = IFFT[u_k] * IFFT[(-\mathcal{T}_x \omega_k)] + IFFT[v_k] * IFFT[(-\mathcal{T}_y \omega_k)] \quad (2.12)$$

where $IFFT$ stands for inverse Fourier transform.

2.1.0.1 Anti-aliasing or de-aliasing

Aliasing is a kind of numerical error, which generally arises when a function is discretely sampled. According to Nyquist sampling theorem, “the sampling frequency should be at least twice of the highest frequency in the signal”. In Navier-Stokes case, the spectral discretization is in space, therefore the idea about sampling frequency of Nyquist theorem is applied for wave number space. Hence, if L and N are the system size and number of grid points respectively, then step size will be $\Delta x = L/N$, the wave number $k = 2\pi/L$ must be in the range of $-k_{Nyquist} < k < +k_{Nyquist}$, where $k_{Nyquist} = (1/2)(2\pi/\Delta x) = \pi/\Delta x$ (highest frequency) is the Nyquist wave-number. For non-linear term present in the Navier-Stokes equation, the Nyquist frequency criteria should be well satisfied. Let us

discuss a one dimensional case. Let $f_1(x) = \exp(\mathcal{T}k_1x)$, $f_2(x) = \exp(\mathcal{T}k_2x)$, then nonlinear term is $f_1(x)f_2(x) = \exp(\mathcal{T}(k_1 + k_2)x)$. If f_1 and f_2 are presented on the numerical grid, then $k' = (k_1 + k_2)$ may exist outside the the Nyquist limits ($k_{Nyquist}$) and can no more be represented on the grid. For example, [see Fig.2.1], consider **K**-grid in the range $[k_{t\ ax}] = [-K_0 + K_0]$. As discussed $k_1 + k_2$ may lie “outside” $[-K_0, K_0]$ and hence way calculated erroneously. This is an aliasing effect and leads to error and numerical instability.

There are several methods which one can use to remove such errors, which are known as anti-aliasing or de-aliasing. The easiest being the two-thirds rule introduced by Orszag [64]. Let $k_{t\ ax} = k_0$ denote the highest wave number resolved by the numerical grid. Non-linear terms are filtered according to 2/3-rule as follows:

$$\hat{f}(k, t) = \begin{cases} \hat{f}(k, t) & \text{if } k \leq 2k_{t\ ax}/3 \\ 0 & \text{else (zero padding)} \end{cases}$$

where $\hat{f}(k, t)$ is Fourier transform of function $f(x, t)$. As described earlier, to avoid the aliasing error in non-linear terms in Fourier space, zero-padding method is used. In 2/3 dealiasing rule, one sets to zero the last 1/3 of the high frequency modes and keeps the first 2/3 of the Fourier modes unchanged.

For a given **K**, Eq.2.11 is time dependent ordinary differential equation. There are several methods to solve time dependent differential equation, for example, Adams-Bashforth method [60], Crank-Nicolson method [61], Runge-Kutta method of order four [62] and Rahman midpoint predictor/corrector. However, for our purpose we have chosen Nordsieck-Gear predictor-corrector [66, 67] time stepping numerical method. In general, predictor-corrector methods, the corrector step may repeated to achieve accuracy in results. Due to the high accuracy of the Nordsieck-Gear predictor-corrector [66, 67], it is not necessary for the Nordsieck/Gear method to include corrector steps.

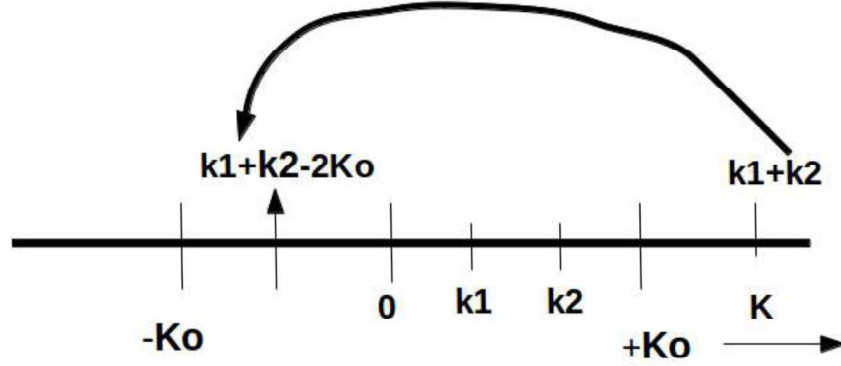


Figure 2.1: Figure shows the aliasing error: suppose as $k_1 + k_2$ arises out of a nonlinear interaction such that $k_1 + k_2$ lies “outside” $[-K_0, K_0]$. Hence, due to periodic boundaries, the information about $k_1 + k_2$ comes inside the simulation region wrongly.

2.1.0.2 Nordsieck-Gear predictor-corrector method

Nordsieck [1962] and Gear [1966, 1971] developed a time integration scheme on the basis of Taylor expansion [66, 67]. To describe how this method works, let us consider a simple second order differential equation, a simplest example being:

$$\frac{d^2 r}{dt^2} = F(t) \quad (2.13)$$

Using Taylor expansion, one can predict the quantities at time $(t + h)$ [where h is the step in time] from positions and their derivatives. Let us define variables in the following form: $q_1(t) = h \frac{dr(t)}{dt}$, $q_2(t) = \frac{h^2}{2!} \frac{d^2 r(t)}{dt^2}$, $q_3(t) = \frac{h^3}{3!} \frac{d^3 r(t)}{dt^3}$

Predicted values using Taylor expansions are:

$$r^p(t + h) = r(t) + q_1(t) + q_2(t) + q_3(t) \quad (2.14)$$

$$q_1^p(t + h) = q_1(t) + 2q_2(t) + 3q_3(t) \quad (2.15)$$

$$q_2^p(t + h) = q_2(t) + 3q_3(t) \quad (2.16)$$

$$q_3^p(t+h) = q_3(t) \quad (2.17)$$

Error in the acceleration $\delta q_2(t+h) = h^2 \frac{F(t+h)}{2} - q_2^p(t+h)$.

Corrected values using error value are:

$$r^c(t+h) = r(t+h) + c_0 \delta q_2(t+h) \quad (2.18)$$

$$q_1^c(t+h) = q_1(t+h) + c_1 \delta q_2(t+h) \quad (2.19)$$

$$q_2^c(t+h) = q_2(t+h) + c_2 \delta q_2(t+h) \quad (2.20)$$

$$q_3^c(t+h) = q_3(t+h) + c_3 \delta q_2(t+h) \quad (2.21)$$

where $c_0 = 1/6$, $c_1 = 5/6$, $c_2 = 1$, $c_3 = 1/3$ are magic numbers considered to maximize the stability of the numerical algorithm. To solve Navier-Stokes equation third order of Nordsieck-Gear predictor-corrector Eq.2.14-Eq.2.21 method has been used in our code.

2.1.0.3 Courant-Friedrichs-Lewy (CFL) condition

The problem of stability and convergence are important issues in the numerical solution of partial differential equations. The relationship between stability and convergence in numerical studies was first pointed out by Richard Courant, Kurt Friedrichs and Hans Lewy in 1920's, hence commonly used as "CFL condition" [68]. In a numerical scheme, to solve time and space dependent partial differential equation, it is found that by increasing the time steps while keeping the mesh size fixed or decrease the mesh size while keeping the time steps fixed, numerical scheme eventually becomes unstable. Therefore, it is clear that the choice of the time step or mesh size cannot be independent. For example, for a one-dimensional discretized differential equation, the CFL condition is

$$CFL = \frac{|u|dt}{dx} < 1 \quad (2.22)$$

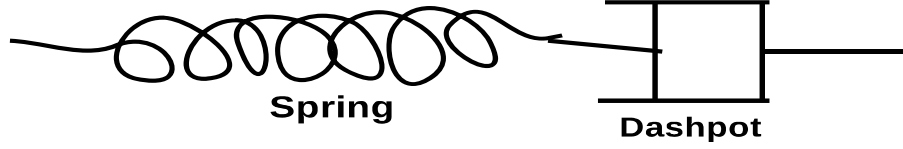


Figure 2.2: Maxwell model: Stress relaxation behavior using a spring and dashpot in series.

where u is the magnitude of the typical velocity in most cases the largest velocity in the system at which information can propagate while dx and dt are step sizes in space and time respectively. Non-linear pseudo-spectral code is parallelized using MPI [69] and Parallel FFTW library [65]. More details about parallelization is given in the Appendix-D.

2.1.1 Dusty plasma as a continuum medium

Computational Fluid Dynamics (CFD) provides a qualitative and sometimes quantitative prediction of fluid flows. In general, the governing equations for Newtonian fluid dynamics is Navier-Stokes equations. Strongly coupled dusty plasma can be often treated like a fluid and modeled by generalized hydrodynamic model [10] within the range of fluid limit (for $1 < \Gamma < \Gamma_t$) [5], here Γ_t is the liquid to the solid phase transition point. The physics of strong coupling of the dust fluid is incorporated via a viscoelastic coefficient $E_t = \frac{\eta}{G}$, where G , η are rigidity modulus and dynamic viscosity respectively. Viscoelasticity is the property of fluid having both the property of viscosity as well elasticity. In such viscoelastic medium, stress relaxes with time exponentially i.e as e^{-t/τ_m} .

To give a brief description about viscoelasticity and exponential stress relaxes with time, we describe Maxwell's Spring-Dashpot model [70, 71, 72] in a simple fashion. A dash-pot is a piston cylinder arrangement, filled with a viscous fluid responds like a viscous material. However, Spring responds as an elastic material. The series arrangement of spring (elastic) and dashpot (viscous) is called Maxwell's Spring-Dashpot model [as shown in Fig.2.2]. Suppose after applying stress σ , the

Chapter 2. Molecular and computational fluid dynamics

strain generated by spring and dashpot are ϵ_1 and ϵ_2 respectively. The total strain in the system.

$$\epsilon = \epsilon_1 + \epsilon_2 \quad (2.23)$$

According to Hooke's law $E = \sigma/\epsilon_1$, where E is Young's modulus. Dashpot follows Newton's law of viscosity (for a given temperature and pressure, the ratio of shear stress to shear rate is a constant, and is defined as the coefficient of viscosity). This implies $\eta = \sigma/\dot{\gamma}$, where $\dot{\gamma}$ is strain rate ($\dot{\gamma} = d\epsilon_2/dt$). Let us take time derivative of above Eq.2.23 and putting the values of ϵ_1 and ϵ_2 .

$$\frac{d\epsilon}{dt} = \frac{d\epsilon_1}{dt} + \frac{d\epsilon_2}{dt} \quad (2.24)$$

$$\frac{d\epsilon}{dt} = \frac{1}{E} \frac{d\sigma}{dt} + \frac{\sigma}{\eta} \quad (2.25)$$

In stress relaxation experiments $\frac{h\epsilon}{ht} = 0$. Then

$$\frac{d\sigma}{dt} = -\frac{E\sigma}{\eta} \quad (2.26)$$

Let us for now consider $F_t = \sigma/\eta$ is a coefficient and integrate the above equation.

$$\int_{\sigma_0}^{\sigma(t)} \frac{d\sigma}{\sigma} = -F_t \int_0^t dt \quad (2.27)$$

$$\sigma(t) = \sigma_0 e^{-t/\tau_m} \quad (2.28)$$

Eq.2.28 expresses three different states, which depend upon relaxation F_t parameter and timescale of interest t .

- For solids, stress never relaxed, i.e $F_t \longrightarrow \infty$ or $t/F_t \ll 1$.
- For viscous liquids, stress relaxes very fast, i.e $F_t \longrightarrow 0$ or $t/F_t \gg 1$.
- For viscoelastic fluids, stress relaxes with time as e^{-t/τ_m} .

It is important to note that in dusty plasma medium, relaxation time F_t is a constant parameter, representing several physical effects combined together [9, 10].

Also, in real dusty plasma experiments, multiple relaxation time scales may exist. Set of modified hydrodynamic equations for strongly coupled dusty plasma medium are as follow. Details about hydrodynamic equations are given in Appendix-A.

The continuity equation for dust fluid is as follows.

$$\frac{\partial \rho}{\partial t} + \nabla \cdot (\rho \vec{U}) = 0 \quad (2.29)$$

Momentum conservation equation (force balance equation) for dust fluid is as follows [11]

$$\left\{ 1 + F_t \frac{d}{dt} \right\} \left[\frac{d\vec{U}}{dt} + F'_b \right] = - \left[\nu \nabla^2 + \left(\frac{\nu}{3} + \xi' \right) \nabla(\nabla \cdot) \right] U \quad (2.30)$$

Here F'_b is body force per unit mass, this can be any external force for example, gravitational, electrostatic, pressure and driven forces. Let us consider for dusty plasma medium with density n_h and mass density $\rho_h = M_h n_h$, there are following forces applied

- Pressure force per unit mass: $-\frac{\nabla P}{\rho_d}$
- Electrostatic force per unit mass: $-\frac{q_d n_d \nabla \phi}{\rho_d} = -\frac{q_d \nabla \phi}{M_d}$

where q_h and M_h are mean charge and mass of dust as $\rho_h = M_h n_h$. Then the modified hydrodynamic equation will look as follows:

$$\left\{ 1 + F_t \frac{d}{dt} \right\} \left[\frac{d\vec{U}}{dt} + \frac{q_h}{M_h} \vec{\nabla} \phi + \frac{1}{\rho_h} \vec{\nabla} p \right] = - \left[\nu \nabla^2 + \left(\frac{\nu}{3} + \xi' \right) \nabla(\nabla \cdot) \right] U \quad (2.31)$$

where $\frac{h}{ht}$ is the total derivative given by $\frac{h}{ht} = \frac{\partial}{\partial t} + \vec{U} \cdot \nabla$, ν is kinematic viscosity $= \eta / \rho_h$. \vec{U} , $\rho_h (= M_h n_h)$, n_h , q_h , p , ϕ , η are average fluid dust velocity, mass density, dust density, dust charge, pressure, electrostatic potential and absolute or dynamic

viscosity respectively. Electrostatic potential ϕ is obtained, using Poisson's equation given by:

$$\nabla^2 \phi = \frac{e}{\epsilon_0} [n_h - n_i + n_e] \quad (2.32)$$

$$n_i = n_{i0} e^{-e\phi/k_B T_i} \quad (2.33)$$

$$n_e = n_{e0} e^{e\phi/k_B T_e} \quad (2.34)$$

To perform the computational fluid dynamics study of grain medium, the non-linear coupled set of fluid equations Eq.2.29, 2.31 and Eq.2.32 have been solved numerically by above explained methodology using a pseudo spectral method. For this purpose, a massively parallelized Advanced Generalised SPECTral Code (AG-Spect) has been developed and benchmarked against linear eigen value solver^{†0}.

2.1.1.1 Advanced Generalised SPECTral Code (AG-Spect)

AG-Spect is capable of solving coupled set of two dimensional coupled time dependent fluid equations.

- **Performance of Parallelization:** Fig.2.3 shows the scalability of the code with number of grid points and number of CPUs. Parallelization works better for higher grid size [$N_x \times N_y = 1024 \times 1024$]. It is clear from the figure that a sensible combination of number of grid-pints ($N_x \times N_y$) and number of CPUs will provide direction on what would be the optimal combination of spatial/temporal discretization to attain a desired accuracy on the solution while minimizing the computational time.
- **External Libraries:** Massage Passing Interface (MPI) [69], Fastest Fourier Transform in west (FFTW) [65].
- **Further Development:** Code is easily extendable to three-dimensional multi-field system (3D system).

⁰Results are in chapter-5

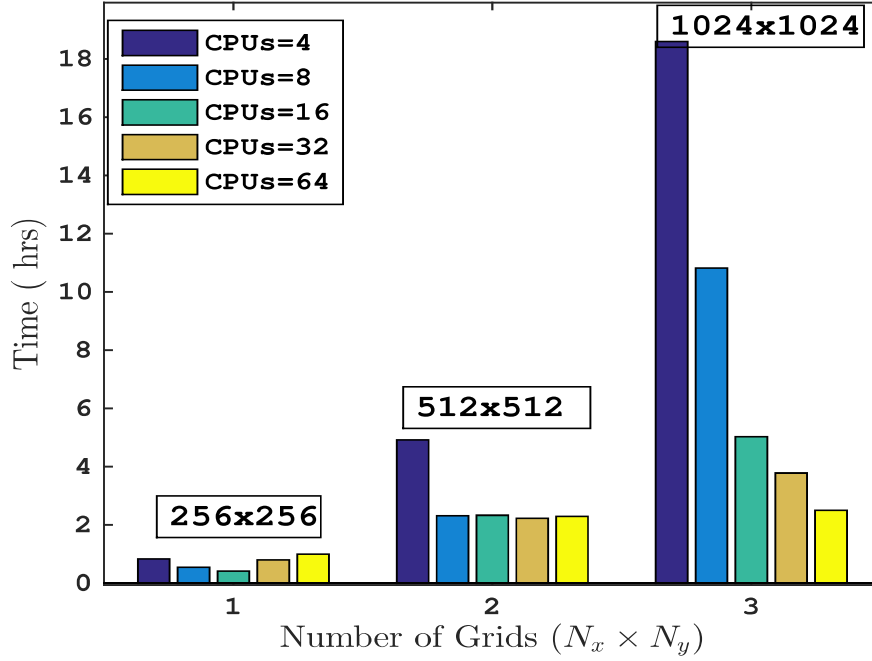


Figure 2.3: Scalability of the code for different grid sizes. Typical input parameters are $E_t = 10$, $\nu = 2.0$, $dt = 1e - 4$ (in normalized unit) and total time=5.0 (in normalized unit).

- **Possible Applicability:** Newtonian and non-Newtonian fluids in both incompressible and compressible limits may be solved using AG-Spect. Multi-component flows such as fluids with polymer concentration dynamics may be studied. For example, Hyaluronan/hyaluronic acid which comprises of long unbranched polymer of various concentration in synovial fluid flow and its shear-thinning/thickening dynamics may be modeled [26].

As discussed earlier, hydrodynamic like flows are generally studied by modeling the medium as a continuum. However, there are substances, for example, granular material, colloids, for which one needs to perform the study of flows at the kinetic level, i.e, at the level of individual particles. In laboratory experiments using CCD camera or video microscopy particle positions and velocities can be recorded to study the phase space evolution with time. Dusty plasma or strongly correlated

liquids are yet another example which allows direct experimental observation of position and velocity of each dust grain and hence molecular dynamics simulation becomes very useful. In molecular dynamics study, classical Newton's second law of motion is solved for each particle. In this method force between dust-grain is calculated by interaction potential. In the next section, we present the algorithm for classical molecular dynamics simulation for the two-dimensional system.

2.2 Dusty plasma as molecular medium

A massive grain in a plasma attains mean charge Q_h and electron and ion follow Boltzmann distribution in the slow time scale of dust dynamics. Thus the potential due to single grain (Poisson's Equation) is as follows:

$$\nabla^2 \phi = -\frac{e}{\epsilon_0}(n_i - n_e) - \frac{Q_h}{\epsilon_0} \delta(r) \quad (2.35)$$

When electron and ion densities are considered as Boltzmann response, n_e and n_i become:

$$n_e = n_{e0} e^{-e\phi/T_e} \quad (2.36)$$

$$n_i = n_{i0} e^{+e\phi/T_i} \quad (2.37)$$

For condition $e\phi \ll T_e$ and $e\phi < T_i$, one can linearize the Boltzmann equations Eq.2.36 and Eq.2.37 and using equilibrium quasi-neutrality condition, solution Eq.2.35 for $r \neq 0$ in spherical symmetric condition is given by.

$$\phi(r) = \frac{Q_h}{4\pi\epsilon_0 r} e^{-r/\lambda_d} \quad (2.38)$$

where r and Q_h are the length between two dust grain and charge on the individual dust grain respectively and $\lambda_h = \sqrt{q_i^2 n_{i0}/\epsilon_0 k_B T_i + q_e^2 n_{e0}/\epsilon_0 k_B T_e}$ is the Debye length of the background electron-ion plasma, where n_{i0} , n_{e0} , $T_{i,e}$, $q_{i,e}$ correspond to density, temperature and charge of the ion and electron respectively. The force

on the grain T by grain j is :

$$F_{ij} = \frac{Q_h^2}{4\pi\epsilon_0 r_{ij}^2} \left(\frac{1}{r_{ij}} + \frac{1}{\lambda_h} \right) e^{-r_{ij}/\lambda_d} \mathbf{r}_{ij} \quad (2.39)$$

where $\mathbf{r}_{ij} = \mathbf{r}_i - \mathbf{r}_j$ is the distance between “ i^{th} ” and “ j^{th} ” particle. N-body problem has been solved using this force Eq. 2.39.

$$m\mathbf{r}_i = \mathbf{F}_i = \sum_{j=1, j \neq i}^N \mathbf{F}_{ij} \quad (2.40)$$

In two-dimensional system the inter-grain spacing “ a ” can be calculated by the Wigner-Seitz radius $a = 1/\sqrt{\bar{n}\pi}$. Time, distance and energy are normalized to inverse of dust plasma frequency $\bar{\omega}_{ph}^{-1} = \omega_0^{-1}$, mean inter-grain spacing a and average Coulomb energy of dust particle $\frac{Q_h^2}{4\pi\epsilon_0 a}$ respectively. Hence, all physical quantities appearing henceforth are dimensionless. Now Eq.2.38 becomes:

$$U(r) = \frac{e^{-\kappa r}}{r} \quad (2.41)$$

The N -body problem is then numerically integrated using our parallel code Multi Potential Molecular Dynamics (MPMD) [34]. In our simulations, the size of the system is decided by average number of dust particles \bar{n} . Grains in a conventional plasma are trapped in the quasi two-dimensional sheath generated by compensation of electrostatic force and gravitational force. In a grain medium, the inter-grain spacing $a \approx 0.35\text{mm}$, the thickness of the grain bed is $\delta z \approx 10a - 15a$, the size of the grain bed $L_x \times L_y = 36 \times 22\text{mm}^2$ [Ref. Yan Feng et. al, PRL, 105, 025002 (2010)], hence, the ratio of $\delta z/L_x \simeq \delta z/L_y \ll 1$, which results in a 2D grain bed with negligible variation along the vertical direction. In this thesis, we address spherical charged grains restricted to quasi-2D beds interacting via 3D Yukawa potential. We understand that to simulate infinitely long rods using molecular dynamics simulation in ideal two dimensional system, a logarithmic potential should be used $\phi(r, L, \lambda) = 2\lambda \log(L/r)$, where λ and L are line charge density and length of the

wire respectively. To study long range hydrodynamic phenomena from atomistic point of view, we use Multi Potential Molecular Dynamics (MPMD). [34].

2.2.1 MPMD code

Multi Potential Molecular Dynamics (MPMD) code is fully parallelized molecular dynamics code capable of simulating both pair-wise and many body force fields and can handle Lennard Jones, Yukawa and Tersoff-Brenner potentials. This Code can simulate various thermodynamic ensembles such as NVT , NVE and NPT . To set up the system at desired temperature, Gaussian thermostat [73] and Braga-Travis thermostat [52, 53] have been used. The later one has been developed during the course of present Thesis work [20]. In MPMD code, Leap-frog time integration method has been used to get the phase trajectory of N particles for each step of time.

2.2.2 Leap-frog integration

For a single degree of freedom (one-dimensional), the equations of motion are:

$$\frac{dx}{dt} = v \quad (2.42)$$

$$\frac{dv}{dt} = F(x) = -\frac{dU(x)}{dx} \quad (2.43)$$

where $F(x)$ is the force on the particle when it is at x , $U(x)$ is the inter-grain potential (for dusty plasma system, U is Yukawa potential), and for simplicity we set the mass equal to unity. In this time stepping method, position and velocity are calculated at integer and integer plus half time step respectively, hence known as “Leap-Frog method”.

$$v(t + \Delta t/2) = v(t - \Delta t/2) + \Delta t F(t) \quad (2.44)$$

$$x(t + \Delta t/2) = x(t) + \Delta t v(t + \Delta t/2) \quad (2.45)$$

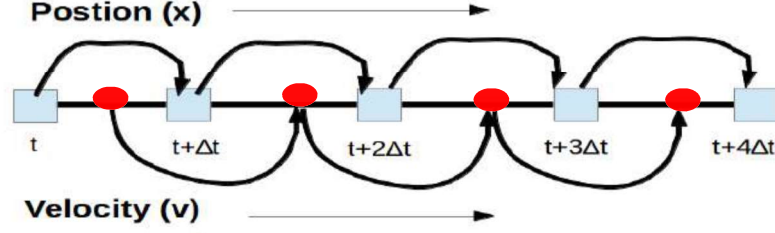


Figure 2.4: Diagram showing the structure of the Leap-Frog method

velocity at time t can be calculated as

$$v(t) = v(t - \Delta t) + (\Delta t/2)F(t) \quad (2.46)$$

There are following benefits of using Leap-Frog method.

- Time reversal invariant
- Second order accuracy
- Conserves Angular Momentum
- Symplectic i.e area preserving

Boundary condition is periodic. Hence, the contribution from the replicated systems due to periodic boundaries becomes important when the size of simulation box is much small and because of that the energy contribution of charged particles comes back inside the simulation box. In present work, Ewald sums [74] are not considered because of sufficiently large system size. The details about Ewald sums are given in the Appendix-E.

In the following Chapters, evolution and dynamics of unstable parallel and rotational shear flow using non-equilibrium molecular dynamics and fluid dynamics simulation have been described.

3

Shear flow in a Yukawa liquid: A Molecular dynamics study

3.1 Introduction

Laminar to turbulent transition has been and continues to be one of the most intriguing and fundamental problems of fluid dynamics. Hydrodynamic like flows (e.g. two stream instabilities) are generally studied to understand stability and transition of flows. Conventionally for Navier-Stokes fluids, such hydrodynamic flow related problems are described by modeling the systems as continuum, as the average number density (\bar{n}) of the medium is sufficiently high (for example, for water $\bar{n} = 3.33 \times 10^{28} \text{ m}^{-3}$ and for ideal gas $\bar{n} = 2.5 \times 10^{25} \text{ m}^{-3}$) in spite of the range of the interaction between particles constituting the “continuum” being very short.

On the other hand, in spite of relatively low number density, grains ($\bar{n} = 10^7 - 10^8 \text{ m}^{-3}$) form liquid phase. This is largely due to the magnitude of grain charge and the range of interaction. As described earlier in the Introduction, due to the low density and large mass of the dust grains, the experiments allow direct observation of instantaneous position and instantaneous velocity of each dust grain.

Chapter 3. Shear flow in a Yukawa liquid: A Molecular dynamics study

This unique capability of the dusty plasma medium makes molecular dynamics an ideal tool to simulate and understand this medium and permits comparison with laboratory experiments at microscopic level.

It is well known that, whenever there is a shear in the macroscopic velocity profiles, viscous shear heating occurs at the microscale [Fig.3.2]. In some fluids, shear heating is not necessary lead to increase in the local temperature at the shear layer. This is because heat conduction can be so rapid at the location of the velocity shear where the heat is generated that as soon as heat is generated, it is carried away or transported away due to thermal conduction. In general, the effect of viscous shear heating and thermal conduction may be measured by a dimensionless parameter, known as Brinkman number [45, 46] $B_r \approx \eta(\Delta V)^2/\lambda\Delta T$ (where η , λ are shear viscosity and thermal conductivity and ΔV , ΔT are difference in mean flow velocity and temperature respectively) [46]. (This number can also be represented by the product of two other non-dimensional number, viz. $B_r = P_r E_c$, where P_r and E_c are Prandtl and Eckert numbers. Prandtl number is the ratio of momentum diffusivity to thermal diffusivity and signifies how fast the thermal diffusion takes place in comparison to momentum diffusion [47]. Eckert number is the ratio of the kinetic energy to the enthalpy driving force for heat transfer). When the value of dimensionless number B_r is less than 1 i.e $B_r \ll 1$, the effect of energy dissipation or shear heating can be neglected relative to heat conduction in the fluid [48]. For example, for Navier-Stokes like fluids, B_r which is the ratio of viscous heating to thermal conduction, is much smaller than unity ($\approx (1 - 17) \times 10^{-8}$) [49] and hence shear heating does not alter the local transport properties in any significant way. Crucial to this discussion is the fact that thermal conduction λ is, typically, dependent on the average number density \bar{n} of the system. Thus in general, for high \bar{n} , Brinkman number B_r can be expected to be much less than one and for low \bar{n} , B_r may be expected to be comparable to 1.

It is important to recollect that dusty plasma modeled as Yukawa liquids are very

Chapter 3. Shear flow in a Yukawa liquid: A Molecular dynamics study

low density soft matter [44], for example, $\bar{n}_{grain} \sim 10^8 m^{-3}$ as compared to water $\bar{n}_{water} \simeq 10^{25} m^{-3}$. Hence these system in liquid state have relatively less thermal conductivity compared to higher density liquids such as water. Consequently, if the thermal conductivity of the medium is relatively small, generated heat may be accumulated in the shear zone. In the past, using classical molecular dynamics (MD) simulations, the development and propagation of a nonlinear heat front and shear heating in parallel shear flows of a strongly coupled such as, Yukawa liquid, was identified [8]. In laboratory experiments, macroscopic shear flows have been induced by external laser-drive [6, 31]. In one of these experiment [31], a co-evolving shear heating was observed.

A detailed study of shear heating in macroscopic flows in Yukawa liquids using molecular dynamics simulation has not yet been addressed where the grains interact with each other through a shielded Coulomb potential, due to the screening provided by background free electrons and ions. Therefore, it is worthwhile to ask as to what would be the flow dynamics for large Brinkman number ($B_r \sim 1$) fluids system such as Yukawa liquids when the macroscale shear flow is initialized? Can one expect the viscous heat to alter the local transport coefficient of the medium in a non-trivial fashion? What would be the effect of shear heating over large scale (macro-scale) vortex dynamics due to small scale molecular heating (micro-scale) and due to these effects how does average coupling strength (Γ) of the system change and in turn alters the vortex dynamics? To address some of these questions, it becomes necessary to perform classical first principle simulation such as molecular dynamics where no assumption or approximations regarding transport coefficients are introduced.

The present Chapter is divided into two Sections to study shear flow dynamics, shear heating phenomena, vortex dynamics, elastic-like wave propagation in rotational shear flows and other non-equilibrium properties of the grain medium, viz

Chapter 3. Shear flow in a Yukawa liquid: A Molecular dynamics study

- Parallel shear flow study using Kolmogorov flow as an initial condition
- Rotational shear flow study using Rankine vortex as an initial condition

It is important to note that, in the parallel flow, shear heating zones are inseparably embedded in the region of vortex dynamics while in the rotational flows, the region of shear heating may be reasonably well separated in space from the nonlinear wave propagation region. Thus fluid study may help delineate as to what kind of shear flow profiles are seriously impacted due to shear heating.

3.2 Parallel Shear flow: Kolmogorov flow

To study shear heating phenomena from atomistic (or particle) level, we perform classical first principle MD study considering a Kolmogorov flow (continuous gradient in velocity profile), as the initial flow profile. A Kolmogorov flow is chosen because of the following reasons:

- Laminar to turbulent transition is at low R_c , where R_c is stable to unstable transition point of Reynolds number.
- Continuous gradient in shear flow profile such as a Kolmogorov flow would be relatively easily attainable in laboratory dusty plasma experiments than sharp velocity gradient profiles [34].
- Due to the number of equilibrium period in initial flow profile (as will be discussed below), heat generated by the shear flow would be substantial and will be embedded in the region of vortex dynamics and as well as non-local.

The details and importance about Kolmogorov flow are described in the next section.

3.2.1 Kolmogorov flow

Kolmogorov flow is an unsteady, unbounded periodic, driven flow. In Fig.3.1, the velocity profile of Kolmogorov flow in two dimensional doubly periodic domain

Chapter 3. Shear flow in a Yukawa liquid: A Molecular dynamics study

$(x, y) \in [-\pi, \pi] \times [-\pi, \pi]$ is presented where, red and blue color strips show the positive and negative velocities respectively. Velocity profile of Kolmogorov flow has the form

$$\mathbf{U}_0(x, y) = U_0 \cos(k_x x)(1 + \delta \cos(k_y y))\hat{y} \quad (3.1)$$

where U_0 , δ are magnitude of initial velocity of Kolmogorov flow and magnitude of perturbation respectively. Wave numbers are given by $k_x = 2\pi n_0/L_x$, $k_y = 2\pi m_0/L_y$ where n_0 , m_0 , L_x , L_y are equilibrium mode number, perturbation mode number, size of the system along x and y directions respectively. For better representation of Fig.3.1, the corresponding one dimensional velocity profile has been plotted in Fig.3.2, which shows the continuous gradient in equilibrium velocity profile. Note that for doubly periodic boundaries as employed in this Thesis, it does not matter if equilibrium flow is along \hat{x} or \hat{y} .

For conventional fluids e.g Navier Stokes fluids, Kolmogorov proposed a class of flows, which exhibits laminar to turbulence transition at low Reynolds number and at the same time are amenable to analytical methods. Starting from Navier-Stokes equation, Meshalkin and Sinai 1961 [15] performed linear stability analysis of such flows in an unbounded domain and obtained the critical value of Reynolds number to be $R_c < \sqrt{2}$, where R_c is laminar to turbulent transition point. Using Kolmogorov flow as initial condition, various kinds of phenomena including “Anti turbulence” [75], metastability and vortex pairing study [76] and other nonlinear phenomena such as bifurcation [77, 78, 79] have been addressed. In the laboratory experiments, Kolmogorov flow has been studied in magnetized electrolyte fluid [16, 17, 80]. The behavior of Kolmogorov flow in the granular matter [81] has also been reported. Statistical properties [82] and hydrodynamic fluctuation in the linear regime [83] have been investigated in the past. Kolmogorov flow for polymer solution modeled as a visco-elastic fluid, using the Oldroyd-B model has been addressed by G. Boffeta et.al.[84]. Instability in 2D Kolmogorov flow [85] and the effect of compressibility on the stability of wall-bounded Kolmogorov flow [86]

Chapter 3. Shear flow in a Yukawa liquid: A Molecular dynamics study

have also been performed. Quasi-two-dimensional Kolmogorov flows in the labo-

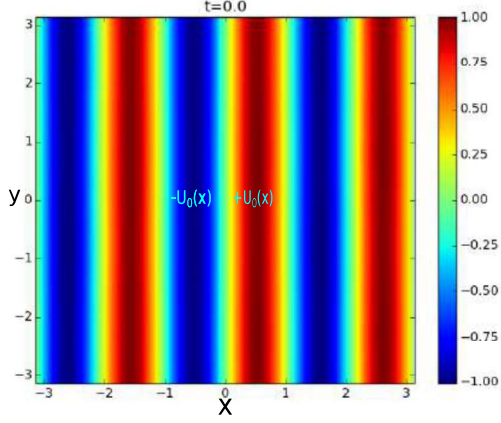


Figure 3.1: Initial velocity profile of Kolmogorov flow. Red and blue coloured contour show the positive and negative direction of velocity respectively

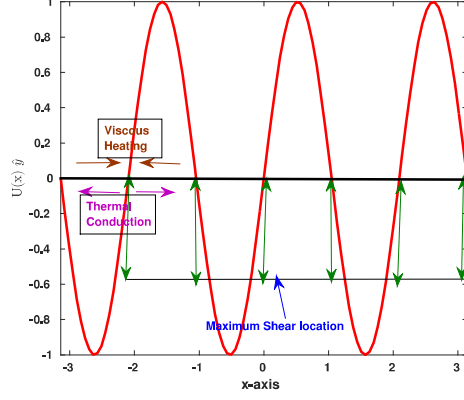


Figure 3.2: Figure shows the viscous heating and thermal conduction at maximum shear location.

ratory using flowing soap films [18, 87] and electromagnetically driven thin-layer flows [16, 80, 88, 89] are also interesting. For example, in soap film experiments, a horizontal film stretched across a metal frame is suspended over a set of belts with alternate belts moving in opposite directions to generate spatially periodic Kolmogorov flow and found the critical value of Reynolds number $R_c \cong 70$ [18]. In electrolyte fluid experiment, Kolmogorov flow had been set-up in laboratory using permanent magnets. Permanent magnets are arranged in the form of opposite polarity [17] and the resulting $J \times B$ force was used to drive the flow with $R_c \simeq 61$.

As described in Chapter-1, when spherical, micron sized grain (conduction or dielectric) are introduced in low temperature plasma, the grains are found to acquire large negative bare charge ($\sim 10^4 e$). The background plasma shields this charge, thus making the grain-grain interaction to be shielded Coulomb interaction or Yukawa-type interaction. Due to their relatively large mass and high charge, grains tend to be repelled by the negative sheath in the direction of gravity and attain

Chapter 3. Shear flow in a Yukawa liquid: A Molecular dynamics study

“equilibrium” in a plane perpendicular to gravity just above the sheath region. This grain bed in laboratory is found to behave like quasi-two-dimensional system with only a small variation in the direction of gravity. These variations are known to be small over a broad range of experimental conditions. This bed exhibits gas-like, liquid-like and solid-like phases. As discussed, dusty plasma is often modeled as Yukawa liquids. It has been found that shear flows may be induced by external low power laser-drive in such Yukawa liquids [6, 31]. Low power laser allows initialization of smooth velocity profiles in the quasi-2D grain beds, which further motivates one to study Kolmogorov flow for such system. Also as described earlier, due to low density of grains and relatively large size, the instantaneous velocities and positions of the grains can be measured. This facilitates comparison of grain-level dynamics with MD simulation and provides an unprecedented opportunity to study large scale hydrodynamic-like flows using molecular dynamics simulation at microscale and macroscale level without approximating the transport coefficients. The Kolmogorov flow can be thought as a simplified channel flow without boundaries. In the present Chapter, to study the shear heating phenomena in detail Kolmogorov flow as an initial input profile (as an initial value problem) has been considered. In this Chapter, we report an atomistic study of laminar to turbulent transition in a model Yukawa liquid using molecular dynamics simulations.

3.2.2 Particle or molecular dynamics studies

In molecular dynamics studies, the N-body problem of interacting classical grains has been solved, assuming for simplicity all molecules (or bodies) to be point-like spherical objects and of equal mass. The details of molecular dynamics procedure have been described in Chapter-2. As discussed earlier, the interaction between grains of complex/dusty plasma may be modeled as a Yukawa interaction given by the inter-particle potential :

$$U(r_{ij}) = \frac{Q_h}{4\pi\epsilon_0} \frac{e^{-r_{ij}/\lambda_D}}{r_{ij}} \quad (3.2)$$

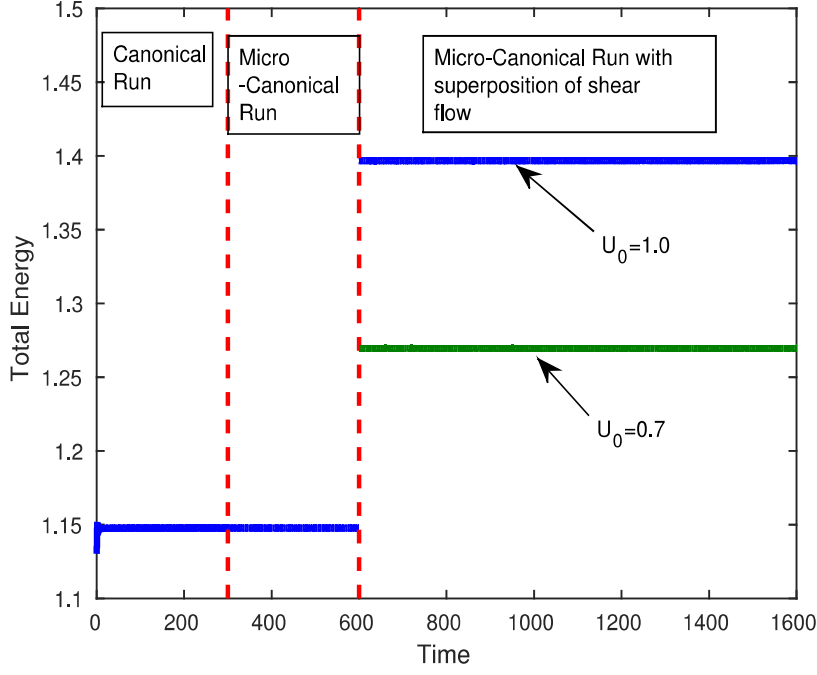


Figure 3.3: Total energy vs time for initial coupling parameter $\Gamma_0 = 50$, screening parameter $\kappa(t = 0) = 0.5$, spatial period number $n_0 = 3$ in canonical $[(0 - 300)\omega_0^{-1}]$ and micro-canonical $[(300 - 600)\omega_0^{-1}]$ runs. At $[(600 - 1600)\omega_0^{-1}]$ of shear flow profile over thermally equilibrated dust bed (micro-canonical Run). Superposition of shear flow increases the velocity of particles, hence the value of total energy changes from 1.147 to 1.3967 (for $U_0 = 1.0$) with $\delta E_{total}^{Nut\ erical} = 0.24$ from Eq.3.4 it is $\delta E_{total} = 0.25$. Similarly for $U_0 = 0.7$ with $\delta E_{total}^{Nut\ erical} = 0.12$, which is same as the value obtained from Eq.3.4 .

where $r_{ij} = |r_i - r_j|$ is the distance between i^{th} and j^{th} dust grain. Note that due to the relatively fast dynamics of background plasma consisting of electrons and ions, we consider background plasma properties to be invariant on the time scale of grains and model only grain dynamics. The N -body grain problem is then numerically integrated using our parallel code MPMD [34]. We choose density $\bar{n} = \pi^{-1}$ and total number of particles $N_h = 62500$ such that $L_x = L_y = L = 443.12$. Screening parameter κ is chosen to be 0.5. The Yukawa liquid is first

Chapter 3. Shear flow in a Yukawa liquid: A Molecular dynamics study

thermally equilibrated by connecting the system to a Gaussian thermostat [34] at desired Γ and is evolved for time $t = 300\omega_0^{-1}$. For the next $300\omega_0^{-1}$, the system is isolated from heat-bath and evolved micro-canonically. In Fig.3.3 the total energy as a function of time is shown. As can be expected, in the Canonical phase (see Fig.3.3) a mean energy is attained for a constant value of coupling parameter Γ and in the micro-canonical phase, the total energy is seen to be conserved. As can be expected, when shear flow of certain magnitude U_0 is superimposed over thermally equilibrated dust particles, the total energy changes (see Fig.3.3). To confirm that the total energy is consistent, kinetic energies with and without shear flow for two different equilibrium velocity flows $U_0 = 1$ and $U_0 = 0.7$ is evaluated. The difference in total energy can be calculated by $\delta E_{total} = E_{total}$ (with shear flow) - E_{total} (without shear flow), where E_{total} implies the sum of kinetic and potential energies. Note that the potential energy before and after superposition of shear flow is equal, hence will not take part in the calculation of δE_{total} . Therefore,

$$\delta E_{total} = \frac{1}{L_x} \int_0^{L_x} \frac{1}{2} \{U_{shear}^2(x, y) - U_{ranhot}^2(x, y)\} dx \quad (3.3)$$

From Eq.3.8

$$\delta E_{total} = \frac{1}{L_x} \int_0^{L_x} \frac{1}{2} U_0^2 \cos(k_x x)^2 dx = \frac{U_0^2}{4} \quad (3.4)$$

Therefore, $\delta E_{total}=0.25$ and 0.12 for $U_0 = 1$ and $U_0 = 0.7$ respectively which is consistent with the obtained numerical values (see Fig.3.3 and caption). For the rest of the Chapter, we consider $U_0 = 1.0$.

Macroscopic quantities from microscopic information

- process of “fluidization”:

A mesh-grid of size 55×55 is superimposed on the particles of the system to calculate the macroscopic or “fluid” variables from microscopic velocities and positions. We call “mesh” an Eulerian grid (x_G, y_G) . Average local fluid velocities along x and y directions are calculated as $\bar{U}_x = (1/N_b) \sum_{i=1}^{N_b} v_{ix}$, $\bar{U}_y = (1/N_b) \sum_{i=1}^{N_b} v_{iy}$, where v_{ix} and v_{iy} are individual instantaneous particle velocities along x and y direction and

Chapter 3. Shear flow in a Yukawa liquid: A Molecular dynamics study

N_b is the total number of particles present in an individual bin. Each bin contains approximately 20 particles [$N_b = N_h/(55 \times 55) \simeq 20$ with $N_h = 62500$]. It is important to note that the number of particles or molecules in each bin should be adequate enough so that the quantities like density and mean velocity are meaningful and reasonable and mimic fluid-like features. We have performed fluid average on various grid sizes such that average number of particles in a single bin to be in the range of 20 - 30 and find that about 20 particles to be adequate to capture the mean fluid properties. From average local velocities, we calculate the average local vorticity $\bar{\omega}(x_G, y_G) = \nabla \times \bar{\mathbf{U}}$ at the Eulerian grid location (x_G, y_G) . The average local temperature and average local coupling parameter are given as follows:

$$\bar{T}(x_G, y_G, t) = (2/3) \sum_{i=1}^{N_b} \left((v_{ix} - \bar{U}_x)^2 + (v_{iy} - \bar{U}_y)^2 \right) / N_b \quad (3.5)$$

$$\bar{\Gamma}(x_G, y_G, t) = \frac{1}{\bar{T}(x_G, y_G, t)} \quad (3.6)$$

To see the effect of velocity shear over the coupling parameter, a figure of coupling parameter vs time has been plotted in Fig.3.4. It shows that the coupling parameter is constant before superposition of shear profile. However, as shear profile superimposed on thermally equilibrated dust grains and the system is evolved further the value of coupling parameter decays as shear heating sets in.

Data shown in Fig.3.4 is divided into three regions. In the first region (a), the coupling parameter $\bar{\Gamma}(t)$ with time $(0 - 300)\omega_0^{-1}$ has been plotted in Canonical phase where thermostat is turned on, in second region (b), the same variable is plotted against time $(300 - 600)\omega_0^{-1}$ with the thermostat turned off (micro-canonical phase). In the last region (c) after the superposition of shear flow $U_0(x)\hat{y}$ (see Sec. 3.2.3 for details of shear flow) over system of particle velocities, a dynamic coupling parameter $\bar{\Gamma}$ is plotted for time $(600 - 1600)\omega_0^{-1}$. In the next sub section, we report early and late time behavior of shear flow in strongly correlated Yukawa liquids. It is noted that the shear flow is adiabatic (non-thermostatted) which

implies that heat transfer away from the shear layer is minimal or in other words leads to localized heating.

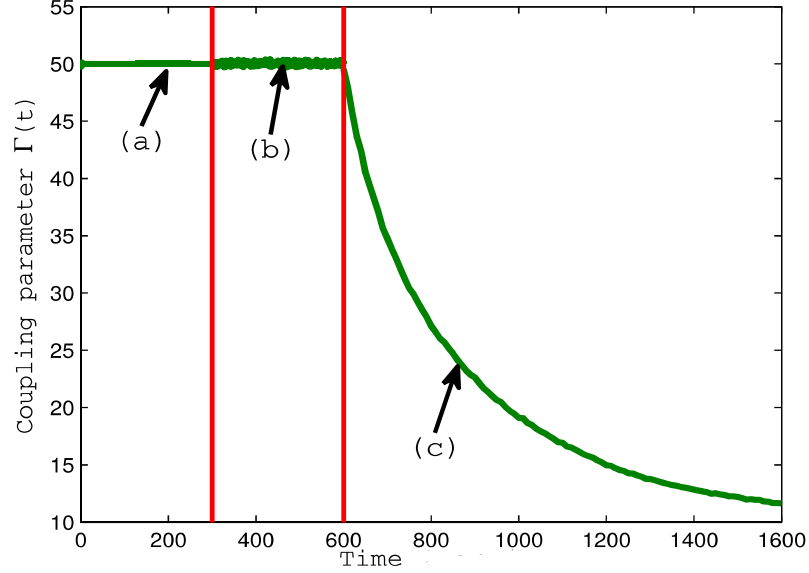


Figure 3.4: A plot of average coupling parameter $\bar{\Gamma}(t)$ vs time for initial coupling parameter $\Gamma_0 = 50$, screening parameter $\kappa = 0.5$ spatial period number $n_0 = 3$ and shear velocity $U_0=1$. (a) canonical run for time $(0 - 300)\omega_0^{-1}$, (b) micro-canonical run for time $(300 - 600)\omega_0^{-1}$, wherein peak to peak fluctuation 1.406%, (c) micro-canonical run for time $(600 - 1600)\omega_0^{-1}$ after superposition of shear flow profile over thermally equilibrated particles of the system

3.2.3 Kolmogorov flow as an initial value problem in Yukawa liquid

Kolmogorov shear flow has been superposed over thermally equilibrated dust particles at a desired temperature and allowed it to evolve Micro-canonically upto $1000\omega_0^{-1}$ without a heat-bath. The initial input parameters are $U_0 = 1$ (the magnitude of equilibrium velocity), $n_0 = 3$ (spatial period number), $\delta = 0.01$ (magnitude of perturbation), $m_0 = 2$ (perturbed mode number). The coupling

Chapter 3. Shear flow in a Yukawa liquid: A Molecular dynamics study

parameter $\Gamma(t)$ at time $t = 0$ is $\Gamma_0 = \Gamma(t = 0) = 50$, for which the thermal velocity $v_{th} = \sqrt{\frac{2}{\Gamma_0}} = 0.2$. It is estimated that the longitudinal sound speed C_s of the system for $\Gamma_0 = 50$ and $\kappa = 0.5$ is within the range of $C_s = 1.5 - 2.0$ [25]. Hence, equilibrium velocity ($U_0 = 1$) is greater than thermal speed ($v_{th} = 0.2$) but is smaller than sound speed ($C_s = 1.5 - 2.0$) of the system, therefore the flow is regarded as “subsonic” in nature.

Note that, in the present Chapter, the entire macroscopic flow speed is along \hat{y} direction initially. The transition from laminar to turbulent flow to an unstable macroscopic dynamic state may be identified by calculating the change in perturbed kinetic energy along \hat{x} direction as defined in Eq. 3.7 below.

$$\left| \frac{\delta E_{kin}(t)}{\delta E_{kin}(0)} \right| = \frac{\int \int [v_x^2(t) - v_x^2(0)] dx dy}{\int \int v_x^2(0) dx dy} \quad (3.7)$$

In Fig.3.5, perturbed kinetic energy along x - direction and coupling parameter is plotted on a log-linear scale against time t . The growth rate of perturbation is found to be approximately 5.5×10^{-2} . In Fig.3.5, perturbed kinetic energy along with decay of average coupling parameter Γ are plotted in the same figure. It is important to note that, the molecular shear heating reduces the value of average coupling parameter by 50% or more ($\Gamma \simeq 26$ at $t = 220\omega_0^{-1}$) from its initial value ($\Gamma_0 = 50$ at $t = 0$). From Fig.3.5, it is evident that the molecular shear heating is very fast at initial phase of shear flow (before $t = 0$ to $t = 220\omega_0^{-1}$). It is important to note that the Zero in time-axis is shown in Fig.3.5 is after the superposition of shear flow.

Let us look at the viscosity of 2D Yukawa bed at density $\bar{n} = 1/\pi$ and various values of (Γ, κ) under equilibrium condition [22]. The viscosity obtained under equilibrium condition is a non monotonous function of Γ and for various value of κ as shown in Fig.3.6. Similarly the diffusion coefficient and thermal conductivity are shown in Fig.3.7 and Fig.3.8. Thus, for whatever reason, if Γ varies, one expects variations in diffusion coefficient [Fig.3.7] and thermal conductivity [Fig.3.8] as well. These changes would affect the local transport in a non-trivial

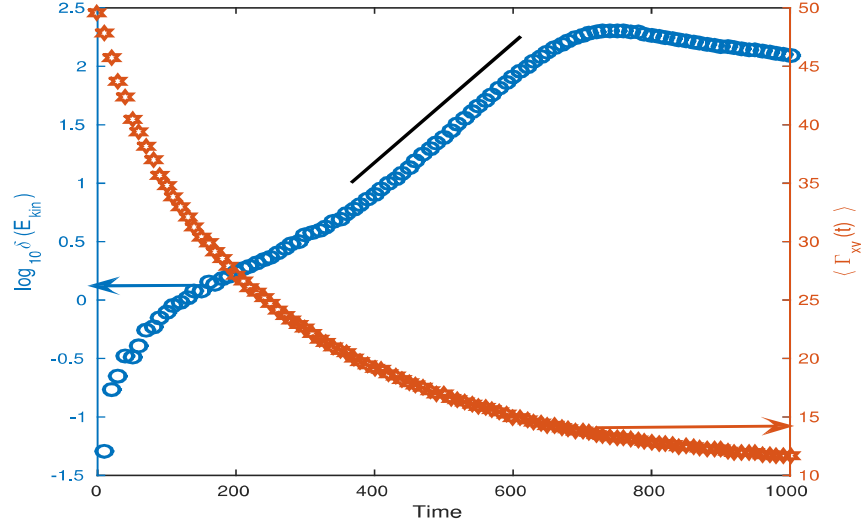


Figure 3.5: A plot of perturbed kinetic energy (left y-axis) and decay of coupling parameter (right y-axis) in a linear-log scale for number for perturbation mode $m_0 = 2$, initial coupling parameter $\Gamma_0(t = 0) = 50$, screening parameter $\kappa = 0.5$, spatial period number $n_0 = 3$ and shear velocity $U_0=1$. Calculated growth rate from simulation is 5.5×10^{-2} . The zero of time-axis shown in Fig.3.5 is after the superposition of shear flow

fashion and cannot be calculated using a fluid model, which, by construction, assumes particular values for transport coefficients. This point highlights the need for performing a classical first principle based non-equilibrium MD for our problem.

In late time regime, inertial effects dominate over the stabilizing viscous effects. The fluid undergoes a laminar to turbulent flow transition and late time saturation in perturbed kinetic energy is seen. In Fig.3.10, the time evolution of vorticity structure in Yukawa liquid at initial coupling parameter $\Gamma_0 = 50$ has been presented. As described earlier, to construct these vorticity structures we first obtain the local velocity by “fluid” dust particle velocities over a 55×55 meshgrid. In vorticity evolution plot [Fig.3.10] it is depicted that in initial time perturbed mode $m_0 = 2$ first grows and in late time mode-mode interactions dominate and nonlin-

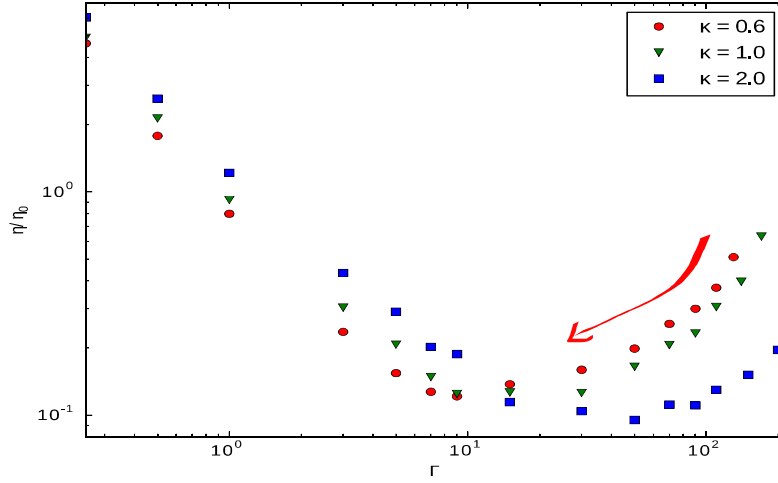


Figure 3.6: Shear viscosity vs coupling strength plot for different κ values. Here Γ is same as Γ_0 . After Ref: [22]

ear patterns are obtained. It is found that after some time the vorticity structures are destroyed because of microscale molecular shear heating, the details of which will be discussed in Sec.3.2.4

In Fig.3.11 results from a parametric study for the maximum growth-rate of perturbed modes with initial Reynolds number $R = U_0 l \bar{n} / \eta$ have been shown, where l , η are the shearing length and initial shear viscosity of the flow respectively. Here, the value of shear viscosity η is calculated using the Green-Kubo formalism [22, 90]. It is depicted in Fig.3.12 that for a given value of Γ_0 and κ , the flow is neutrally stable below $R < R_c$, where R_c is the critical value of Reynolds number and for $R > R_c$ flow becomes unstable and eventually turbulent [see Fig.3.12]. In the same way, in Fig.3.12, a parametric study for maximum growth-rate has been shown for reduced Reynolds number $R^* = R - R_c(\Gamma_0)$, which shows also the laminar to turbulent transition. In this figure $R_c = 59, 47, 18$ for coupling strength $\Gamma_0 = 10, 50$ and 130 respectively. It is tempting to speculate from the result shown in Fig.3.12 that such laminar to turbulent transition in our system would lead to

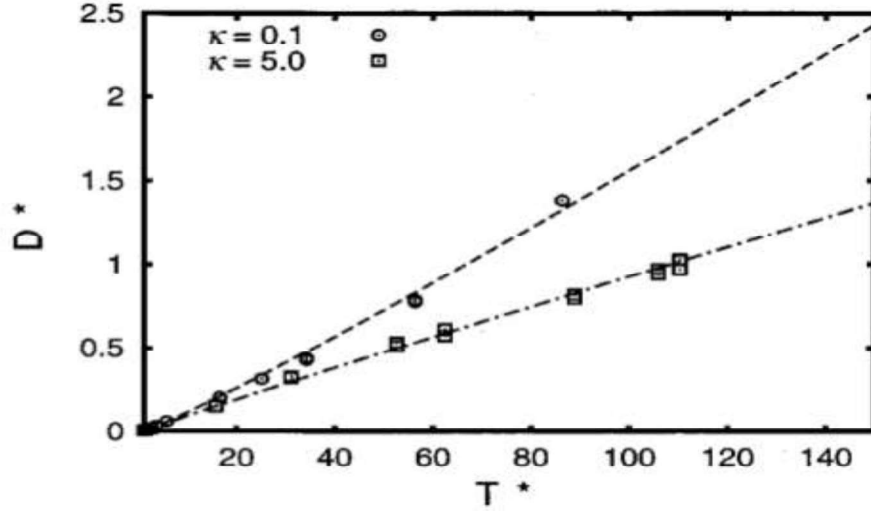


Figure 3.7: A plot of self-diffusion coefficient D^* obtained from equilibrium MD simulation vs reduced temperature $T^* = T/T_c$ or Γ_c/Γ (where T_c and Γ_c are melting temperature and coupling strength for low value of κ , where diffusion coefficient D^* are normalized by $\omega_E a^2$ with ω_E being the Einstein frequency. [After Ref: [23]]

a standard bifurcation [91] (The mathematical nature of this transition is not addressed here). Interestingly, we find that a higher value of coupling parameter Γ decreases the critical value of Reynolds number R_c . In the next section, the effect of viscous heating on shear flow has been studied.

3.2.4 Molecular heating due to shear flow

It is found that whenever there is a shear in macroscopic velocity profiles, viscous shear heating occurs at the microscale [Fig.3.13]. Conventionally, the effect of viscous shear heating and thermal conduction is measured by a dimensionless parameter, known as Brinkman number [45, 46] $B_r \approx \eta(\Delta V)^2/\lambda\Delta T$ (where η , λ are shear viscosity and thermal conductivity and ΔV , ΔT are difference in mean flow velocity and temperature respectively) [46]. For most fluids, B_r which is the ratio of viscous heating to thermal conduction is smaller than the unity. The higher value of B_r , the lesser will be the heat conduction and hence larger the tempera-

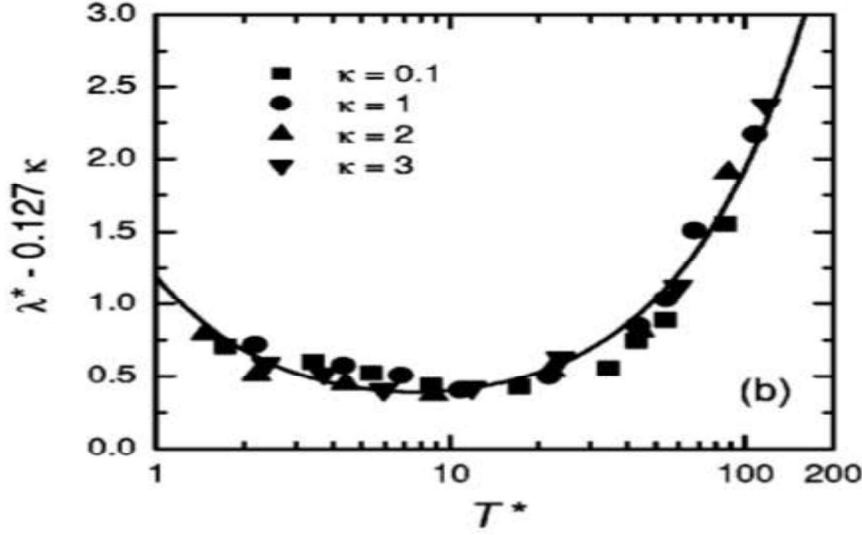


Figure 3.8: Reduced thermal conductivity λ^* normalized by the Einstein frequency as a function of the reduced temperature $T^* = T/T_c$ or Γ_c/Γ for different κ values (equilibrium MD simulation). After Ref: [24]

ture rise near the shear layer. For example, for Taylor-Couette flow in Newtonian and visco-elastic fluids trapped between concentric and rotating cylinders, value of B_r is found to be 0.00359 [92] and for conventional water flow in a channel [49] its value is approximately in the range of $(1 - 17) \times 10^{-8}$.

In recent dusty plasma experiments, using a laser driven shear flow study, high temperature peaks are reported [6] in the regions of velocity shear in two-dimensional layer. These high temperature peaks are due to shear heating, which occurs due to collisional scattering at region of shear location. In such dusty plasma experiments, value of B_r is estimated to be 0.5 [6]. We have estimated the Brinkman number from our numerical simulation and found that initial $B_r = 0.9445$ for our system parameters. For example, for $\Gamma_0 = 50$, $\kappa = 0.5$, $\eta(t = 0) = 0.2$ [22] and $\lambda(\Gamma_0 = 50, \kappa = 0.5) = 0.4235$ [41, 93], the value of ΔT and ΔV are 0.02 and 0.2 from Fig.3.14 and Fig.3.15, $B_r = 0.9445$.

In the shear layers, frequency of collisions between dust grain can be expected

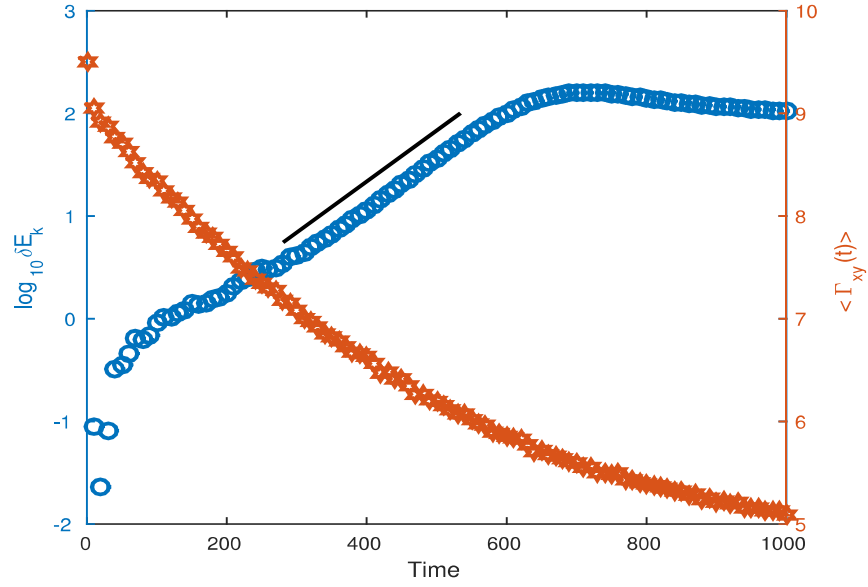


Figure 3.9: A plot of perturbed kinetic energy in linear-log scale for number for perturbation mode $m_0 = 2$, initial coupling parameter $\Gamma_0(t = 0) = 10$, screening parameter $\kappa = 0.5$, spatial period number $n_0 = 3$ and shear velocity $U_0 = 1$. Calculated growth rate from simulation is 4.5×10^{-2} . Zero in Time-axis shown in Fig.3.9 is after the superposition of shear flow.

to be high. These collisions increase the random thermal velocity of particles. Temperature of dust grains depends upon the random thermal velocity which is directly related to kinetic energy. Moreover, viscous dissipation effects become important when either the viscosity is larger or when the fluids have a low thermal conductivity, which increases the temperature gradients. As discussed earlier, low thermal conductivity is a relative consequence of low number density. One can clearly see the viscous shear heating at shear locations in Fig.3.14, in which the space dependent temperature profile has been plotted at various times. In these temperature profiles because of a spatial period number 3, six maxima (at the location of interface between two consecutive anti parallel flow) show the shear heating locations. As time increases, magnitude of temperature increases and at time $t = 1000\omega_0^{-1}$, the temperature starts to saturate. In Fig.3.15, space dependent

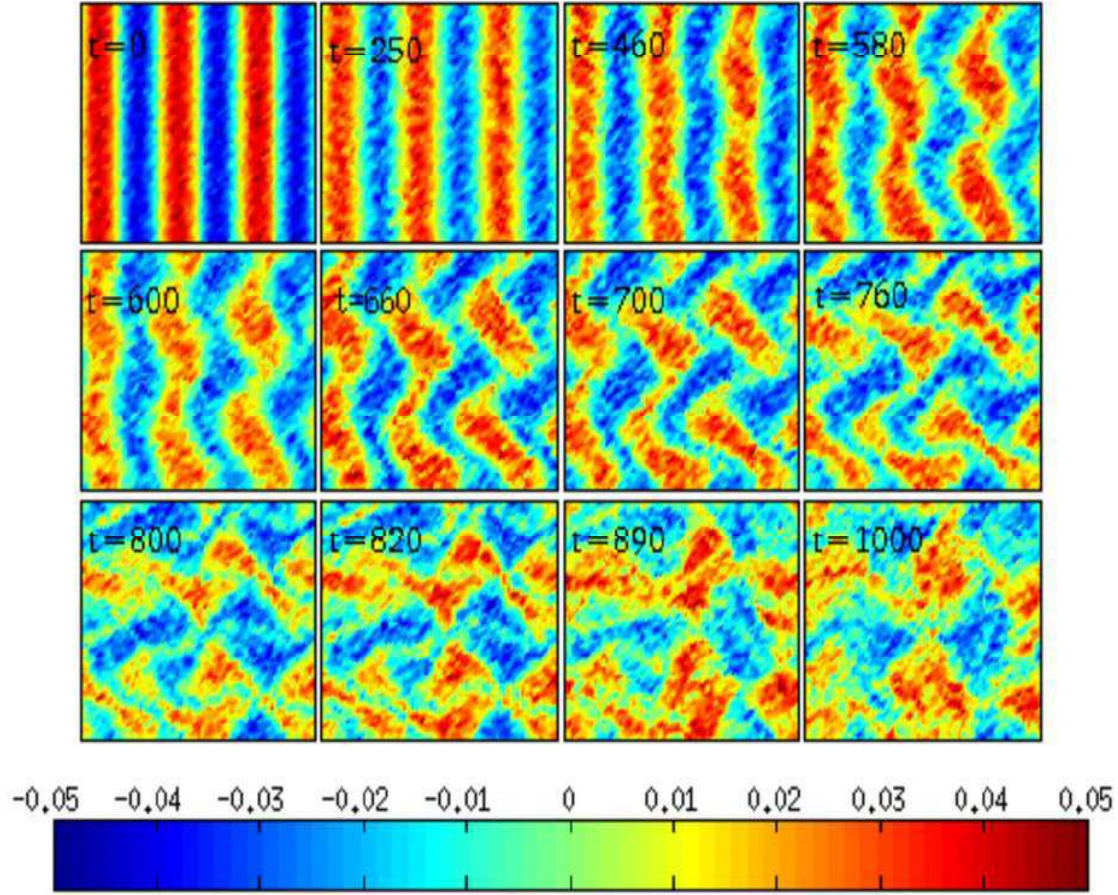


Figure 3.10: Contour plot of fluid vorticity ($\omega = \nabla \times \vec{U}$) obtained from molecular data. The grain velocity in the bins are fluidized through a 55×55 grid to construct vorticity. The horizontal color bar at the bottom show the magnitude of vorticity and blue and red strips show the opposite sign vorticity respectively. Perturbation mode $m = 2$, initial coupling parameter $\Gamma_0 = 50$, screening parameter $\kappa = 0.5$ equilibrium spatial period number is $n_0 = 3$, initial Reynolds number $R = 235.149$ and shear velocity $U_0=1$. Vorticity plots generated from microscopic velocity show Kolmogorov instability in Molecular Dynamics, the micro scale heating quickly destroy the vorticity structures.

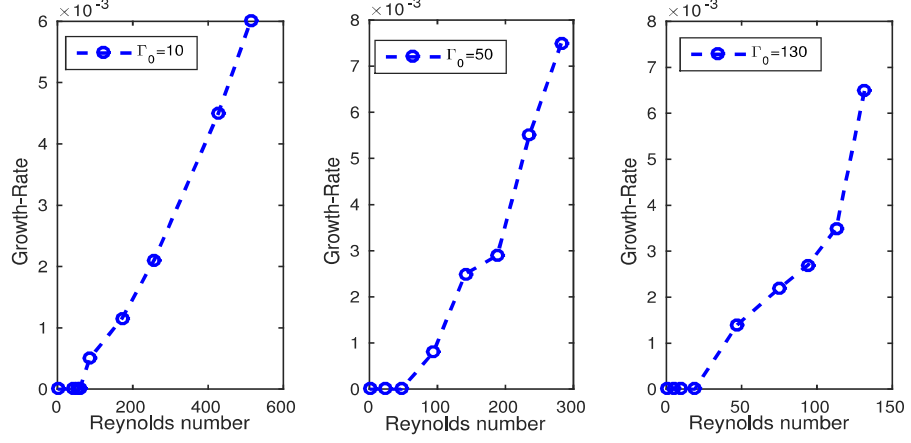


Figure 3.11: Growth-Rate vs initial Reynolds number R for different initial value of Γ_0 with $\kappa = 0.5$.

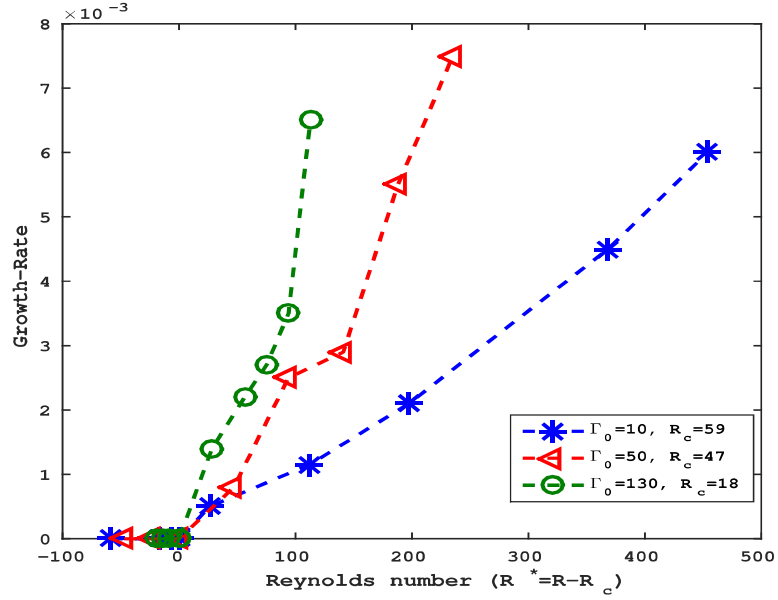


Figure 3.12: Growth-Rate vs initial Reynolds number R showing bifurcation for all the three initial Γ_0 values. R_c for various initial coupling strength $\Gamma_0 = 10, 50$ and 130 are $59, 47, 18$ respectively.

“fluidizing” velocity profile has been plotted on $y = 0$ axis. Again a clear signal of molecular shear heating is visible, which shows that because of shear heating,

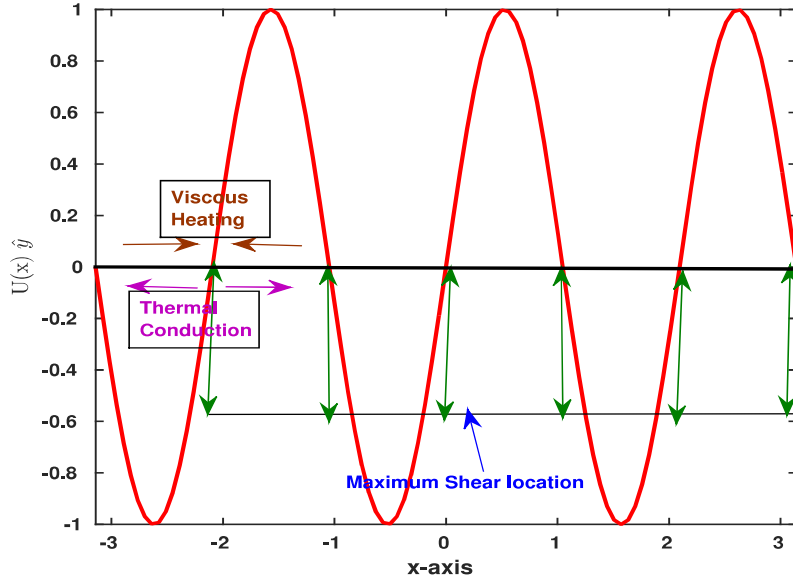


Figure 3.13: Figure shows the location of maximum shear and localized shear heating zones and the thermal conduction away from the shear heating zone. Vertical lines \updownarrow show the node points (shear heating zones) in velocity profile.

vorticity structures are destroyed. In Fig.3.16, we have plotted average Γ which is inverse of temperature as a function of time. The thermal speed ($v_{th} = \sqrt{2/\Gamma_0}$) for $\Gamma_0 = 50, 100, 150$ are 0.2, 0.14142 and 0.11547 respectively and are much smaller than equilibrium velocity speed $U_0 = 1$ (therefore the shear heating phenomena occurs and results the decay in the Γ value). It is found that decay-rate is dependent on equilibrium flow velocity. To better understand the interplay between heat conduction and viscous heating, we define a parameter α which is a ratio of equilibrium speed of shear flow to the thermal speed $\alpha = U_0/v_{th}$.

The observations are divided into three categories::

(a) $\alpha = 0.5$ or ($U_0 < v_{th}$): For this case the thermal speed is greater than the equilibrium velocity speed. In Fig.3.17 the shear heating is very small for $\alpha = 0.5$ for various values of coupling parameter. One can say that for larger value of ther-

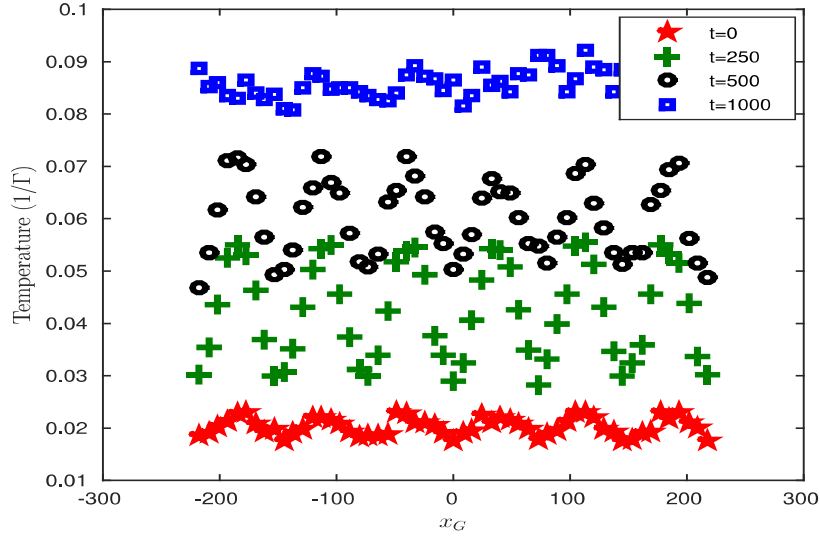


Figure 3.14: $\bar{T}(x_G) = \langle \bar{T}(x_G, 0, t) \rangle$, temporal evolution of temperature profile as a function of x_G for different time for $\Gamma_0 = 50$, equilibrium velocity magnitude $U_0 = 1$, screening parameter $\kappa = 0.5$.

mal speed, the coupling parameter will be constant with very small fluctuations throughout the simulation. (b) $\alpha = 2.0$ or ($U_0 > v_{th}$): In this case it is found that the decay rate of higher $\Gamma_0 = 100, 150$ is quite close, however it is slightly smaller for $\Gamma_0 = 50$. (c) $\alpha = 6.0$ or ($U_0 \gg v_{th}$): For this case the thermal speed is much smaller than the equilibrium velocity speed and results a faster decay for high $\Gamma_0 = 100, 150$. For $\Gamma_0 = 100, 150$ decay-rate is close each other while for $\Gamma_0 = 50$ it is slower compare to the higher Γ_0 .

In Fig.3.18 we have plotted the decay-rate data with an exponential fit $a[1 + b \exp(-\beta t)]$, where $a = 0.2$, $b = 4.0$, β are the intercept, coefficient of exponential part and decay-rate respectively. β describes how rapidly the coupling parameter decreases as the time increases. The decay rate β of coupling parameter is approximately 3.4×10^{-3} qualitatively. To see the dependency of decay rate on equilibrium velocity to thermal velocity ratio ($\alpha = U_0/v_{th}$) we have plotted decay rate vs α in Fig.3.19 for coupling parameter $\Gamma_0 = 50$. It is clear that the decay

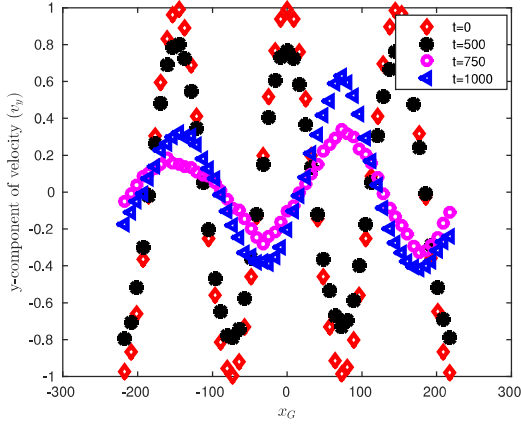


Figure 3.15: $v_y(x_G) = \langle v(x_G, 0, t) \rangle$, temporal evolution of velocity profile as a function of x_G for different time for $\Gamma_0 = 50$, equilibrium velocity magnitude $U_0 = 1$, screening parameter $\kappa = 0.5$.

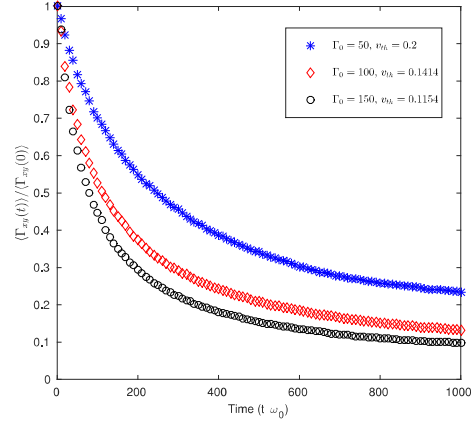


Figure 3.16: Spatial average coupling parameter Γ vs time plot for different value of initial Γ_0 for equilibrium velocity magnitude $U_0 = 1$, screening parameter $\kappa = 0.5$ at $y_G = 0$ axis.

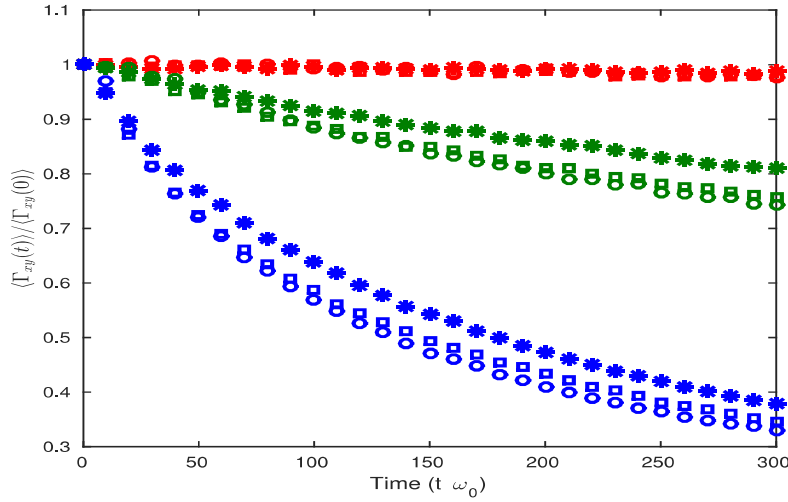


Figure 3.17: Spatially averaged coupling parameter $\Gamma(t)$ as a function of time for three different values of initial Γ_0 , namely $\Gamma_0 = 50(*)$, $100(box)$ and $150(o)$. Colors correspond to the cases $\alpha = 0.5$ (red), 2 (green) and 6 (blue).

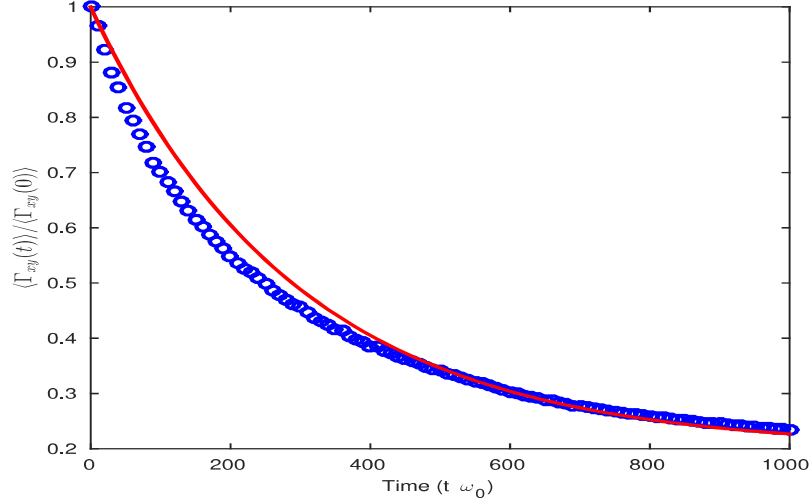


Figure 3.18: A plot of $\langle \Gamma \rangle_{xy}$ vs time plot for $\Gamma_0 = 50$, equilibrium velocity to thermal velocity ratio, say $\alpha = U_0/v_{th} = 5$. Fit line is $0.2[1 + 4.0 \exp(-\beta t)]$. Calculated decay rate is $\beta = 3.4 \times 10^{-3}$. Solid line shows the exponential fit.

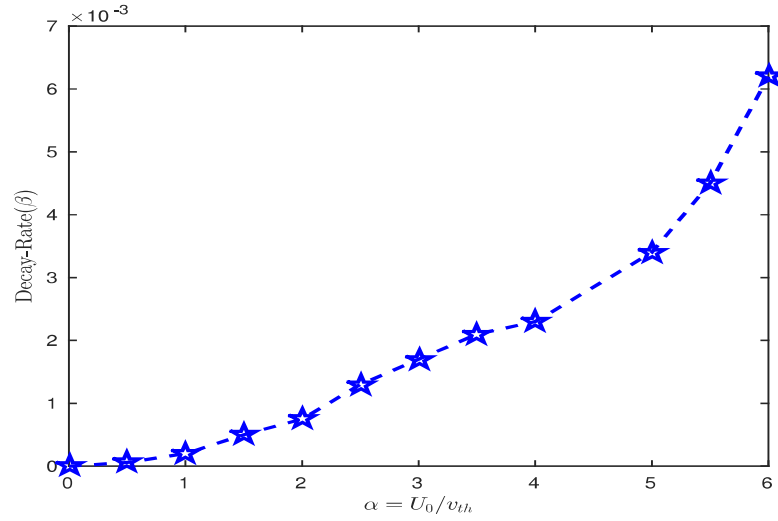


Figure 3.19: Decay rate vs $\alpha = U_0/v_{th}$ plot for number of perturbation mode $m = 2$, coupling parameter $\Gamma_0 = 50$, screening parameter $\kappa = 0.5$ equilibrium spatial period number $n_0 = 3$.

Chapter 3. Shear flow in a Yukawa liquid: A Molecular dynamics study

rate of particular coupling parameter monotonically increases with the value of α .

In the next subsection, we present the molecular dynamics study of rotational shear flow evolution of a finite size Rankine vortex of size R .

3.3 Rotational shear flow

Unlike parallel shear flows studied earlier, there is another important class of shear flows, namely rotational or circular shear flows. Strong coupling effects tend to couple transverse or optical wave dynamics to compressional wave dynamics. In the earlier study, the shear heating regions were embedded in the regions of vortex dynamics. It would be interesting to ask about what would be the effect of shear heating on the dynamics of a nonlinear phenomena with strong separation of regions of finite vorticity and zero vorticity, one such example is Rankine vortex. How does shear heating affect the dynamics of evolution on such nonlinear propagation structures. Therefore, in the present chapter, for the first time, using Molecular dynamics simulation a detailed study about the effect of strong correlation in presence of coherent vortex has been performed. We study the emergence of non-linear elastic waves due to azimuthal motion of localized rotational flow and the effect of strong correlation of the medium over nonlinear waves. We investigate the speed of nonlinear wave for different values of azimuthal velocity. Understanding of such wave propagation has many important applications in geophysics, petroleum engineering and mining, earthquakes and seismology [55]. Seismic waves have been studied theoretically and numerically for viscoelastic medium [94].

3.3.1 Rankine Vortex

To study the vortex flow dynamics of rotational shear flow in strongly correlated liquids, for the reasons discussed earlier, the Rankine vortex [95, 96] is considered. Rankine vortex is an azimuthal flow. The Rankine vortex has two regions (a)

Chapter 3. Shear flow in a Yukawa liquid: A Molecular dynamics study

The inner region of the flow $v_\theta(r) < R$, this region rigid rotator like flows profile, however it is liquid (b) The outer region $v_\theta(r) \geq R$ with zero vorticity but finite circular flow. The mathematical expression of Rankine velocity profile is as follow

$$\mathbf{V} = v_r \hat{r} + v_\theta \hat{\theta} + v_z \hat{z} \quad (3.8)$$

where

$$v_r = 0, v_\theta = \begin{cases} V_0 r/R & \text{if } r < R \\ V_0 R/r & \text{if } r \geq R \end{cases}, v_z = 0$$

where v_r , v_θ , v_z are radial, azimuthal and axial velocities respectively. Here, V_0 is the strength of azimuthal velocity, r and R are radial coordinate and radius of Rankine vortex core respectively. Vorticity profile of Rankine vortex has interesting features. At $t = 0$, the vorticity is constant in magnitude in the inner part of the region, however at the outer region its value is zero.

$$\omega = \hat{\theta} \cdot \nabla \times \mathbf{V} = \hat{\theta} \begin{cases} 2V_0 r/R & \text{if } r < R \\ 0 & \text{if } r \geq R \end{cases}$$

It is important to note that Rankine vortex can be described by the characteristics that it has a continuous velocity field over the entire region, however has a discontinuity in vorticity. In Cartesian co-ordinates the x and y components of velocities are $V_x = v_\theta \sin \theta$ and $V_y = v_\theta \cos \theta$.

In Fig.3.20, the vorticity profile of Rankine vortex has been plotted, where the radius of Rankine vortex is considered to be $R=10$. In this figure black colored arrows shows the velocity field, which shows the linear increase in rotation of the velocity field in the inner core until $r = R = 10$. It is important to note that the total energy (E) of the 2D Yukawa liquid before and after the superposition of rotational shear flow remains constant throughout the simulation. Total energy for N number of particles is as follow:

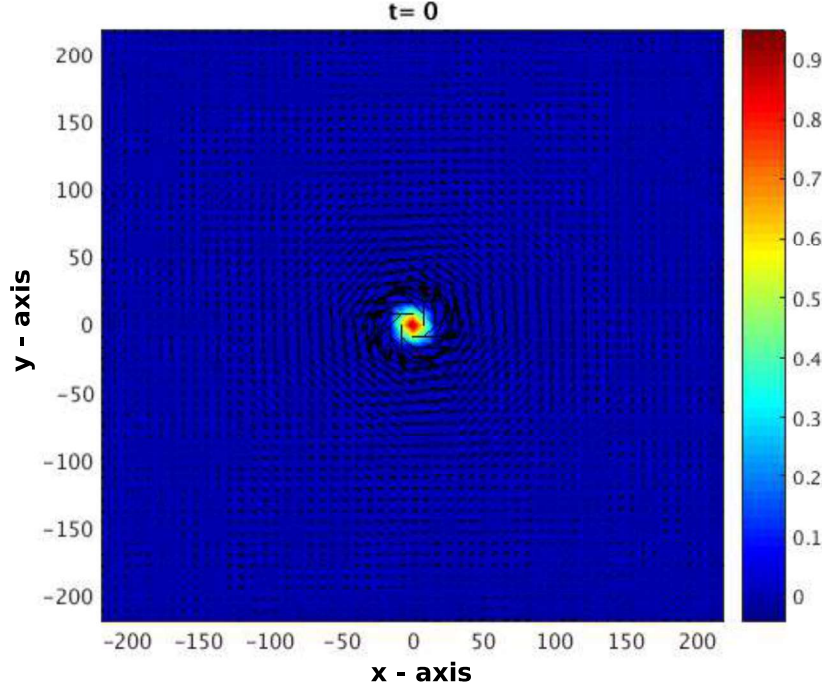


Figure 3.20: Rankine vortex profile ($\omega = \nabla \times V$) for $\Gamma_0 = 70$, $\kappa = 1.0$, $R = 10$ and $V_0 = 5$. The magnitude of vorticity inside the inner core $\omega = 2V_0r/R = 1.0$. Black colored arrows show the direction of velocity field at $t = 400$, the time of superposition of Rankine vortex.

$$E = \frac{1}{2} \left[\sum_{i=1}^N v_i^2 + \sum_{i \neq j}^N \frac{1}{r_{ij}} e^{-\kappa r_{ij}} \right] \quad (3.9)$$

Total energy of the system has been shown in Fig.3.21 for $\Gamma_0 = 70$ and $\kappa = 1.0$ before and after superposition of rotational shear flow with various equilibrium velocity magnitude $V_0 = 5, 8, 10$. The discontinuity at time $t = 400$ is because of the addition of mean equilibrium velocity with thermal velocity. In the following, we will describe a study of a novel radially propagating wave which we believe is due to a combination of strong coupling and compressibility of the medium. It is important to note that throughout this Thesis, we called it non-linear elastic wave.

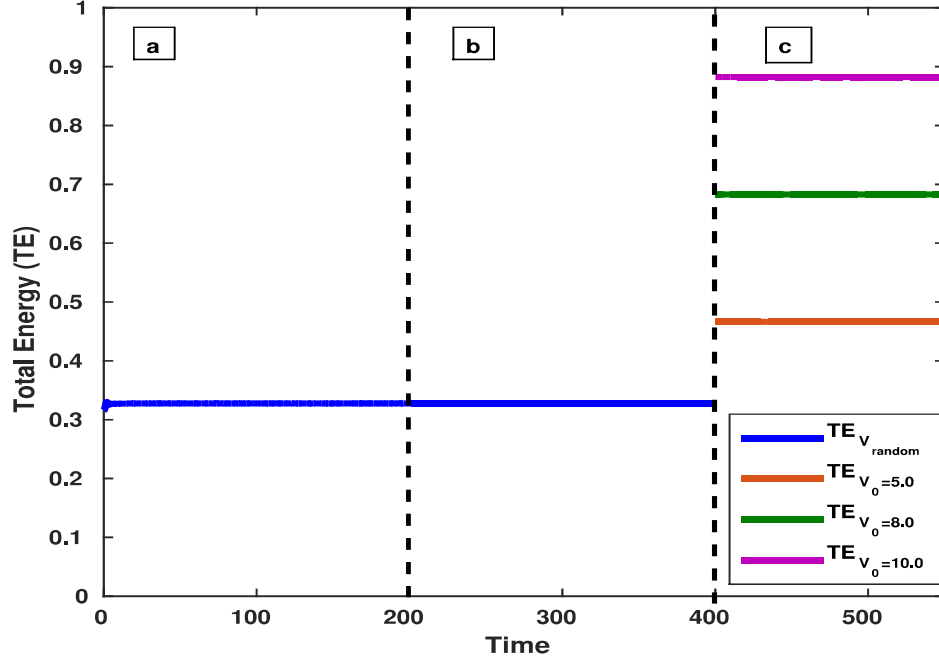


Figure 3.21: Total energy plot for $\Gamma_0 = 70$ and $\kappa = 1.0$. (a) in canonical run (b) in micro-canonical run (c) in micro-canonical run after superposition of rotational shear flow with various equilibrium velocity magnitudes, viz $V_0 = 5.0, 8.0$ and 10.0 .

3.3.2 Study of non-linear elastic wave

To study the rotational shear flow and emergence non-linear elastic wave, a Rankine vortex profile has been superimposed over thermalised particle velocities and all measurements have been taken at microcanonical run [constant volume, total energy and particles number]. This simply implies that a flow profile \mathbf{V} is loaded only at $t = 0$ and no attempt is made to control the mean flow at later times. The shear flow profile, which has been superimposed over thermalised particles is the same as given in Eq.3.8. To see the fluid-like vortex flow, here we have considered a large number of particles $N_h = 62500$ to study large-scale hydrodynamic phenomena using MD simulation. Due to the large size of the simulation box $L_x = L_y = L = 443.12$, we do not consider Ewald sums [74]. The value

Chapter 3. Shear flow in a Yukawa liquid: A Molecular dynamics study

of screening parameter κ is kept 1.0. To obtain macro-scale quantities for example, averaged velocity and averaged vorticity from microscopic information, we perform a “process of fluidization”. For that, a mesh-grid of size 55×55 is superimposed on the particles of the system to calculate the macroscopic or “fluid” variables. Average local fluid velocities along x and y directions are calculated as $\bar{V}_x = (1/N_b) \sum_{i=1}^{N_b} v_{ix}$, $\bar{V}_y = (1/N_b) \sum_{i=1}^{N_b} v_{iy}$, where v_{ix} and v_{iy} are individual instantaneous particle velocities along x and y direction and N_b is the total number of particles present in an individual bin. Each bin contains approximately 20 particles [$N_b = N_h/(55 \times 55) \simeq 20$ with $N_h = 62500$]. From average local velocities, we calculate the average local vorticity $\bar{\omega}(x_G, y_G) = \nabla \times \bar{\mathbf{V}}$ and the average local temperature $\bar{T}(x_G, y_G) = (2/3) \sum_{i=1}^{N_b} ((v_{ix} - \bar{V}_x)^2 + (v_{iy} - \bar{V}_y)^2)/N_b$ at the Eulerian grid location (x_G, y_G) . It is important to note that all the quantities for example, velocities (v_x and v_y), averaged density, averaged vorticity are calculated from above mentioned fluidized procedure.

In Fig.3.22, the time evolution of Rankine vortex for $\Gamma_0 = 70$, $\kappa = 1.0$ and $V_0 = 5$ has been shown. It can be clearly seen that the azimuthal rotation of circular vortex generates the waves towards outward direction because of adequate elasticity of the medium. In Fig.3.23 the magnitude of the peak of velocity along x and y directions have been plotted against time, which show that the emergence of non-linear wave is isotropic and non-dispersive and generates from the edge of rotating vortex ($R=10$). To check whether the Yukawa fluid behaves like a incompressible or as compressible medium maximum the value of spatially averaged density and divergence of velocity ($\nabla \cdot \mathbf{U}$) have been plotted in Fig.4.20 and Fig.3.25. Figures reveal that the medium behaves as locally compressible.

To see the effect of azimuthal speed over emergence of such non-linear wave the wave propagation 3D plot has been plotted for different values of V_0 in Fig.3.26.

It has been observed that the increasing speed of rotational vortex enhance the velocity of propagation of non-linear wave. Wave generated from higher rotational velocity (e.g $V_0 = 10$) touch the boundary first as compared to those generated in

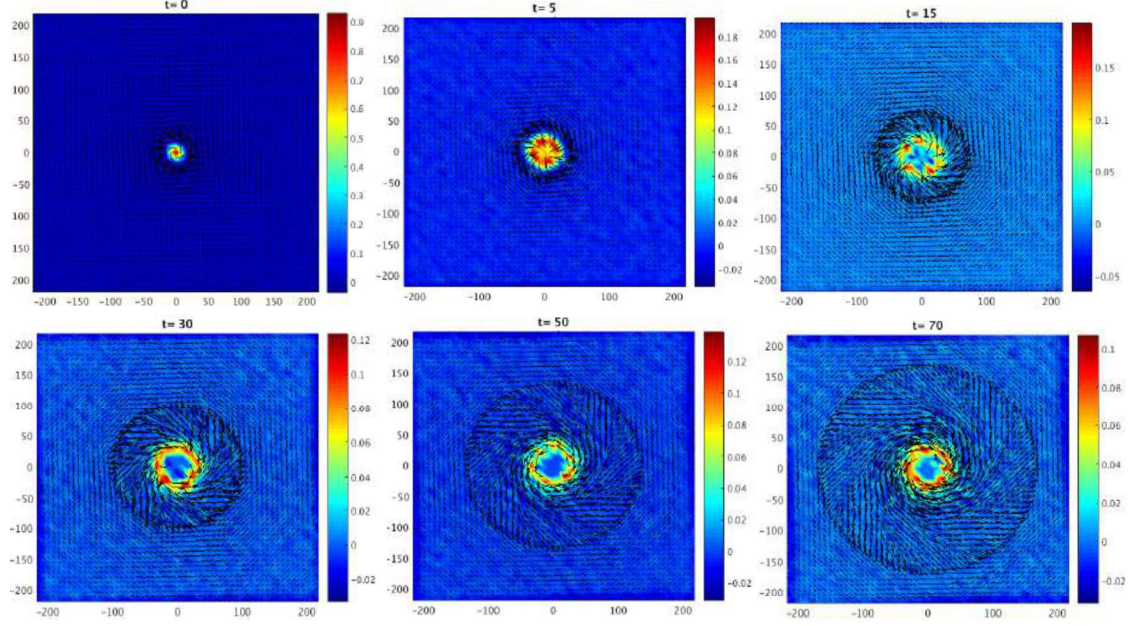


Figure 3.22: Time evolution plots of Rankine vortex for $\Gamma_0 = 70$, $\kappa = 1.0$ and $V_0 = 5$. Black coloured arrows show the direction of velocity field.

the case with $V_0 = 5.0$. In these cases [see Fig.3.26 (a), (b) and (c)], wave touches the boundary and because of periodic boundary condition it comes back through other side of the simulation box. Velocity of the emerging non-linear wave has been calculated by $C_{NLW} = \sqrt{C_x^2 + C_y^2}$, where C_{NLW} means speed of non-linear wave. It is important note that here C_x and C_y are speed of nonlinear wave along x and y directions respectively. In the same way, in Fig.3.27, propagation of density variation has been shown. It is evident from the figure [see Fig.3.27 (a), (b) and (c)], wave has same velocity magnitude as demonstrated in Fig.3.26.

It is important to note that this non-linear wave generates because of strong spatial correlation of the medium. In this regard, the results are presented for $\kappa = 1.0$ and a wide range of Γ values. To see the effect of this spatial correlation, a series of simulations have been performed for various values of equilibrium coupling strength and plotted in Fig.3.28.

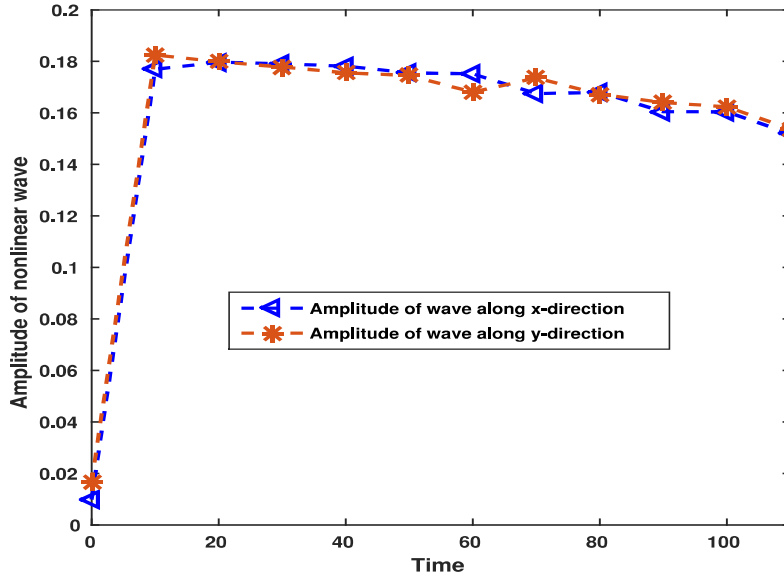


Figure 3.23: Maximum amplitude of nonlinear waves along x and y directions for $\Gamma_0 = 70$, $\kappa = 1.0$, $R = 10$ and $V_0 = 5$.

Fig.3.28 reveals that the coupling strength does not have any effect on the non-linear wave emergence and generation or perhaps the effects are so small that it is not reflected from in this figure. To see the impact of coupling strength on the propagation of the wave, we have calculated the speed of propagation of wave for different values of equilibrium coupling strength as shown in Fig.3.29 and Fig.3.30. It shows that as the medium becomes more and more strongly correlated, the speed of non-linear waves is suppressed. For the range of coupling strength $[\Gamma = 5 - 130]$, the speed of propagation of non-linear wave decreases with in the range $C_{NLW} = 4.6 - 4.0$. Fig.3.31 shows that, for different values of coupling strength, increasing azimuthal speed of Rankine vortex increases the speed of non-linear wave propagation.

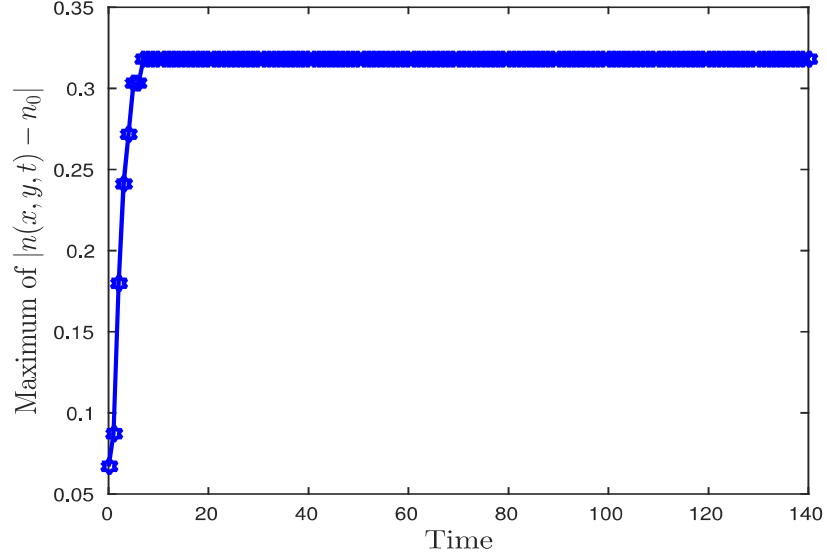


Figure 3.24: Time evolution of maximum value of spatially averaged density $\langle |n(x, y, t) - n_0| \rangle_{xy}$ for $\Gamma_0 = 70$, $\kappa = 1.0$ and equilibrium velocity $U_0 = 5$. Initial density is $n_0 = 1/\pi$

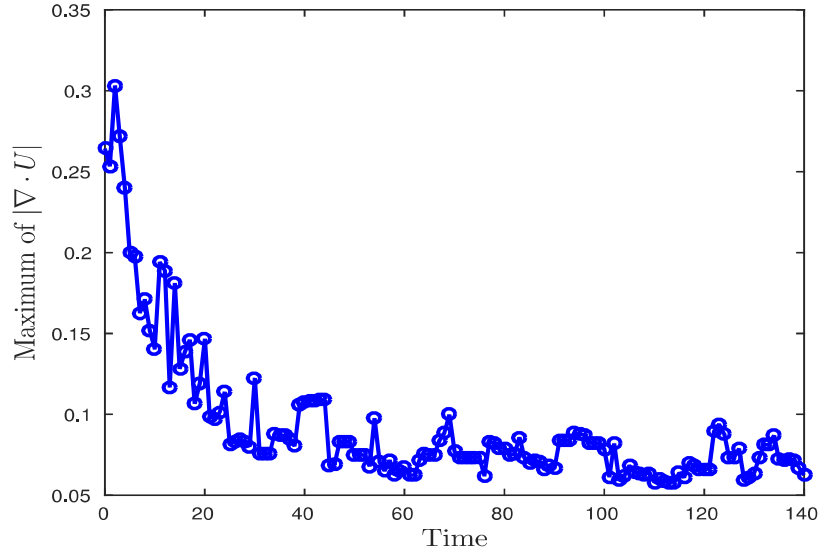


Figure 3.25: Time evolution of maximum value of spatially averaged divergence of velocity $\langle |\nabla \cdot U| \rangle_{xy}$ for $\Gamma_0 = 70$, $\kappa = 1.0$ and equilibrium velocity $V_0 = 5$.

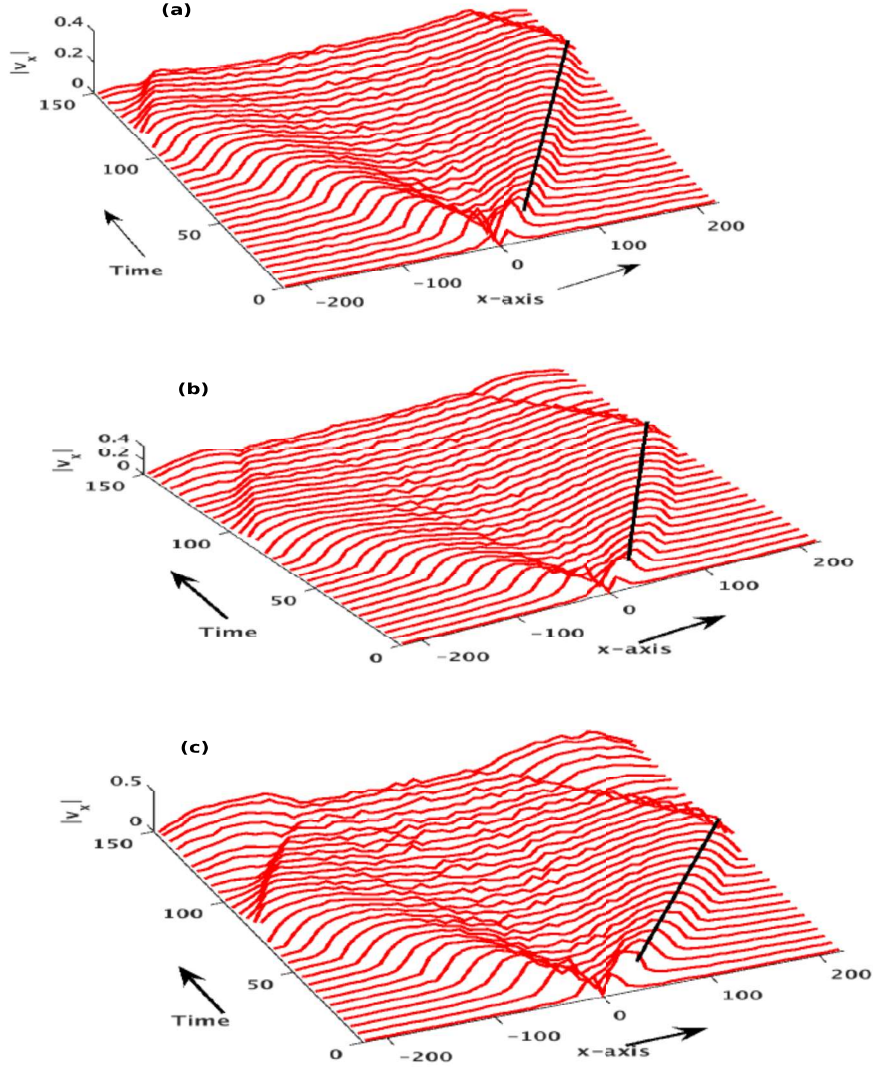


Figure 3.26: Propagation of nonlinear wave for $\Gamma_0 = 70$, $\kappa = 1.0$ and different values of azimuthal equilibrium velocity (a) $V_0 = 5$, $C_x = 2.109$, $C_{NLW} = 2.98$ (b) $V_0 = 8$, $C_x = 2.687$, $C_{NLW} = 3.8$ and (c) $V_0 = 10$, $C_x = 2.833$, $C_{NLW} = 4.0$, where C_{NLW} is calculated by $\Delta x / \Delta t$. Similar structure is seen along y -axis.

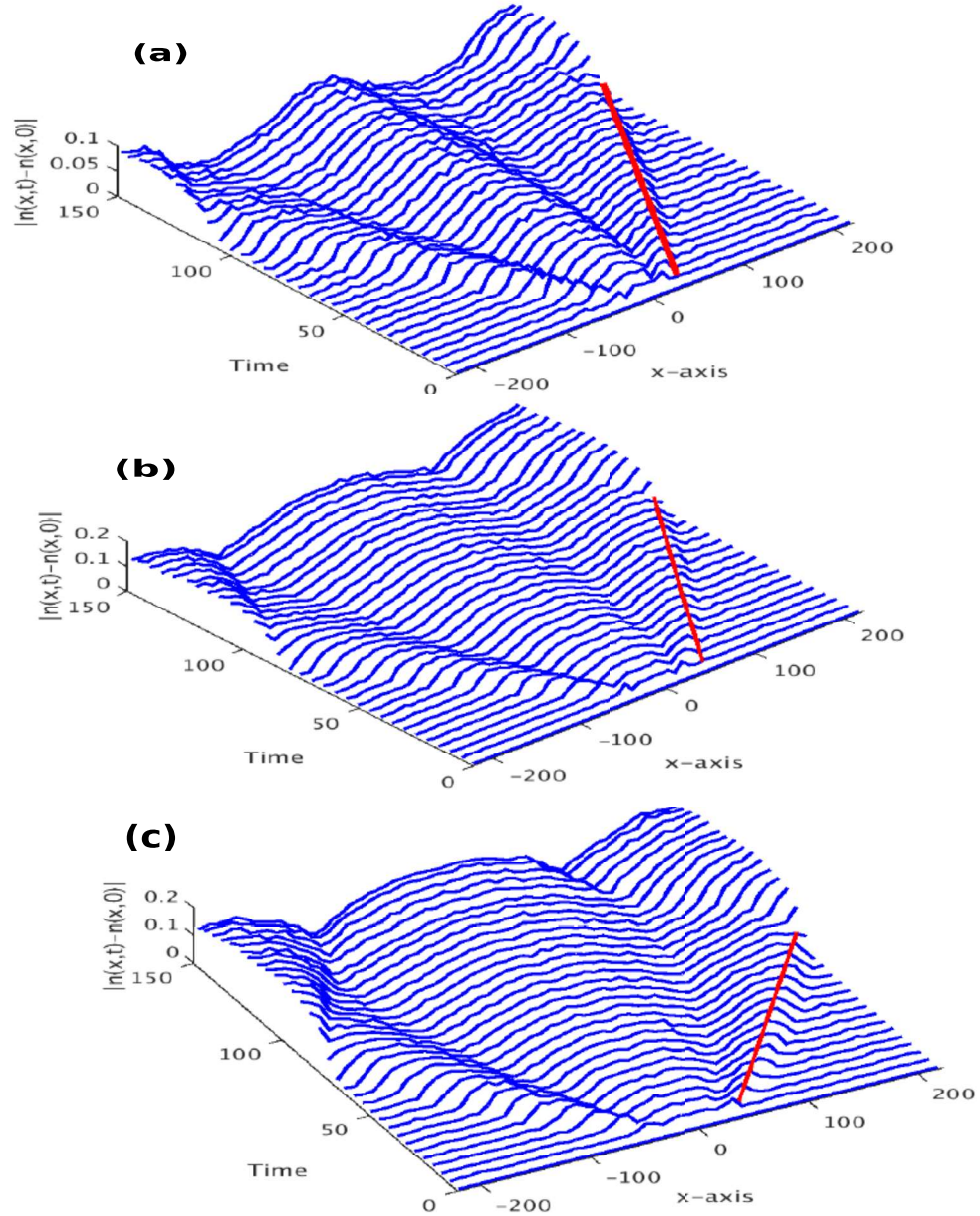


Figure 3.27: Propagation of density wave (or compression wave) for $\Gamma_0 = 70$, $\kappa = 1.0$ and different values of azimuthal equilibrium velocity (a) $V_0 = 5$, $C_x = 2.2$, $C_{NLW} = 3.11$ (b) $V_0 = 8$, $C_x = 2.6$, $C_{NLW} = 3.68$ and (c) $V_0 = 10$, $C_x = 2.96$, $C_{NLW} = 4.18$, where C_{NLW} is calculated by $\Delta x / \Delta t$. Similar structure is seen along y -axis.

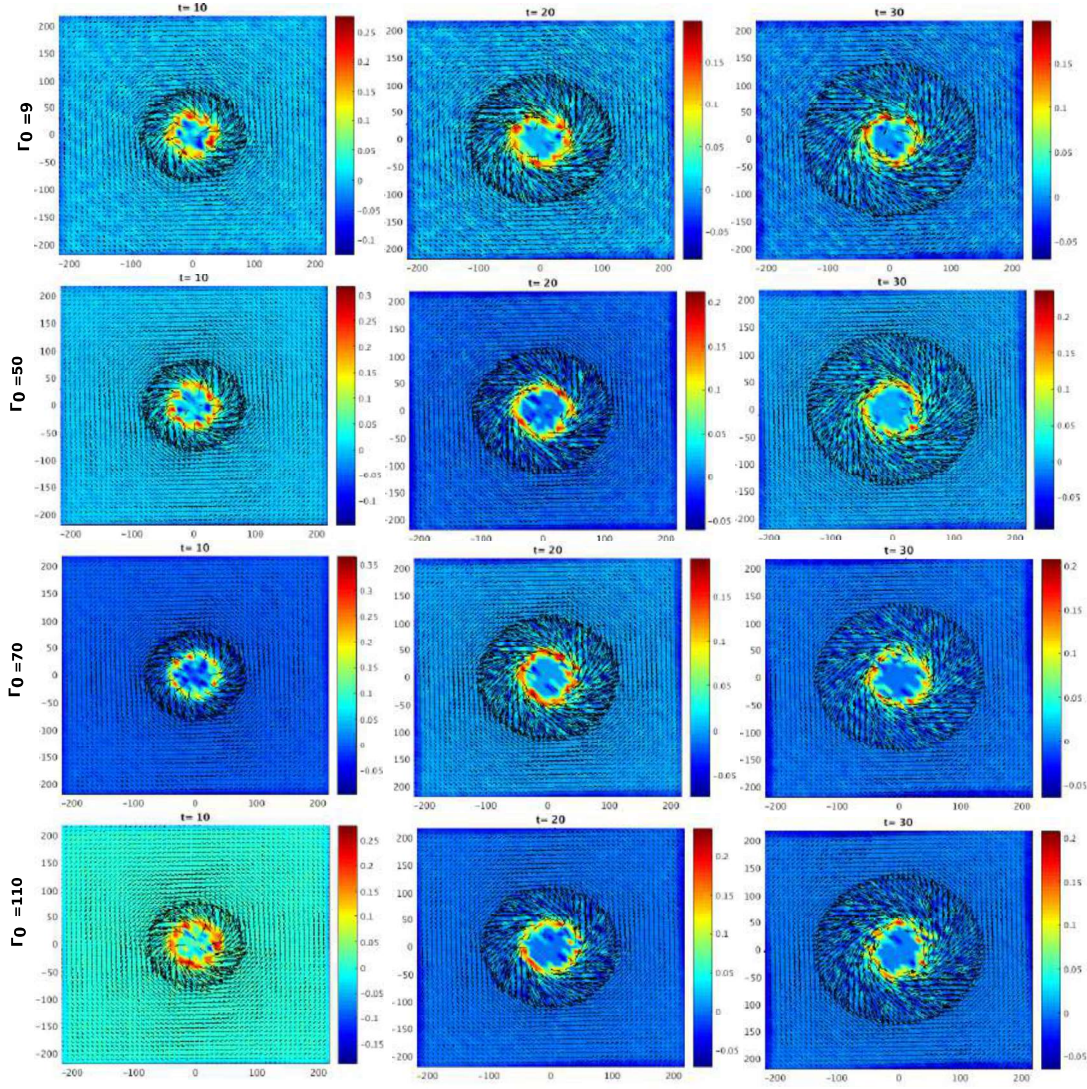


Figure 3.28: Effect of coupling strength over time evolution of Rankine vortex for $\kappa = 1.0$ and $V_0 = 10$. Black colored arrows show the direction of velocity field.

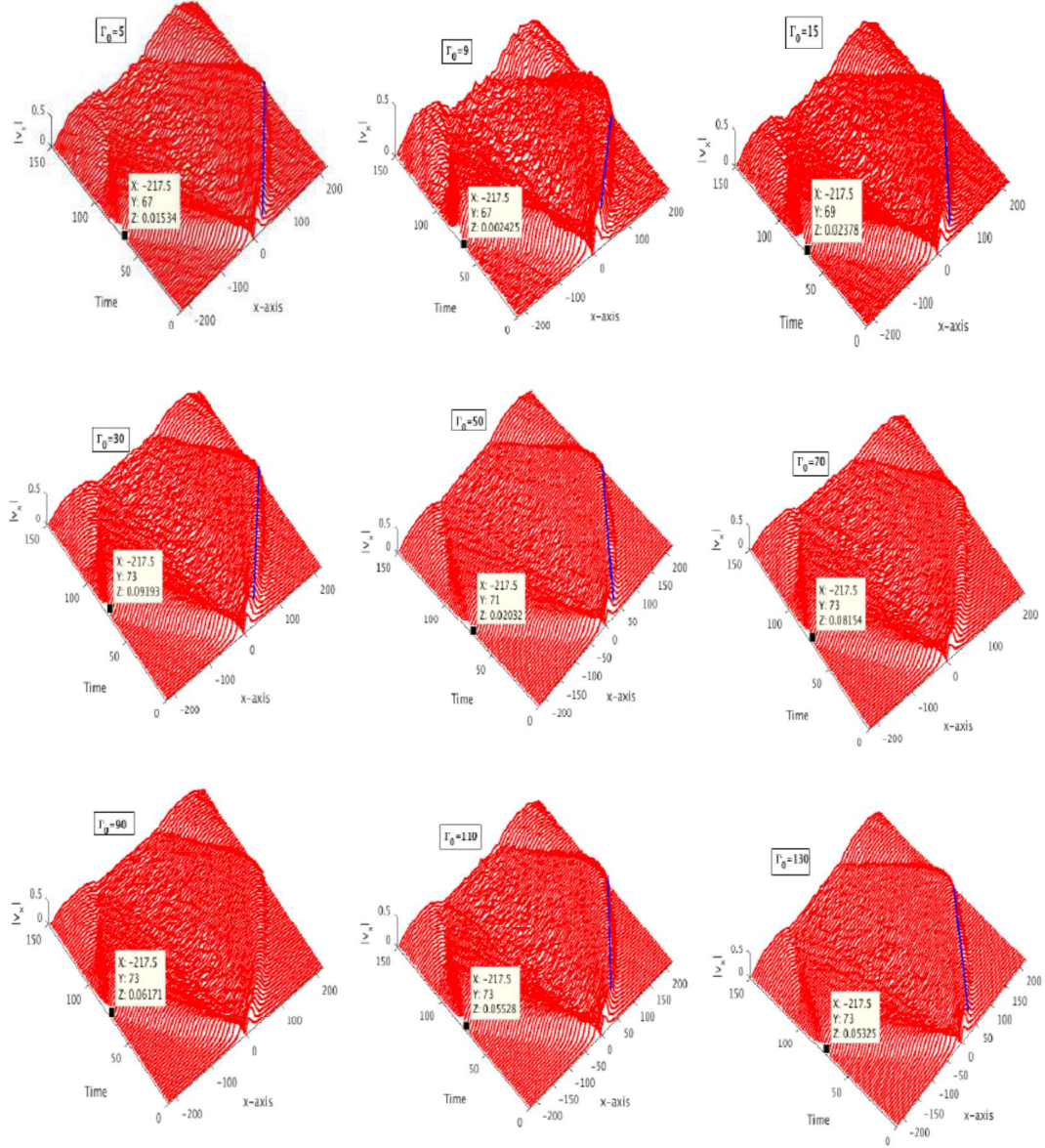


Figure 3.29: Effect of coupling strength on nonlinear wave speed for $\kappa = 1.0$ and $V_0 = 10$. Similar structure is seen along y -axis. Speed of nonlinear wave ($C_{NLW} = \sqrt{C_x^2 + C_y^2}$) are 4.6, 4.6, 4.45, 4.21, 4.32, 4.21, 4.21, 4.21, 4.21 for $\Gamma_0=1, 9, 15, 30, 50, 70, 90, 110, 130$ respectively.

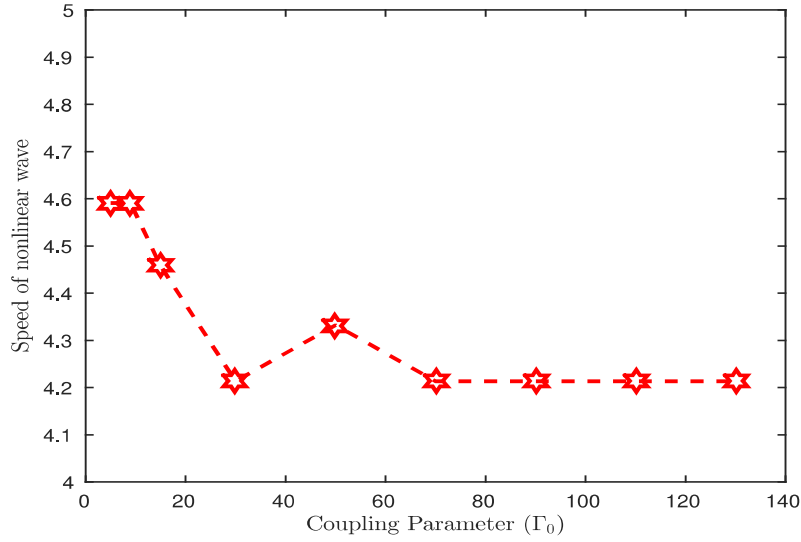


Figure 3.30: Speed of non-linear wave with various equilibrium coupling strength for $\kappa = 1.0$ and $V_0 = 10$.

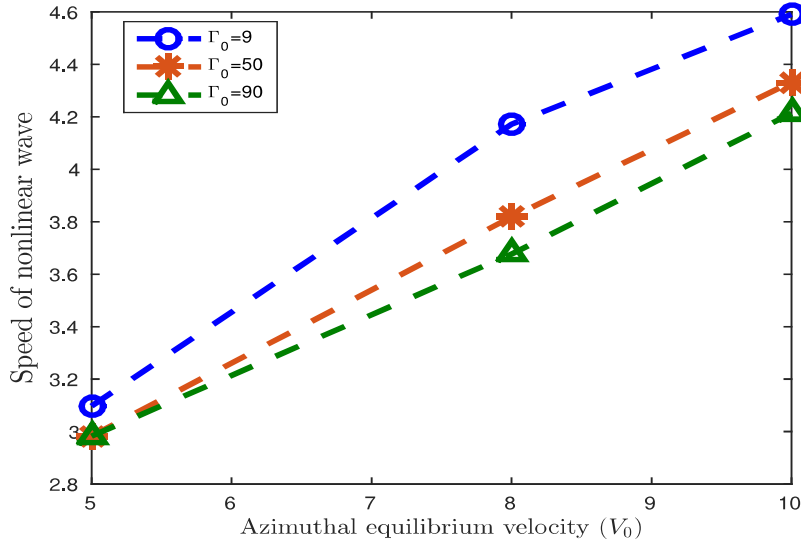


Figure 3.31: Speed of non-linear wave variation with equilibrium coupling strength for different values of azimuthal speed with screening parameter $\kappa = 1.0$

3.3.3 Onset of the nonlinear wave structure

To understand the nature of this radially propagating structure, let us first consider the transverse speed C_T and longitudinal speed C_L in a strongly coupled plasma medium, say, at $\Gamma = 50$. As is well known [25, 97], normal modes or sound speeds are sensitive to values of κ than Γ . In Fig.3.32, following Khrapak [97], we show the dependency of C_L on κ for $\Gamma = 50$. Now let us fix the azimuthal speed V_0

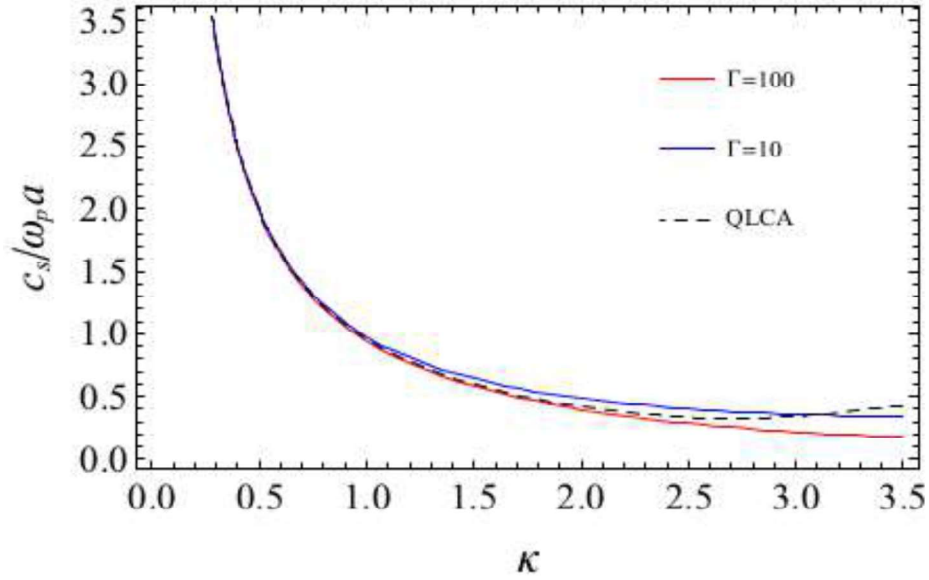


Figure 3.32: Longitudinal sound velocity $C_s/\omega_p a$ is same as C_L used in the text. The plot represents the C_L as a function of κ for $\Gamma = 10$ and 100 . (After Ref.[25]). The values of C_L, C_T for $\kappa = 4$ are 0.289 and 0.12 respectively.

of the Rankine initial condition to be $V_0 = 0.75$ and perform MD simulations in a Yukawa liquid for $\kappa = 1, 2, 3, 4$ with Mach speeds $M_{CL} = V_0/C_L$ are $0.65, 1.2, 1.89, 2.59$ and $M_{CT} = V_0/C_T$ are $2.34, 3.3, 4.7, 6.25$. Clearly, as we change κ values, all M_{CT} values are greater than 2.0 while M_{CL} values start from 0.62 , cross 1 and go up to 2.59 . The results are shown in Fig.3.33 which clearly demonstrate that as compressibility effects set in for $M_{CL} > 0.5$, the radial structures form and propagate at different speeds and become more prominent for values of $M_{CL} > 1$. It is important to realize that for all values of κ considered here $M_{CT} > 1$. However,

Chapter 3. Shear flow in a Yukawa liquid: A Molecular dynamics study

the mode is triggered when M_{CL} is increased beyond a certain value, in other words, due to compressibility effects, but, propagates radially out due to the strong coupling nature of the medium.

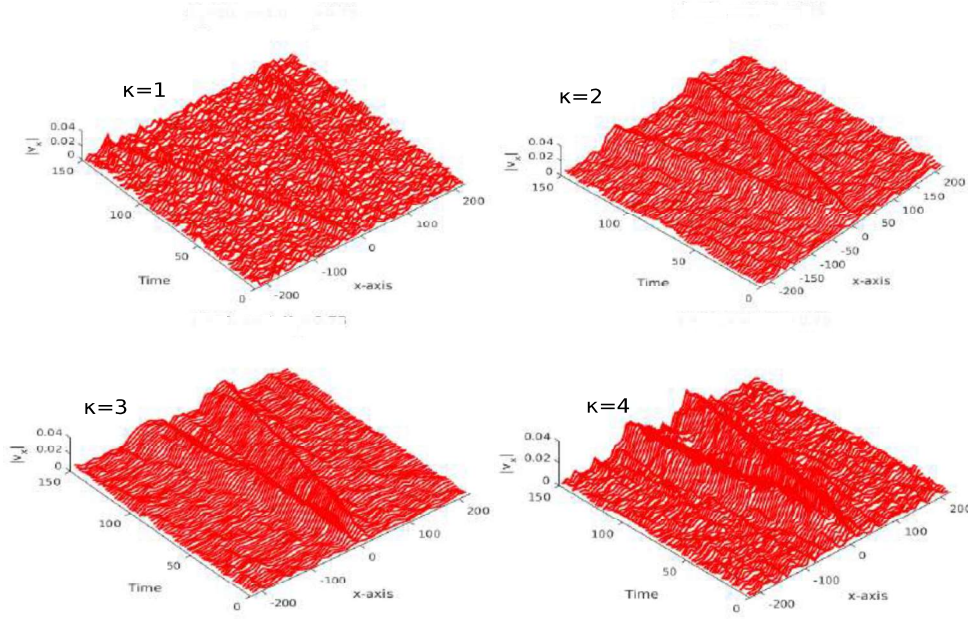


Figure 3.33: Propagation of nonlinear wave with various value of screening parameter κ for $V_0 = 0.75$, $\Gamma_0 = 50$.

In Fig.3.34 the numerically obtained speed of the wave $C_{NLW} = \sqrt{C_x^2 + C_y^2}$ with varying longitudinal Mach number $M_{CL} = V_0/C_L$ is shown. In the Fig.3.34 wave and longitudinal sound speed has been demonstrated for different values of screening parameter. Note that as M_{CL} increases, the value of C_{NLW} increases beyond C_L values for each κ , thus demonstrating that the wave becomes increasingly nonlinear with increasing compressibility effects. We believe that, due to strong coupling effects and compressibility, the rotational shear flow couples the angular and radial directions and the radial shear triggers a radially propagating disturbance [98] which becomes nonlinear as M_{CL} increases beyond the regular compressibility threshold of $M_{CL} > 0.5$. Let us now come back to our results with $V_0 = 5, 8, 10$ for $\kappa = 1$ obtained in earlier Sections. Clearly these are cases with extremely large

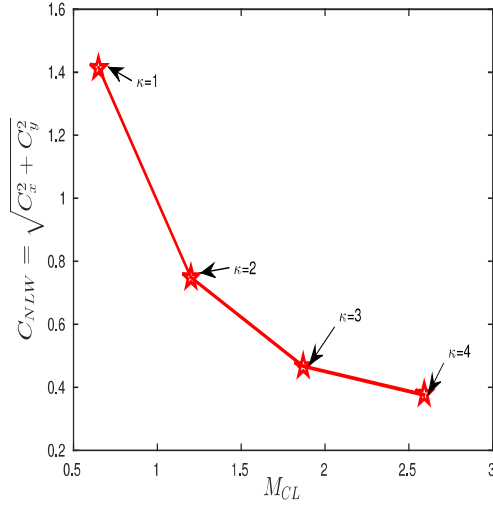


Figure 3.34: Speed of nonlinear wave (C_{NLW}) vs longitudinal Mach number (M_{CL}) for $V_0 = 0.75$, $\Gamma_0 = 50$ with various values of screening parameter κ .

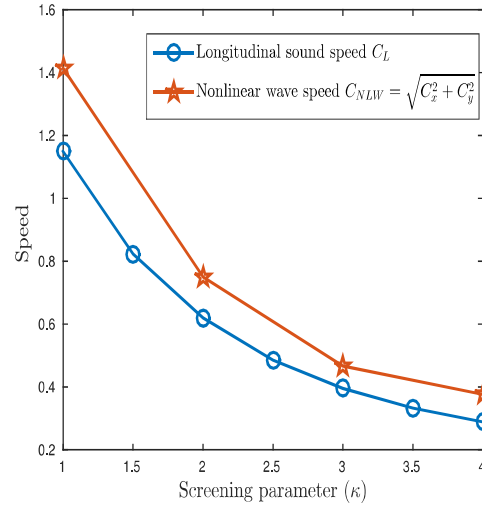


Figure 3.35: Speed of longitudinal sound C_L and nonlinear wave (C_{NLW}) vs screening parameter (κ) plot for $V_0 = 0.75$, $\Gamma_0 = 50$. Sound speeds are calculated from our MD simulation. As shown in Fig.3.30 as V_0 increases the value of C_{NLW} increases.

M_{CL} values. As C_L is weakly dependent on Γ for a given κ , for a given V_0 and κ , the extreme nonlinear wave speed is therefore more or less independent of Γ (see Fig.3.30). Expectedly, for a fixed Γ , increasing values of V_0 , would increase the nonlinear wave speed (see Fig.3.31). We shall come back to the discussions on rotational flows in Chapter-4, in the context of shear heating.

3.4 Summary

In this Chapter, laminar to turbulent transition of Kolmogorov flow in strongly coupled Yukawa liquid using “first principle” based classical molecular dynamics simulation has been investigated. Parametric study for range of initial Reynolds number R has been performed and reveal that the Yukawa liquid in neutral stable

Chapter 3. Shear flow in a Yukawa liquid: A Molecular dynamics study

state for $R < R_c$ and unstable for $R > R_c$, where R_c is a transition point from where laminar to turbulent transition occurs and R_c is in general a function of (Γ, κ) . The nature of the growth of perturbed mode against Reynolds number exhibits a bifurcation [91]. The coupling parameter decays exponentially in the early phase. At the late times, coherent vortices are destroyed because of molecular shear heating. The description of viscous heating is characterized by a space dependent temperature profile at a given coupling parameter ($\Gamma_0 = 50$) of x at $y = 0$ for different times. These space dependent temperature profiles reveal the rise in temperature at shear location. For our system, for equilibrium condition, Brinkman number ($B_r \approx 1.0$), which suggests strongly that the shear heating due to molecular collisions dominates over thermal conduction of heat. It is also seen that the decay-rate of Γ with time depends upon α the ratio of equilibrium shear velocity to thermal velocity.

In present Chapter, the emergence of non-linear elastic waves from localized coherent vortex sources in strongly correlated Yukawa medium using Molecular dynamics simulation has been studied. We believe that due to strong coupling effects and compressibility, the rotational shear flow couples the angular and radial directions and the radial shear triggers a radially propagating disturbance [98] which becomes nonlinear as M_{CL} increases beyond the regular compressibility threshold of $M_{CL} > 0.5$. It is important to note that, whereas in the parallel flow problem, the shear heating zones are inseparably embedded in the region of vortex dynamics while in the rotational flows, the region of shear heating are reasonably well separated regions of finite vorticity and zero vorticity. The effect of shear heating suppression over elastic waves generated by rotating localized vortex source will be described in the coming Chapter-4.

In general, Yukawa interaction is known to be the predominant force influencing the dynamics of a grain in a Complex plasma experiments. However, the effect of other forces such as dust-neutral collisions resulting neutral drag force, the effect

Chapter 3. Shear flow in a Yukawa liquid: A Molecular dynamics study

of ions accelerated in the sheath region where the 2D grain bed levitates are also known to affect the dynamics of grains. For example, interesting phenomena of dust rotation, crystallization and melting [99, 100] fall under this category. In the present work, neutral drag forces and forces due to ion accelerated in the sheath region have not been included which is important to study more realistic situations. We shall come back to this in Chapter-6 (Conclusions).

Returning to the content of present Chapter, no attempt has been made to control the temperature of the liquid during the simulation, the flow evolved under adiabatic conditions and the shear heat generated due to viscosity remained in the system. Several interesting questions are arised. For example, is it possible to address macroscale vortex dynamics using MD simulation and at the same time maintain the grain bed at the desired temperature ? What would be the spatio-temporal profile of temperature ? These questions are important not only from the physics point of view but also computational and numerical point of views. These important questions have been attempted in the forthcoming Chapter.

4

Molecular shear heating and vortex dynamics in thermostatted two dimensional Yukawa liquids

4.1 Introduction

In Chapter-3, using Kolmogorov flow [15, 16, 17, 82, 83, 101] as an initial shear flow in Yukawa liquids, it was demonstrated using molecular dynamics simulation that molecular shear heating destroys macroscale the vortex dynamics and reduce the coupling strength exponentially [19]. These calculations did not assume any microscale transport coefficients, hence are called as “classical first principle” calculations. In Chapter-3 in parallel shear flows [7, 8, 19] and rotational shear flows, the spatio-temporal evolution of instabilities as an initial value problem have been studied using molecular dynamics in a microcanonical ensemble. As no attempt was made to control the temperature of the liquid during the simulation, the flow evolves under adiabatic conditions and the shear heat generated due to shear heating was shown to remain in the system distributed dynamically in space and time. This led to a gradual increase in overall temperature and also strong localized

Chapter 4. Molecular shear heating and vortex dynamics in thermostatted two dimensional Yukawa liquids

gradients eventually resulting in short lifetimes of large scale vortex structures. Thus to address macroscale vortex dynamics it is highly desirable to “remove” this excess heat from the shear layer without altering the physics of the problem. In the present Chapter, we investigate, whether or not, at least in principle, is it possible to address macroscale vortex dynamics using MD simulation and at the same time maintain the grain bed at the desired temperature. In the following, in continuation of earlier Chapter, we consider Kolmogorov flow and Rankine vortex, which has been studied in Chapter-3 in the context of laminar to turbulent transition [19] wherein it was shown that the average coupling strength decreases exponentially with time due to molecular shear heating has been considered. In the current Chapter, it is proposed and demonstrated here that using MD simulation and thermostat based on configurational space degree of freedom [50, 51, 52, 53] (also called profile unbiased thermostat or PUT), it is possible to “remove” heat from the system generated by shear flow and yet study macroscale vortex dynamics due to shear heating without altering the velocity degree of freedom (DOF). Using this PUT, it is demonstrated that the average coupling strength can be controlled without compromising the effects of strong correlations on the macroscopic shear flow and vortex dynamics. A detailed comparison of the evolution and dynamics of parallel shear e.g Kolmogorov flow in the presence and absence of molecular shear heating, its effect on linear growth rate, non-linear saturation and transition from laminar to turbulence flow has been presented in this Chapter. As discussed earlier, in the parallel flow, shear heating zones are inseparably embedded in the region of vortex dynamics while in the rotational flows, the region of shear heating may be reasonably well separated in space from the nonlinear wave propagation region. In the last section of this Chapter, the emergence and propagation of nonlinear elastic-like waves generated from rotating circular vortex source has also been studied in absence of molecular shear heating. In the following, background for Configurational temperature has been presented first.

4.2 Configurational Temperature

Thermodynamic temperature is an estimate of the average or random kinetic energy of the particles in a homogeneous system. According to kinetic theory of gases, the kinetic temperature can be expressed as:

$$k_B T_{kinetic} = \frac{1}{Nd} \sum_{i=1}^N m_i v_i^2 \quad (4.1)$$

where k_B is Boltzmann constant and m_i, v_i are mass and instantaneous velocity of “ T^h ” particle respectively, N and d are number of particles and dimensionality of the system. Apart from this definition of temperature, assuming ergodicity, one can also define temperature by a purely dynamical time averaging of a function which is related to the curvature of energy surface. For example, H. H. Rugh [50], in 1997, presented a dynamical approach for measuring the temperature of a Hamiltonian dynamical system. Rugh indicates, using statistical thermodynamics for any closed Hamiltonian system, that the kinetic and configurational temperature would be asymptotically identical for a closed system of interacting particle. His definition of configurational temperature is:

$$\frac{1}{k_B T_{config}} = \nabla \cdot \frac{\nabla H}{\|\nabla H\|^2} \quad (4.2)$$

where $\|...\|$ is modulus operator and H is the Hamiltonian of classical dynamical system as ∇ is the phase space gradient. Butler [51] and others [102, 103] generalized Rugh’s idea for any function $B(\Lambda)$ of phase space Λ , such that

$$k_B T = \left\langle \frac{\nabla H(\Lambda) \cdot B(\Lambda)}{\nabla \cdot B(\Lambda)} \right\rangle \quad (4.3)$$

where $\Lambda = \{q_1, q_2, \dots, q_{3N}, p_1, p_2, \dots, p_{3N}\}$ is the phase space vector and (q_j, p_j) are $6N$ generalized coordinates for conjugate positions and momenta respectively. The angular brackets $\langle \dots \rangle$ indicate an ensemble average of the system. The Hamiltonian of the system $H(\Lambda) = K(p_j) + U(q_j)$, where $K(p_j)$ and $U(q_j)$ are kinetic and

Chapter 4. Molecular shear heating and vortex dynamics in thermostatted two dimensional Yukawa liquids

potential energy of the dynamical system respectively. In Eq. 4.3, $B(\Lambda)$ can be any continuous and differentiable vector in phase space. For example, if one chooses $B(\Lambda)$ as $B(\Lambda) = B(p_1, p_2, \dots, p_{3N}, 0, 0, \dots, 0)$, Eq. 4.3 yields the familiar kinetic temperature namely, $(3N/2)k_B T = \sum_{i=1}^N p_i^2 / (2m_i)$, which reduces to Eq. 4.1 for $d = 3$. Similarly when $B(\Lambda) = B(0, 0, \dots, 0, q_1, q_2, \dots, q_{3N}) = -\nabla U$ (say), Eq. 4.3 gives configurational temperature in potential form

$$k_B T_{config} = \left\langle \frac{(\nabla U)^2}{\nabla^2 U} \right\rangle \quad (4.4)$$

Assuming ergodicity, the temperature of the system is determined by averaging large number of time steps. In a closed system, these kinetic and configurational temperatures are expected to be asymptotically identical. In the following, we shall try to demonstrate that kinetic and configurational temperature are close to each other for a system of particle interacting via Yukawa type potential.

4.2.0.1 Kinetic and configurational temperatures

In dusty plasma, larger mass of dust grains as compared to other component (electron and ion) makes dust dynamics slow. Due to slow dynamics of grain medium, ambient plasma properties have been considered invariant and modeled only grain dynamics, which is strongly coupled. The configurational temperature of the grain medium where, grains interact via screened Coulomb or Yukawa potential $U(\mathbf{r})$ has been calculated first using $U(\mathbf{r})$:

$$U(\mathbf{r}_i) = \frac{Q_h}{4\pi\epsilon_0} \sum_{j \neq i}^N \frac{e^{-r_{ij}/\lambda_D}}{r_{ij}} \quad (4.5)$$

where $r_{ij} = |\mathbf{r}_i - \mathbf{r}_j|$ is the inter particle distance of i^{th} and j^{th} particle. The N -body problem is then numerically integrated using our parallelized MD code [34].

Configurational temperature have been calculated by using Eq. 4.4 where, interaction potential $U(\mathbf{r}_i)$ is given by Yukawa potential as in Eq. 4.5. Time, distance

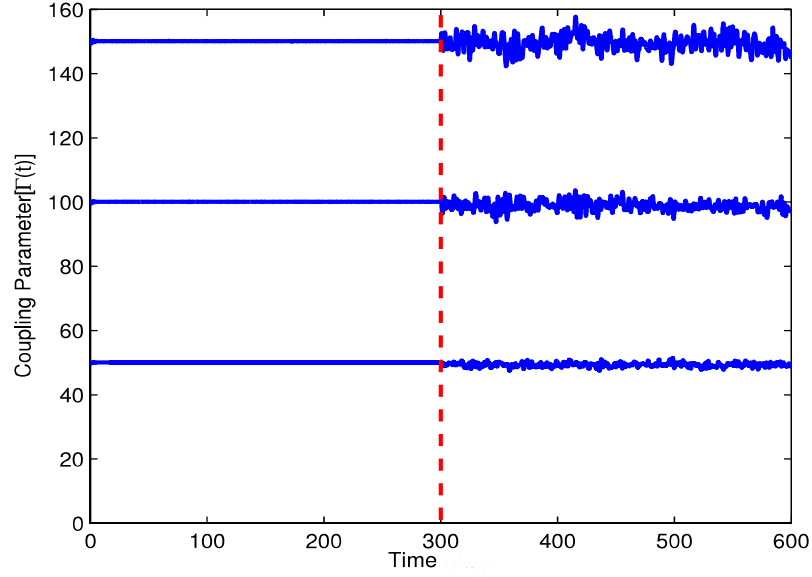


Figure 4.1: Thermalisation of particles using Gaussian thermostat for screening parameter $\kappa = 0.5$ and various desired coupling parameter Γ_0 value. From $0 - 300\omega_0^{-1}$ Gaussian thermostat is ON (canonical run) and after that for next $300\omega_0^{-1}$ thermostat is OFF (microcanonical run) for different $\Gamma_0 = 50, 100, 150$.

and energy are normalized same as described in Chapter.3. Therefore, all physical quantities appearing hereafter in present chapter are non-dimensional. In presented simulations, for a given dust grain density \bar{n} , the size of the system is decided by the total number of particles. For the purpose of demonstrating, kinetic and configurational temperature, we have considered small degree of freedom. For $N = 2500$ and $\kappa = 0.5$, a system has been first brought to the desired Γ using a Gaussian thermostat [104]. In Fig.4.1, we have measured results for various coupling parameter and calculated configurational temperature using Eq.4.4 as a function of time. In this figure particles are thermalised canonically by Gaussian thermostat upto $300\omega_0^{-1}$ and thereafter microcanonically for next $300\omega_0^{-1}$. After this, system is evolved under micro-canonical conditions and notice excellent agreement between temperatures obtained from both kinetic [using Eq.4.1] and configurational [using

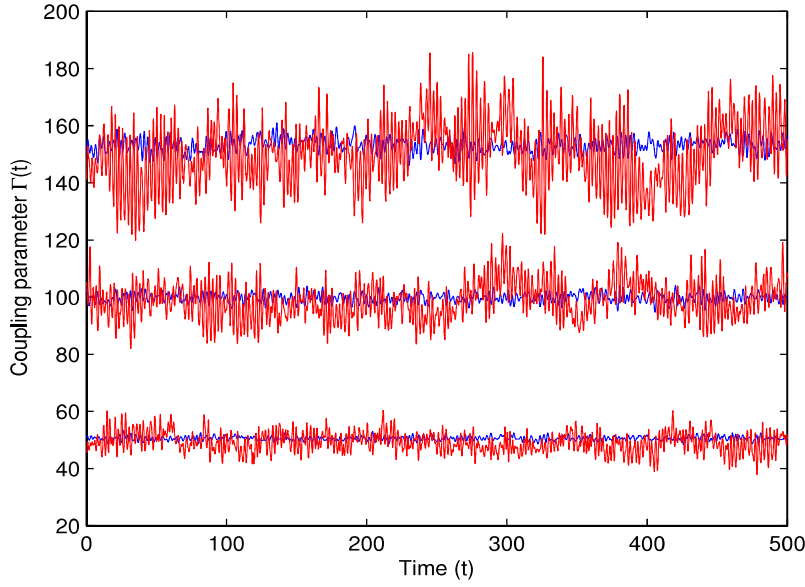


Figure 4.2: Kinetic (blue) and configurational (red) $\Gamma(t)$ extracted under micro-canonical conditions for the Yukawa liquid previously equilibrated at $\Gamma = 50, 100, 150$ with $\kappa = 0.5$

Eq.4.4] degrees of freedom (see Fig.[4.2]). The absence of any noticeable drift in temperature even without a thermostat indicates good numerical stability of our time integration.

4.3 Configurational Thermostat

In conventional MD simulations, thermostats are generally used to maintain the temperature of the system at a desired value in a canonical ensemble. For example, in a typical Gaussian thermostat [104], a Lagrangian multiplier is invoked for instantaneous velocities and equations of motion are augmented (in the Nose-Hoover sense) with a velocity dependent non-holonomic constraint (Constraints that constrain the velocities of particles but not their positions). While the trajectory of the system generated so, strictly conforms to the iso-kinetic ensemble, it can be shown that the observed thermodynamic behavior of the system corresponds

Chapter 4. Molecular shear heating and vortex dynamics in thermostatted two dimensional Yukawa liquids

very well to that of the canonical ensemble in thermodynamic limit. As can be expected, such velocity scaling based thermostats can work only at low shear rates and are immediately rendered useless at high shear rates where secondary flows usually develop. The purpose of this Chapter to show that a profile unbiased thermostat or PUT can be efficiently applied to control the temperature of shear flows and below we present the details of our protocol.

Once a macroscale flow is superimposed onto the thermalized grain bed, the instantaneous particles velocities contain information regarding the “thermal” and the “flow (or average)” parts. Especially at high Reynolds number regime where secondary flows usually develop, it becomes impossible to control temperature using such PBTs which rely only on velocity scaling. Thus controlling the “thermal” component of velocity and letting mean component evolve is impossible using thermostats which use augmented velocity equation as in a Gaussian thermostat. Is it then possible to “thermostat” a system with N particles without modifying the instantaneous velocities of particles ? The answer is yes.

As discussed earlier, a novel method of thermostating namely, configurational thermostat has been introduced. In the past, Rugh [50] and Butler [51] presented a method of calculating the temperature of a Hamiltonian dynamical system. This method of calculating temperature only depends upon the configurational information of the system, hence named configurational temperature. Influenced by the concept of configurational temperature, a new method of thermostating namely configurational thermostat, has been introduced by Delhommelle and Evans [105, 106], Patra and Bhattacharya [107] and, Braga and Travis [52, 53]. Due to its relative simplicity in implementation, the Braga-Travis version of PUT has been chosen. This method amounts to invoking appropriate Lagrange multipliers that will efficiently couple the grain bed to a configurational thermostat, which controls the temperature by using augmented equations of motions for the instantaneous particle positions without disturbing the instantaneous velocity of

Chapter 4. Molecular shear heating and vortex dynamics in thermostatted two dimensional Yukawa liquids

particles. In this PUT, instead of a non-holonomic constraint, a holonomic constraint is augmented to the equation of motion. The temperature of the system is then calculated by using configurational definition [Eq. 4.4] that agrees well with the kinetic temperature calculated using Eq. 4.1. To better understand the ways in which the configurational thermostat differs from its kinetic counterpart, both these schemes have been described below.

The equation of motion corresponding to conventional kinetic Nose-Hoover thermostat are:

$$\dot{\mathbf{r}}_i = \frac{\mathbf{p}_i}{m_i} \quad (4.6)$$

$$\dot{\mathbf{p}}_i = -\frac{\partial U}{\partial \mathbf{r}_i} - \eta \mathbf{v}_i \quad (4.7)$$

$$\dot{\eta} = \frac{1}{Q_\eta} \left(\sum_{i=1}^N \frac{m_i v_i^2}{2} - k_B T_0 \right) \quad (4.8)$$

where m_i , \mathbf{r}_i , \mathbf{p}_i and T_0 are mass, position, momentum of “ T ”-th particle and desired temperature respectively. Lagrange multiplier η is a dynamical variable and Eq. 4.6-Eq. 4.8 are the new augmented equations of motion. Q_η is damping constant or effective mass [108, 109]. In the same way, for “ T ”-th particle the augmented equations of motion corresponding to configurational temperature based Nose-Hoover thermostat as defined by Braga and Travis [52, 53] are :

$$\dot{\mathbf{r}}_i = \frac{\mathbf{p}_i}{m_i} - \mu \frac{\partial U}{\partial \mathbf{r}_i} \quad (4.9)$$

$$\dot{\mathbf{p}}_i = -\frac{\partial U}{\partial \mathbf{r}_i} \quad (4.10)$$

$$\dot{\mu} = \frac{1}{Q_\mu} \left(\sum_{i=1}^N \left(\frac{\partial U}{\partial \mathbf{r}_i} \right)^2 - k_B T_0 \sum_{i=1}^N \frac{\partial^2 U}{\partial r_i^2} \right) \quad (4.11)$$

In above equations, the Lagrange multiplier μ is a dynamical variable. In configurational thermostat, Q_μ is an empirical parameter which behaves as the effective mass associated with thermostat. The value of Q_μ decides the strength of coupling

Chapter 4. Molecular shear heating and vortex dynamics in thermostatted two dimensional Yukawa liquids

between system and heat-bath. It is found that the value of damping constant or effective mass Q_μ is sensitive to the desired coupling parameter Γ values. For a desirable Γ , it is found that for low values of damping constant, the system arrives at the desired Γ faster and vice-versa. In the limit $Q_\mu \rightarrow \infty$ the configurational thermostat is de-coupled and formulation becomes micro-canonical ensemble. In Fig.[4.3], it is shown that how coupling parameter is sensitive to the value of damping constant or effective mass Q_μ . Here we have taken three different values of effective mass $Q_\mu = 2 \times 10^5, 2 \times 10^6$ and 2×10^7 . It is found that for low value of damping constant the system equilibrated at desired temperature faster rather than high Q_μ values. In the limit $Q_\mu \rightarrow \infty$ the Configurational thermostat is de-coupled and formulation becomes microcanonical ensemble. Extended Hamiltonian H' for various Q values in Fig.[4.4] has been plotted. It is found that, the Q_μ which decides the strength between the system and the heat-bath. For example, larger the value of Q_μ , weaker is the coupling strength between physical system to heat-bath changes the time of conservation of H' because H' depends upon the Q_μ value [see Eq.4.12], it is clear from the Fig.[4.3] that for $Q_\mu = 2 \times 10^6$ after $t = 100\omega_0^{-1}$ coupling parameter starts to reach its desired value $\Gamma = 50$. In this chapter, chosen $Q_\mu = 2 \times 10^6$ has been considered.

$$H'(\vec{r}, \vec{p}, \mu, \phi_\mu) = H(\vec{r}, \vec{p}) + \frac{1}{2}Q_\mu\mu^2 + \phi_\mu \quad (4.12)$$

where,

$$H(\vec{r}, \vec{p}) = \sum_{i=1}^N \frac{p_i^2}{2m_i} + \sum_{j \neq i}^N U(r_{ij}), \quad p_i = m_i v_i \quad (4.13)$$

$$\dot{\phi}_\mu = \mu k_B T_0 \sum_{i=1}^N \frac{\partial^2 U}{\partial r_i^2} \quad (4.14)$$

where T_0 is desired temperature. For the range of Γ values studied here, we find that $Q_\mu = 2 \times 10^6$ allows steady state with in time $t = 100$ and hence is used throughout. Using a PUT, it is depicted in Fig.[4.5] that kinetic and configurational coupling parameter Γ follow the same behavior in canonical and in micro-canonical run as well. In the following section, the evolution of shear

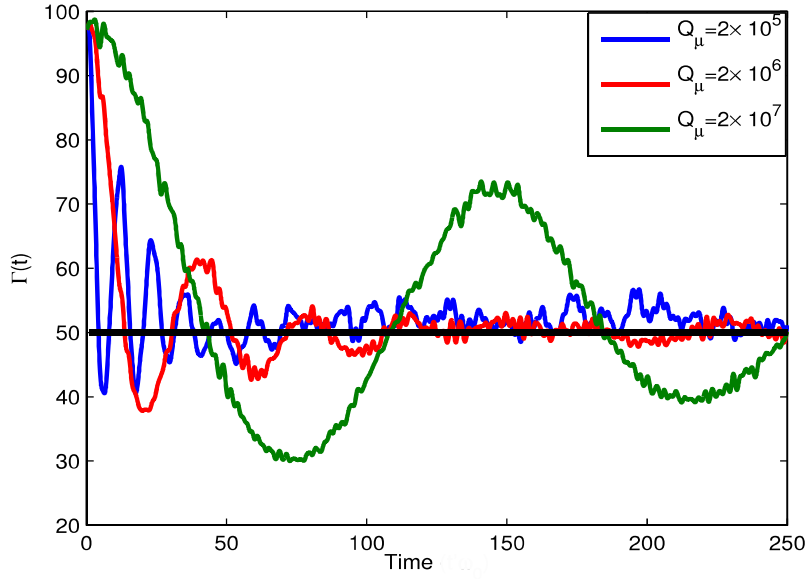


Figure 4.3: Canonical run using B-T thermostat for desired coupling parameter $\Gamma_0 = 50$ with various effective mass Q_μ for $N = 2500$, $\kappa = 0.5$.

flow namely, Kolmogorov flow, in Yukawa liquids in the presence and absence of microscopic or molecular shear heat is presented.

4.4 Kolmogorov Flow as an initial value problem in Yukawa liquid with and without molecular heat generation

To study the shear flow evolution and vortex dynamics from the microscopic dynamics in presence and absence of heat generation phenomena, Kolmogorov flow [15] as an initial value problem has been studied. This simply implies that a flow profile \mathbf{U}_0 is loaded at $t = 0$ and no attempt is made to control the mean flow at later times. At time $t > 0$, a PUT is used to maintain the desired temperature. The loaded shear profile has the form $\mathbf{U}_0(x, y) = U_0 \cos(2\pi n_0 x / L_x)(1 +$

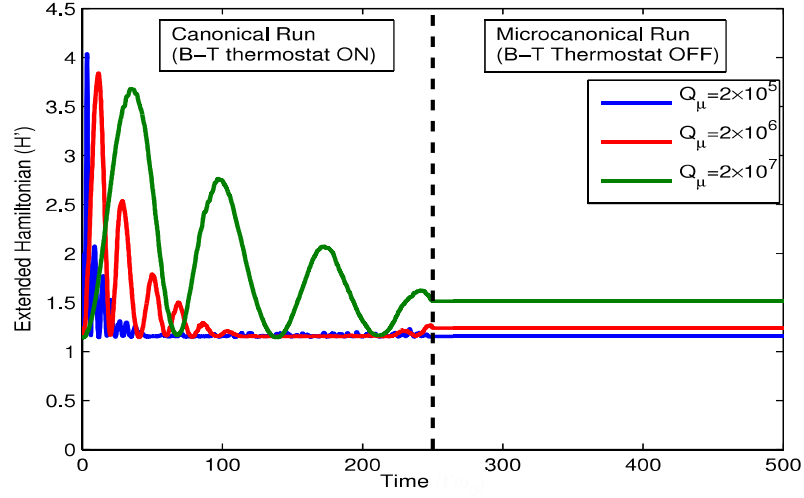


Figure 4.4: Extended Hamiltonian of the system with time. Canonical run from $(0 - 250)\omega_0^{-1}$ and microcanonical run for next $250\omega_0^{-1}$ for various Q_μ values for $N = 2500$, $\kappa = 0.5$ and $\Gamma_0 = 50$.

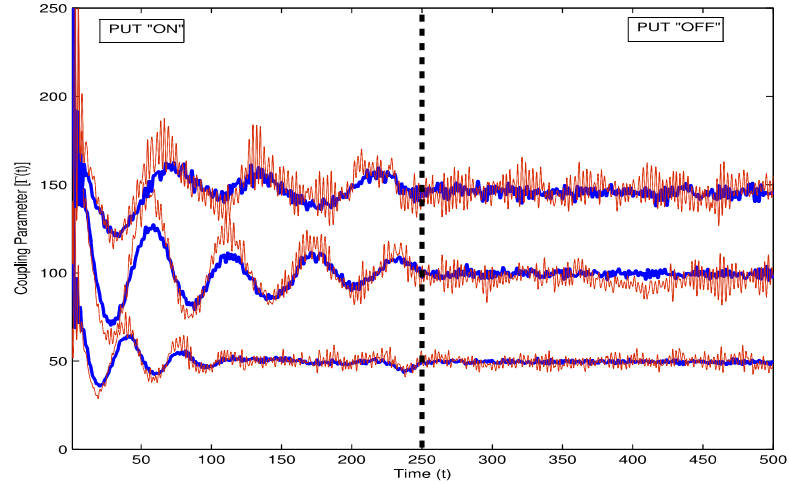


Figure 4.5: Kinetic (blue) and configurational (red) Γ vs time. Parameters used: $Q_\mu = 2 \times 10^6$, $N = 2500$ and $\kappa = 0.5$.

$\delta \cos(2\pi my/L_y))\hat{y}$, where the magnitude of equilibrium velocity $U_0 = 1$, spatial period number $n_0 = 3$, magnitude of perturbation $\delta = 0.01$, perturbed mode

Chapter 4. Molecular shear heating and vortex dynamics in thermostatted two dimensional Yukawa liquids

number $m = 2$. Coupling strength at time $t = 0$ is $\Gamma_0 = \Gamma(t = 0) = 50$, for which calculated thermal velocity is $v_{th} = \sqrt{2/\Gamma_0} = 0.2$, which is much smaller than the equilibrium velocity ($U_0 = 1$). Unlike earlier section [Sec. 4.3], here large number of particles $N_h = 62500$ have been considered to study large-scale hydrodynamic phenomena using MD simulation. Due to the large size of the simulation box $L_x = L_y = L = 443.12$, Ewald sums [74] has not considered. The non-dimensional screening parameter κ is 0.5. It is estimated that the sound speed of the system for $\Gamma_0 = 50$ and $\kappa = 0.5$ is with in the range of 1.6-2.0 [25] which is larger than the equilibrium velocity U_0 . Hence the shear flow is considered to be “subsonic” in nature.

Previously, it has been demonstrated that after superposition of the Kolmogorov flow, the coupling parameter was found to weaken under adiabatic conditions due to molecular shear heating[19]. In the present chapter, it is demonstrated that this average coupling parameter when coupled to the configurational thermostat is approximately constant and close to desired Γ . In Fig.[4.6], earlier results along with the current results of average coupling parameter have been plotted. In Fig.[4.6](a) the system is thermally equilibrated up to time $t = 300$ using a conventional Gaussian thermostat. In (b) it is shown that the microcanonical run in the time interval $300 < t < 600$. At $t = 600$ the shear flow has been superposed just once and then observe the system both with PUT “ON” (c) and with PUT “OFF” (d). As clearly seen from (d), the heat generated due to shear flow remains within the system and weakens the coupling strength Γ . It is found that this decay to be exponential in time (see fit). This is in stark contrast to the regime (c) where this excess heat has been “removed” from the system through heat-bath, which is turn facilitates Γ to remain constant. [The study has been repeated by replacing the Gaussian thermostat in a with a PUT and found identical results]. It has also been seen from Fig.[4.7] that both the configurational and kinetic coupling parameter are close to the initial value $\Gamma_0 = 50$.

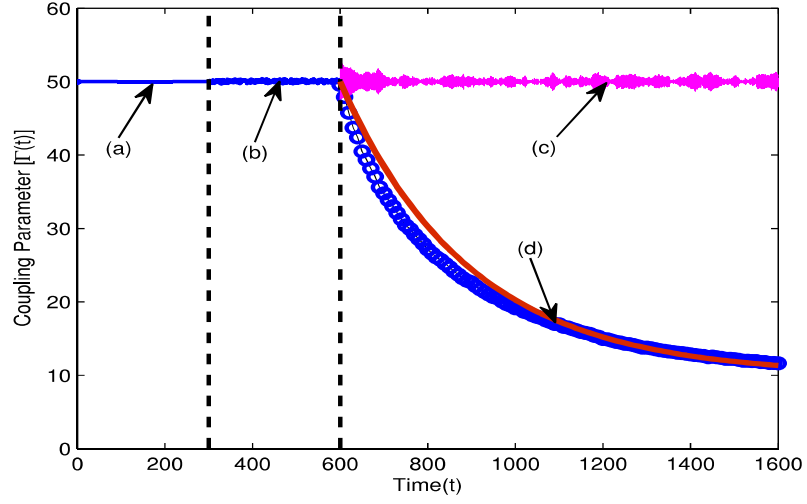


Figure 4.6: Coupling parameter vs time. The system is evolved (a) coupled to Gaussian thermostat (b) under micro-canonical conditions (c) with PUT “ON” and flow superposed at $t = 600$ (d) with PUT “OFF”. A fit (red) to show that weakening of Γ is indeed exponential in time has been provided. Parameters used: $\Gamma_0 = 50$.

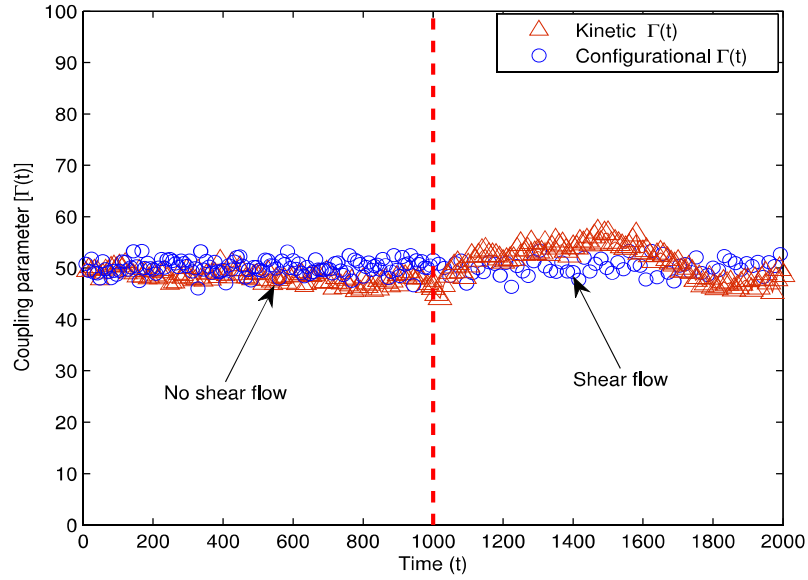


Figure 4.7: Coupling parameter vs time plot with PUT always “ON”. Shear flow is superimposed at time $t = 1000$.

Chapter 4. Molecular shear heating and vortex dynamics in thermostatted two dimensional Yukawa liquids

Macroscopic quantities from microscopic information-process of “fluidization”:

A mesh-grid of size 55×55 is superimposed on the particles of the system to calculate the macroscopic or “fluid” variables. Average local fluid velocities along x and y directions are calculated as $\bar{U}_x = (1/N_b) \sum_{i=1}^{N_b} v_{ix}$, $\bar{U}_y = (1/N_b) \sum_{i=1}^{N_b} v_{iy}$, where v_{ix} and v_{iy} are individual instantaneous particle velocities along x and y direction and N_b is the total number of particles present in an individual bin. Each bin contains approximately 20 particles [$N_b = N_h/(55 \times 55) \simeq 20$ with $N_h = 62500$]. From average local velocities, we calculate the average local vorticity $\bar{\omega}(x_G, y_G) = \nabla \times \bar{\mathbf{U}}$ and the average local temperature $\bar{T}(x_G, y_G) = (2/3) \sum_{i=1}^{N_b} ((v_{ix} - \bar{U}_x)^2 + (v_{iy} - \bar{U}_y)^2)/N_b$ at the Eulerian grid location (x_G, y_G) . In Fig.4.9 time evolution of “fluidized” vorticity after superposition of shear flow both in the presence (top panel) and absence (bottom panel) of PUT has been shown. It is clearly seen that shear heating destroy vortex structures thus resulting in their shorter lifetimes compared to the case when PUT is “ON” where the lifetimes of these vortices become significantly longer. In Fig.4.11 the time evolution of “fluidized” coupling strength after superposition of shear flow both in the presence (top panel) and absence (bottom panel) of PUT has been demonstrated. From these figures, it is clear that due to shear heating [see Fig.4.11 (top)] the coupling strength decreases and becomes weaker and weaker. Unlike, In PUT “ON” case [see Fig.4.11 (bottom)], the coupling strength is maintained. However, there is still local shear heating present at the shear location because thermostat maintained the global temperature of the system not local temperature. In Fig.4.12, it is shown that data for $\bar{T}(x_G, y_G)$ extracted at different times with shear flow imposed. In the absence of PUT (shown with symbols), the temperature first increases and then eventually saturates at a particular value at long times. This is in contrast to the case when PUT is present where the temperature first increases (discussed later) and then saturates at the initial temperature at long times. The value of initial temperature taken was 0.02 ($\Gamma_0 = 50$). In Fig.5.2 and Fig.5.3 the y -component of velocity at various times in the absence and presence of PUT have been plot-

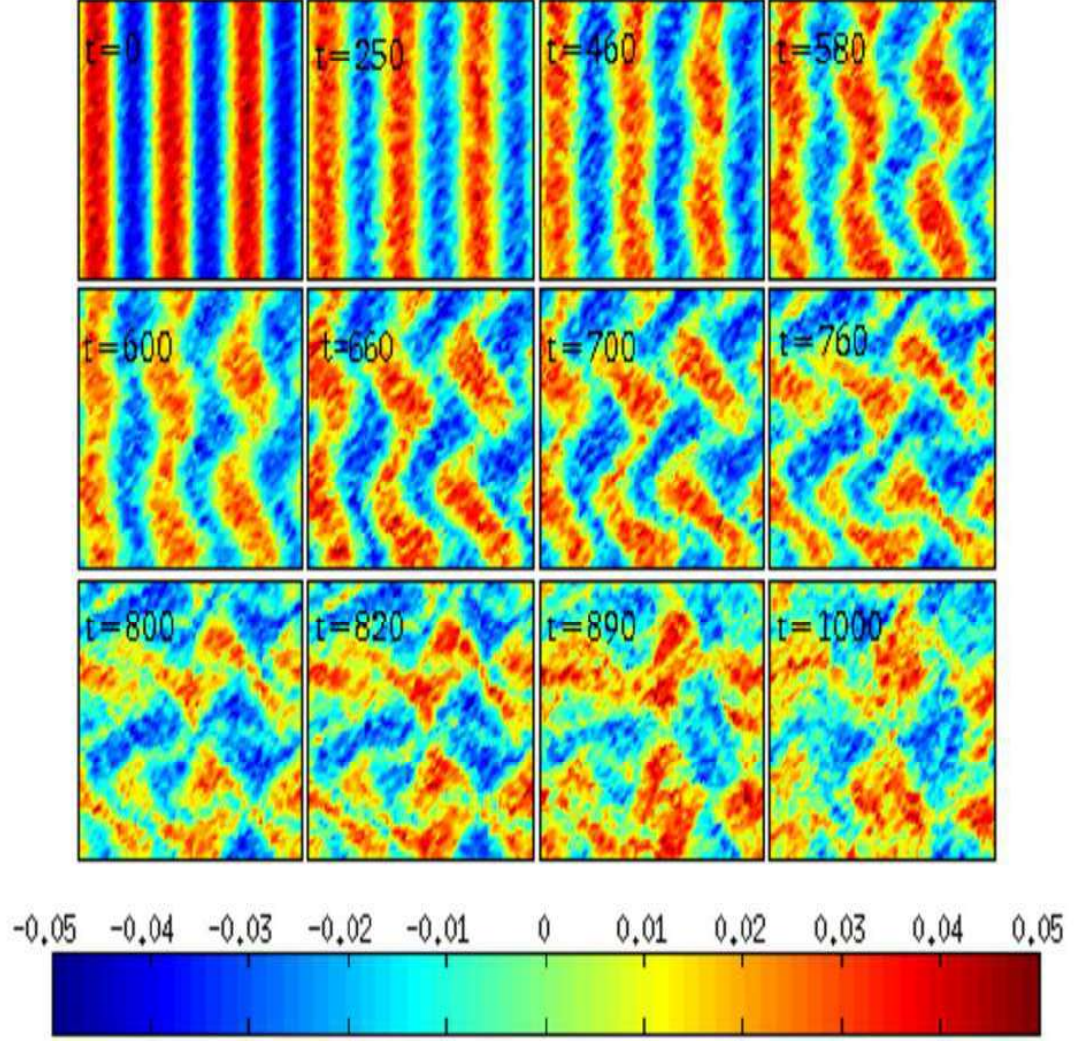


Figure 4.8: “Fluid” vorticity ($\omega = \nabla \times \mathbf{U}$) contour plots. Color bars show the magnitude of local vorticity. Parameters used: perturbation mode $m = 2$, equilibrium spatial period number $n_0 = 3$, $\Gamma_0 = 50$, $\kappa = 0.5$, initial Reynolds number $R = 235.149$ and shear velocity $U_0=1$ with PUT “OFF”. The micro scale heating quickly destroy the vorticity structures when PUT is “OFF”.

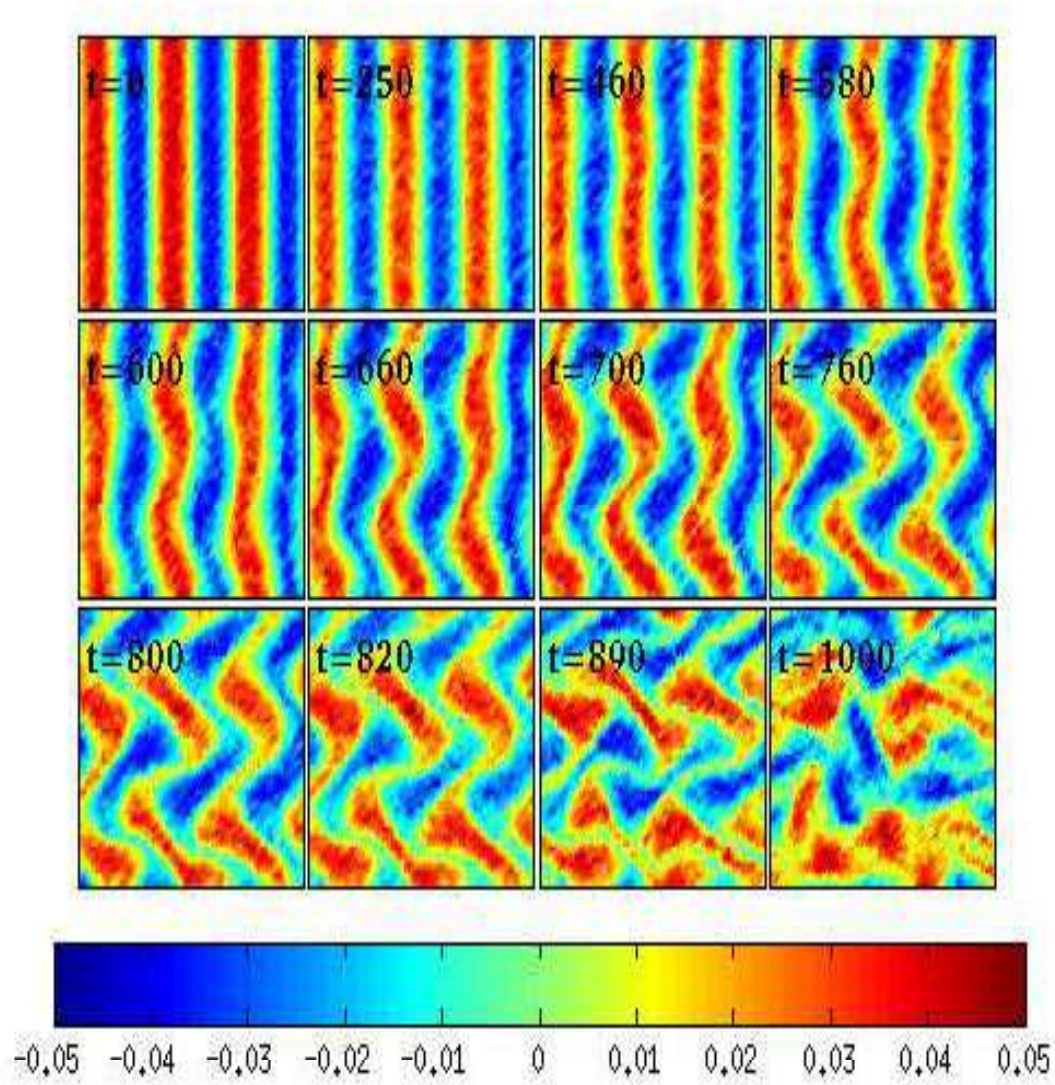


Figure 4.9: “Fluid” vorticity ($\omega = \nabla \times \mathbf{U}$) contour plots. Color bars show the magnitude of local vorticity. Parameters used: perturbation mode $m = 2$, equilibrium spatial period number $n_0 = 3$, $\Gamma_0 = 50$, $\kappa = 0.5$, initial Reynolds number $R = 235.149$ and shear velocity $U_0=1$ with PUT “ON”. When PUT is “ON”, vortex structures sustain for longer time.

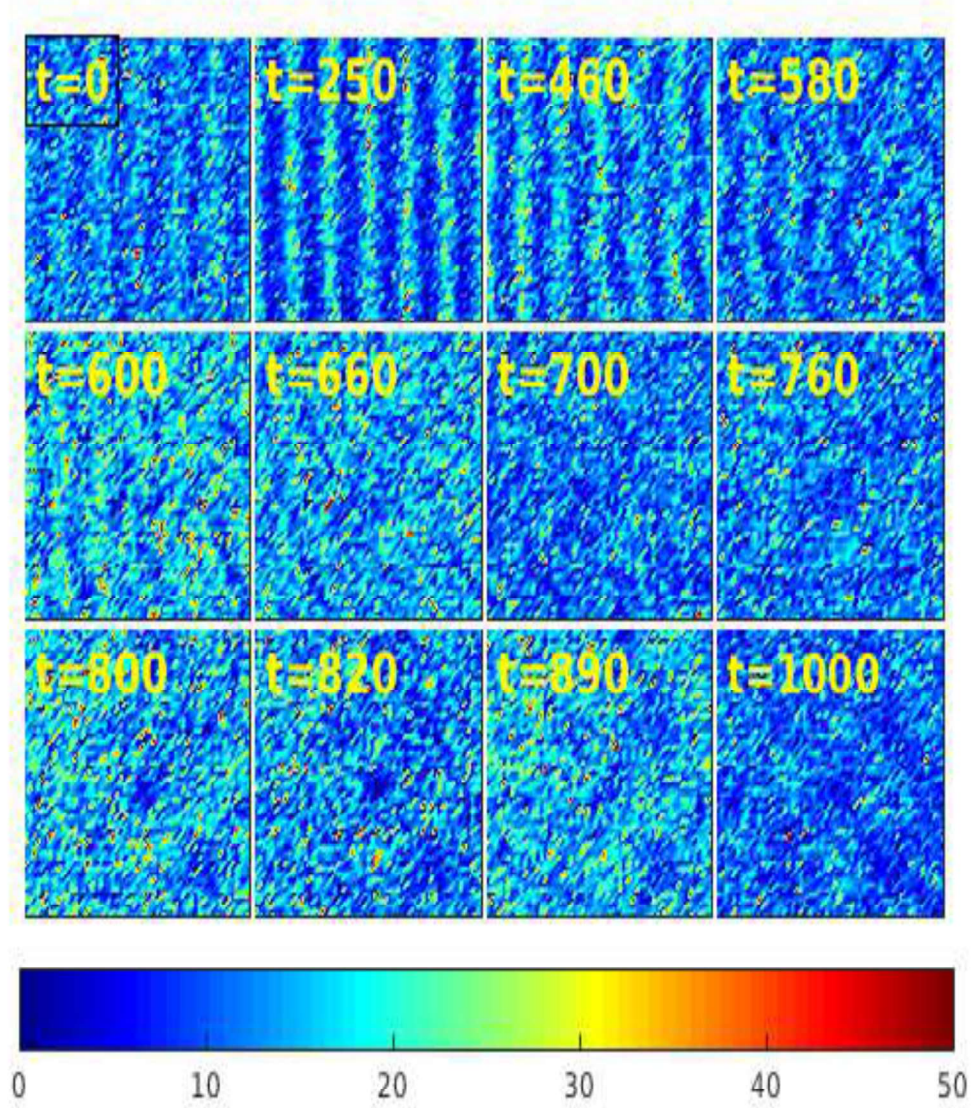


Figure 4.10: Spatial distribution of $\Gamma(x, y, t)$ -Contour plots of Coupling parameter Γ . Parameters used: perturbation mode $m = 2$, equilibrium spatial period number $n_0 = 3$, $\Gamma_0 = 50$, $\kappa = 0.5$, initial Reynolds number $R = 235.149$ and shear velocity $U_0=1$ with PUT “OFF”.

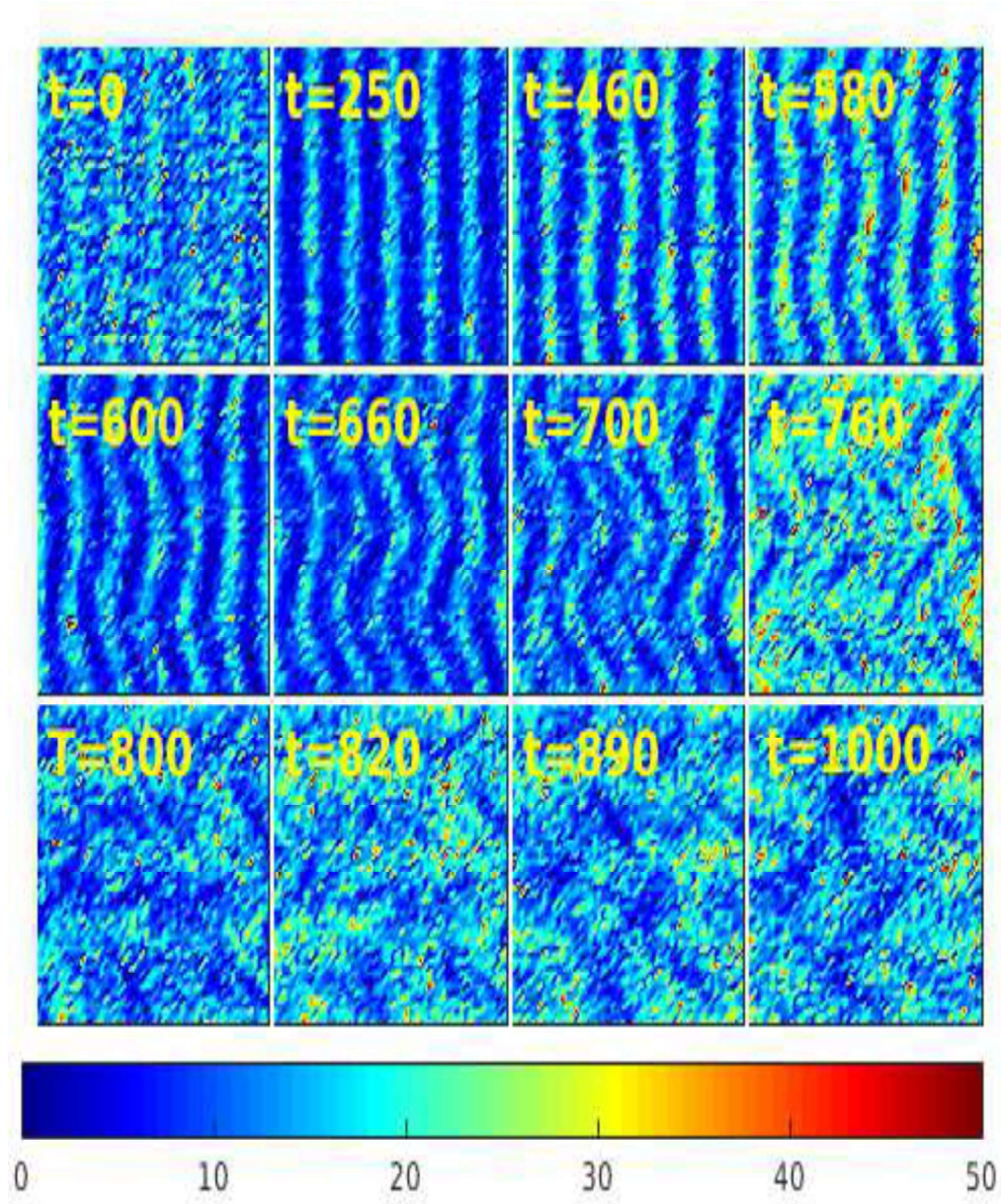


Figure 4.11: Contour plots of Coupling parameter. Parameters used: perturbation mode $m = 2$, equilibrium spatial period number $n_0 = 3$, $\Gamma_0 = 50$, $\kappa = 0.5$, initial Reynolds number $R = 235.149$ and shear velocity $U_0=1$, when PUT is “ON”.

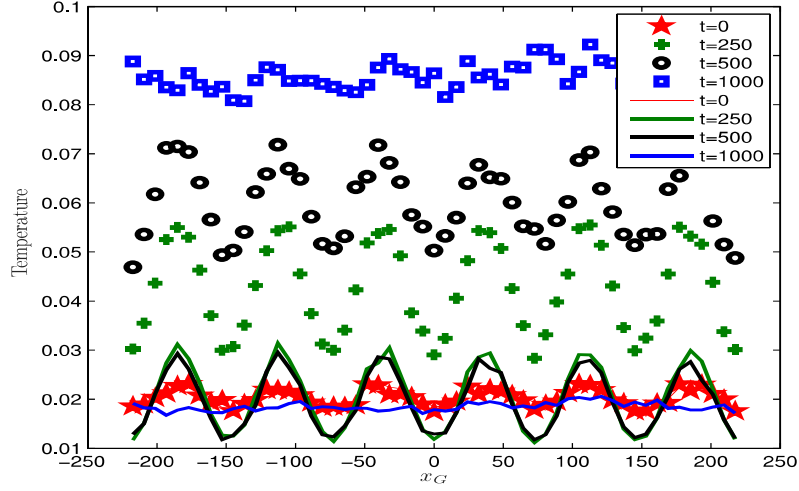


Figure 4.12: y - averaged temperature profiles ($\bar{T}(x_G, y_G, t)$) at various times after the shear flow is superimposed. Parameters used are $\Gamma_0 = 50$, $U_0 = 1$ and $\kappa = 0.5$. Symbols show the temperature profile with PUT “OFF” and solid lines show temperature variation with PUT “ON”.

ted respectively. It is found that in both the cases the velocity profiles have not changed much between the linear and non-linear regimes of shear flow evolution. They remain qualitatively similar and differ only quantitatively. The perturbed x component of kinetic energy δE_{kx} is obtained from the expression below and it is used to calculate the growth rate shown in the Fig.4.15.

$$\left| \frac{\delta E_{kx}(t)}{E_{kx}(0)} \right| = \frac{\int \int [v_x^2(t) - v_x^2(0)] dx dy}{\int \int v_x^2(0) dx dy} \quad (4.15)$$

It is found that the calculated growth rate γ_h in the absence and presence of PUT are very close with the difference being only marginal ($< 10\%$). In Fig.[4.17], it have been shown that the results of a parametric study for maximum growth-rate of perturbed mode with initial Reynolds number $R = U_0 l \bar{n} / \eta_0$, where l , η_0 are the shearing length and initial shear viscosity of the flow respectively. Here, the initial value of shear viscosity η_0 is calculated using the Green-Kubo formalism [22, 90] before Kolmogorov flow superimposed. It is depicted from figure that for

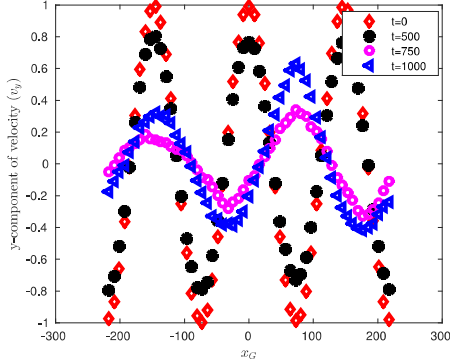


Figure 4.13: Temporal evolution of y averaged velocity $v_y(x_G)$ profile for $\Gamma_0 = 50$, equilibrium velocity magnitude $U_0 = 1$, screening parameter $\kappa = 0.5$, in the presence of heating (PUT “OFF”). Time t here are shown after superimposition of shear flow.

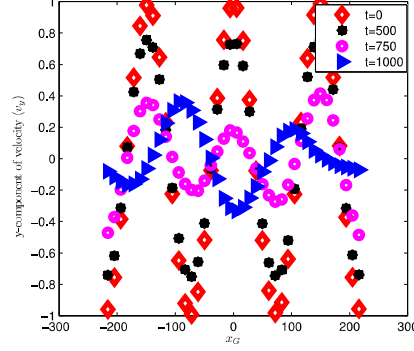


Figure 4.14: Temporal evolution of y averaged velocity $v_y(x_G)$ profile for $\Gamma_0 = 50$, equilibrium velocity magnitude $U_0 = 1$, screening parameter $\kappa = 0.5$, in the presence of heating (PUT “ON”). Time t here are shown after superimposition of shear flow.

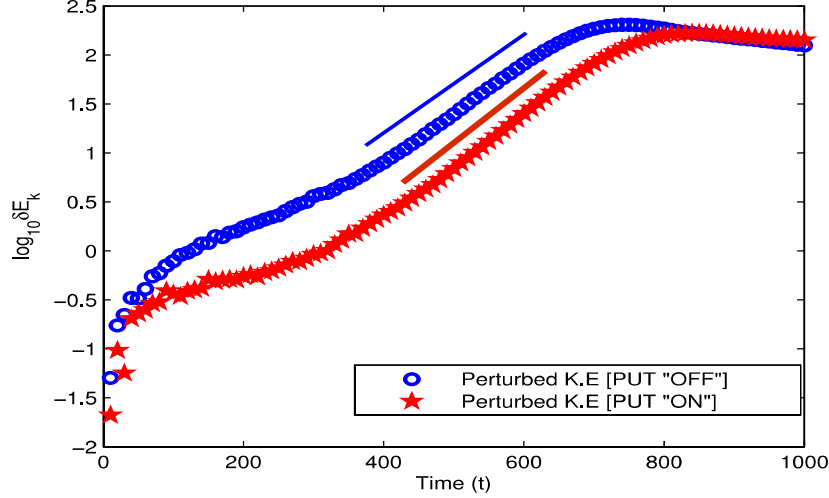


Figure 4.15: Perturbed kinetic energy in linear-log scale with and without PUT. Calculated growth rates from simulation are 5.5×10^{-2} and 6.0×10^{-2} for PUT “OFF” and “ON” case respectively.

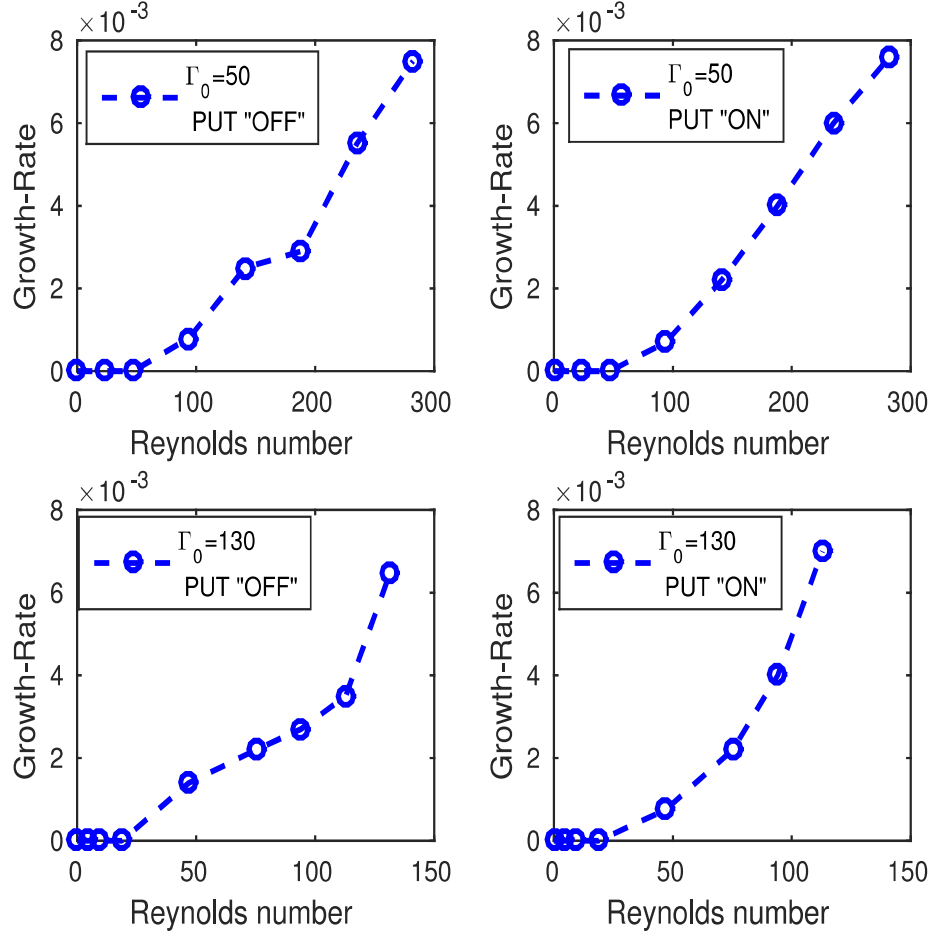


Figure 4.16: Growth-Rate vs initial Reynolds number ($R = \frac{U_0 l \bar{n}}{\eta_0}$) plot for screening parameter $\kappa = 0.5$.

given value of Γ_0 and κ , flow is neutrally stable below $R < R_c$, where R_c is critical value of Reynolds number and for $R > R_c$ flow becomes unstable and eventually turbulent. Such laminar to turbulent transition in our system might be a trans-critical bifurcation [91]. Interestingly, It is found that higher values of coupling parameter Γ decreases the critical value of Reynolds number R_c . Also the critical value of Reynolds number R_c is found to be independent of heat generation. It is evident from Fig.[4.17] that the growth-rate of perturbed mode ($m = 2$) is not

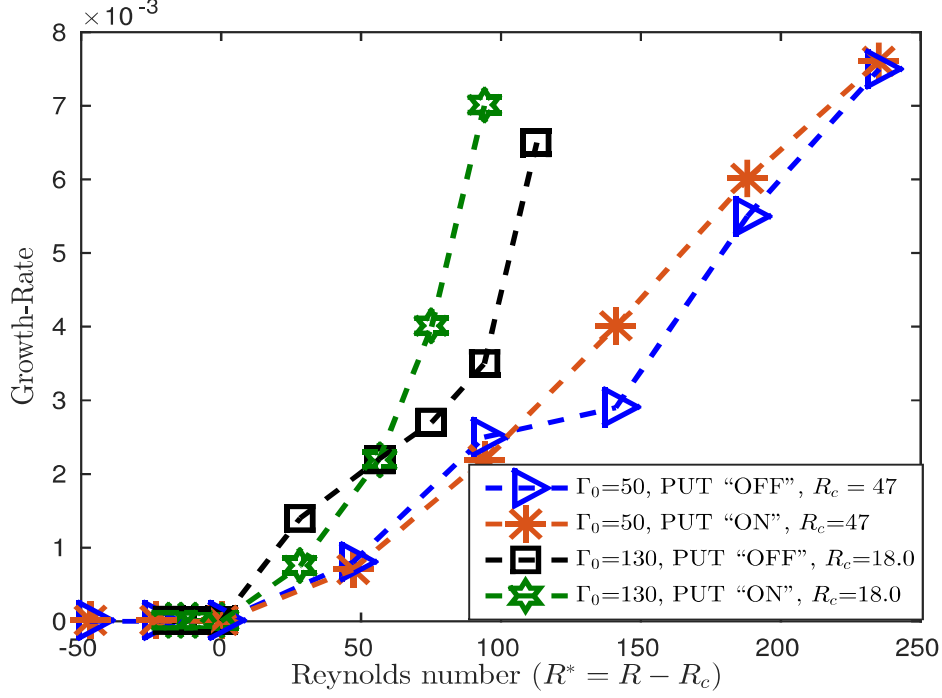


Figure 4.17: Growth-Rate vs initial Reynolds number $R^* = R - R_c$ plot showing trans-critical kind of bifurcation for screening parameter $\kappa = 0.5$, where $R_c = 47$ and 18.80 for $\Gamma_0 = 50$ and 130 respectively.

affected by molecular or microscopic heating, which shows that the suppression of heat generation does not modify the shear flow dynamics in early phase of simulation.

4.5 Rotational shear flow

In the past, various wave related phenomena have been studied in strongly correlated grain medium for example, compressional and shear modes [98, 110], Mach cones [111], transverse waves [112] and driven transverse wave [113]. Also, using molecular dynamics simulation and experiment the radiation of elastic waves in a plasma crystal using small dipole source has been observed [54]. In this Section we address several important questions for example, what would be the effect

Chapter 4. Molecular shear heating and vortex dynamics in thermostatted two dimensional Yukawa liquids

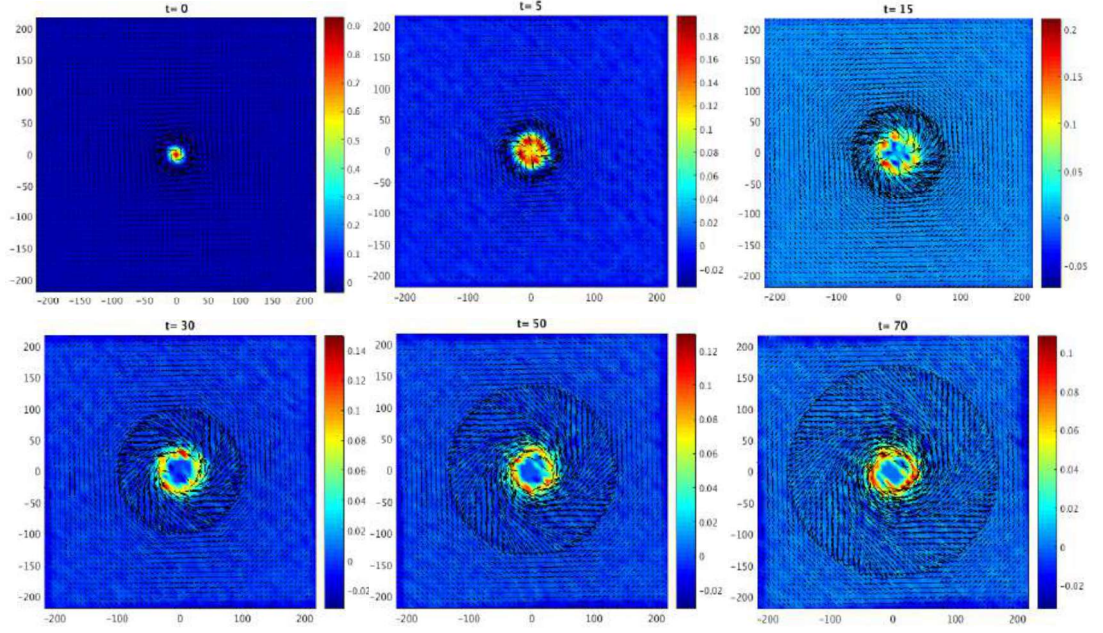


Figure 4.18: Time evolution plots of Rankine vortex for $\Gamma_0 = 70$, $\kappa = 1.0$ and $V_0 = 5$ with configurational thermostat. Black coloured arrows show the direction of velocity field.

of strong correlation over the shear wave in presence of coherent localized vortex with configurational thermostat, where temperature is constant through out the simulation [as described in Sec.4.3]?, How the shear wave changes its nature with azimuthal speed of coherent localized vortex. To study the rotational shear flow and emergence non-linear elastic wave, Rankine vortex profile has been superimposed over thermalised particles velocities and configurational thermostat is “ON” through out the simulation time (canonical run) [constant volume, constant total temperature and constant particles number]. It is important to note that the input profile (Rankine vortex) is same as given in Chapter-3. In Fig.4.18, time evolution of Rankine vortex for $\Gamma_0 = 70$, $\kappa = 1.0$ and $V_0 = 5$ has been shown. It can be clearly seen that the azimuthal rotation of circular vortex generates the waves towards periodic boundaries. Non-linear wave propagation in 3D plot has been plotted for $V_0 = 5.0$ in Fig.4.19. In the same way, in Fig.4.20, propagation of density variation (compression wave) has been shown. It is found that the velocity

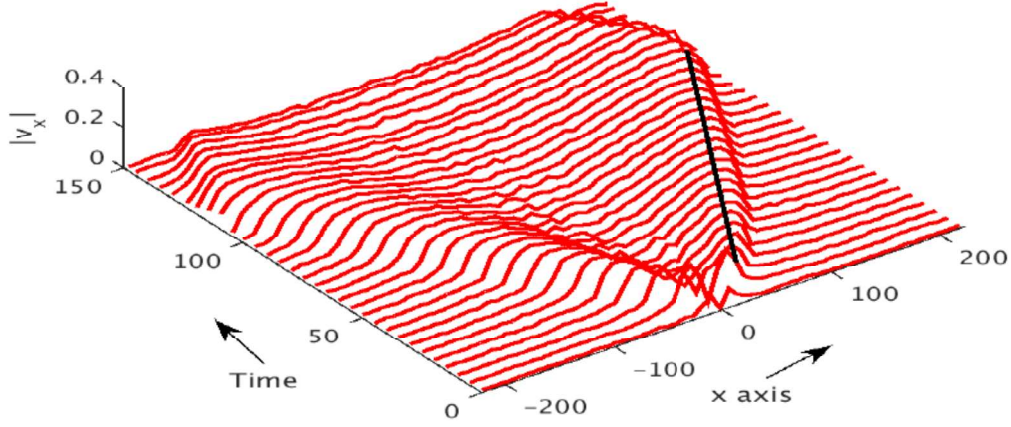


Figure 4.19: Propagation of nonlinear wave for $\Gamma_0 = 70$, $\kappa = 1$ and $V_0 = 5$ [$C_x = \Delta x / \Delta t = 2.109$, $C_{NLW} = \sqrt{C_x^2 + C_y^2} = 2.98$] with configurational thermostat. Similar structure is seen along y -axis.

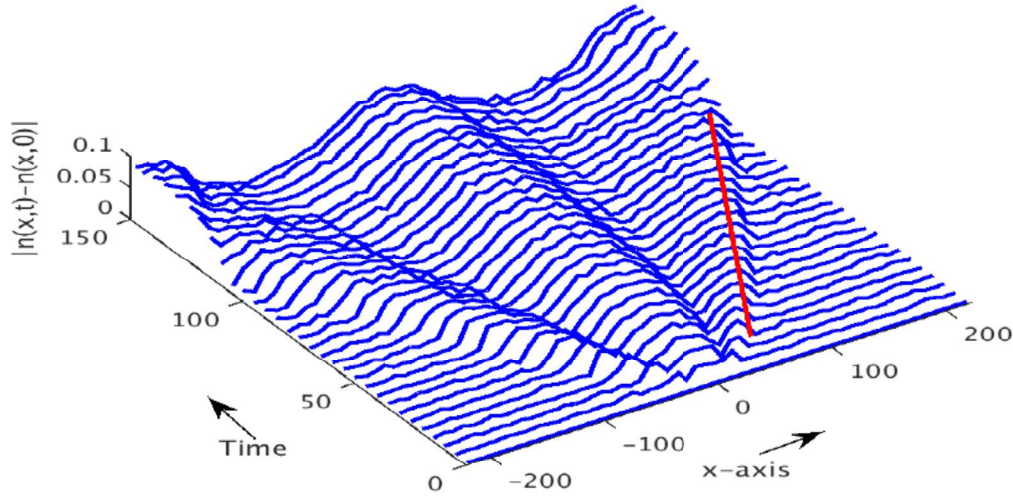


Figure 4.20: Propagation of density wave (or compression wave) for $\Gamma_0 = 70$, $\kappa = 1.0$ and $V_0 = 5$ with configurational thermostat. Similar structure is seen along y -axis. The nonlinear wave speed $C_x = \Delta x / \Delta t = 2.22$, $C_{NLW} = 3.1395$.

of nonlinear wave propagation in the presence and the absence [See Chapter-3] of configurational thermostat does not show much difference.

4.6 Summary

In the present chapter, taking Kolmogorov flow as an initial condition, the role of molecular shear heating in strongly coupled Yukawa liquids has been investigated using configurational thermostat. The results are compared with earlier chapter using micro-canonical ensemble [19]. In both the cases, depending on the initial (Γ, κ) values, it is observed that the laminar to turbulent transition of Kolmogorov shear flow crucially depends upon Reynolds number R and shows existence of a critical value of Reynolds number R_c and is more or less independent of the presence or absence of heat generation. Parametric study of growth-rate of perturbed mode over the range of Reynolds number shows the neutrally stable and unstable nature of Yukawa fluids undergoing Kolmogorov flow for $R < R_c$ and $R > R_c$ case respectively. It is important to note that the critical value of Reynolds number in the presence and absence of heat generation is nearly same. Molecular shear heat is found to decrease the coupling strength exponentially in time and hence destroys the secondary coherent vortices. In this work, using the method of configurational thermostat, it has been demonstrated that the average or global temperature of the system can be maintained at a desirable value in spite of molecular shear heating. This in turn is found to help sustain the secondary coherent vortices dynamics for relatively longer time span. In thermostatted Yukawa liquids, it is found that the vortex structures which were destroyed by molecular shear heating are now sustained. In dusty plasma lab experiments, this is possible by incorporation of neutral dust collisions via increasing the neutral gas pressure [43]. However, dust neutral collision alters the instantaneous particle velocities and destroys the vortex dynamics. Therefore, at this point of time, it is not clear as to how to realize configurational thermostat in real experiment. In the non-linear states obtained with PUT “ON”, spatially non-uniform profiles of temperature is observed in the

Chapter 4. Molecular shear heating and vortex dynamics in thermostatted two dimensional Yukawa liquids

regions of strong velocity shear. However, average temperature of the system is controlled by the configurational thermostat. For example when, PUT is “ON”, it is observed that the peaks of local temperature profile at the shear flow location, are much lesser in magnitude and global average temperature of the system is maintained as compared to the case with PUT “OFF”.

As described earlier, a dusty plasma medium may be treated as a fluid medium or as a collection of interacting particles. To study the behavior of parallel (Kolmogorov flow) and circular shear flow (Rankine, Gaussian, Dipole etc.) using compressible continuum model are presented in the coming chapter.

5

Compressible and incompressible shear flow in strongly coupled liquids: A computational fluid dynamics study

5.1 Introduction

As described in Chapter-3 and Chapter-4, Kolmogorov flow [15, 16] is a two-dimensional flow and becomes unstable as Reynolds number increases beyond a critical value. This is a classic problem of fluid dynamics. As described in the Introduction (Chapter-1), strongly coupled dusty plasma can be often treated like a fluid and modeled by hydrodynamic models [10] within the range of fluid limit for $\Gamma \ll \Gamma_t$, here Γ_t is the liquid to solid phase transition point [5]. For a 2D system, Γ_t is found to be in the range of 130-135 and in general depends on the screening parameter κ . It has been found that several phenomena common to conventional hydrodynamic fluids, such as Kelvin-Helmholtz [11, 59], nonlinear saturation, vortex roll formation have been investigated in the field of strongly coupled dusty

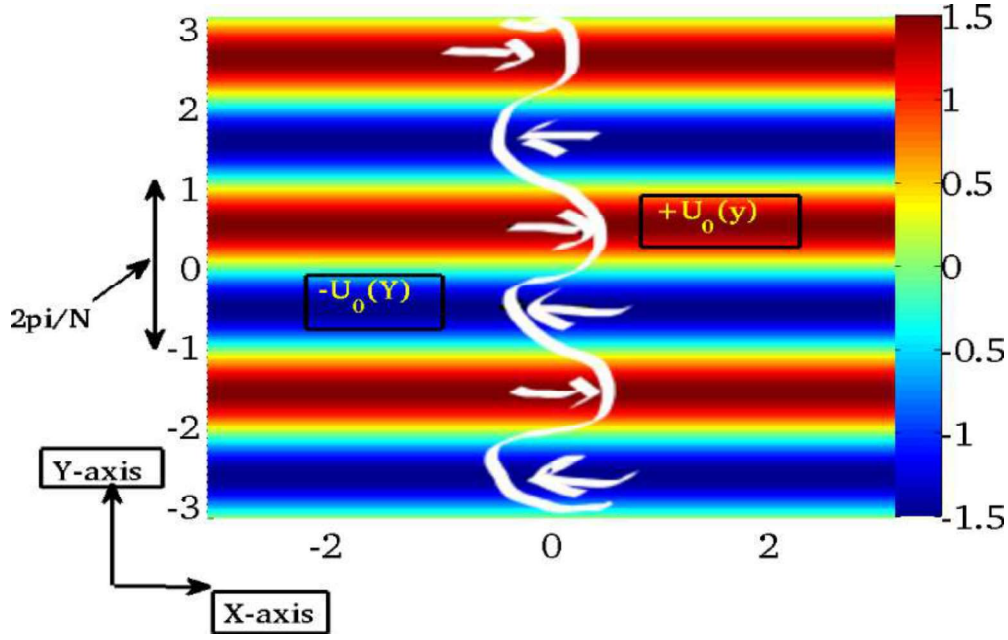


Figure 5.1: Equilibrium vorticity contour plot showing the direction of velocity flow and shearing length

plasma using generalized hydrodynamic model. It is well known that a variety of flows can be initialized in 2D strongly coupled dusty plasma experiments with coupling strengths from weak to very strong coupling [29]. In present Chapter, the transition of stable Kolmogorov flow to the unstable regime is demonstrated for strongly coupled dusty plasma using a generalized hydrodynamic fluid model where in strong coupling effects are incorporated via viscoelastic relaxation time E_t .

Kolmogorov flow [15, 16, 101] is a two-dimensional flow with a sinusoidal periodic equilibrium velocity $\vec{u}_0(y) = U_0 \cos(Ny) \hat{x}$, where N is the equilibrium wave number. Note that the direction of equilibrium flow (x or y) does not matter because of doubly periodic boundary condition.

In fluid dynamics approach, the effect of shear heating as found in Chapter-3 and its effects on vortex dynamics of parallel shear flow are considered. Fig.5.1 shows the periodic array of vorticity of the Kolmogorov flow with equilibrium wave number

Chapter 5. Compressible and incompressible shear flow in strongly coupled liquids: A computational fluid dynamics study

$N=3$. Flow is in two dimensional doubly periodic domain $(x, y) \in [-\pi, \pi] \times [-\pi, \pi]$. As described in the Introduction, in practice, such a grain flow profile may be generated by the appropriate external forcing of the dust fluid. To study the linear and non-linear properties of such flow by means of the macroscopic point of view, a generalized hydrodynamic model has been used. The description of this model is given in the next section.

5.2 Generalized Hydrodynamic model and Governing equations

In general, the governing equations for Newtonian fluid dynamics is Navier-Stokes equations and have been known for over 150 years. As discussed earlier, strongly coupled dusty plasma can be often treated like a fluid and modeled by generalized hydrodynamics model [10]. Recently, a generalized hydrodynamic model for strongly coupled plasma system referred as the viscoelastic-density functional (VEDF) model using density functional method [13] have described. In an other work, another generalized hydrodynamic approach to simplify the calculation of dynamical structure factor of strongly coupled plasmas using fluctuation-dissipation theorem has been described [14]. More detailed, discussion about Ref.[13] and [14] are given in the Appendix-B and C. Yet another model due to J. Frenkel [9] has been adopted to study the low-frequency modes in strongly coupled dusty plasma system [10]. In this model, the effect of strong correlations are introduced by a single viscoelastic coefficient (F_t). Typically F_t depends upon the coupling strength and many other statistical parameters [114]. One can also calculate Maxwell's relaxation time F_t , which is the ratio of shear viscosity and bulk modulus by means of equilibrium molecular dynamics simulation. As discussed earlier, to address the problem of Kolmogorov flow in strongly coupled plasma, a phenomenological viscoelastic generalized hydrodynamic model, [9, 10] which has been used extensively in the past has been considered. In this study, only the dynamics of the dust

Chapter 5. Compressible and incompressible shear flow in strongly coupled liquids: A computational fluid dynamics study

fluid medium is considered and the background plasma medium is considered to respond in a Boltzmann-like fashion. The continuity equation of the dust fluid is as follows.

$$\frac{\partial \rho}{\partial t} + \nabla \cdot (\rho \vec{U}) = 0 \quad (5.1)$$

The momentum conservation equation (force balance equation) for dust fluid is as follows.

$$\left\{ 1 + F_t \frac{d}{dt} \right\} \left[\frac{d\vec{U}}{dt} + \frac{q_h}{M} \vec{\nabla} \phi + \frac{1}{M n_h} \vec{\nabla} p \right] = \frac{\partial \sigma_{ij}}{\partial x_j} \quad (5.2)$$

where $\frac{h}{ht}$ is the total derivative given by $\frac{h}{ht} = \frac{\partial}{\partial t} + \vec{U} \cdot \nabla$ and the stress tensor $\sigma_{ij} = \eta' \left(\frac{\partial U_i}{\partial x_j} + \frac{\partial U_j}{\partial x_i} \right) + \left(\xi' - \frac{2}{3} \eta' \right) \delta_{ij} (\nabla \cdot \vec{U})$, \vec{U} , $\rho_h (= M n_h)$, n_h , q_h , p , ϕ , η , η' , ξ' are the average fluid dust velocity, mass density, dust density, dust charge, pressure, electrostatic potential, dynamic viscosity, shear and bulk viscosities per unit number density respectively. Electrons and ions respond “instantaneously” as compared to dust fluid and are considered as inertialess. Hence, the equations of motion of the electron and the ion fluids become $k_B T_e n_e = n_e e \nabla \phi$ and $k_B T_i n_i = -n_i e \nabla \phi$ which results as Boltzmann distributions of electrons and ions. That is, $n_e = n_{e0} e^{e\phi/k_B T_e}$ and $n_i = n_{i0} e^{-e\phi/k_B T_i}$, where n_s , T_s [where $s = e$ (electron) and $T(\text{ion})$] are the number density and temperature of the particular species respectively. The normalized Poisson's equation is:

$$\nabla^2 \phi = \frac{e}{\epsilon_0} (n_h - n_i + n_e) \quad (5.3)$$

As described in Appendix-A, a 2D bed of strongly coupled dust fluid whose coupling strength is measured via a viscoelastic relaxation time or Maxwell's relaxation time namely, F_t has been considered.

5.3 Incompressible limit

In this Section, to begin with, a simpler form of the fluid model (vorticity form) has been considered. In Section. 5.4 a fully compressible limit is addressed. Note that

Chapter 5. Compressible and incompressible shear flow in strongly coupled liquids: A computational fluid dynamics study

for an incompressible fluid such as present Chapter, specifying equilibrium velocity profile [and hence the vorticity profile] completely defines the initial condition. A fluid is said to be incompressible when the mass density of a co-moving volume element does not change appreciably as the element moves through regions of varying pressure. The conservation of mass density for such a dust fluid element (also called the continuity equation) is given in Eq.A.20. For addressing phenomena where the disturbances travel at speeds much less than the sound speed of the system, density variations are negligible i.e $\frac{h\rho}{ht} = 0$, resulting in $\nabla \cdot \vec{U} = 0$ leading to incompressibility of the dust fluid. To keep things simple, potential variations in Eq.A.33 are considered to be ignorable (These effects have been included in Section.5.4). This allows us to introduce a stream function $\psi(x, y)$. For an incompressible fluid, in general, vorticity-stream function formulation make the calculations easier than velocity formulation because it changes vector velocity equation into scalar stream function equation. Vorticity ω is a curl of velocity defined as

$$\omega = \hat{z} \cdot \nabla \times \vec{U} = \frac{\partial v}{\partial x} - \frac{\partial u}{\partial y} \quad (5.4)$$

where u and v are x and y component of velocity. Velocity component (u, v) can be expressed in terms of $\psi(x, y)$ as $u = \frac{\partial \psi}{\partial y}$, $v = -\frac{\partial \psi}{\partial x}$ which gives $\omega = -\nabla^2 \psi$. Taking the curl of Eq.A.33, the incompressible generalized hydrodynamic equation in terms of the dust fluid vorticity becomes as

$$\left\{ 1 + F_t \frac{\partial}{\partial t} \right\} \left[\frac{d\omega}{dt} \right] + F_t \nabla \times \left[\vec{U} \cdot \nabla \frac{d\vec{U}}{dt} \right] = \nu \nabla^2 \omega \quad (5.5)$$

where $\nabla^2 = \frac{\partial^2}{\partial x^2} + \frac{\partial^2}{\partial y^2}$, $\nu = \frac{\eta}{\rho}$ and $\frac{h}{ht} = \frac{\partial}{\partial t} + \vec{U} \cdot \nabla$ as mentioned earlier. In the following, the above-said model to address the linear stability and nonlinear phase for an initial velocity profile described by the Kolmogorov flow of dust fluid has been used.

5.3.1 Study of linear stability of viscoelastic Kolmogorov flow

Perturbations of small amplitude that grow when superimposed on an equilibrium state of the flow render the base flow unstable. One of the standard mathematical techniques to describe such fundamental problem is eigenvalue analysis. Let us consider the Kolmogorov flow described earlier as the equilibrium flow and the corresponding vorticity $\omega_0(y)$. Let us now perturb the velocity such that the total vorticity $\omega(x, y, t)$ is given by $\omega(x, y, t) = \omega_0(y) + \tilde{\omega}(x, y, t)$ and total velocity $\vec{U}(x, y, t)$ is given by $\vec{U}(x, y, t) = (u_0(y) + \vec{u}(x, y, t))\hat{x} + \vec{v}(x, y, t)\hat{y}$, where $\tilde{\omega}$ is small perturbation such that $\frac{\tilde{\omega}}{\omega_0} \ll 1$.

Let us linearise Eq.A.39 keeping only first order terms for addressing stability. Using the incompressibility condition, one will get a fourth order differential equation of stream function. After linearization and taking normal modes ansatz, $\psi(x, y, t) = \phi(y)e^{i(kx - \xi t)}$, where k and ξ are wave number and frequency respectively. An obtained eigen value equation is

$$\begin{aligned} & \left(\frac{d^2}{dy^2} - k^2 \right)^2 \phi(y) \\ = & \mathcal{R} \left[\{1 + \mathcal{F}_t (u_0 - c)\} \left\{ (u_0 - c) \left(\frac{d^2}{dy^2} - k^2 \right) - \frac{d^2 u_0}{dy^2} \right\} \right. \\ & \left. + \mathcal{F}_t \frac{du_0}{dy} \left\{ (u_0 - c) \frac{d}{dy} - \frac{du_0}{dy} \right\} \right] \phi(y) \end{aligned} \quad (5.6)$$

For $\mathcal{F}_t = 0$, this eigen-value equation reduces to famous Orr-Sommerfeld Equation for Navier stokes fluid. where $R = U_0 l / \nu$, $l = \frac{2\pi}{N}$, eigen value $\xi = kc$, c and k are the phase velocity and wave number of the perturbed wave respectively. Eq.5.6 is quadratic in eigen value ξ and can be written as:

$$\left[B_0 - B_1 \xi - \beta B_2 \xi^2 \right] \phi(y) = 0 \quad (5.7)$$

Chapter 5. Compressible and incompressible shear flow in strongly coupled liquids: A computational fluid dynamics study

where β is a artificial parameter which is introduced here for further discussion to understand the role of viscoelastic parameter F_t . Unless stated others β is always equal to 1. In Eq.5.7, ϕ is the eigen function and the coefficient B_0, B_1, B_2 are as follows:

$$B_0 = (D^2 - k^2)^2 - kRu_0 (T - F_t ku_0) (D^2 - k^2) + \mathcal{R}k \frac{d^2 u_0}{dy^2} + k^2 R F_t u_0 \frac{d^2 u_0}{dy^2} + k^2 R F_t u_0 \frac{du_0}{dy} D - k^2 R F_t \left(\frac{du_0}{dy} \right)^2 \quad (5.8)$$

$$B_1 = (2R F_t ku_0 - \mathcal{R}) (D^2 - k^2) + k R F_t \frac{d^2 u_0}{dy^2} + k R F_t \frac{du_0}{dy} D \quad (5.9)$$

$$B_2 = -R F_t (D^2 - k^2) \quad (5.10)$$

where $D \doteq \frac{h}{hy}$. Note that while terms B_0 and B_1 survive for $F_t = 0$ leading to Navier Stokes fluid, B_2 is found to be the term that changes the nature of the eigen value problem from nonlinear to linear in ξ when $F_t \equiv 0$, thus indicating that the limit $F_t \rightarrow 0$ and $F_t \equiv 0$ are mathematically different problems. More discussion will come in next section.

Using eigen value methods Eq.5.6 has been numerically solved which gives us eigen values and corresponding eigen functions. The positive and negative value of imaginary part of eigen value is the growth rate and damping rate of perturbation respectively. In the following section, numerical results of linear stability analysis have been presented.

5.3.2 Numerical results of linear stability analysis

The fourth order differential equation Eq.5.6 has been solved numerically to obtain eigen values and corresponding eigen functions. The results are the following.

Case.1 Navier Stokes fluid ($F_t = 0$):

As one increases R , for the system size considered here, the flow is known [15] to

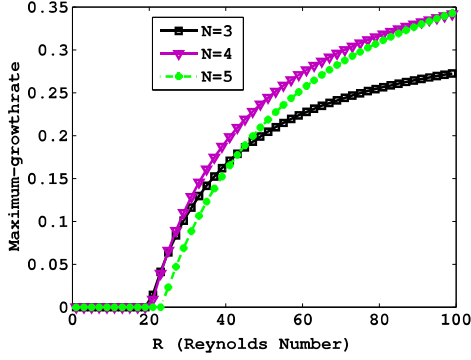


Figure 5.2: Growth rate vs Reynolds number plot with different value of N value for $F_l = 0$, Navier Stokes case. Notice that R_c is nearly independent of N .

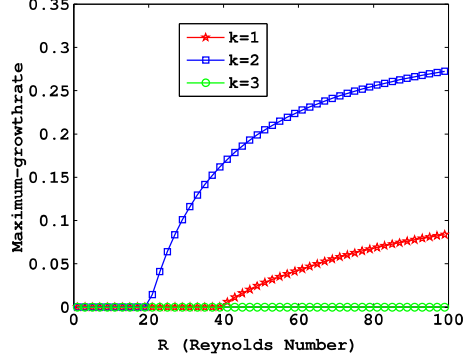


Figure 5.3: Growth rate vs Reynolds number plot with different value of k value for $F_l = 0$, Navier Stokes case

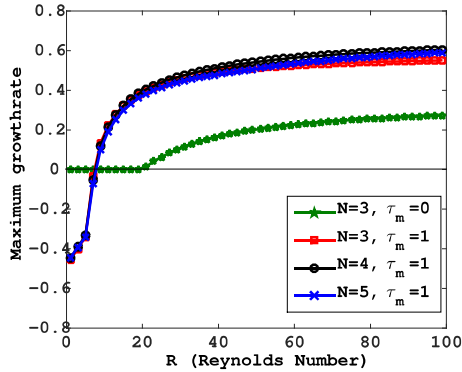


Figure 5.4: Growth rate vs Reynolds number plot with different value of N value for $F_l = 1$

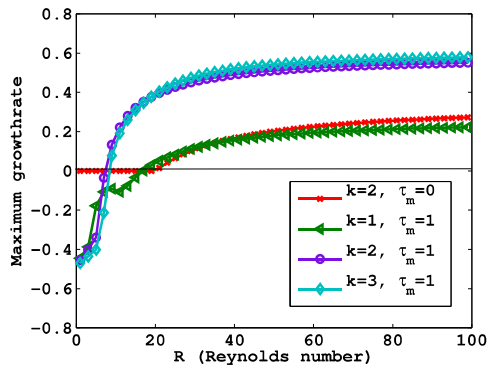


Figure 5.5: Growth rate vs Reynolds number plot with different value of k value $F_l = 1$

be neutrally stable until $R = R_c$ from below, after which the stability changes and the flow becomes unstable . The growth rate obtained from the eigen value solver for $N=3, 4, 5$ and $k=2$ is shown in Fig.5.2. In Fig.5.3, N is held constant at $N = 3$ and the growth rate spectrum is obtained for different k values, namely $k=1, 2, 3$. Instability growth is seen to be a function of Reynolds number R as is clear from Fig.5.2. For Navier Stokes limit ($F_l = 0$), it is well known that the growth rate vs

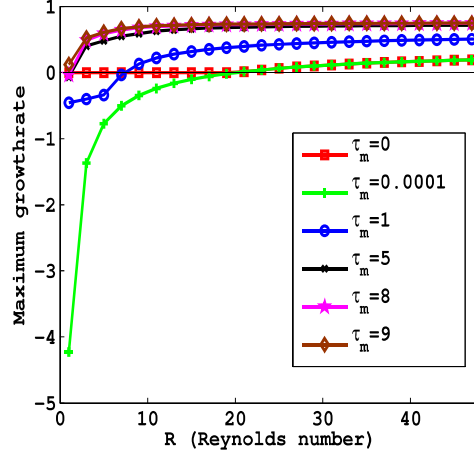


Figure 5.6: Growth rate vs vs Reynolds number (R) for various values of viscoelastic coefficient E_t and perturbed mode number $k = 2$

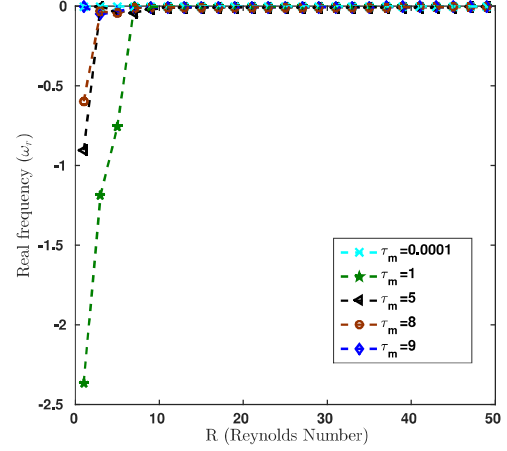


Figure 5.7: Real frequency ω_r vs Reynolds number (R) for various values of viscoelastic coefficient E_t and perturbed mode number $k = 2$. For $E_t = 0$, ω_r is identical zero and not shown here.

R plot shows a super critical Hopf-like bifurcation as shown in Fig.5.2 and Fig.5.8. In the following, it is shown that the nature of this transition depends nontrivially on the value of E_t .

Case.2 Viscoelastic fluid ($E_t \neq 0$):

In Fig.5.4 and 5.5, the growth-rates for $k = 2$ have been plotted, for various N values and $N=3$ for various k values respectively. There are two important observation to be made. (a) The nature of the stability or transition $E_t \rightarrow 0$ is observed to be different from that of the case with $E_t = 0$. (b) The R_c reduces with increasing E_t and thereby increasing the window of the instability.

Importantly, modes previously stable in Navier Stokes fluid, for example $k=1$, $E_t = 0$, for $E_t \neq 0$ are now found to be unstable, thus increasing the window of instability, which appears to be a direct consequence of strong coupling effect

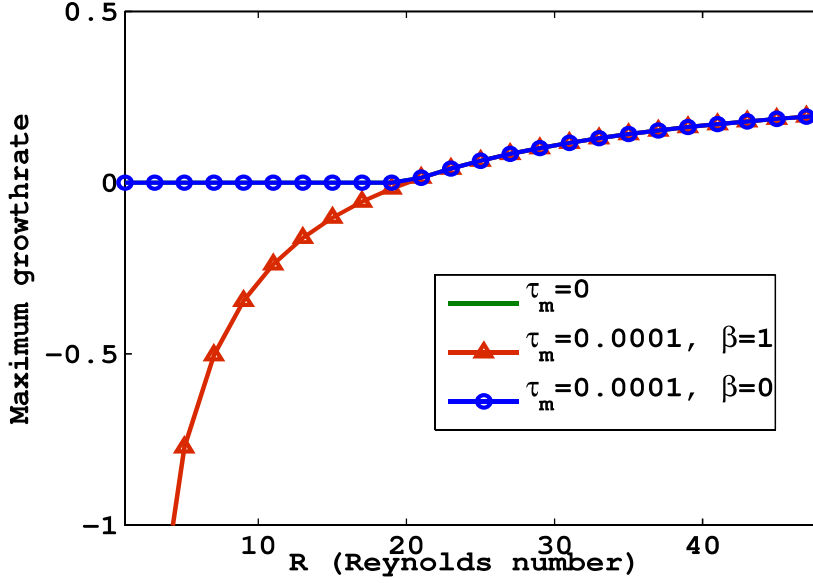


Figure 5.8: Growth rate vs vs Reynolds number (R) for various values of viscoelastic coefficient F_l and perturbed mode number $k = 2$

represented in our model by viscoelastic relaxation time F_l . Fig.5.6 shows that on increasing viscoelasticity (by increasing viscoelastic coefficient F_l) decreases the magnitude of critical Reynolds number. There is a critical value of viscoelastic coefficient beyond which Kolmogorov flow becomes unconditionally unstable (that is independent of Reynolds number R). For example, for $k=2$, $N=3$ the critical value of $F_l \approx 9$ for lower value of N . F_l may be larger [see Fig.5.6]. It implies that the flow will always be unstable for $k = 2$, $N = 3$ and $F_l \geq 9$. In Fig.5.7, the real frequencies of the perturbed mode $k = 2$ has been plotted against Reynolds number show the frequency of oscillations. We shall come back to Fig.5.7 when we discuss the nonlinear results in the next section [for example, see Fig.5.12].

It is observed that unlike Navier Stokes case ($F_l = 0$), for finite F_l , however small, no neutral stability is found in this incompressible viscoelastic model for Kolomogorov flow for $R < R_c$ [see Fig.5.8 (red colour)] . This can be rephased as

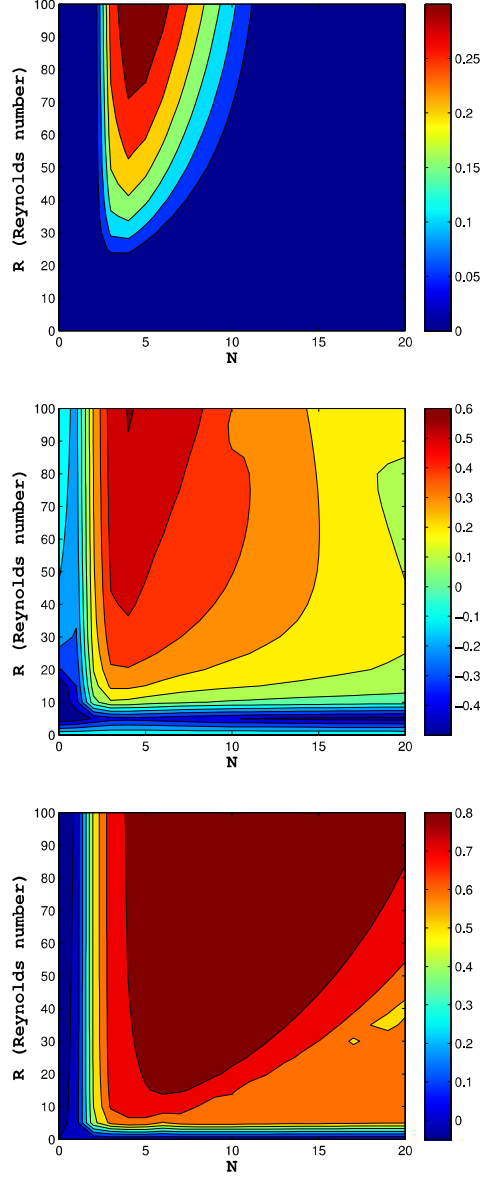


Figure 5.9: Contour plot of growth rate of Kolmogorov flow with variation of N and R for $F_t = 0$ (Upper plot), $F_t = 1$ (middle Plot), $F_t = 10$ (lower Plot)

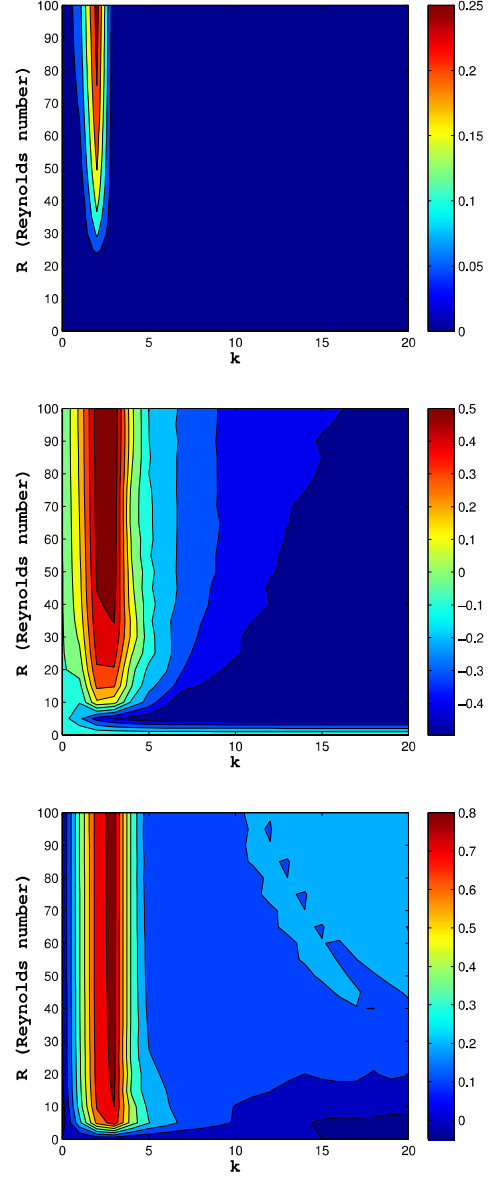


Figure 5.10: Contour plot of growth rate of Kolmogorov flow with variation of k and R for $F_t = 0$ (Upper plot), $F_t = 1$ (middle Plot), $F_t = 10$ (lower Plot)

Chapter 5. Compressible and incompressible shear flow in strongly coupled liquids: A computational fluid dynamics study

follows : the case of $F_t = 0$ (Navier Stokes) and the case of $F_t \rightarrow 0$ (viscoelastic) are not identical as for $R < R_c$ regime is considered with in the incompressible model.

Note that for $R > R_c$, the unstable eigen values asymptote correctly to $F_t \rightarrow 0$ limit and match with $F_t = 0$ results. To understand this mathematically, as discussed in Eq.5.7, an artificial factor β has been multiplied with the coefficient of nonlinear eigen value term (B_2) such that if $\beta = 0$ the nonlinear eigen value term which results out of $F_t \frac{\partial^2}{\partial t^2}$ in Eq.5.7 vanishes [Note that the correct eigen value problem is for $\beta = 1$]. For small F_t , say $F_t = 10^{-4}$, the eigen value for $R > R_c$ correctly asymptotes to the Navier Stokes limit ($F_t = 0$). On the other hand, for $F_t = 10^{-4}$, the behavior of the eigen value for $R < R_c$ is seen to crucially depend on the viscoelasticity driven nonlinear eigenvalue term $B_2\xi^2$ in Eq.5.7. For $F_t = 10^{-4}$ for $\beta = 1$ and 0, the same study has been performed. The results shown in Fig.5.8 indicate viscoelasticity (B_2) alter the stability for $R < R_c$ quite interestingly. Thus, the quadratic eigen value term which is a consequence of viscoelastic effect in our model is seen to bring important changes in the entire R domain. This observation indicates that viscoelasticity effect alter the nature of the laminar to turbulent in a fundamental way. For better understanding of Fig.5.2 and 5.4, in Fig.5.9 for $F_t = 0$ (upper) has been plotted, $F_t = 1$ (middle) and $F_t = 10$ (lower) as function of (N, R) , which shows the range of N for which $k=2$ is unstable. In the same way, to better understand Fig.5.3 and 5.5, in Fig.5.10, maximum growth rate is given as function of (k, R) . It is clear from Fig.5.9 and 5.10 that for Navier Stokes limit or simply the hydrodynamic fluid has less domain of instability as compared to viscoelastic fluids for the values of F_t , R considered here.

In the this Section, we described linear stability analysis of Kolmogorov flow in strongly coupled dusty plasma system. However, when the amplitude of perturbation is quite small, one can take a first order approximation as the modes of perturbation will not interact with each other. As amplitude of perturbation becomes

Chapter 5. Compressible and incompressible shear flow in strongly coupled liquids: A computational fluid dynamics study

larger, one can not ignore the higher order nonlinear terms which are responsible for mode-mode interaction and nonlinear saturation. Therefore nonlinear stability analysis has been performed in the next Section.

5.3.3 Nonlinear study of Kolmogorov flow using incompressible viscoelastic model

Modified hydrodynamic equations are a system of non-linear partial differential equation in which the non-linear terms play an important role in determining the evolution of the flow. To study the nonlinear vortex dynamics and other nonlinear properties of Kolmogorov flow, a nonlinear study of such modified hydrodynamic equations has been performed.

5.3.3.1 Initial value problem

To investigate the linear stability and nonlinear fate of viscous undriven, incompressible Kolmogorov flow for strongly coupled dusty plasma, the vorticity formulation of the generalized hydrodynamic model has been used. Let us take Eq.(3), as vorticity (local angular velocity) completely describes the flow dynamics.

$$\left\{ 1 + F_t \frac{\partial}{\partial t} \right\} \left[\frac{d\omega}{dt} \right] + F_t \nabla \times \left[\vec{U} \cdot \nabla \frac{d\vec{U}}{dt} \right] = \nu \nabla^2 \omega \quad (5.11)$$

Perturbation in equilibrium vorticity have the following form :

$$\omega = \omega_0 + \Delta \cos(kx) \quad (5.12)$$

$$\omega_0 = \nabla \times \vec{U} = U_0 N \sin(Ny) \quad (5.13)$$

where ω_0 , Δ , $k = 2\pi m/L_x$ are initial vorticity profile, magnitude of perturbation (≈ 0.01), wave number in perturbation and m is number of modes, $L_x = 2\pi$ is size of the system along x direction respectively. To obtain the growth rate of a particular mode at a given Reynolds number R and viscoelastic coefficient F_t the

Chapter 5. Compressible and incompressible shear flow in strongly coupled liquids: A computational fluid dynamics study

evolution of perturbed kinetic energy with time along velocity shearing direction has been studied .

$$|\delta E_{KE}^2| = \frac{\int \int (v_y^2(t) - v_y^2(0)) dx dy}{\int \int v_y^2(0) dx dy} \quad (5.14)$$

Consistent with the equilibrium flow here, it is observed that the total circulation $C = \frac{\iint \omega dx dy}{\iint dx dy}$ is zero through out the simulation time [Not Shown here].

5.3.3.2 Numerical modeling and results

Linear Regime: Eq.5.11 is a nonlinear partial differential equation which is second order in time. To find out the non-stationary solutions of this nonlinear differential equation, here pseudo spectral method [115] has been used. Nordsieck Predictor-corrector method has been used for time-stepping. As described in Chapter-2, a pseudo-spectral method is used here, to avoid the aliasing error, there are several methods which one can use such as $\frac{3}{2}$ -rule [116], $\frac{2}{3}$ -rule (zero-padding method) [117]. In our nonlinear pseudo spectral simulation zero-padding method is used in calculation of nonlinear terms in Fourier space. In these simulations, Courant Friedrichs Lewy condition (CFL condition) is well satisfied. For example, for our nonlinear pseudo spectral simulation runs parameters used are number of grids along x and y axis $N_x=N_y=1024$, initial velocity $U_0 = 0.5$, step in time $\Delta t=0.0005$, step in space $\Delta x = \frac{2\pi}{N_x}$, $CFL=\frac{U_0 \Delta t}{\Delta x}$ value is 0.0407, which is quite smaller than 1. MPI based [116] parallelized code is used effectively along with FFTW library [65] for Fourier transform.

Fig.10 shows the linear growth of perturbed kinetic energy for k , $E_t = 10$ and $N=3$ on log-linear scale. The purple line is a linear fit to the linear growth rate. The linear growth rate obtained from the pseudo spectral simulation of Eq.5.11 is close to eigen values obtained earlier as observed in the caption of Fig.5.11. Fig.5.12 reveals the decay of perturbed mode for Reynolds number $R=1$, $E_t = 5$, where the value of R is chosen to be less than critical Reynolds number $R_c \approx 1.5$. Again, the rate of damping observed from the pseudo spectral simulation is close to that

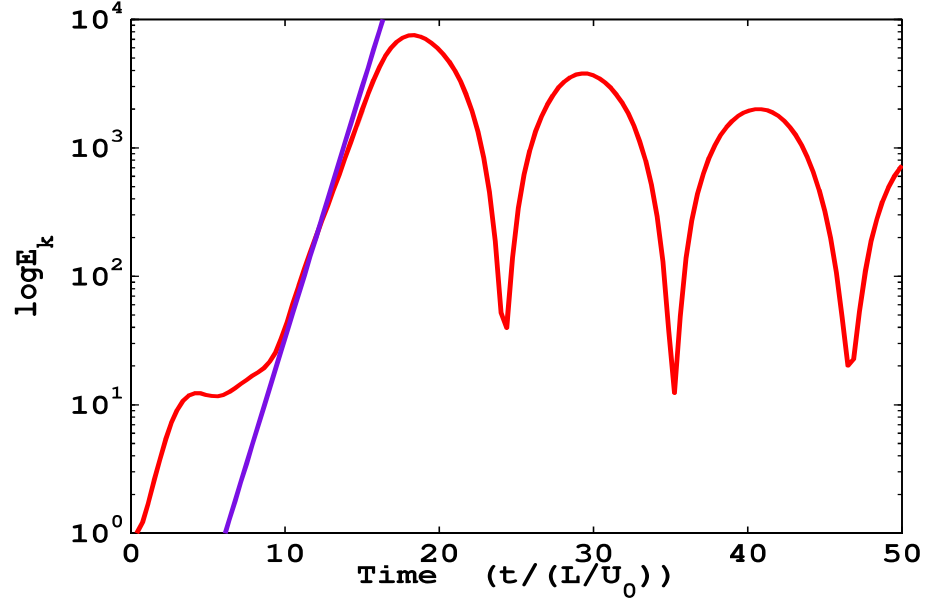


Figure 5.11: Growth rate from simulation is 0.45 and from eigen value solver is 0.48 for Reynolds number $R=2$, Number for perturbation mode $k=2$, Maxwell's relaxation time $F_t = 10$, equilibrium wave number $N=3$ and shear velocity $U_0=0.5$

obtained from eigen value solver. To further benchmark nonlinear pseudo spectral results, we plot the linear growth rate with various values of Reynolds number for $F_t = 10$ and $F_t = 5$ and compare it with eigen value solver. The correctness of the pseudo spectral code is seen from Fig.5.13 as the linear growth rates match well with results from the eigen value solver. Having established the correctness of the pseudo spectral code, in the following, let us now focus on nonlinear regime.

Nonlinear Regime: For times beyond the linear regime ($t > 12$), Fig.5.11 shows the oscillations in perturb kinetic energy, which is an evidence of viscoelasticity nature of the fluid. Fig.5.15 shows the evolution of Kolmogorov flow vorticity with time. It is clear from the Fig.5.15 that as time increases perturbed mode first grows linearly and becomes nonlinear.

Because of viscoelastic nature of fluid, elasticity makes it to come back to near-

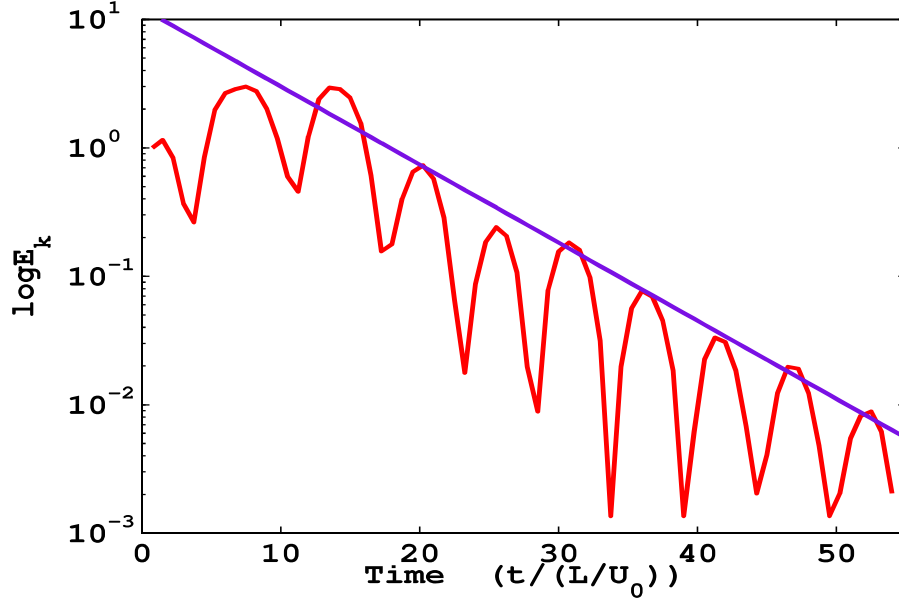


Figure 5.12: Damping rate from simulation is -0.07 and from eigen value solver is -0.0722 for Reynold number $R = 1 < R_c$, Number for perturbation mode $k=2$, Maxwell's relaxation time $E_t = 5$, equilibrium wave number $N=3$ and shear velocity $U_0=0.5$. Note that the real frequency of damping $2\omega_r$ is close to $\frac{2\pi}{\tau_m}$, which corresponds to ω_r^{linear} , See Fig.5.7

equilibrium states and viscosity pushes it away leading to a decaying cyclicity. At time $t=1$ the initial vorticity contour plot showing equilibrium wave number N three (vorticity strip=3) along x direction (horizontal). As the perturbation amplitude starts to grow, the vorticity strip becomes vertical along y direction at $t=3.75$ (more clear at $t=16.5$) and the cycles continue. For example, vorticity strip starts with horizontal state, converts into vertical state followed by a variety of pattern formation as time evolves. These novel features are addressed here for the first time in the context of strongly coupled dusty plasma. These features of the perturb mode show the cyclicity as is clear from the Fig.5.15. These oscillations in perturbed kinetic energy are a consequence of viscoelasticity. To unveil that these oscillations in perturbed kinetic energy are because of nature of the fluid, a contour of perturbed kinetic energy for only viscous fluid where $E_t = 0$ (Navier

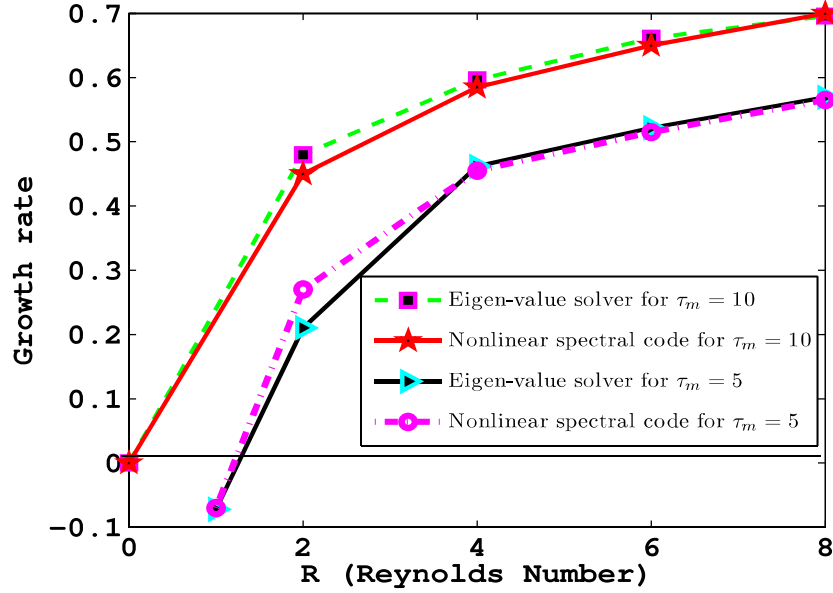


Figure 5.13: Comparison of growth rate between eigen value solver and nonlinear pseudo spectral code for perturbation mode number $k=2$, Maxwell's relaxation time $E_t = 10$ (upper) and $E_t = 5$ (lower), equilibrium wave number $N=3$ and shear velocity $U_0=0.5$. For above given parameters, real frequency in this case is very small $\sim 10^{-4}$ [Not shown here, see fig.5.7]

Stokes fluid) has been demonstrated in Fig.5.15. It is clear from that, once the shear flow become unstable and achieve vertical strips of vorticity from horizontal equilibrium flow, vorticity strip does not come back because of non-existence of solid like elastic property in the Navier-Stokes fluid i.e ($E_t = 0$).

5.4 Compressible Limit

Compressibility is a natural fluid (liquid and gas) property. A fluid is said to be incompressible fluid, when the variation in density is so small, as to be negligible. In other words, the speed of sound is expected to be large enough that no density variation, in space and time, is sustainable. Hence, compared to flow

Chapter 5. Compressible and incompressible shear flow in strongly coupled liquids: A computational fluid dynamics study

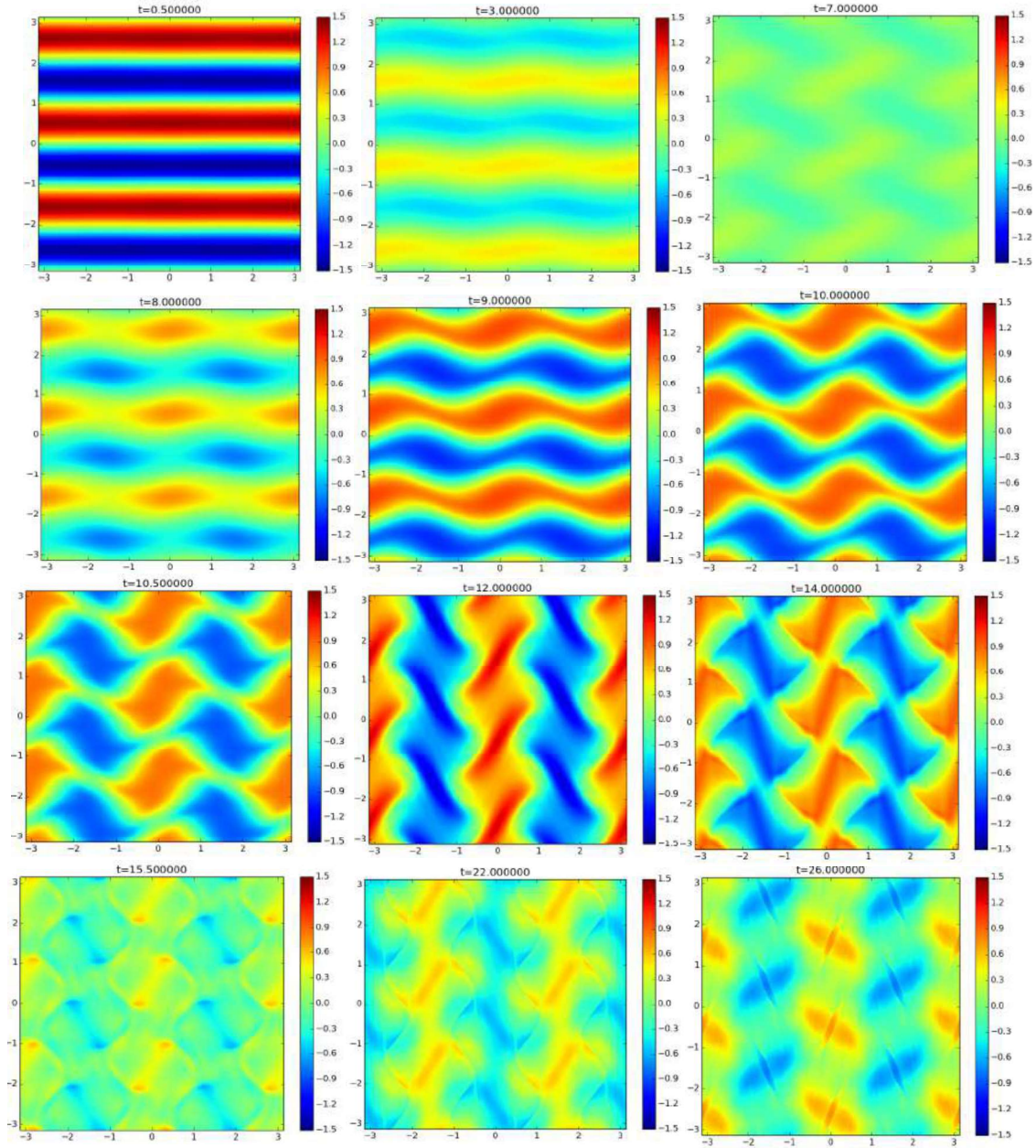


Figure 5.14: Vorticity contour show a variety of pattern formation at different time with Kolmogorov initial condition for Reynold number $R=2$, Number for perturbation mode number $k=2$, Maxwell's relaxation time $E_t = 10$, equilibrium wave number $N=3$ and shear velocity $U_0=0.5$

Chapter 5. Compressible and incompressible shear flow in strongly coupled liquids: A computational fluid dynamics study

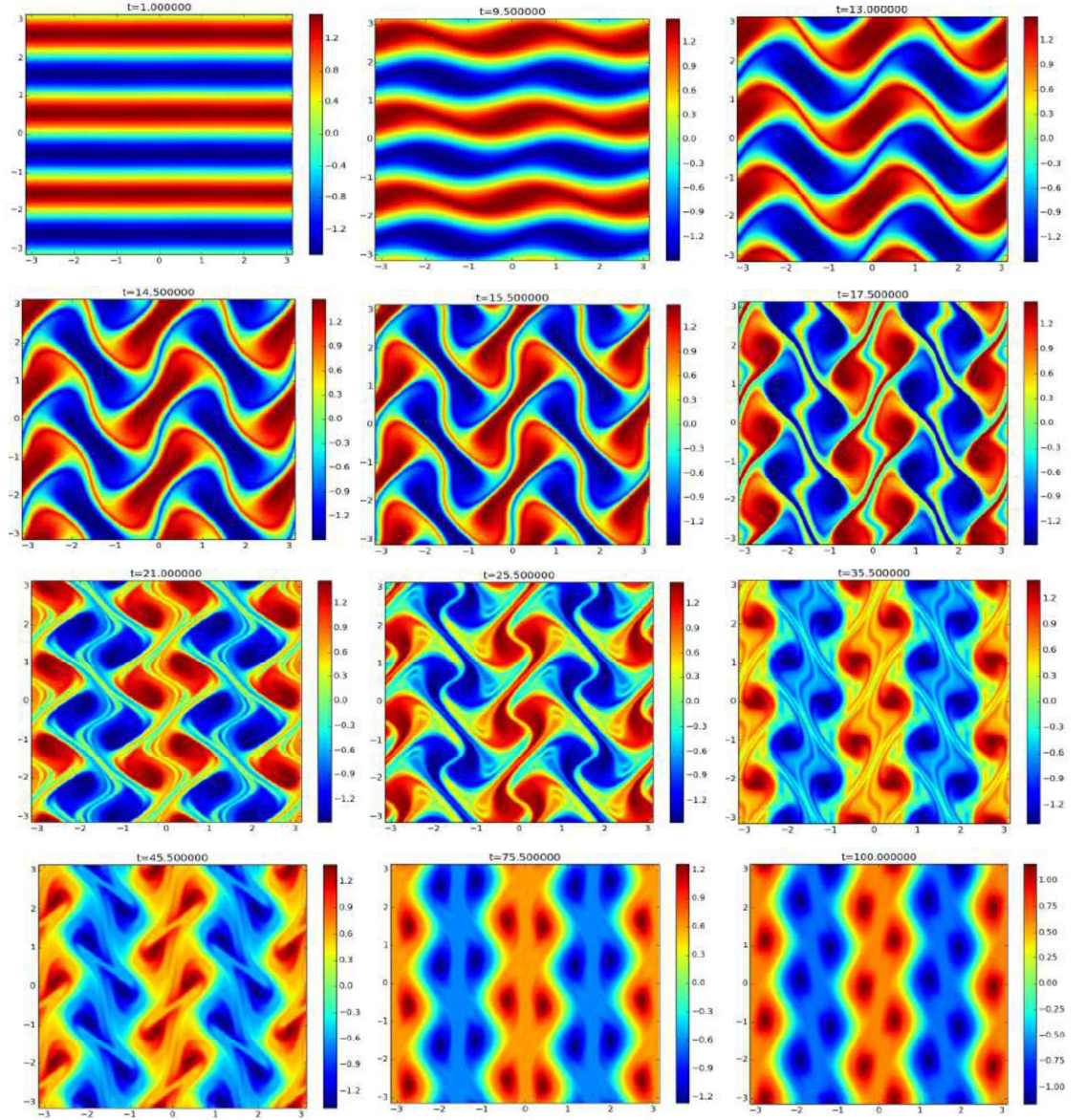


Figure 5.15: Vorticity contour show a variety of pattern formation at different time with Kolmogorov initial condition for Reynold number $R=5000$, Number for perturbation mode number $k=2$, Maxwell's relaxation time $\bar{E} = 0$ (Navier-Stokes fluid), equilibrium wave number $N=3$ and shear velocity $U_0=0.5$. The choice of such high Reynold number is just to show the laminar to turbulent transition, note that for $R=2$, Navier Stokes fluid is stable for our case, see Fig.5.3.

Chapter 5. Compressible and incompressible shear flow in strongly coupled liquids: A computational fluid dynamics study

speeds U_0 of interest, the sound speed C_s can be thought to be infinitely large or $M = U_0/C_s \ll 1$. On the other hand, a fluid is said to be compressible, when Mach number $M = U_0/C_s \rightarrow 1$ or > 1 . The compressibility effect on shear flow is an important problem in the field of hydrodynamic flows and is addressed by many authors in the past using both atomistic [56, 57] (MD) and continuum (fluid) approaches. In general, an instability in incompressible limit is relatively stabilized by compressibility effects. It was found that compressibility stabilizes the instability and changes the nature of stability from “exchange of instability” to “over-stability” [58]. Similarly strongly coupled plasma, Kelvin-Helmholtz instability in the presence of significant compressibility with quasi-neutrality and mixed boundary (periodic along flow and bounded along the direction perpendicular to the flow) conditions [11] has also been shown to be relatively stable.

5.4.1 Generalized Hydrodynamic model and Governing equation

To address the problem of Kolmogorov flow in strongly coupled plasma, we consider a phenomenological viscoelastic generalized hydrodynamic model,[9, 10] which has been used extensively in the past. We consider only the dynamics of dust fluid medium and the background plasma medium is considered to respond in Boltzmann-like fashion. Normalized continuity equation of dust fluid is as follows:

$$\frac{\partial \rho}{\partial t} + \nabla \cdot (\rho \vec{U}) = 0 \quad (5.15)$$

Momentum conservation equation (force balance equation) for dust fluid is as follows [11]

$$\left\{ 1 + E_t \frac{d}{dt} \right\} \left[\frac{d\vec{U}}{dt} - \vec{\nabla} \phi + C_s^2 \frac{\vec{\nabla} n_h}{n_h} \right] = \nu \nabla^2 \vec{U} \quad (5.16)$$

Chapter 5. Compressible and incompressible shear flow in strongly coupled liquids: A computational fluid dynamics study

Normalized Poisson's equation:

$$\nabla^2 \phi = n_h - n_i + n_e \quad (5.17)$$

A detailed description about the compressible model and its formalism are given in the Appendix-A. In generalized fluid model Eq.(5.15-5.17) all equations are dimensionless and the normalization quantities are given in Table.5.3. Here Debye

S.No	Quantity	Normalized quantity
1.	Distance (r)	$r/\lambda_{Dt \text{ } ix}$
2.	Time (t)	$t\omega_{ph}$
3.	Potential (Φ)	$\phi e/K_B T_i$
4.	Density ($n_{\alpha 0}$, $\alpha = e, T, d$)	$n_{\alpha 0}/Z_h n_{h0}$

Table 5.1: Table for normalized quantities, here length $\lambda_{Dt \text{ } ix}^2 = \frac{\epsilon_0 k_B T_i}{Z_d e^2 n_{d0}} \simeq \frac{\epsilon_0 k_B T_i}{e^2 n_{i0}} \simeq \lambda_{Di}^2 \simeq \lambda_D^2$, dust plasma frequency $\omega_{ph}^2 = (Q_h^2 n_{h0}/\epsilon_0 M_h)$, $Q_h = Z_h e$ and M_h are charge and mass of single dust particle.

length $\lambda_D^2 = (\epsilon_0 K_B T_i / n_{h0} Q_h^2)$, dust plasma frequency $\omega_{ph}^2 = (Q_h^2 n_{h0} / \epsilon_0 M_h)$, $Q_h = Z_h e$ and M_h are charge and mass of single dust particle. Note that, For $\kappa = 1$, our normalization for fluid equations is same as molecular dynamics simulation. Therefore, we can chose F_t and η from molecular dynamics simulation. For our study of shear flow, we consider F_t ($\Gamma(t = 0) = \Gamma_0, \kappa) = 5$ and $\eta(\Gamma(t = 0) = \Gamma_0, \kappa) = 0.3$ corresponding to $\Gamma_0 = 110$ and $\kappa = 1$ [22]. To study the stable and unstable shear flow properties and behavior of Kolmogorov flow, we carried out the linear and nonlinear studies of shear flow.

5.4.2 Linear stability analysis

To perform the linear stability analysis of Kolmogorov flow, equations of generalized fluid model Eq.(5.15-5.17) are linearised. Let us consider the Kolmogorov flow as described earlier, as an equilibrium flow and the corresponding velocity $U_0(x)$. Let us now perturb the velocity such that total velocity $\vec{U}(x, y, t)$ is given by $\vec{U}(x, y, t) = \vec{u}(x, y, t)\hat{x} + (U_0(x) + \vec{v}(x, y, t))\hat{y}$. After linearization and taking

Chapter 5. Compressible and incompressible shear flow in strongly coupled liquids: A computational fluid dynamics study

normal modes ansatz, $\psi_{(x,y,t)} = \phi_{(x)} e^{i(k_y y - \xi t)}$, where k_y and ξ are wave number and frequency respectively, we obtain an eigen value equations as :

$$\mathcal{T}n_0 k_y u_1 + n_0 D v_1 + \mathcal{T}U_0(x) k_y n_1 = \mathcal{T}\xi n_1 \quad (5.18)$$

$$\{1 - \mathcal{T}\mathcal{E}_t (\xi - k_y U_0)\} \left[-\mathcal{T}(\xi - k_y U_0) u_1 + C_s^2 D n - D \phi \right] = \nu (D^2 - k_y^2) u_1 \quad (5.19)$$

$$\{1 - \mathcal{T}\mathcal{E}_t (\xi - k_y U_0)\} \left[-\mathcal{T}(\xi - k_y U_0) v_1 + \mathcal{T}k_y C_s^2 n_1 - \mathcal{T}k_y \phi_1 \right] = \nu (D^2 - k_y^2) v_1 \quad (5.20)$$

$$(D^2 - k_y^2) \phi_1 = n_1 + \phi_1 \quad (5.21)$$

where $D = \frac{\hbar}{h\omega}$. To calculate the growth rate of perturbation mode, the above set of equations (Eq.5.18 – Eq.5.21) have been solved numerically using central difference formula with periodic boundary conditions. In Fig.5.16 growth rates vs Reynolds number ($1/\nu$) have been plotted for different perturbation modes. It is clear from the figure that for lower mode numbers $k_y = 2\pi m/L_y = 1, 2$, growth rates of perturbation are finite while higher modes $k_y = 4$, are stable.

We have also performed the parametric study of growth rate of perturbation with Reynolds number for various equilibrium mode number in Fig.5.17. For our system parameters, we find that the equilibrium flow is neutrally stable for $k_x = 1, 2$ and becomes unstable for higher values. In Fig.5.18, growth rate of perturbation has been plotted with Reynolds number for various values of Mach number ($M = U_0/C_s$) which decides the compressibility of the fluid. In earlier studies, it was found that for viscous flow compressibility effect suppress the mode of perturbation and reduce the growth rate. Qualitative a similar trend is found for viscoelastic fluid. Growth rate decreases with increasing value of Mach number.

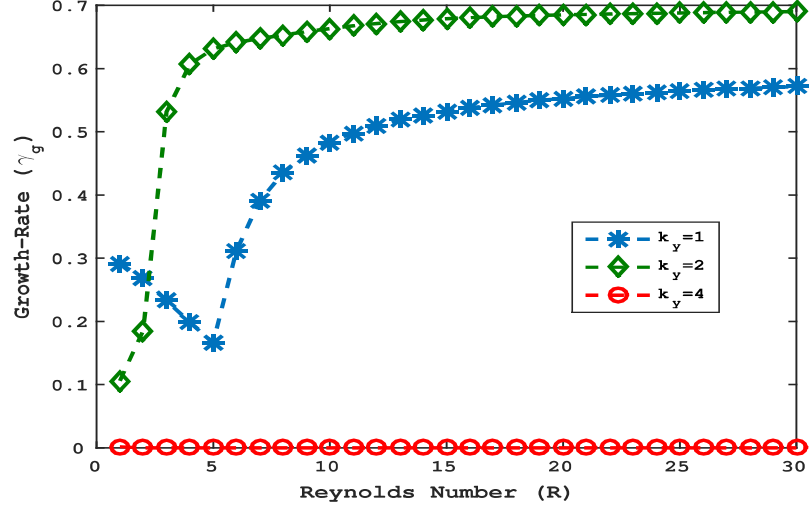


Figure 5.16: Growth rates (γ_g) vs Reynolds number (R) plot for various perturbation wave number k_y for equilibrium wave number $k_x = 3$, equilibrium velocity $U_0 = 1$, relaxation time $F_l = 5$ and Mach number $= U_0/C_s = 0.5$

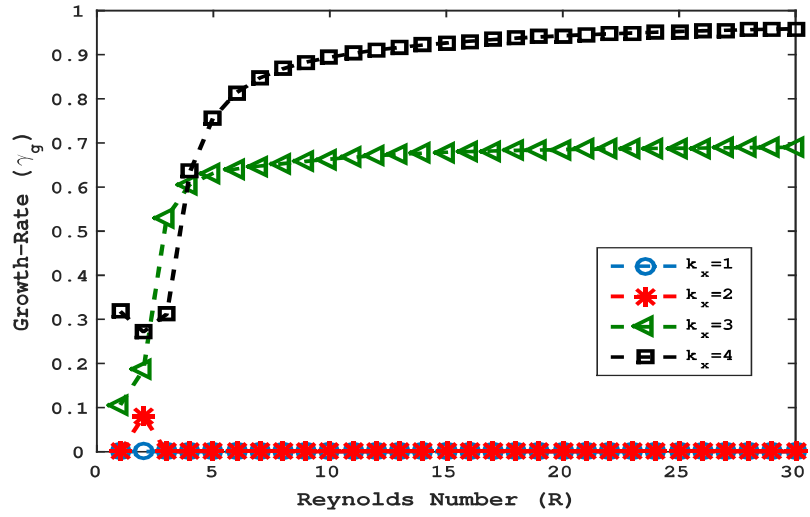


Figure 5.17: Growth rates (γ_g) vs Reynolds number (R) plot for various equilibrium wave number k_x for perturbation wave number $k_y = 2$, equilibrium velocity $U_0 = 1$, relaxation time $F_l = 5$ and Mach number $= U_0/C_s = 0.5$

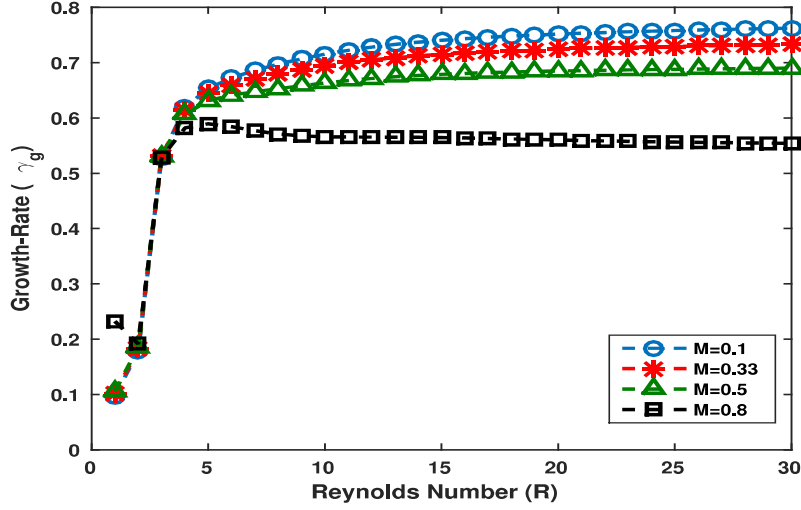


Figure 5.18: Growth rates (γ_g) vs Reynolds number (R) for various Mach number for equilibrium wave number $k_x = 3$ for perturbation wave number $k_y = 2$, equilibrium velocity $U_0 = 1$, relaxation time $F_t = 5$.

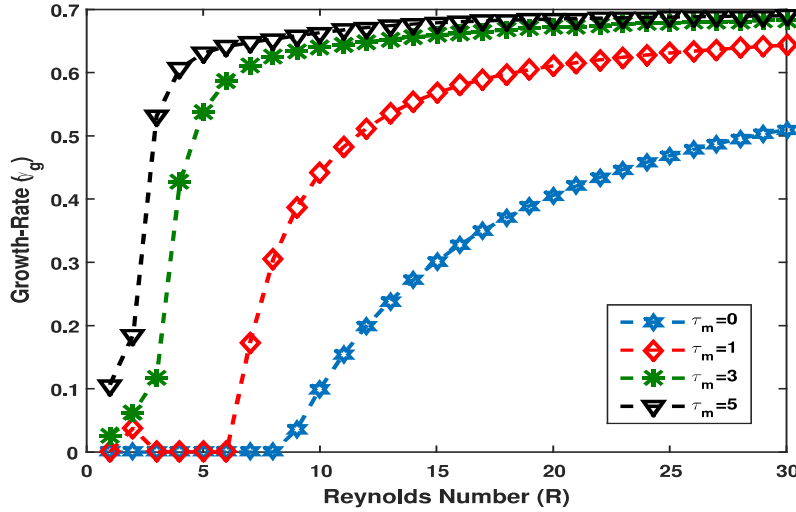


Figure 5.19: Growth rates (γ_g) vs Reynolds number (R) for various relaxation time F_t for equilibrium wave number $k_x = 3$, equilibrium velocity $U_0 = 1$, perturbation wave number $k_y = 2$ and Mach number $= U_0/C_s = 0.5$

Chapter 5. Compressible and incompressible shear flow in strongly coupled liquids: A computational fluid dynamics study

In Fig.5.19, growth rates are plotted against Reynolds number for various values of relaxation time (F_t). It is found that the growth rate increases with increasing value of F_t . For lower value of F_t , there is a critical value of Reynolds number R_c exists below which the perturbed modes are neutrally stable and above R_c modes become unstable. In this plot one can clearly see the laminar to unstable flow transition is sensitive to the value of R_c .

5.4.3 Nonlinear Simulation

In linear stability analysis, we consider only first order approximation and discard the nonlinear terms, which describe the interaction of perturbation. To study the fate of perturbations at longer times, when amplitude of perturbation becomes large, we consider the higher order terms present in linear stability analysis as mode-mode interaction starts to play an important role in convective terms. The set of non-dimensional nonlinear hydrodynamics equations are as follows:

$$\frac{\partial n_h}{\partial t} + \nabla \cdot (n_h \vec{U}) = 0 \quad (5.22)$$

$$\nabla^2 \phi = n_h - n_i + n_e \quad (5.23)$$

$$\left\{ 1 + F_t \frac{d}{dt} \right\} \left[\frac{d\vec{U}}{dt} - \vec{\nabla} \phi + \frac{C_s^2 \vec{\nabla} n_h}{n_h} \right] = \nu \nabla^2 \vec{U} \quad (5.24)$$

where d/dt is a material derivative $d/dt = \partial/\partial t + \vec{U} \cdot \nabla$. It is important to note that, in our non-linear simulation linearized Poisson's equation has been considered. We follow here the velocity-vorticity formulation of generalized hydrodynamic equation and to estimate vorticity from this formulation, curl of velocity is used ($\omega = \hat{z} \cdot \vec{\nabla} \times \vec{U} = \partial v/\partial x - \partial u/\partial y$). This way of initialization comes handy to get velocity information from vorticity inputs. However, this procedure is strictly true only for incompressible systems. These above nonlinear partial differential equations (Eq.5.22-Eq.5.24) are solved numerically. In CFD, the spectral method is often considered in combination with Fourier expansions to

Chapter 5. Compressible and incompressible shear flow in strongly coupled liquids: A computational fluid dynamics study

study the periodic flows. Spectral methods are computationally less expensive and easier in implementation than finite element methods, to simulate turbulence related problem [118]. To find out the time dependent nonlinear solutions of PDEs, we have chosen pseudo spectral method. Spatial derivatives are computed using Fourier transform in Fourier space $\mathbf{k} = (k_x, k_y)$. On the contrary, temporal derivatives are solved in real space \mathbf{R} . As pseudo spectral method is used here, to avoid the aliasing error, there are several methods which one can use such as $\frac{3}{2}$ -rule[116], $\frac{2\sqrt{2}}{3}$ -rule [64], $\frac{2}{3}$ -rule (zero-padding method)[117]. In our nonlinear pseudo spectral simulation zero-padding method is used in calculation of nonlinear terms in Fourier space. Spatial and temporal discretisation are in such way that they must satisfy the Courant-Friedrichs-Lewy (CFL) condition. It is important to note that, in this time dependent numerical study, we have considered linearised Poisson's equation for simplification of numerical procedure. Nordsieck Predictor-corrector method has been used for time-stepping. Initial profile of velocities are $u(x, y, t) = \delta \cos(k_y y)$, $v(x, y, t) = U_0 \cos(k_x x)(1 + \delta \cos(k_y y))$, where u and v are x and y component of velocity respectively. Initial density profile is $n_h(x, y, t) = n_0 + \delta \cos(k_y y)$, where $n_0 = 1.0$, $\delta = 0.005$ and $k_y = 2$.

As a part of this Thesis, a two-dimensional Advanced Generalized Spectral Code (AG-Spect) has been developed to study the linear and nonlinear features of Kolmogorov flow in incompressible and compressible limit. To check the correctness of the code in the linear regime we first estimated the growth rate of perturbed wave number $k_y = 2$ with different dynamic viscosity coefficient ν for the parameters $U_0 = 1$, $F_t = 5$, Mach number $M = 0.5$, equilibrium wave number $k_x = 3$. Obtained growth rates have been plotted against Reynolds number $R = U_0 l / \nu$, where l is shearing length of the system. In Fig.5.20, perturbed kinetic energy is plotted against time in linear-log scale. As can be expected, in the early phase, the perturbed mode grows linearly in time and eventually attains nonlinear saturation as mode-mode coupling sets in. In non-linear regime, nonlinear modes start to saturate for a small time and then show the oscillation because of visco-elastic nature

Chapter 5. Compressible and incompressible shear flow in strongly coupled liquids: A computational fluid dynamics study

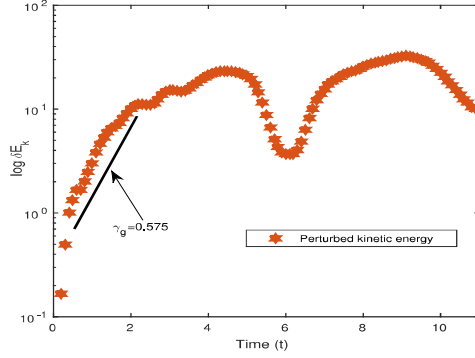


Figure 5.20: Perturbed kinetic energy vs time plot for perturbation wave number $k_y = 2$, equilibrium wave number $k_x = 3$, equilibrium velocity $U_0 = 1$, relaxation time $F_t = 5$, $\eta = 0.33$ and Mach number $M = 0.5$.

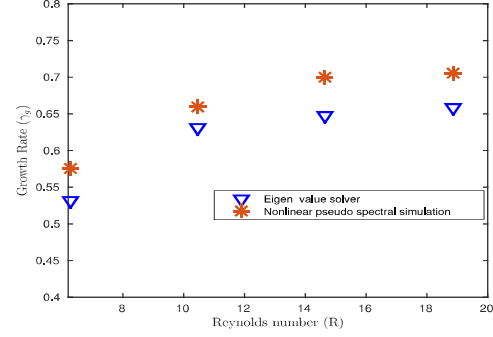


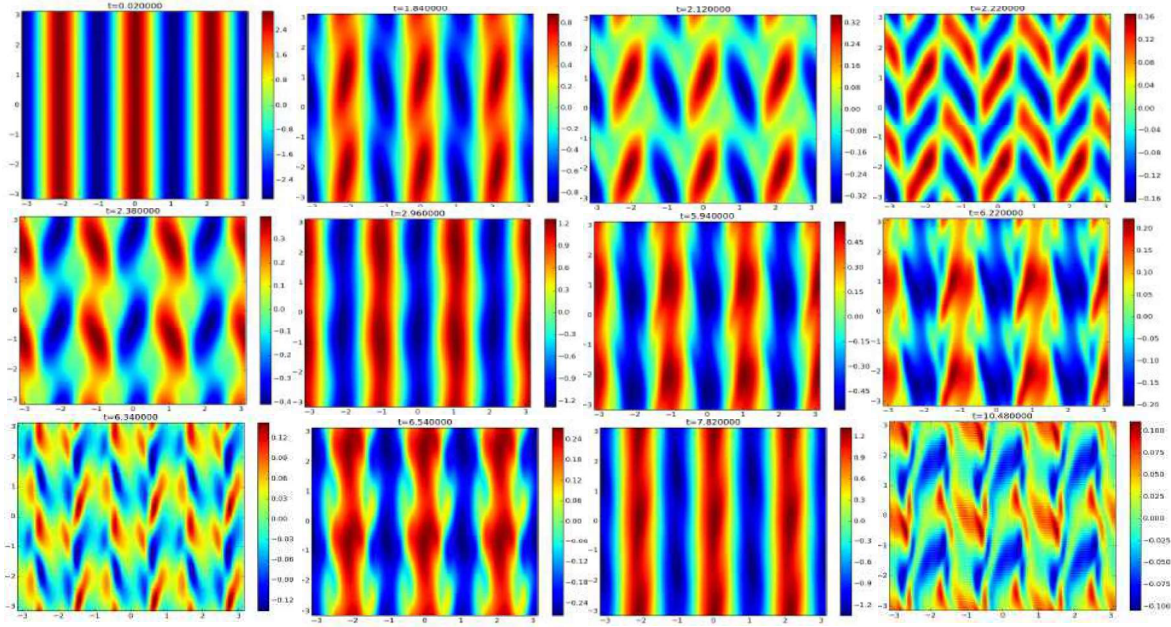
Figure 5.21: Growth-rate (γ_g) vs Reynolds number (R) plot for Mach number $M=0.5$, perturbation wave number $k_y = 2$, equilibrium wave number $k_x = 3$, equilibrium velocity $U_0 = 1$ and relaxation time $F_t = 5$.

of fluid. Linear growth rate of the perturbed mode is obtained using Eq.5.25.

$$\left| \frac{\delta E_{kx}(t)}{E_{kx}(0)} \right| = \frac{\int \int [u^2(t) - u^2(0)] dx dy}{\int \int u^2(0) dx dy} \quad (5.25)$$

In Fig.5.22, we show the time evolution of Kolmogorov flow for $U_0 = 1, \eta = 0.33$, $k_x = 3$, $F_t = 5$ and $k_y = 2$ and Mach number $M=0.5$. It is interesting to note that while in our fluid model, time is normalized to dust plasma frequency ω_{ph} defined in Table.5.3, where as in our earlier studies using Molecular dynamics (Chapter-3 and Chapter-4), time was normalized to ω_0 which is related to ω_{ph} as $\omega_0 = \omega_{ph}/\sqrt{(2)}$. We shall come back to this again later. Fig.5.23 shows the contour plot of divergence of velocity ($\nabla \cdot U = \partial u/\partial x + \partial v/\partial y$). The divergence of the velocity is positive shows flow expansion (red colored contour). In contrast, the negative sign shows the compression of fluid in opposite direction of expansion (blue colored contour). In Fig.5.21 we plot growth rates obtained from our nonlinear pseudo spectral code and linear eigen value solver together. We find that the linear growth rates obtained from AG-Spect are in good agreement with the eigen value solver.

Chapter 5. Compressible and incompressible shear flow in strongly coupled liquids: A computational fluid dynamics study



5.4.4 Rotational Shear flow: Nonlinear coherent structures in strongly coupled dusty plasma in the compressible limit using generalized fluid model

Using AG-Spect, we first perform benchmark studies for $M < 0.3$, i.e, in the weakly compressible limit following which we perform a series of studies for $M > 0.3$. In this code, the velocity formulation of momentum equation has been used. Therefore, for time evolution of momentum equation, velocities (u and v) are required as an input velocity profile. Vorticity-stream function formulation makes the calculations easier than vorticity-velocity formulation because it changes vector velocity equation into scalar stream function equation [119]. Vorticity ω is a curl of velocity defined as

$$\omega = \hat{z} \cdot \nabla \times \vec{U} = \frac{\partial v}{\partial x} - \frac{\partial u}{\partial y} \quad (5.26)$$

where u and v are x and y component of velocity. Velocity component (u, v) can be expressed in terms of $\psi(x, y)$ as $u = \frac{\partial \psi}{\partial y}, v = -\frac{\partial \psi}{\partial x}$ which gives $\omega = -\nabla^2 \psi$. For our purpose, as an input profile we provide vorticity to start the time evolution part of momentum equation, we first calculate the stream function and then velocities accordingly and the velocities become the input velocity of the momentum equation. Strictly speaking, this procedure is valid for an incompressible fluid.

In fluid dynamics, nonlinear states are typically found to be dominated by turbulence and embedded coherent structures. Depending on the dimensionality of the problem and the physics model, the existence and interaction of these coherent structures with themselves as well as with the background turbulence is considered as an important issue. Such problems are abound in conventional Navier-Stokes turbulence as well as in Super-fluids, Astroplasmas, Tokamaks, to mention a few.

In the following, we investigate, the viscoelastic (or memory dependent), compressible, nonlinear evolution of a typical class of coherent structures, which have been

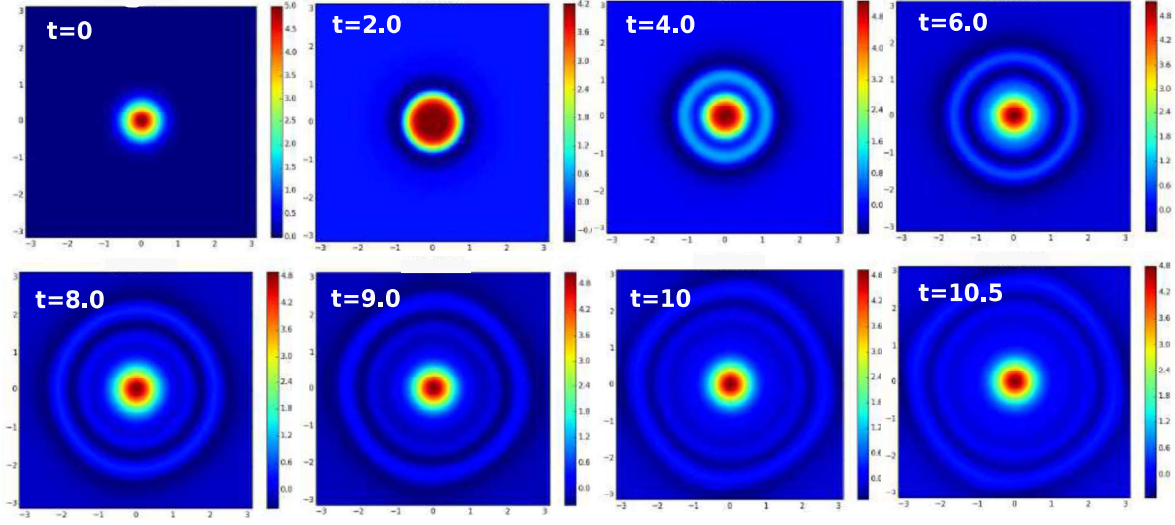


Figure 5.24: Vortex evolution plots of Gaussian profile for $\omega_0 = 5.0$, $F_t = 5$, $\eta = 0.3$ and Mach number $M = 0.5$ (compressible limit).

frequently studied and often observed in as embedded in a sea of Navier-Stokes turbulence. Some of these are a Gaussian Vortex, a Pair of Co-rotating Gaussian vortices, a Pair of Counter-rotating Gaussian vortices and an large Elliptic vortex. They have been evolved in time until the dynamics reaches the periodic boundaries.

Gaussian vortex: Initial input profile of vortex $\omega = \omega_0 e^{-(x^2+y^2)}$, where $\omega_0 = 5.0$. In Fig.5.24, time evolution of Gaussian profile are shown, where we can see the emergence and propagation of transverse shear wave towards periodic boundaries.

Co-rotating vortex: Co-rotating vortex interaction is a very fundamental phenomena in complex fluids. In vortex dynamics simulation, various kinds of processes occur in vortex interaction for example, merger, periodic motion, separation without elongation, and separation with elongation. In earlier studies, it is found that these kinds of interaction depend upon the sign and the strength of the background shear relative to the vorticity of the vortices. It has also been noticed that in absence of shear the vortex merger phenomena crucially depends upon the aspect ratio which is the ratio of core size of vortex and separation distance be-

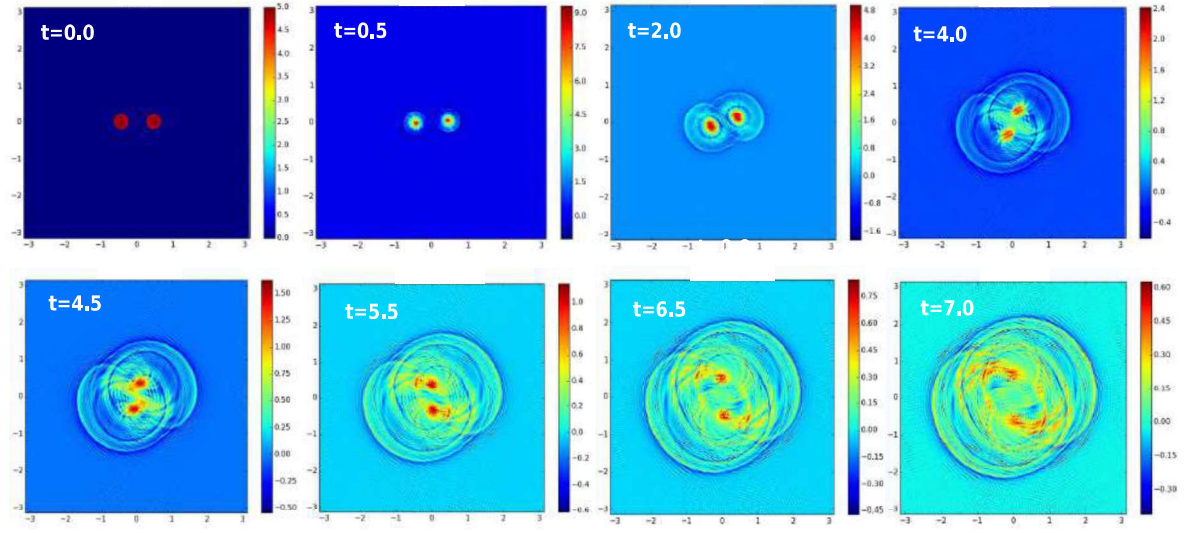


Figure 5.25: Vortex evolution plots of co-rotating vortex of equal magnitude separated by a distance such that total circulation $C = \frac{\iint \omega dx dy}{\iint dx dy}$ is non-zero through out the simulation for $\omega_0 = 5.0$, $E_t = 5$, $\eta = 0.3$ and Mach number $M = 0.5$ (compressible limit).

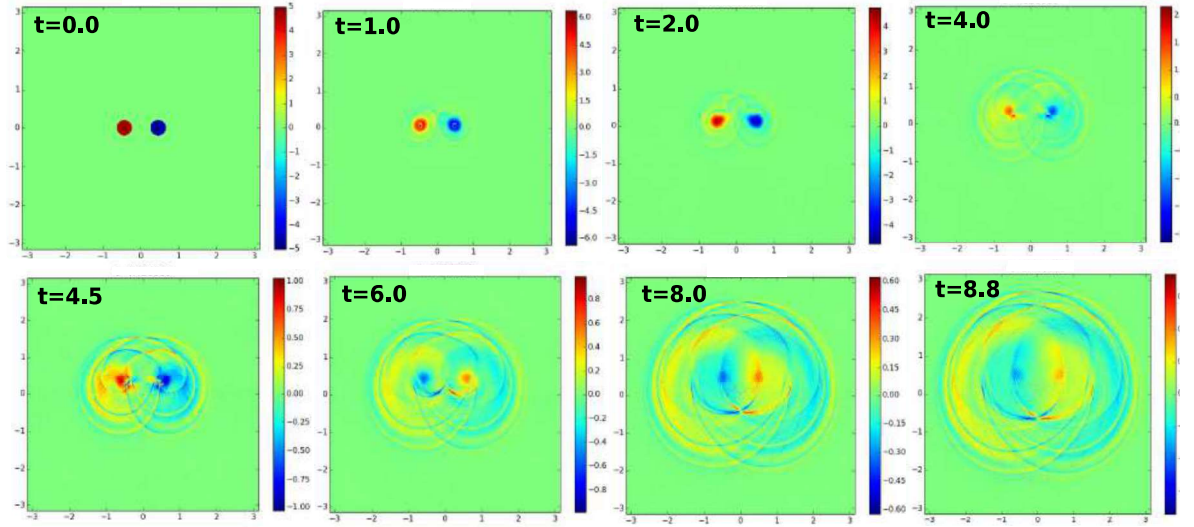


Figure 5.26: Vortex evolution plots of co-rotating unlike profile for $\omega_0 = 5.0$, $E_t = 5$, $\eta = 0.3$ and Mach number $M = 0.5$ (compressible limit). Total circulation $C = \frac{\iint \omega dx dy}{\iint dx dy}$ is zero through out the simulation

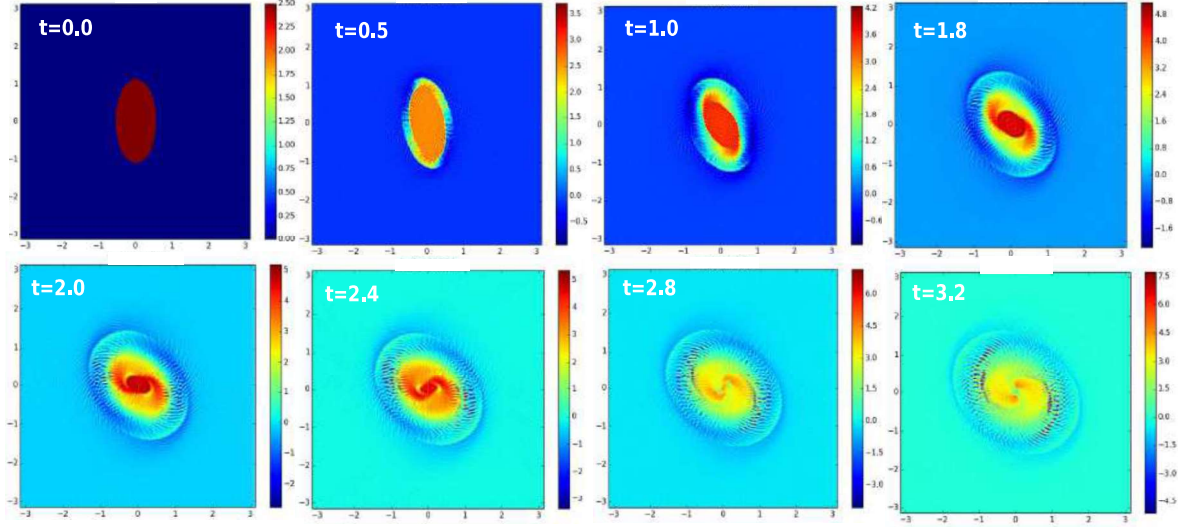


Figure 5.27: Vortex evolution plots of elliptic profile for $\omega_0 = 3.0$, $E_t = 5$, $\eta = 0.3$ and Mach number $M = 0.5$ (compressible limit).

tween vortices [120]. It is found that when this ratio exceeds to the critical value, the vortex merger process happen. In the effect of compressibility, growth rate of the mixing layer reduces and elongation in vortex structures are observed [121]. In Fig.5.25, initial input profile of vortex $\omega = \omega_0 e^{-(x^2+y^2)/\sigma^2}$ at location $(L_x/14, 0)$ and $(-L_x/14, 0)$, where $\omega_0 = 5.0$, $\sigma = 0.5$, radius of dipole $r_c = 0.2$. Time evolution of co-rotating vortex are shown, like vortex start to revolve around each other and slowly decrease the distance between them and eventually vortex stars to merge. Fig.5.26 shows the repulsion between unlike vortex and simultaneously propagation of transverse shear wave of co-rotating unlike vortex. Initial input profile of vorticity $\omega = -\omega_0 e^{-(x^2+y^2)/\sigma^2}$ at location $(L_x/14, 0)$ and $\omega = +\omega_0 e^{-(x^2+y^2)/\sigma^2}$ at location $(-L_x/14, 0)$, where $\omega_0 = 5.0$, $\sigma = 0.5$.

Elliptic vortex: Initial input profile of vorticity $\omega = \omega_o$ when $r < r_0$ and otherwise $\omega = 0$, where $r = \sqrt{(x^2 + (ay/b)^2 - a^2)}$, $\omega_0 = 3.0$, a (minor axis)=0.5, b (major axis)=1.0 with eccentricity $\epsilon = b/a = 2.0$. In Fig.5.27 elliptic vortex rotate, nutate, and changes its shape. We find that, this vortex exhibits various types of rotational

motion and nutation around its origin point.

In next Section, compressibility effects on the two-dimensional strongly coupled dusty plasma by means of molecular dynamics (MD) and computational fluid dynamics (CFD) simulations with Kolmogorov flow as an initial shear flow profile, to study nonlinear compressible vortex flow dynamics and other linear and nonlinear properties of such flow in the presence of variable density, pressure and electrostatic potential are addressed.

5.5 A comparative study of compressible parallel shear flow using MD and CFD simulations

The compressibility effect on shear flow is an important problem in the field of hydrodynamic flows and is addressed by many authors in the past using both atomistic (MD) and continuum (fluid) approaches [56, 57]. In the past, in molecular dynamics simulation of compressible hot/cold moving lid-driven microcavity flow in which Mach number is increased by increasing the magnitude of equilibrium velocity [57] has been studied. It was found that compressibility stabilizes the instability and change the nature of stability from “exchange of instability” to “over-stability” [58].

In the field of strongly coupled plasma, Kelvin-Helmholtz instability in the presence of significant compressibility with quasi-neutrality and mixed boundary (periodic along flow and bounded along transverse shear direction) conditions has been demonstrated by means of generalized hydrodynamic model [11].

In present Chapter, we present for the first time, the qualitative and quantitative comparative study of compressible parallel shear flow e.g Kolmogorov flow. To best of our knowledge, such kind of study has not be performed in the past in any kind of viscoelastic fluids. Our focus is to address the compressible flow on

Chapter 5. Compressible and incompressible shear flow in strongly coupled liquids: A computational fluid dynamics study

the onset of laminar to turbulent transition in strongly coupled plasma for non-zero density, pressure and electrostatic potential perturbations using MD and CFD simulations. In present study, we perform the comparative study of compressible parallel shear flow using Molecular dynamics (MD) simulation and computational fluid dynamics (CFD). To study compressible shear flow, we have chosen Mach number to be one on both the studies. In this studies, we chose Kolmogorov flow as an initial condition. The details and speciality about this flow are given in the earlier Chapter. In the present studies, qualitative and quantitative comparison of the evolution of vortex dynamics of Kolmogorov flow using MD and fluid simulation has been presented. In nonlinear regime of vortex evolution, elongated vortex structures, nonlinear saturation, visco-elastic oscillations and pattern formation have been observed.

5.5.1 Normalizations in MD and CFD studies

Normalizations used in MD and CFD are shown in Table 5.2 and Table 5.3 for easy comparison. For $\kappa = a/\lambda_D \simeq 1$, the length and time normalizations are same, except for a factor of “ $\sqrt{2}$ ” in time. We shall come back to this again. An important difference exist in density normalization of our MD and our CFD calculations. While in MD, density is normalized to “a” which implies a normalization of dust density n_{h0} , in CFD, density is normalized to $Z_h n_{h0} \simeq n_{i0} \simeq n_{e0} \simeq n_0$. That is in CFD, dust density is normalized to the background plasma density.

Let us come back to time normalization: In CFD, time is normalized to ω_{ph} while in MD it is normalized to $\omega_0 = \sqrt{2}\omega_{ph}$. Thus $\tilde{t}_{MD} = t\omega_0 = \sqrt{2}t\omega_{ph} = \sqrt{2}\tilde{t}_{CFD}$ or simply $\tilde{t}_{MD} = \sqrt{2}\tilde{t}_{CFD}$. An example which will be useful is the following : Growth rate in MD simulation is obtained by a fitting $\exp(2\gamma_{MD}\tilde{t}_{MD})$ which is $\exp(2\gamma_{MD} * \sqrt{2}\tilde{t}_{CFD})$. Thus $\gamma_{CFD} = \sqrt{2}\gamma_{MD}$.

Chapter 5. Compressible and incompressible shear flow in strongly coupled liquids: A computational fluid dynamics study

S.No	Quantity	Normalised quantity
1.	Distance (r)	r/a
2.	Time (t)	$t\omega_0$
3.	Temperature (T)	$K_b T(4\pi\epsilon_0 a/Q_h^2)$
4.	Density (n)	na^2
5.	Energy (E)	$E(4\pi\epsilon_0 a/Q_h^2)$

Table 5.2: Table for normalized quantities used in MD simulation

S.No	Quantity	Normalized quantity
1.	Distance (r)	$r/\lambda_{Dt \text{ } ix}$
2.	Time (t)	$t\omega_{ph}$
3.	Potential (Φ)	$\phi e/K_B T_i$
4.	Density ($n_{\alpha 0}$, $\alpha = e, T, d$)	$n_{\alpha 0}/Z_h n_{h0}$

Table 5.3: Table for normalized quantities, here length $\lambda_{Dt \text{ } ix}^2 = \frac{\epsilon_0 k_B T_i}{Z_d e^2 n_{d0}} \simeq \frac{\epsilon_0 k_B T_i}{e^2 n_{i0}} \simeq \lambda_{Di}^2 \simeq \lambda_D^2$, dust plasma frequency $\omega_{ph}^2 = (Q_h^2 n_{h0}/\epsilon_0 M_h)$, $Q_h = Z_h e$ and M_h are charge and mass of single dust particle.

5.6 Results

To make close comparison of results for parallel shear flow e.g Kolmogorov flow obtained from CFD and MD simulation, the following important aspects have been considered and incorporated.

- All the non-dimensional parameters are kept same in both the simulation, for example Reynolds $[R(t=0)=235]$ and Mach numbers $[M(t=0)=1]$.
- To make the normalization same in space in both the simulations, we have chosen screening parameter to be 1 ($\kappa = a/\lambda_h = 1$).
- To make the non-dimensional parameters to be same in both the dynamics, we have calculated the number density for CFD and MD appropriately. Another way of relating the densities is by equating the number of particles present in the system of MD and fluid of sizes 443 and 4π respectively.
- In both the studies, time is normalized by dust plasma frequency ω_{ph} . As

Chapter 5. Compressible and incompressible shear flow in strongly coupled liquids: A computational fluid dynamics study

discussed earlier, a simple scale factor of $\sqrt{2}$ would give us identical time normalizations for CFD and MD.

It is important to note that in our earlier fluid simulation, the system size in CFD is much smaller ($L = L_x = L_y = 2\pi$) because of spatial and temporal resolution or CFL condition. Parameters used in both the simulations are given in table.5.4. In

S.No	Parameters	MD	CFD
1	Mach number ($M = U_0/C_s$)	1.0	1.0
2	Reynolds number ($R = U_0 l/\nu$)	235	235
3	Dynamic viscosity (η)	0.2	0.2
4	U_0/L ratio	2×10^{-3}	2×10^{-3}
5	δ/L ratio	2×10^{-5}	2×10^{-5}
6	System size $L_x = L_y = L$	$L_{MD}=443$	$L_{fluid}=4\pi$
7	Equilibrium mode no. (n_0)	3	3
8	Perturbation mode no. (m_0)	2	2

Table 5.4: Table for values of parameters used in MD and CFD simulations. In above table l is shearing length $l = L/n_0$

fluid simulation 512×512 grid resolutions has been used for $4\pi \times 4\pi$ system size. In MD simulation, A mesh-grid of size 55×55 is superimposed on the particles of the system to calculate the macroscopic or “fluid” variables from microscopic velocities and positions.

Quantitative comparison - Linear regime: Linear growth rate of perturbed mode number $m = 2$ is calculated by the formula given in the Eq.5.25. Growth-rate of perturbed mode $m = 2$ has been calculated from MD and CFD simulations in Fig.5.30 and Fig.5.31. It is clear from the figures that, growth rates obtained using MD and CFD are close if the scale factor of $\sqrt{2}$ is taken into account as shown earlier.

Qualitative comparison - Nonlinear regime: As discussed earlier, non-dimensional parameters (Reynolds number and Mach number) in both the cases are kept the same. To do so, equilibrium densities have been rescaled so that the total circula-

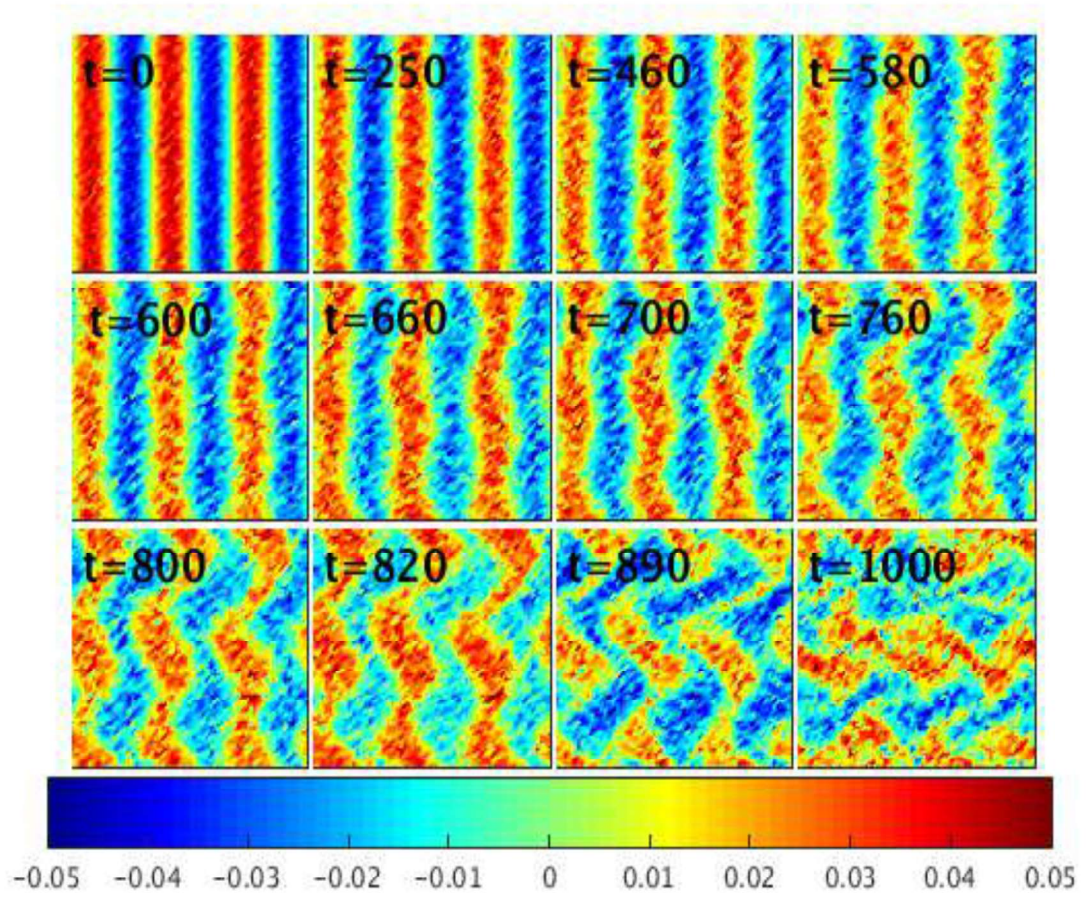


Figure 5.28: Contour plot of fluid vorticity ($\omega = \nabla \times \vec{U}$) obtained from molecular data. The grain velocity in the bins are fluidized through a 55×55 grid to construct vorticity. The horizontal color bar at the bottom show the magnitude of vorticity and blue and red strips show the opposite sign vorticity respectively. Perturbation mode $m = 2$, initial coupling parameter $\Gamma_0 = 50$, screening parameter $\kappa = 1.0$ equilibrium spatial period number is $n_0 = 3$ and shear velocity $U_0=1$. Vorticity plots generated from microscopic velocity show Kolmogorov instability in Molecular Dynamics, the micro scale heating quickly destroy the vorticity structures. The dimensionless parameters are initial Reynolds number $R = 235$ and Mach number $M = 1$. Simulation box is doubly periodic of size $L_x = L_y = 443$.

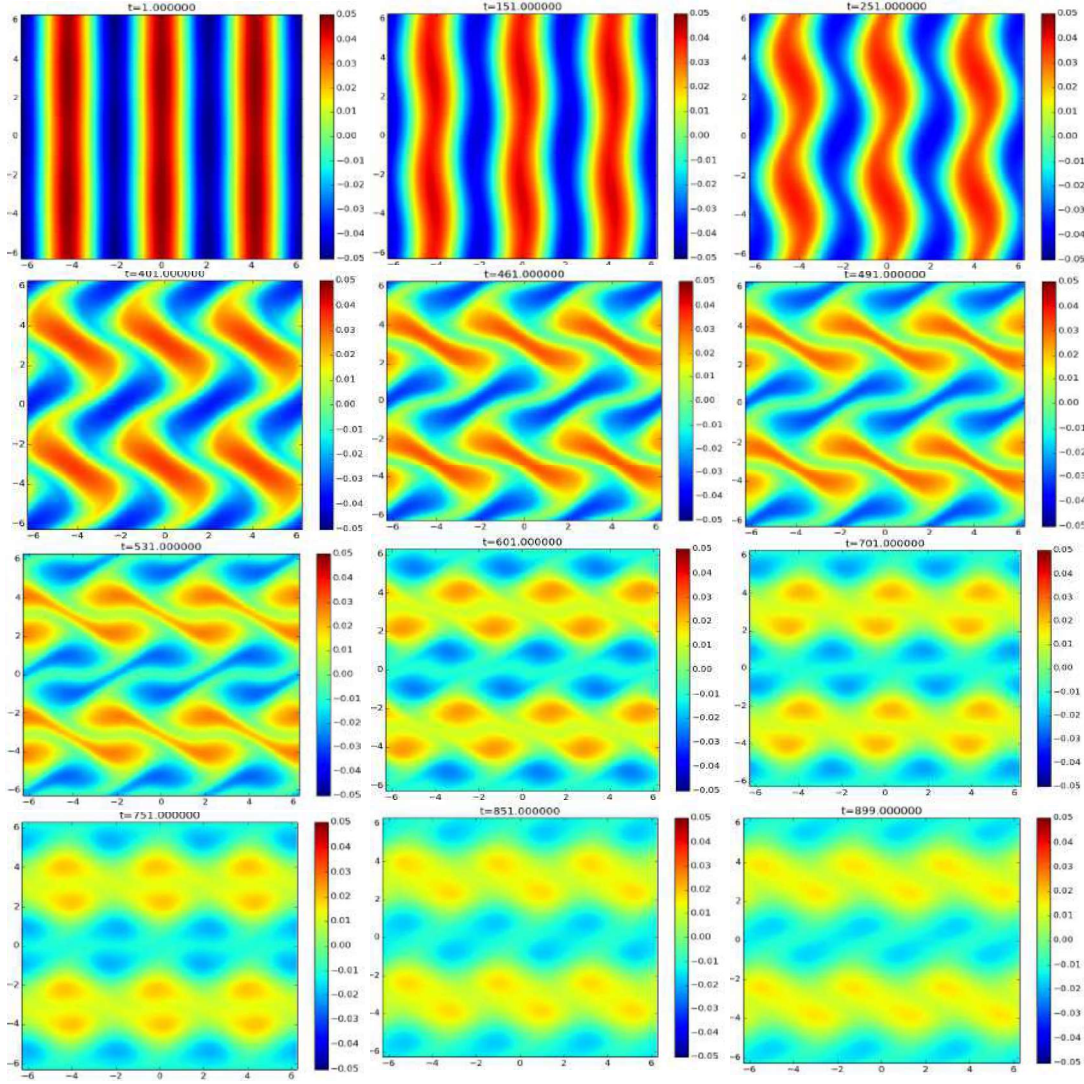


Figure 5.29: Contour plot of fluid vorticity ($\omega = \nabla \times \vec{U}$) obtained from computational fluid dynamics simulation. Input parameters are: number for perturbation mode $m_0 = 2$, initial viscoelastic coefficient E_t ($\Gamma = 50, \kappa = 1.0$) = 2.0, spatial period number $n_0 = 3$ and shear velocity $U_0 = 0.028$ with system size $L_x = L_y = 4\pi$. The dimensionless parameters are initial Reynolds number $R = 235$ and Mach number $M = 1$.

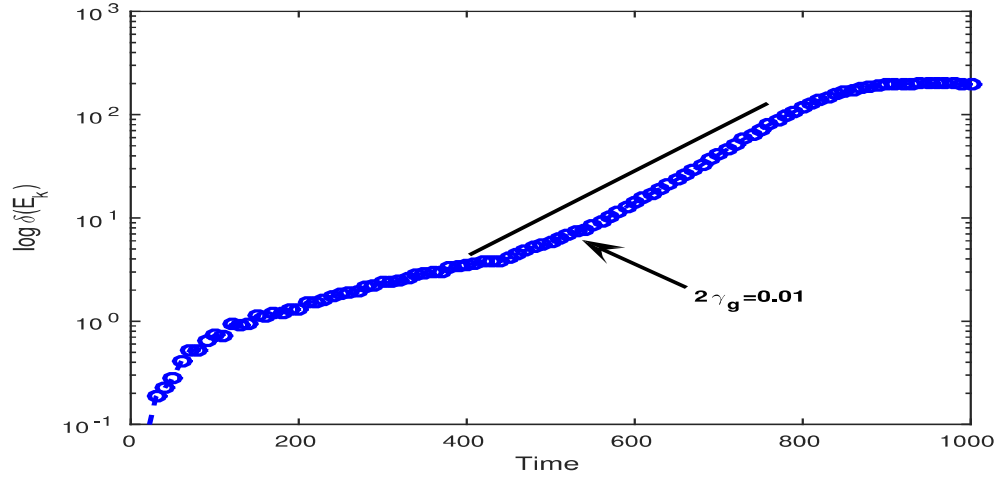


Figure 5.30: Perturbed kinetic energy in linear-log scale for number for perturbation mode $m_0 = 2$, initial coupling parameter $\Gamma_0(t = 0) = 50$, screening parameter $\kappa = 1.0$, spatial period number $n_0 = 3$ and shear velocity $U_0=1$, Reynolds number $R = 235$ and Mach number $M = 1.0$. Calculated growth rate (γ_g) from simulation is 0.01 with system size and number density $L_x = L_y = 443$ and $\bar{n} = 1/\pi$

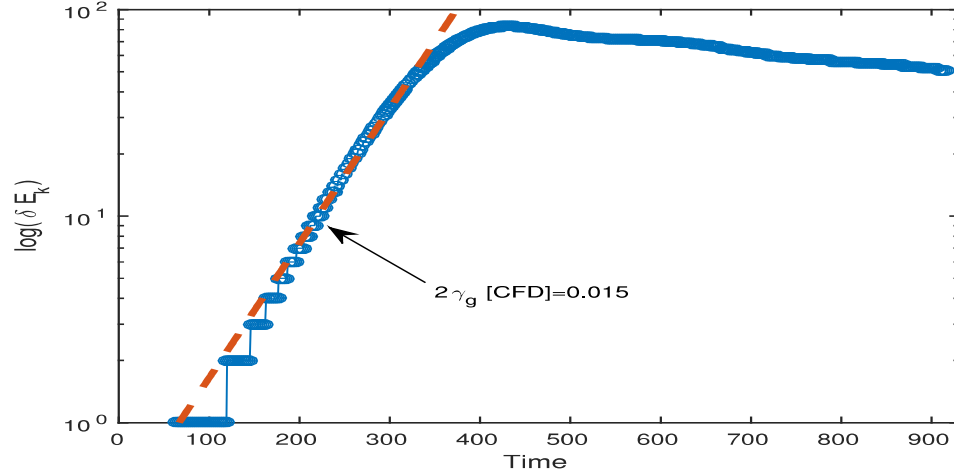


Figure 5.31: Perturbed kinetic energy in linear-log scale for number for perturbation mode $m_0 = 2$, initial viscoelastic coefficient F_t ($\Gamma = 50, \kappa = 1.0$) = 2.0, spatial period number $n_0 = 3$ and Reynolds number $R = 235$ and Mach number $M = 1.0$. Calculated growth rate (γ_g) from simulation is 0.015. System size and number density are $L_x = L_y = 4\pi$ and $\bar{n} = 400$.

Chapter 5. Compressible and incompressible shear flow in strongly coupled liquids: A computational fluid dynamics study

tion in MD and CFD simulations are identical. It is important to realize that in MD simulation, the transport coefficients are calculated self-consistently without any approximation whereas in CFD model the transport coefficient chosen at the initial time $t = 0$ are external to the model and remain the same through out the time evolution.

In Fig.5.28 and Fig.5.29 vorticity contour plot of evolution of vorticity of Kolmogorov flow from molecular dynamics and computational fluid dynamics has been shown. It is clear from figure that fluidized vortex structures are destroyed at late times [see Fig.5.28] in MD simulation because of molecular shear heating as described in Chapter-3. However, in our computational fluid dynamics (using continuum model), we have not incorporated a temperature evolution equation. Hence, the heating effects are not directly included in this model. Hence, one would expect the vortex structures to be sustain for longer time scale compare to MD simulations. However, comparison of Fig.5.28 and Fig.5.29 shows that the peak vorticity values and vortex structures are better preserved in MD as compared to CFD at least for the dimensionless parameters and the procedure used by us in this comparative study. It is interesting to note that the saturated amplitudes obtained using MD and CFD differ by a factor of 2.5, similarly the time at which the saturation happen is different for the two cases.

A brief summary of the results and discussions of the studies made in the present Chapter is given in the next Section.

5.7 Summary

In the first part of this Chapter, using an incompressible generalized hydrodynamic model [9, 10] the linear and nonlinear properties of undriven Kolmogorov flow as an initial value problem in strongly coupled dusty plasma has been addressed . The transition from stable to unstable flow has been found to occur at a critical value of Reynolds number R_c such that for $R < R_c$, growth rate is less than zero or damped and for $R > R_c$ growth rate greater than zero or unstable. A novel observation is that unlike Kolmogorov flow in Navier Stokes hydrodynamics which is neutrally stable for $R < R_c$, Kolmogorov flow in strongly coupled dusty plasma has no such neutral stability, however small the non zero value of E_t may be. This interesting feature is shown to be a direct consequence of the viscoelasticity induced nonlinear (quadratic) eigen value. Real frequency of perturbed mode $k = 2$ with Reynolds number with increasing value of viscoelastic coefficient E_t has been observed, which shows that the oscillation of modes decreases with increasing value of E_t . The linear growth rate from eigen value solver is close to linear growth rate obtained from nonlinear spectral simulation in its linear regime, for entire range of R . A complete stability diagram is obtained for low Reynolds numbers R and for a range of viscoelastic relaxation time E_t [$0 < E_t < 10$]. It is observed that the critical value of Reynolds number R_c for strongly coupled viscoelastic fluid is always smaller than the viscous hydrodynamic fluid. Viscoelasticity changes the nature of perturbed kinetic energy in the nonlinear regime and exhibits viscoelastic oscillation, cyclicity and pattern formation. It is found for given (N, k) as E_t increases $R_c \rightarrow 0$ i.e the Kolmogorov flow losses its criticality and become unconditionally unstable.

In the later part of this Chapter, the effect of compressibility limit, density and potential variations have not been considered. In reality, all fluids are found to be compressible fluids. When density and temperature of the fluid element have spatio-temporal variation, one can not ignore the concept of compressibility. We

Chapter 5. Compressible and incompressible shear flow in strongly coupled liquids: A computational fluid dynamics study

have investigated in detail effect of compressibility on the two-dimensional strongly coupled dusty plasma by means of computational fluid dynamics (CFD) with Kolmogorov flow as an initial shear flow profile. The compressibility allows transverse wave propagation along with longitudinal variation because of viscoelastic response of fluid. To study the compressibility effects on shear flow, a generalized hydrodynamic model has been used, where the weak and strong coupling between fluid elements is controlled by Maxwell relaxation time E_t (viscoelastic coefficient). It is found from the statistical calculation and also from molecular dynamics simulation that E_t and η both are not capricious parameters. In the liquid regime of strongly coupled dusty plasma, for the range of coupling strength Γ and screening length κ , E_t lies in the domain of $\Gamma=[1-10]$. Henceforth, in our study of shear flow, we have elected η and E_t from MD simulation. A massively parallelized pseudo-spectral code has been developed, which is capable of solving coupled set of two-dimensional time-dependent fluid equations. Good agreement in linear growth rates obtained from eigen value solver and from pseudo spectral simulation has been observed and used as a benchmarking of spectral code in the linear regime. Like Navier-Stokes fluids, in our shear flow study, the growth rates are observed to be suppressed by increasing value of Mach number. In contrast, E_t responds in opposite fashion, i.e increasing value of E_t decreases the value of growth-rate γ_g and critical value of R_c . In nonlinear simulation, the suppression of instability, elongated vortex structures, nonlinear saturation, visco-elastic oscillations in perturbed kinetic energy and pattern formation have been observed for Kolmogorov shear profile.

Qualitative difference is found between MD simulation and GHD. In both the study, the transition from stable to unstable flow has been found to occur at a critical value of Reynolds number R_c such that for $R < R_c$, growth rate is close to zero or damped and for $R > R_c$ growth rate greater than zero or unstable. The growth-rate of perturbed mode with Reynolds number show different trend of variation above $R > R_c$ regime in compressible fluid model and MD simulation.

Chapter 5. Compressible and incompressible shear flow in strongly coupled liquids: A computational fluid dynamics study

Linear growth-rates calculated from phenomenological fluid model is found to be close to that obtained from MD simulation for the same non-dimensional parameters, initial coupling and screening parameter as well as initial transport coefficients. However, with the procedures used for the comparison between MD and CFD, in the non-linear regime we find that there are some essential differences. For example, the peak vorticity value is better preserved in MD whereas in CFD model we find that the peak vorticity is dissipated relatively earlier. Similarly we find a substantial difference in the nonlinear saturation amplitude as well as the time of saturation between MD and CFD results.

We summarize the major findings and future scope of present Thesis in the next Chapter.

6

Conclusion

In this Chapter, we summarize the major findings and future scope of present Thesis.

Relatively massive grains when immersed in a low temperature plasma can attain high inter particle potential energy per grain as compared to its kinetic energy, leading to strong coupling effects within the grain medium. Depending on the grain density and temperature, the grain medium can exist in solid-like, liquid-like or gas-like phase. These structures are now routinely studied in plasma laboratories worldwide. Strongly coupled plasma is fascinating not only because of its applications to white dwarf matter, dust rings, the interplanetary medium but also one of the rare system whose kinetic observation of the dynamics can be made in the laboratory due to slow time scale and long length scale. These systems can be addressed by computer simulation and also using phenomenological generalized hydrodynamic models.

Shear flows are ubiquitous in nature. A variety of fluid phenomena in strongly coupled fluids are studied. A parallel flow is possible to set up in laboratory strongly coupled plasma. Far-from-equilibrium questions, such as transition from laminar to turbulent flows, vortex-vortex interactions, an interaction of embedded coherent

structures or rotational structures with the background turbulence etc - for these fundamental questions, even a qualitative comparative study of strongly correlated fluids using fluid model and molecular dynamics has not been attempted yet.

Kolmogorov Flows are a class of flows which exhibit laminar to turbulence transition at low Reynolds number and are amenable to analytical methods in conventional fluids. Using large scale non-equilibrium molecular dynamics, the early phase and late time dynamics of this parallel shear flow in strongly coupled plasma are addressed. A parametric study of the stability of the flow with Reynolds number R has been performed and found that below a critical value of Reynolds number R_c , flow exhibits a neutral stability. However, above $R > R_c$, a transition occurs from laminar to the unstable state and eventually turning into a turbulent flow. It is found that the value of R_c decreases with increasing value of coupling strength.

It is observed that for the given value of initial coupling parameter and screening parameter, molecular shear heating strongly reduces the magnitude of coupling parameter and its decay-rate is mainly found to be dependent upon the ratio of equilibrium shear velocity to thermal velocity. It is found that the magnitude of coupling parameter decays exponentially by the end of the growth phase, thus altering the state of background grains dramatically. To understand the vortex dynamics of strongly coupled molecular fluids undergoing macroscale shear flows in the absence of molecular heat, MD simulation has also been performed, which allows the macroscopic vortex dynamics to evolve, while at the same time removes the microscopically generated heat without using the velocity degrees of freedom. It is demonstrated that by using a configurational thermostat (Profile Unbiased Thermostat or “PUT”) in a novel way, the microscale heat generated by the shear flow can be thermostatted out efficiently without compromising the large scale vortex dynamics. In this work, using MD simulations, a comparative study of shear flow evolution in Yukawa liquids in the presence and absence of molecular or microscopic heating is presented [20]. However, when PUT is “ON” it is

observed that the peaks of local temperature profile at the shear flow location are much lesser in magnitude and global average temperature of the system is maintained as compared to the case with PUT “OFF”. Above mentioned study has also been done with the rotational shear flow, wherein visco-elastic nonlinear wave evolution, nonlinear interaction has been observed. The emergence of non-linear elastic waves from localized coherent vortex sources in strongly correlated Yukawa medium using Molecular dynamics simulation has been studied. We believe that, due to strong coupling effects and compressibility, the rotational shear flow couples the angular and radial directions and the radial shear triggers a radially propagating disturbance [98] which becomes nonlinear as M_{CL} increases beyond the regular compressibility threshold of $M_{CL} > 0.5$.

Using a Generalized Hydrodynamic model the linear and nonlinear properties of undriven incompressible Kolmogorov flow in strongly coupled dusty plasma has been addressed. The transition from stable to unstable flow has been found to occur at a critical value of Reynolds number R_c such that for $R < R_c$, the growth rate is less than zero or damped and for $R > R_c$ growth rate greater than zero or unstable. A novel observation is that unlike Kolmogorov flow in Navier Stokes hydrodynamics which is neutrally stable for $R < R_c$, Kolmogorov flow in strongly coupled dusty plasma has no such neutral stability, however small the non zero value of E_t may be. This interesting feature is shown to be a direct consequence of the viscoelasticity induced nonlinear (quadratic) eigen value. The linear growth rate from eigen value solver is close to linear growth rate obtained from nonlinear spectral simulation in its linear regime, for the entire range of R . It is observed that the critical value of Reynolds number R_c for strongly coupled viscoelastic fluid is always smaller than the viscous hydrodynamic fluid. Viscoelasticity changes the nature of perturbed kinetic energy in the nonlinear regime and exhibits viscoelastic oscillation, cyclicity and pattern formation. It is found for given (N, k) as E_t increases $R_c \rightarrow 0$ i.e the Kolmogorov flow losses its criticality and become unconditionally unstable.

When density and temperature of the fluid element have spatio-temporal variation, one can not ignore the concept of compressibility. Linear and nonlinear properties of such flow in the presence of variable density, pressure and electrostatic potential are addressed using generalized compressible hydrodynamic model. The compressibility allows transverse wave propagation along with longitudinal variation because of viscoelastic response of fluid. To study the compressibility effects on shear flow, a generalized hydrodynamic model has been used, where the weak and strong coupling between fluid elements is controlled by Maxwell relaxation time F_t (viscoelastic coefficient). It is found from the statistical calculation and also from molecular dynamics simulation that F_t and η both are not capricious parameters. In the liquid regime of strongly coupled dusty plasma, for the range of coupling strength Γ and screening length κ , F_t lies in the domain of $\Gamma=[1-10]$. Henceforth, in our study of shear flow, we have elected η and F_t from MD simulation. A massively parallelized pseudo-spectral code has been developed, which is capable of solving coupled set of two-dimensional time-dependent fluid equations. Good agreement in linear growth rates obtained from eigen value solver and from pseudo spectral simulation has been observed and used as a benchmarking of spectral code in the linear regime. Like Navier-Stokes fluids, in our shear flow study, the growth rates are observed to be suppressed by increasing value of Mach number. In contrast, F_t responds in opposite fashion, i.e increasing value of F_t decreases the value of growth-rate γ_g and critical value of R_c . In the nonlinear simulation, the suppression of instability, elongated vortex structures, nonlinear saturation, visco-elastic oscillations in perturbed kinetic energy and pattern formation have been observed for a Kolmogorov shear profile.

The qualitative difference is found between MD simulation and GHD. In both the study, the transition from stable to unstable flow has been found to occur at a critical value of Reynolds number R_c such that for $R < R_c$, growth rate is close to zero or damped and for $R > R_c$ growth rate greater than zero or unstable. The growth-rate of perturbed mode with Reynolds number show a different trend of

variation above $R > R_c$ regime in compressible fluid model and MD simulation.

Linear growth-rates calculated from the phenomenological fluid model is found to be close to that obtained from MD simulation for the same non-dimensional parameters, initial coupling and screening parameter as well as initial transport coefficients. However, with the procedures used for the comparison between MD and CFD, in the nonlinear regime, we find that there are some essential differences. For example, the peak vorticity value is better preserved in MD whereas in CFD model we find that the peak vorticity is dissipated relatively earlier. Similarly, we find a substantial difference in the nonlinear saturation amplitude as well as the time of saturation between MD and CFD results.

Summary :

Before projecting possible future directions, we would like to present a list of interesting findings from this Thesis work:

As has been discussed several times in the Thesis, Dusty plasma is a unique complex system which provides an opportunity to understand fundamental aspects of non-equilibrium physics problems in a strongly coupled medium. One of the fascinating aspects is its ability to provide space and time resolved single particle, kinetic-level information on the micron-sized dust grains which may be set up at weak, intermediate or strongly coupled limits to form gas-like, liquid-like and solid-like grain phases respectively. Our main focus is in shear flows in the liquid-like state of the grain medium. The typical grain densities are of the order $\bar{n}_{grain} \simeq 1 \times 10^8 \text{ m}^{-3}$ which is several ten's of orders smaller in density as compared to any other liquid forming medium that we are aware of. This charged grain-based liquid medium wherein grains interact with each other via a shielded Coulomb interaction or a Yukawa interaction is also called a "Yukawa liquid" is an example of "soft matter".

To understand various physical phenomena in this “soft Yukawa matter”, typically particle-level Molecular Dynamics simulations and Hydrodynamic models based on Visco-elastic memory have commonly been used to support/understand experimental findings. Of particular interest are MD simulations because they raise the possibility of a particle-level comparison of nonlinear, far-from-equilibrium physics problems with Dusty plasma experiments.

This Thesis work may be broadly split into two components: First part is the development and benchmarking of MD code MPMD with a new Configurational Thermostat as well as development and benchmarking of an Advanced Generalized pseudo SPECTral code AG-SPECT which has been developed from the scratch for Hydrodynamics studies performed in this Thesis. The second part of this Thesis is dedicated to the study of parallel and circular 2D shear flows using MD and pseudo-spectral Hydrodynamics codes.

Some of the interesting findings are :

- For low density “soft Yukawa matter” characterized by Brinkman number of order 1, the MD study of micro-scale shear heating, its effect on macro-scale vortex dynamics for parallel Kolmogorov shear flows and circular Rankine-like shear flows, indicate that the initial coupling strength Γ_0 reduces by 70% or more, depending on the type of flow.
- While shear heating does not affect the linear growth rate of the unstable modes, the nonlinear features are found to be strongly influenced by the MD studies. This is confirmed by a novel application of configuration thermostat which “removes” the generated shear heat without affecting the velocity degrees of freedom. As an aside, this procedure may be used in experiments where trajectories of individual grains are measured as a function of time, to estimate coupling strength Γ .
- Bifurcation of Kolmogorov flow and its dependency on coupling strength as well as generation of radially propagating modes triggered by a combination of compressibility and strong coupling strength is demonstrated. It is shown

that as the magnitude of initial poloidal flow strength is increased, the radial mode is found to increase in amplitude and speed, much beyond the speed of longitudinal and transverse equilibrium speeds.

- MD simulations are “first principles” based, meaning, no assumptions have been made regarding transport coefficients or shear heating. The very same flows - except the size of the system - have been addressed using Hydrodynamic code AG-SPECT with input values of initial transport coefficients from MD simulations, as well as without shear heating effects. In general, linear growth rates are found to be unaffected, while nonlinear vortex dynamics is found to be qualitatively different than MD results. This study has been performed with both incompressible and compressible models. As the system sizes in MD and AG-SPECT models are necessarily different, a careful consideration of initial density values for the Kolmogorov flow was made so that the dimensionless numbers such as Reynolds number and Mach number as well as total particles in the system are identical in MD and AG-SPECT models. The results clearly demonstrate the importance and usefulness of our comparative study.

6.1 Future scope

In this Thesis, a large scale hydrodynamics flows have been studied from continuum and discrete point of view. This Thesis points out to several interesting directions for future work. Some of them are:

- In general, Yukawa interaction is known to be the predominant force influencing the dynamics of a grain in complex plasma experiments. However, the effect of other forces such as dust-neutral collisions resulting neutral drag force and the effect of ions accelerated in the sheath region where the 2D grain bed levitates are also known to affect the dynamics of grains. The effect of such drag force may alter the nonlinear propagation of elastic wave and will

provide a more realistic close comparison to laboratory experiments. One can perform such studies in molecular dynamics simulation.

- As performed in the later Section of Chapter-5, for given non-dimensional parameters (Mach number and Reynolds number), it would be interesting to perform the comparative study of rotational shear flow, for example, Dipole, Gaussian, Rankine etc in strongly coupled dusty plasma using Molecular dynamics and Computational fluid dynamics.
- In present Thesis, to demonstrate the shear flow instability in Dusty plasma medium which also treated like a continuum medium, memory dependent model has been used. In this model, viscoelastic response of strongly correlated fluid is incorporated by a non-local viscoelastic operator which incorporates memory effect and long-range order, via a single relaxation time \bar{E}_t [9, 10, 11, 114, 122]. In 2015, Diaw and Murillo [13] described yet another hydrodynamic model for strongly coupled plasma system suggested called as the viscoelastic-density functional (VEDF) model using density functional method. The results obtained from this model for near equilibrium problem. In this hydrodynamic model, coulomb coupling, viscous damping, and the high-frequency or viscoelastic response impact have been incorporated via free energy functional, which were incorporated in earlier model by only a single parameter \bar{E}_t . Therefore, the results obtained by using (VEDF) model closure to molecular dynamics simulation, generalized hydrodynamic models, Singwi-Tosi-Land-Sjolander approximation [123, 124] and the quasi-localized charge approximation. So it would be interesting to perform compare and contrast studies using these two modified hydrodynamic model for far from equilibrium kind of problem, for example, driven (Initial value problem) and undriven (forced problem) shear flow instabilities.
- In this Thesis, the presence of bifurcation in 2D Kolmogorov flows using MD and CFD has been demonstrated for Yukawa liquids and for strongly coupled dusty plasma. However, the mathematical nature of the bifurcation has

not been addressed. In the past, using external forcing of Kolmogorov flow type, several steady states, traveling waves, modulated traveling waves and dynamics of reversals and condensates have been addressed for incompressible Navier-Stokes equation [101]. If driven forcing is enough, the shear flow becomes unstable and reaches to chaotic states. In this study bifurcation and pattern formation has been observed. It would be interesting to perform such studies for strongly coupled dusty plasma system using hydrodynamic model.

- External drive in fluid model: *Rayleigh – Benard* convection cell (RBCC) is the buoyancy-driven flow of a fluid heated from below and cooled from above. This model of thermal convection is a paradigm for nonlinear and chaotic dynamics, pattern formation and fully developed turbulence [125]. In the past, formation of Rayleigh-Benard convection cells (RBCC) in two-dimensional strongly coupled Yukawa liquids, characterized by coupling strength Γ and screening parameter κ was addressed by using Molecular dynamics simulation [126]. However, to best of our knowledge, the detailed linear and nonlinear stability analysis of RBCC problem has not studied yet using modified fluid model. In our pseudo spectral code, the boundary condition is doubly-periodic, one can change the boundary condition and study the problem which crucial depend upon the boundary condition. One can add the reflecting boundary condition in the fluid code and add the gravity as a body force in the momentum equation to study body force depend on the problem, for example, Rayleigh Benard convection cell and Rayleigh Taylor instability.
- Generally, non-Newtonian fluids are complex mixtures: slurries, pastes, gels, polymer solutions, Synthetic polymers, human tissue, biological fluids such as synovial fluids found in joints [26] etc. As described in the Introduction (Chapter-1), dusty plasma medium also behaves like a non-Newtonian fluid. It would be interesting to study the linear and nonlinear stability of dusty plasma as a non-Newtonian fluid in presence of velocity shear flow.

- In this Thesis, the shear flow has been studied in unmagnetized plasma. One can incorporate magnetic field and understand magnetized hydrodynamics (MHD). Basic equations for this study have been written in the framework of a generalized magneto-hydrodynamic model to include viscoelastic effects. It is found that for both longitudinal and transverse perturbations, elasticity modified Alfvén type modes can propagate that can be termed magneto-elastic modes [127].
- In the present Thesis, we have focused only on 2D studies. However, to make a direct comparison with laboratory dusty plasma experiments, it would be useful to extend the MD and CFD codes to 3D as well as to generalize the codes to arbitrary boundary conditions.

Appendix A

A Complex viscosity and viscoelastic operator $(F_m \frac{d}{dt})$ based Modified Hydrodynamic model

J. Frenkel [9], Ichimaru et.al [122] and M. A. Berkovsky [114] addressed viscoelasticity through a memory effect via Maxwell's relaxation time F_t . This model was adopted by Kaw and Sen [10] in 1998 for weakly correlated dusty plasma without equilibrium flow. In the following, for the sake of completion, an outline of the model for arbitrary initial condition is presented.

Navier-Stokes equation with mean body force density, velocity, mass and density \vec{F}_b , \vec{U} , M and n respectively is given by:

$$Mn \frac{d\vec{U}}{dt} + \vec{F}_b = \eta \nabla^2 \vec{U} + \left(\frac{\eta}{3} + \xi' \right) \vec{\nabla}(\vec{\nabla} \cdot \vec{U}) \quad (\text{A.1})$$

$$\frac{d\vec{U}}{dt} + \frac{\vec{F}_b}{Mn} = \frac{\eta}{Mn} \nabla^2 \vec{U} + \left(\frac{\eta}{3Mn} + \frac{\xi'}{Mn} \right) \vec{\nabla}(\vec{\nabla} \cdot \vec{U}) \quad (\text{A.2})$$

where ∇^2 is a Laplacian operator. In above equation, η and ξ are dynamic shear and bulk viscosities respectively. The above equation can also be written as

$$\frac{d\vec{U}}{dt} + \vec{F}_b = \nu \nabla^2 \vec{U} + \left(\frac{\nu}{3} + \xi \right) \vec{\nabla}(\vec{\nabla} \cdot \vec{U}) \quad (\text{A.3})$$

Here $\vec{F}_b = \vec{F}'_b/Mn$, $\nu = \eta/Mn$ and $\xi = \xi'/Mn$ are force per unit mass density, kinematic shear viscosity and kinematic bulk viscosity respectively.

To incorporate the effect of strong correlation in space and time (viscoelastic effects), let us consider the kinematic viscosity as a non-local operator, its convolution and cross-correlation in time and space respectively. For example, let us

Appendix

consider

$$\frac{d\vec{U}}{dt} + \vec{F}_b = \int_{-\infty}^t dt' \int \nu(\vec{r} - \vec{r}', t - t') \vec{U}(\vec{r}', t') d\vec{r}' \quad (\text{A.4})$$

Comparing Eq.A.3 and Eq.A.4

$$\int_{-\infty}^t dt' \int \nu(\vec{r} - \vec{r}', t - t') \vec{U}(\vec{r}', t') d\vec{r}' = \nu \nabla^2 U + \left(\frac{\nu}{3} + \xi \right) \vec{\nabla}(\vec{\nabla} \cdot \vec{U}) \quad (\text{A.5})$$

Let us take Fourier transform in space with kernel $K(k, r) \simeq e^{i\vec{k} \cdot \vec{r}}$ and using convolution theorem in Fourier space to get:

$$\int_{-\infty}^t dt' \int \int_{-\infty}^{\infty} e^{i\vec{k} \cdot \vec{r}} \nu(\vec{r} - \vec{r}', t - t') \vec{U}(\vec{r}', t') d\vec{r} d\vec{r}' = \left[-\nu k^2 - \left(\frac{\nu}{3} + \xi \right) \vec{k}(\vec{k} \cdot) \right] U(\vec{k}, t)$$

$$\int_{-\infty}^t dt' \int \int_{-\infty}^{\infty} e^{i\vec{k} \cdot (\vec{r} - \vec{r}')} d\vec{r} \nu(\vec{r} - \vec{r}', t - t') e^{i\vec{k} \cdot \vec{r}'} \vec{U}(\vec{r}', t') d\vec{r}' = - \left[\nu k^2 + \left(\frac{\nu}{3} + \xi \right) \vec{k}(\vec{k} \cdot) \right] U(\vec{k}, t)$$

Using change variable $\vec{r} - \vec{r}' = \vec{R}$, hence $d\vec{r} = d\vec{R}$, where R is constant, we get.

$$\int_{-\infty}^t dt' \int_{-\infty}^{\infty} e^{i\vec{k} \cdot \vec{R}} \nu(\vec{R}, t - t') d\vec{R} \int_{-\infty}^{\infty} e^{i\vec{k} \cdot \vec{r}'} \vec{U}(\vec{r}', t') d\vec{r}' = - \left[\nu k^2 + \left(\frac{\nu}{3} + \xi \right) \vec{k}(\vec{k} \cdot) \right] U(\vec{k}, t)$$

$$\int_{-\infty}^t \nu(\vec{k}, t - t') U(\vec{k}, t') dt' = - \left[\nu k^2 + \left(\frac{\nu}{3} + \xi \right) \vec{k}(\vec{k} \cdot) \right] U(\vec{k}, t)$$

Splitting the domain of integral, we get:

$$\int_{-\infty}^0 \nu(\vec{k}, t - t') U(\vec{k}, t') dt' + \int_0^t \nu(\vec{k}, t - t') U(\vec{k}, t') dt' = - \left[\nu k^2 + \left(\frac{\nu}{3} + \xi \right) \vec{k}(\vec{k} \cdot) \right] U(\vec{k}, t)$$

Let us take the differentiation of above equation in time with assumption $\frac{hU(\vec{k}, t)}{ht} = 0$.

$$\begin{aligned} \int_{-\infty}^0 \frac{d\nu(\vec{k}, t-t')}{dt} U(\vec{k}, t') dt' + \int_0^t \frac{d\nu(\vec{k}, t-t')}{dt} U(\vec{k}, t') dt' \\ = - \left[\nu k^2 + \left(\frac{\nu}{3} + \xi \right) \vec{k}(\vec{k} \cdot) \right] \frac{dU(\vec{k}, t)}{dt} \end{aligned} \quad (\text{A.6})$$

Using the following:

$$\int_{-\infty}^{\infty} f(t) dt = \int_{-\infty}^0 f(t) dt + \int_0^{\infty} f(t) dt \quad (\text{A.7})$$

$$\int_{-\infty}^0 f(t) dt = \int_{-\infty}^{\infty} f(t) dt - \int_0^{\infty} f(t) dt \quad (\text{A.8})$$

Eq.A.6 becomes

$$\begin{aligned} \int_{-\infty}^{\infty} \frac{d\nu(\vec{k}, t-t')}{dt} U(\vec{k}, t') dt' - \int_0^{\infty} \frac{d\nu(\vec{k}, t-t')}{dt} U(\vec{k}, t') dt' \\ + \int_0^t \frac{d\nu(\vec{k}, t-t')}{dt} U(\vec{k}, t') dt' = - \left[\nu k^2 + \left(\frac{\nu}{3} + \xi \right) \vec{k}(\vec{k} \cdot) \right] \frac{dU(\vec{k}, t)}{dt} \end{aligned} \quad (\text{A.9})$$

Taking the Laplace transform in time on both side with kernel $K(\omega, t) \approx e^{-\omega t}$ and using property $L \left[\frac{hf}{ht} \right] = \omega f(\omega) - f(0)$. It is important to note that we have used two Laplace transform property (convolution):

$$\begin{aligned} L \left[\int_0^{\infty} \frac{d\nu(\vec{k}, t-t')}{dt} U(\vec{k}, t') dt' \right] &= \omega \nu(\vec{k}, \omega) U(\vec{k}, \omega) \\ L \left[\int_0^t \frac{d\nu(\vec{k}, t-t')}{dt} U(\vec{k}, t') dt' \right] &= \omega \nu(\vec{k}, \omega) U(\vec{k}, \omega) \end{aligned}$$

Using these property, the above equation becomes

$$\int_0^{\infty} e^{-\omega t} dt \int_{-\infty}^{\infty} \frac{d\nu(\vec{k}, t-t')}{dt} U(\vec{k}, t') dt' = - \left[\nu k^2 + \left(\frac{\nu}{3} + \xi \right) \vec{k}(\vec{k} \cdot) \right] \{ \omega U(\vec{k}, \omega) - U(k, 0) \} \quad (\text{A.10})$$

$$\int_0^\infty e^{-\omega(t-t')} \frac{d\nu(\vec{k}, t-t')}{dt} dt \int_{-\infty}^\infty e^{-\omega t'} U(\vec{k}, t') dt' = - \left[\nu k^2 + \left(\frac{\nu}{3} + \xi \right) \vec{k}(\vec{k} \cdot) \right] \omega U(\vec{k}, \omega)$$

It is important to note that in these calculation no equilibrium shear flow has not been considered (Mathematical formulation is true for equilibrium and near-equilibrium system).

$$\begin{aligned} & \int_0^\infty e^{-\omega(t-t')} \frac{d\nu(\vec{k}, t-t')}{dt} dt \left[\int_{-\infty}^0 e^{-\omega t'} U(\vec{k}, t') dt' \right. \\ & \left. + \int_0^\infty e^{-\omega t'} U(\vec{k}, t') dt' \right] = - \left[\nu k^2 + \left(\frac{\nu}{3} + \xi \right) \vec{k}(\vec{k} \cdot) \right] \omega U(\vec{k}, \omega) \end{aligned} \quad (\text{A.11})$$

In Laplace transform the kernel $K(\omega, t) = 0$ in the range $[-\infty, 0]$. There are two important kernels to be noticed

- kernel with operator $\nu(\vec{k}, t-t')$ has two terms:
one is because of viscosity and other one is due to elasticity of the medium.
Therefore, $\omega = \omega_\nu = \omega_r - \mathcal{E}_{it}$. Here ω_r is the real frequency $\omega_r = 1/F_t$.
- For R.H.S kernel will be only real frequency dependent $\omega = \omega_r = 1/F_t$.

Now Eq.A.11 will become

$$\begin{aligned} & \omega \nu(\vec{k}, \omega) U(\vec{k}, \omega) - \nu(k, 0) U(k, 0) \\ & = - \left[\nu k^2 + \left(\frac{\nu}{3} + \xi \right) \vec{k}(\vec{k} \cdot) \right] (1/F_t) U(\vec{k}, \omega) \end{aligned} \quad (\text{A.12})$$

$$\omega \nu(\vec{k}, \omega) = - \left[\nu k^2 + \left(\frac{\nu}{3} + \xi \right) \vec{k}(\vec{k} \cdot) \right] (1/F_t) \quad (\text{A.13})$$

L.H.S frequency is replaced by imaginary and real terms.

$$\left(\frac{1}{F_t} - \mathcal{E} \right) = - \left[\nu k^2 + \left(\frac{\nu}{3} + \xi \right) \vec{k}(\vec{k} \cdot) \right] (1/F_t) \quad (\text{A.14})$$

$$\nu(\vec{k}, \omega) = \frac{- \left[\nu k^2 + \left(\frac{\nu}{3} + \xi \right) \vec{k}(\vec{k} \cdot) \right]}{1 - \mathcal{E} F_t} \quad (\text{A.15})$$

Now taking the Fourier and Laplace transform of Eq.A.6 and putting back the calculated non-local kinematic viscosity operator on R.H.S and taking the inverse Fourier and Laplace transform.

$$\left\{1 + E_t \frac{d}{dt}\right\} \left[\frac{d\vec{U}}{dt} + \vec{F}_b' \right] = - \left[\nu \nabla^2 + \left(\frac{\nu}{3} + \xi \right) \vec{\nabla}(\vec{\nabla} \cdot) \right] \vec{U} \quad (\text{A.16})$$

Here F_b' is body force per unit mass-density, this can be any external force for example, gravitational, electrostatic, pressure and driven forces. Let us consider for dusty plasma medium with density n_h and mass density $\rho_h = M_h n_h$, there are following forces applied

- Pressure force: $-\nabla P$
- Electrostatic force: $-q_h n_h \nabla \phi$

where q_h and M_h are mean charge and mass of dust. Then the modified hydrodynamic equation will become:

$$\left\{1 + E_t \frac{d}{dt}\right\} \left[\frac{d\vec{U}}{dt} + \frac{q_h n}{\rho_h} \vec{\nabla} \phi + \frac{1}{\rho_h} \vec{\nabla} p \right] = - \left[\nu \nabla^2 + \left(\frac{\nu}{3} + \xi \right) \nabla(\nabla \cdot) \right] \vec{U} \quad (\text{A.17})$$

The physics of strong coupling of the dust fluid, is incorporated via a viscoelastic memory coefficient E_t . Viscoelasticity is the property of fluid having both the virtue of viscosity as well elasticity. In such visco-elastic medium, stress relaxes with finite time (t) which provide an exponential decay in time as e^{-t/τ_m} . E_t is also called Maxwell's relaxation time. It is the response time taken by the fluid element to get back to its original state, when perturbed due to "elastic" nature of the fluid. As E_t goes to zero the model reduces to conventional hydrodynamic fluid. In practice, the magnitude of E_t , Maxwell's relaxation time (or viscoelastic coefficient) for strongly coupled plasma will have to be calculated from experiments or Molecular dynamics simulations which depends explicitly on the strong coupling parameters (κ and Γ are screening and coupling parameters respectively) and some

Appendix

other statistical parameters, For example in Ref.[114, 122], $E_t(\kappa, \Gamma)$ is defined as:

$$E_t(\kappa, \Gamma) = \frac{(\frac{4}{3}\eta + \xi')}{(3 - \gamma\mu_h)n_h + \frac{4}{15}u}\Gamma = \frac{(\frac{4}{3}\nu + \xi)}{(3 - \gamma\mu_h) + \frac{4}{15}\frac{u}{n_d}}\Gamma \quad (\text{A.18})$$

where n_h , η , ξ and γ are density, shear viscosity, bulk viscosity and adiabatic index (for two-dimensional system $\gamma = 2$). μ_h is compressibility

$$\mu_h = \left(\frac{1}{T}\right) \left(\frac{\partial P}{\partial T}\right)_T = 1 + \frac{u(\Gamma)}{3} + \left(\frac{\Gamma}{9}\right) \frac{\partial u(\Gamma)}{\partial \Gamma} \quad (\text{A.19})$$

where $u(\Gamma)$ is excess internal energy of the system [128, 129]. Inputs of η , ξ , μ_h , $u(\Gamma)$, Γ come from MD simulation and experiments. Hence, it is important to note that the physics of large number of parameters namely, η , ξ , μ_h , $u(\Gamma)$, Γ are combined in to a single E_t [9, 10]. Therefore, the model is phenomenological.

A.1 Compressible hydrodynamic model and suitable normalization : Two velocity field formulation

Continuity equation:

$$\frac{\partial \rho_h}{\partial t} + \nabla \cdot (\rho_h \vec{U}) = 0 \quad (\text{A.20})$$

Momentum equation:

$$\left\{ 1 + E_t \frac{d}{dt} \right\} \left[\frac{d\vec{U}}{dt} + \frac{q_h n_h}{\rho_h} \vec{\nabla} \phi + \frac{1}{\rho_h} \vec{\nabla} p \right] = - \left[\nu \nabla^2 + \left(\frac{\nu}{3} + \xi \right) \nabla(\nabla \cdot) \right] \vec{U} \quad (\text{A.21})$$

where $d/dt = \partial/\partial t + \vec{U} \cdot \nabla$. Momentum equations for electrons and ions fluids are :

$$\begin{aligned} m_e n_e \left(\frac{\partial \vec{U}_e}{\partial t} + \vec{U}_e \cdot \nabla \vec{U}_e \right) &= -\vec{\nabla} P_e + n_e e \vec{\nabla} \phi \\ m_i n_i \left(\frac{\partial \vec{U}_i}{\partial t} + \vec{U}_i \cdot \nabla \vec{U}_i \right) &= -\vec{\nabla} P_i - n_i e \vec{\nabla} \phi \end{aligned}$$

where m_s, n_s, U_s, P_s, T_s [where, s = e (electron) and i (ion)] are mass, number

density, velocity, pressure and temperature of the particular species respectively. Equations of states for electron and ion fluids are $P_e = n_e k_B T_e$ and $P_i = n_i k_B T_i$ respectively. Electrons and ions may be considered inertia-less particles as compared to dust. Hence, equations of motion of electron and ion fluids become $\nabla P_e = n_e e \nabla \phi$ and $\nabla P_i = -n_i e \nabla \phi$ which leads to Boltzmann distributions of electrons and ions as follows: Poisson's equation:

$$\begin{aligned}\nabla^2 \phi &= \frac{e}{\epsilon_0} [Z_h n_h - n_i + n_e] \\ n_i &= n_{i0} e^{-e\phi/k_B T_i} \\ n_e &= n_{e0} e^{e\phi/k_B T_e} \\ \nabla^2 \phi &= \frac{e}{\epsilon_0} [Z_h n_h - n_{i0} e^{-e\phi/k_B T_i} + n_{e0} e^{e\phi/k_B T_e}]\end{aligned}$$

First order approximation of above equation

$$\begin{aligned}\nabla^2(\phi_0 + \phi_1) &= \frac{e}{\epsilon_0} [Z_h n_{0h} + Z_h e n_{h1} - n_{i0} + n_{i0} e\phi/k_B T T \\ &\quad + n_{e0} + n_{e0} e\phi/k_B T e]\end{aligned}\tag{A.22}$$

Imposing the condition of quasi-neutrality $n_{i0} = n_{e0} + Z_h n_{h0}$

$$\nabla^2 \phi_1 = \frac{e}{\epsilon_0} [n_{i0} e\phi_1/k_B T T + n_{e0} e\phi_1/k_B T e + Z_h e n_{h1}]\tag{A.23}$$

$$\nabla^2 \phi_1 = n_{i0} e^2 \phi_1 / \epsilon_0 k_B T T + n_{e0} e^2 \phi_1 / \epsilon_0 k_B T e + Z_h e^2 n_{h1} / \epsilon_0\tag{A.24}$$

where

$$\begin{aligned}\frac{1}{\lambda_{Di}^2} &= \frac{n_{i0} e^2 \phi_1}{\epsilon_0 k_B T T} \\ \frac{1}{\lambda_{De}^2} &= \frac{n_{e0} e^2 \phi_1}{\epsilon_0 k_B T e} \\ \frac{1}{\lambda_D^2} &= \frac{1}{\lambda_{Di}^2} + \frac{1}{\lambda_{De}^2} \simeq \frac{1}{\lambda_{Di}^2}\end{aligned}$$

Appendix

$$\nabla^2 \phi_1 - \frac{\phi_1}{\lambda_D^2} = \frac{Z_h e^2 n_{h1}}{\epsilon_0} \quad (\text{A.25})$$

Normalised Potential $\bar{\Phi} = \frac{e\phi_1}{k_B T_i}$

$$\nabla^2 \bar{\Phi} - \frac{\bar{\Phi}}{\lambda_D^2} = \frac{Z_h e^2 n_{h1}}{k_B T_i \epsilon_0} \quad (\text{A.26})$$

For a while let us consider that normalized length to be some arbitrary length L and normalization in density i.e $n_{h1} = n_{h0} \bar{n}_h$.

$$\bar{\nabla}^2 \bar{\Phi} - \frac{L^2 \bar{\Phi}}{\lambda_D^2} = \frac{Z_h e^2 n_{h0} L^2 \bar{n}_h}{\epsilon_0 k_B T_i} \quad (\text{A.27})$$

$$\bar{\nabla}^2 \bar{\Phi} - \frac{L^2 \bar{\Phi}}{\lambda_D^2} = \frac{L^2 \bar{n}_h}{\lambda_{Dt \text{ } ix}^2} \quad (\text{A.28})$$

where $\frac{1}{\lambda_{Dmix}^2} = \frac{Z_d e^2 n_{d0}}{\epsilon_0 k_B T_i}$, where $\lambda_{Dt \text{ } ix}$ is mixed length scale and also equivalent to $\lambda_{Dt \text{ } ix} \simeq \lambda_{Di}$. It is important to note that from here onwards in the calculation, length is normalized by $\lambda_{Dt \text{ } ix} \simeq \lambda_{Di}$. After choosing $L = \lambda_D$ and $\lambda_D^2 = \lambda_{Di}^2$ (for high temperature of electron, we neglect the contribution of electron Debye length in Eq.A.25) the Poisson's equation becomes.

Normalized Poisson's equation:

$$\bar{\nabla}^2 \bar{\Phi} = \frac{\lambda_{Dt \text{ } ix}^2}{\lambda_{Di}^2} \bar{n}_h + \bar{\Phi} \quad (\text{A.29})$$

$$\bar{\nabla}^2 \bar{\Phi} = \left(\frac{n_{io} e^2}{\epsilon_0 k_B T_i} \right) \times \left(\frac{\epsilon_0 k_B T_i}{n_{ho} Z_h e^2} \right) \bar{n}_h + \bar{\Phi} \quad (\text{A.30})$$

$$\bar{\nabla}^2 \bar{\Phi} = \left(\frac{n_{io}}{n_{ho} Z_h} \right) \bar{n}_h + \bar{\Phi} \quad (\text{A.31})$$

As $n_{i0} = n_{ho} Z_h$ then normalized Poisson's equation will be:

$$\bar{\nabla}^2 \bar{\Phi} = \bar{n}_h + \bar{\Phi} \quad (\text{A.32})$$

Hence, in present fluid model all equations are dimensionless and the normalization

quantities are given in table.1. Equation of state for dust fluid is $P = \mu_h \gamma_h n_h k_B T_h$,

S.No	Quantity	Normalized quantity
1.	Distance (r)	$r/\lambda_{Dt \text{ } ix}$
2.	Time (t)	$t\omega_{ph}$
3.	Potential (Φ)	$\phi e/K_B T_i$
4.	Density ($n_{\alpha 0}$, $\alpha = e, T, d$)	$n_{\alpha 0}/Z_h n_{h0}$

Table 1: Table for normalized quantities. where length $\lambda_{Dt \text{ } ix}^2 = \frac{\epsilon_0 k_B T_i}{Z_d e^2 n_{d0}} = \lambda_{Di}^2$, dust plasma frequency $\omega_{ph} = (Q_h^2 n_{h0}/\epsilon_0 M_h)$. $Q_h = Z_h e$ and M_h are charge and mass of single dust particle.

where μ_h and γ_h are compressibility and adiabatic index ($\gamma_h = c_p/c_v$) respectively.

Normalized Momentum eq:

$$\left\{ 1 + E_t \frac{d}{dt} \right\} \left[\frac{d\bar{U}}{dt} + \bar{\nabla} \bar{\Phi} + \frac{C_s^2}{\bar{n}_h} \bar{\nabla} \bar{n}_h \right] = - \left[\bar{\nu} \bar{\nabla}^2 + \left(\frac{\bar{\nu}}{3} + \bar{\xi} \right) \bar{\nabla} (\bar{\nabla} \cdot) \right] \bar{U} \quad (\text{A.33})$$

where $C_s^2 = \mu_h \gamma_h k_B T_h / Z_h T_i$. It is important to note that in present Thesis the last term $\left(\frac{\bar{\nu}}{3} + \bar{\xi} \right) \bar{\nabla} (\bar{\nabla} \cdot)$ on the R.H.S has not considered for simplicity.

Normalized Continuity eq:

$$\frac{\partial \bar{n}_h}{\partial t} + \bar{\nabla} \cdot (\bar{n}_h \bar{U}) = 0 \quad (\text{A.34})$$

Final set of fluid equations which we have used in our Advanced Generalized Spectral Code (AG-Spect) are:

$$\frac{\partial n_h}{\partial t} + \nabla \cdot (n_h \vec{U}) = 0 \quad (\text{A.35})$$

$$\nabla^2 \phi = n_h + \phi \quad (\text{A.36})$$

$$\left\{ 1 + E_t \frac{d}{dt} \right\} \left[\frac{d\vec{U}}{dt} - \vec{\nabla} \phi + \frac{C_s^2 \vec{\nabla} n_h}{n_h} \right] = \nu \nabla^2 \vec{U} \quad (\text{A.37})$$

A.2 Incompressible hydrodynamic model : Vorticity-Stream function formulation

A fluid is said to be incompressible when the mass density of a co-moving volume element does not change appreciably as the element moves through regions of varying pressure. An incompressible fluid is a fluid that does not change the volume of the fluid due to external pressure. The conservation of mass density for such a dust fluid element (also called the continuity equation) is given in Eq.A.20. For addressing phenomena where the disturbances travel at speeds less than sound speed of the system, density variations are negligible i.e $\frac{h\bar{n}_d}{ht} = 0$, resulting in $\nabla \cdot \vec{U} = 0$ leading to incompressibility of the dust fluid. In this context, the following assumption has been taken in the Eq.A.33

- Density variations are not sustainable in time and space. Hence $\frac{h\bar{n}_d}{ht} = 0$
- Potential variations in Eq.A.33 is considered to be ignorable.

This allows us to introduce a stream function $\psi(x, y)$. For incompressible fluid, in general, vorticity stream function formulation make the calculations easier than velocity formulation because it changes vector velocity equation into scalar stream function equation. Vorticity ω is a curl of velocity defined as

$$\omega = \hat{z} \cdot \nabla \times \vec{U} = \frac{\partial v}{\partial x} - \frac{\partial u}{\partial y} \quad (\text{A.38})$$

where u and v are x and y component of velocity. Velocity component (u, v) can be expressed in terms of $\psi(x, y)$ as $u = \frac{\partial \psi}{\partial y}$, $v = -\frac{\partial \psi}{\partial x}$ which gives $\omega = -\nabla^2 \psi$. Taking the curl of Eq.A.33, the incompressible Generalized Hydrodynamic equation in terms of dust fluid vorticity becomes as

$$\left\{ 1 + E_t \frac{\partial}{\partial t} \right\} \left[\frac{d\omega}{dt} \right] + E_t \nabla \times \left[\vec{U} \cdot \nabla \frac{d\vec{U}}{dt} \right] = \nu \nabla^2 \omega \quad (\text{A.39})$$

where $\nabla^2 = \frac{\partial^2}{\partial x^2} + \frac{\partial^2}{\partial y^2}$, $\nu = \frac{\eta}{\rho}$ and $\frac{h}{ht} = \frac{\partial}{\partial t} + \vec{U} \cdot \nabla$ as mentioned earlier.

B Viscoelastic-Density Functional (VEDF) based hydrodynamic model

Diaw and Murillo [13] have described a generalized hydrodynamic model for strongly coupled plasma system referred as the viscoelastic-density functional (VEDF) model using density functional method. In this model, exact equations of the Bogoliubov-Born-Green-Kirkwood-Yvon hierarchy is used to obtain the density, momentum, and stress tensor-moment equations and the moment equations are closed with two closures, one that guarantees an equilibrium state given by density-functional theory and another that includes collisions in the relaxation of the stress tensor. Momentum Eq. for this model is

$$\left\{1 + F_t \frac{d}{dt}\right\} \left[\rho_h \frac{d\vec{U}}{dt} + \nabla P + \frac{\delta F[n_h]}{\delta n_h} \right] = \eta \nabla^2 U + (\eta/3 + \xi) \nabla(\nabla \cdot U) \quad (\text{B.1})$$

In above equation η and ξ are dynamic shear and bulk viscosity respectively. where $F[n_h]$ is free energy functional $F[n_h] = F^{ih}[n_h]$ (noninteracting free energy) + $F^{ext}[n_h]$ (External energy) + $F^{Hartee}[n_h]$ (Hartee energy) + $F^{corr}[n_h]$ (correlation functional). $\frac{\delta F(n_d)}{\delta n_d} = Q_h n_h \vec{\nabla} \phi + \vec{\nabla} P + \frac{\delta F^{corr}(n_d)}{\delta n_d}$. In this hydrodynamic model, coulomb coupling, viscous damping, and the high-frequency or viscoelastic response impact have been incorporated via free energy functional. Therefore, the results obtained by using this model are very closed to molecular dynamics simulation, generalized hydrodynamic models, Singwi-Tosi-Land-Sjolander approximation [123, 124] and the quasilocalized charge approximation.

C Fluctuation-dissipation theorem based hydrodynamic model

In general, dynamic structure factors for strongly coupled plasma is calculated by the molecular dynamics (MD) simulations. For this purpose, particle-particle

particle-mesh (P3M) scheme has been used, which is much time consuming method. More recently, Di Luo et.al [14] introduced another generalized hydrodynamic approach to simplify the calculation of dynamical structure factor of strongly coupled plasmas using fluctuation-dissipation theorem. This model is benchmarked against a particle-particle particle-mesh molecular dynamics simulation results for dynamic structure factors.

D Parallelization of pseudo spectral code

In spectral simulation, main time consuming part is fast Fourier transform. Therefore, parallelization of spectral code becomes important. The MPI routines are significantly different from the ordinary FFTW because the transform data here are distributed over multiple processes, so that each process gets only a portion of the array [65]. The MPI directory contains multi-dimensional transforms of real and complex data for parallel machines supporting MPI. MPI FFTW routines for distributed-memory (and shared-memory) machines supporting MPI (Message Passing Interface) has been used.

These MPI subroutines of FFTW can support multi-dimensional real and complex data. In particular, for our purpose complex to complex transform has been considered. For two-dimensional system, an example of program in C-language is as follows [65]:

```
#include <fftw_mpi.h>

int main(int argc, char **argv)

{
    const int NX = ..., NY = ...;
    fftwnd_mpi_plan plan;
    fftw_complex *data;
    MPI_Init(&argc, &argv);
    plan = fftw2d_mpi_create_plan(MPI_COMM_WORLD, NX, NY, FFTW_FORWARD,
    FFTW_ESTIMATE);
}
```

...allocate and initialize data...

```
fftwnd_mpi(p, 1, data, NULL, FFTW_NORMAL_ORDER);
```

.....

.....

.....

```
fftwnd_mpi_destroy_plan(plan);
```

```
MPI_Finalize();
```

The calls to `MPI_Init(&argc, &argv)` and `MPI_Finalize()` are required in all MPI programs. “plan” can be created and many a times used in the program, whenever Forward FFTW is required. In the same manner Reverse FFTW can be planned and called in the program. Grain medium or dusty plasma medium can be model led by the following non-linear fluid dynamics equation.

E Ewald sums

To develop MPMD code, Salin and Cailol [74] reference has been followed. In the Yukawa system N number of charged particles interact via screened long ranged coulomb potential. In molecular dynamics simulation, periodic array of replicated system is created and due to long range potential and periodic boundaries, the interactions effects come inside the simulation box from all sides of replica since no truncation is incorporated. In this case, the sum of potential energy is

$$\phi(\mathbf{r}) = \phi(|r|) + \sum_{\mathbf{n} \neq 0} \phi(|\mathbf{r} + \mathbf{n}L|) \quad (\text{E.1})$$

where $\phi(r)$ is Yukawa potential, L is system size and $\mathbf{n} = (n_x, n_y, n_z)$. It is important to note that when the system size L is much larger than the Debye screening length λ_D , the effect from replicated systems becomes ignorable [130]. In this thesis, the system size is much larger than the Debye length, for example $L_x = L_y = 443a$ and $\lambda_D = 2a$, where a is wigner seitz radius of Yukawa system.

Bibliography

- [1] N. N Rao, P. K Shukla, and M. Y Yu. *Planet. Space. Sci*, 38:543, 1990.
- [2] Gregor E. Morfill and Alexei V. Ivlev. Complex plasmas: An interdisciplinary research field. *Rev. Mod. Phys.*, 81:1353, Oct 2009.
- [3] U. de Angelis. Dusty plasmas in fusion devices. *Physics of Plasmas*, 13(1), 2006.
- [4] J. H. Chu and Lin. I. Direct observation of Coulomb crystals and liquids in strongly coupled rf dusty plasmas. *Phys. Rev. Lett.*, 72:4009, Jun 1994.
- [5] Vladimir E. Fortov, Vladimir I. Molotkov, Anatoli P. Nefedov, and Oleg F. Petrov. Liquid- and crystallike structures in strongly coupled dusty plasmas. *Physics of Plasmas*, 6(5):1759–1768, 1999.
- [6] Yan Feng, J. Goree, and Bin Liu. Observation of temperature peaks due to strong viscous heating in a dusty plasma flow. *Phys. Rev. Lett.*, 109(185002), 2012.
- [7] Ashwin J. and R. Ganesh. Kelvin Helmholtz instability in strongly coupled Yukawa liquids. *Phys. Rev. Lett.*, 104:215003, May 2010.
- [8] Ashwin Joy and R. Ganesh. Co-evolution of inverse cascade and nonlinear heat front in shear flows of strongly coupled Yukawa liquids. *Physics of Plasmas*, 18(8), 2011.
- [9] Y. I. Frenkel. *Kinetic Theory of Liquids (Clarendon, Oxford)*, 1946.
- [10] P. K. Kaw and A. Sen. Low frequency modes in strongly coupled dusty plasmas. *Physics of Plasmas*, 5:(10), 3552, 1998.

Bibliography

- [11] Sanat Kumar Tiwari, Amita Das, Dilip Angom, Bhavesh G. Patel, and Predhiman Kaw. Kelvin-Helmholtz instability in a strongly coupled dusty plasma medium. *Physics of Plasmas (1994-present)*, 19(7), 2012.
- [12] Akanksha Gupta, R. Ganesh, and Ashwin Joy. Kolmogorov flow in two dimensional strongly coupled dusty plasma. *Physics of Plasmas*, 21(7), 2014.
- [13] A. Diaw and M. S. Murillo. Generalized hydrodynamics model for strongly coupled plasmas. *Phys. Rev. E*, 92:013107, Jul 2015.
- [14] Di Luo, Bin Zhao, GuangYue Hu, Tao Gong, YuQing Xia, and Jian Zheng. Coherent dynamic structure factors of strongly coupled plasmas: A generalized hydrodynamic approach. *Physics of Plasmas*, 23(5), 2016.
- [15] L. D. Meshalkin and Y. G. Sinai. *J. Appl. Math. Mech*, 25:1700, 1961.
- [16] A M Obukhov. Kolmogorov flow and laboratory simulation of it. *Russian Mathematical Surveys*, 38:113, 1983.
- [17] Douglas H. Kelley and Nicholas T. Ouellette. Using particle tracking to measure flow instabilities in an undergraduate laboratory experiment. *American J. of Physics*, 79:267, 2011.
- [18] John M. Burgess, C. Bizon, W. D. McCormick, J. B. Swift, and Harry L. Swinney. Instability of the Kolmogorov flow in a soap film. *Phys. Rev. E*, 60:715–721, Jul 1999.
- [19] Akanksha Gupta, Rajaraman Ganesh, and Ashwin Joy. Kolmogorov flow in two dimensional strongly coupled Yukawa liquid: A molecular dynamics study. *Physics of Plasmas*, 22(10), 2015.
- [20] Akanksha Gupta, Rajaraman Ganesh, and Ashwin Joy. Molecular shear heating and vortex dynamics in thermostatted two dimensional Yukawa liquids. *Physics of Plasmas*, 23(7), 2016.

- [21] Akanksha Gupta and R. Ganesh. Compressible Kolmogorov flow in strongly coupled dusty plasma: A study using computational fluid dynamics. *Physics of Plasmas* (*Manuscript under preparation*).
- [22] Ashwin Joy and Abhijit Sen. Microscopic origin of shear relaxation in a model viscoelastic liquid. *Phys. Rev. Lett.*, 114:055002, Feb 2015.
- [23] H. Ohta and S. Hamaguchi. Molecular dynamics evaluation of self-diffusion in Yukawa systems. *Physics of Plasmas*, 7(11):4506–4514, 2000.
- [24] Z. Donkó and P. Hartmann. Thermal conductivity of strongly coupled Yukawa liquids. *Phys. Rev. E*, 69:016405, Jan 2004.
- [25] Sergey A. Khrapak and Hubertus M. Thomas. Fluid approach to evaluate sound velocity in Yukawa systems and complex plasmas. *Phys. Rev. E*, 91(033110), 2015.
- [26] P Pustejovská. Mathematical modeling of synovial fluids flow. *WDS'08 Proceedings of Contributed Papers, Part, 3*:32–37, 2008.
- [27] Siegfried H. Glenzer and Ronald Redmer. X-ray thomson scattering in high energy density plasmas. *Rev. Mod. Phys.*, 81:1625–1663, Dec 2009.
- [28] J. J. Bollinger and D. J. Wineland. Strongly coupled nonneutral ion plasma. *Phys. Rev. Lett.*, 53:348–351, Jul 1984.
- [29] H. Thomas, G. E. Morfill, V. Demmel, J. Goree, B. Feuerbacher, and D. Möhlmann. Plasma crystal: Coulomb crystallization in a dusty plasma. *Phys. Rev. Lett.*, 73:652, Aug 1994.
- [30] G. E. Morfill, H. M. Thomas, U. Konopka, and M. Zuzic. The plasma condensation: Liquid and crystalline plasmas. *Physics of Plasmas*, 6(5):1769–1780, 1999.

Bibliography

- [31] Wen-Tau Juan, Ming-Heng Chen, and Lin I. Nonlinear transports and microvortex excitations in sheared quasi two dimensional dust Coulomb liquids. *Phys. Rev. E*, 64:016402, Jun 2001.
- [32] V. Nosenko and J. Goree. Shear flows and shear viscosity in a two dimensional Yukawa system (dusty plasma). *Phys. Rev. Lett.*, 93(15), 2004.
- [33] H. Ohta and S. Hamaguchi. *Phys. Plasmas*, 13(39), 2000.
- [34] Ashwin Joy and R. Ganesh. Effect of external drive on strongly coupled Yukawa systems: A nonequilibrium molecular dynamics study. *Phys. Rev. E*, 80:056408, Nov 2009.
- [35] J. P Boeuf. Characteristics of a dusty nonthermal plasma from a particle-in-cell monte carlo simulation. *Physical Review A*, 46(12):7910, 1992.
- [36] Kenneth I Golden and Gabor J Kalman. Quasilocalized charge approximation in strongly coupled plasma physics. *Physics of Plasmas*, 7(1):14–32, 2000.
- [37] M Rosenberg and G Kalman. Dust acoustic waves in strongly coupled dusty plasmas. *Physical Review E*, 56(6):7166, 1997.
- [38] JE Allen. Probe theory-the orbital motion approach. *Physica Scripta*, 45(5):497, 1992.
- [39] J Goree. Charging of particles in a plasma. *Plasma Sources Science and Technology*, 3(3):400, 1994.
- [40] I. L. Semenov, S. A. Khrapak, and H. M. Thomas. Momentum transfer cross-section for ion scattering on dust particles. *Physics of Plasmas*, 24(3):033710, 2017.
- [41] P. Hartmann, G. J. Kalman, Z. Donkó, and K. Kutasi. Equilibrium properties and phase diagram of two-dimensional Yukawa systems. *Phys. Rev. E*, 72:026409, Aug 2005.

-
- [42] H. Ohta and S. Hamaguchi. *Phys. Rev. Lett.*, 84:6026, 2000.
- [43] Matthias Wolter and André Melzer. Laser heating of particles in dusty plasmas. *Phys. Rev. E*, 71:036414, Mar 2005.
- [44] Bruce J. Ackerson and Noel A. Clark. Shear-induced melting. *Phys. Rev. Lett.*, 46:123–126, Jan 1981.
- [45] J.D. Huba. *NRL Plasma Formulary*, (Naval Research Laboratory, Washington, DC, 1994).
- [46] A. F. Mills. Heat and mass transfer. page 377, 1995.
- [47] FH Busse and RM Clever. Instabilities of convection rolls in a fluid of moderate prandtl number. *Journal of Fluid Mechanics*, 91(02):319–335, 1979.
- [48] Ching-Lai Hwang, Philip J. Knieper, and Liang-Tseng Fan. Effects of viscous dissipation on heat transfer parameters for flow between parallel plates. *Zeitschrift für angewandte Mathematik und Physik ZAMP*, 16(5):599–610, 1965.
- [49] C.P. Tso and S.P. Mahulikar. Experimental verification of the role of brinkman number in microchannels using local parameters. *International Journal of Heat and Mass Transfer*, 43(10):1837 – 1849, 2000.
- [50] Hans Henrik Rugh. Dynamical Approach to Temperature. *Physical Review Letters*, 78(5):772–774, feb 1997.
- [51] B. D. Butler, Gary Ayton, Owen G. Jepps, and Denis J. Evans. Configurational temperature: Verification of Monte Carlo simulations. *Journal of Chemical Physics*, 109(16):6519–6522, 1998.
- [52] Carlos Braga and Karl P. Travis. A configurational temperature nose-hoover thermostat. *The Journal of Chemical Physics*, 123(13), 2005.

Bibliography

- [53] Karl P. Travis and Carlos Braga. Configurational temperature control for atomic and molecular systems. *The Journal of Chemical Physics*, 128(1), 2008.
- [54] A. Piel, V. Nosenko, and J. Goree. Experiments and molecular-dynamics simulation of elastic waves in a plasma crystal radiated from a small dipole source. *Phys. Rev. Lett.*, 89:085004, Aug 2002.
- [55] Robert W Graves. Simulating seismic wave propagation in 3d elastic media using staggered-grid finite differences. *Bulletin of the Seismological Society of America*, 86(4):1091–1106, 1996.
- [56] M Sun and C Ebner. Molecular-dynamics simulation of compressible fluid flow in two-dimensional channels. *Physical Review A*, 46(8):4813, 1992.
- [57] Ilyas Kandemir and Alaattin Metin Kaya. Molecular dynamics simulation of compressible hot/cold moving lid-driven microcavity flow. *Microfluidics and nanofluidics*, 12(1-4):509–520, 2012.
- [58] A Manela and J Zhang. The effect of compressibility on the stability of wall-bounded Kolmogorov flow. *Journal of Fluid Mechanics*, 694:29–49, 2012.
- [59] D. Banerjee, M. S. Janaki, and N. Chakrabarti. Shear flow instability in a strongly coupled dusty plasma. *Phys. Rev. E*, 85:066408, Jun 2012.
- [60] Dale R Durran. The third-order adams-bashforth method: An attractive alternative to leapfrog time differencing. *Monthly weather review*, 119(3):702–720, 1991.
- [61] Saul A Teukolsky. Stability of the iterated crank-nicholson method in numerical relativity. *Physical Review D*, 61(8):087501, 2000.
- [62] Antony Jameson, Wolfgang Schmidt, and Eli Turkel. Numerical solution of the euler equations by finite volume methods using runge kutta time stepping schemes. In *14th fluid and plasma dynamics conference*, page 1259, 1981.

- [63] David Gottlieb and Steven A Orszag. *Numerical analysis of spectral methods: theory and applications*. SIAM, 1977.
- [64] G. S. Patterson and Steven A. Orszag. Spectral calculations of isotropic turbulence: Efficient removal of aliasing interactions. *Physics of Fluids (1958-1988)*, 14(11):2538–2541, 1971.
- [65] <http://www.fftw.org>.
- [66] Nordsieck Arnold. On numerical integration of ordinary differential equations,. *Math. Comp.*, 16:22–49, 1962.
- [67] Gear. W.C. The numerical integration of ordinary differential equations,. *Math. Comp.*, 21:146–156, 1967.
- [68] TF Russell et al. Stability analysis and switching criteria for adaptive implicit methods based on the cfl condition. In *SPE Symposium on Reservoir Simulation*. Society of Petroleum Engineers, 1989.
- [69] Message P Forum. Mpi: A message-passing interface standard. Technical report, Knoxville, TN, USA, 1994.
- [70] David Roylance. Engineering viscoelasticity. *Department of Materials Science and Engineering–Massachusetts Institute of Technology, Cambridge MA*, 2139:1–37, 2001.
- [71] Kevin S Fancey. A mechanical model for creep, recovery and stress relaxation in polymeric materials. *Journal of materials science*, 40(18):4827–4831, 2005.
- [72] F Akyildiz, RS Jones, and K Walters. On the spring-dashpot representation of linear viscoelastic behaviour. *Rheologica Acta*, 29(5):482–484, 1990.
- [73] Denis J Evans. A non-equilibrium free energy theorem for deterministic systems. *Molecular Physics*, 101(10):1551–1554, 2003.

Bibliography

- [74] Gwenaël Salin and Jean-Michel Caillol. Transport coefficients of the Yukawa one-component plasma. *Phys. Rev. Lett.*, 88:065002, Jan 2002.
- [75] Carlo Marchioro. An example of absence of turbulence for any reynolds number. *Communications in Mathematical Physics*, 105(1):99–106, 1986.
- [76] Zhen Su She. Metastability and vortex pairing in the Kolmogorov flow. *Physics Letters A*, 124(3):161 – 164, 1987.
- [77] A.A. Nepomniashchii. On stability of secondary flows of a viscous fluid in unbounded space. *Journal of Applied Mathematics and Mechanics*, 40(5):836 – 841, 1976.
- [78] H. Okamoto and M. Shōji. Bifurcation diagrams in Kolmogorov’s problem of viscous incompressible fluid on 2-d flat tori. *Japan Journal of Industrial and Applied Mathematics*, 10(2):191–218, 1993.
- [79] F. Feudel and N. Seehafer. Bifurcations and pattern formation in a two-dimensional Navier-Stokes fluid. *Phys. Rev. E*, 52:3506, Oct 1995.
- [80] M. Z. Gak N. F. Bondarenko and F. V. Dolzhansky. *Izv. Akad. Nauk (Fiz. Atmos. Okeana)*, 15:1017, 1979.
- [81] Klaus Roeller, Jürgen Vollmer, and Stephan Herminghaus. Unstable Kolmogorov flow in granular matter. *Chaos*, 19(4):041106, 2009.
- [82] L. D. Landau and E. M. Lifshitz. *Fluid Mechanics (Pergamon, Oxford)*, 1984.
- [83] I. Bena, M. Malek Mansour, and F. Baras. Hydrodynamic fluctuations in the Kolmogorov flow: Linear regime. *Phys. Rev. E*, 59:5503, 1999.
- [84] G. Boffetta et.al. The viscoelastic Kolmogorov flow: eddy viscosity and linear stability,. *J. Fluid Mech*, 523:161, 2005.

- [85] Andre Thess. Instabilities in two - dimensional spatially periodic flows. part i: Kolmogorov flow. *Physics of Fluids A: Fluid Dynamics (1989-1993)*, 4:1385, 1992.
- [86] A. Manela and J. Zhang. The effect of compressibility on the stability of wall-bounded Kolmogorov flow. *Journal of Fluid Mechanics*, 694:29–49, 3 2012.
- [87] Couder, Y. The observation of a shear flow instability in a rotating system with a soap membrane. *J. Physique Lett.*, 42(19):429–431, 1981.
- [88] Solomon, T. H. and Mezic, I. Uniform resonant chaotic mixing in fluid flows. *Nature (London)*, 425(19):376–380, 2003.
- [89] L Rossi, JC Vassilicos, and Y Hardalupas. Electromagnetically controlled multi-scale flows. *Journal of Fluid Mechanics*, 558:207, 2006.
- [90] J. P. Hansen and I. McDonald. *Theory of Simple Liquids: With Applications to Soft Matter, 4th ed. (Academic, Oxford, 2013)*.
- [91] P. G. Drazin. *Intoduction to Hydrodynamic Stability (Cambridge text in applied mathematics University Press, Cambridge, England)*, 2002.
- [92] James M. White and Susan J. Muller. Viscous heating and the stability of newtonian and viscoelastic taylor-couette flows. *Phys. Rev. Lett.*, 84:5130–5133, May 2000.
- [93] G. Faussurier and M. S. Murillo. Gibbs-bogolyubov inequality and transport properties for strongly coupled Yukawa fluids. *Phys. Rev. E*, 67:046404, Apr 2003.
- [94] JM Carcione. Wave propagation in anisotropic linear viscoelastic media: theory and simulated wavefields. *Geophysical Journal International*, 101(3):739–750, 1990.

Bibliography

- [95] D Giaioti and FULVIO Stel. The Rankine vortex model. *October. University of Trieste*, 2006.
- [96] T Loiseleux, JM Chomaz, and P Huerre. The effect of swirl on jets and wakes: Linear instability of the Rankine vortex with axial flow. *Physics of Fluids*, 10(5):1120–1134, 1998.
- [97] Sergey A. Khrapak. Relations between the longitudinal and transverse sound velocities in strongly coupled Yukawa fluids. *Physics of Plasmas*, 23(2):024504, 2016.
- [98] S Nunomura, D Samsonov, and J Goree. Transverse waves in a two-dimensional screened-Coulomb crystal (dusty plasma). *Physical review letters*, 84(22):5141, 2000.
- [99] Edward Thomas Jr and Jeremiah Williams. Experimental measurements of velocity dissipation and neutral-drag effects during the formation of a dusty plasma. *Physical review letters*, 95(5):055001, 2005.
- [100] Bin Liu, John Goree, Vladimir Nosenko, and Laifa Boufendi. Radiation pressure and gas drag forces on a melamine-formaldehyde microsphere in a dusty plasma. *Physics of Plasmas*, 10(1):9–20, 2003.
- [101] Pankaj Kumar Mishra, Johann Herault, Stephan Fauve, and Mahendra K. Verma. Dynamics of reversals and condensates in two-dimensional Kolmogorov flows. *Phys. Rev. E*, 91:053005, May 2015.
- [102] Yilong Han and David G. Grier. Configurational temperatures and interactions in charge-stabilized colloid. *The Journal of Chemical Physics*, 122(6), 2005.
- [103] A C Brańka and S Pieprzyk. Configurational Temperature and Monte Carlo Simulations. *Computational methods in sci. and tech.*, 16(2):119–125, 2011.

- [104] Denis J. Evans and O.P. Morriss. Non-newtonian molecular dynamics. *Computer Physics Reports*, 1(6):297 – 343, 1984.
- [105] Jerome Delhommelle and Denis J. Evans. Configurational temperature thermostat for fluids undergoing shear flow: application to liquid chlorine. *Molecular Physics*, 99:1825–1829, 2001.
- [106] Jerome Delhommelle and Denis J. Evans. Correspondence between configurational temperature and molecular kinetic temperature thermostats. *The Journal of Chemical Physics*, 117(13):6016–6021, 2002.
- [107] P. K. Patra and B. Bhattacharya. A deterministic thermostat for controlling temperature using all degrees of freedom. *Journal of Chemical Physics*, 140(6), 2014.
- [108] D. J. Evans and B. L. Holian. The nose hoover thermostat. *The Journal of Chemical Physics*, 83(8), 1985.
- [109] Glenn J. Martyna, Michael L. Klein, and Mark Tuckerman. Nose hoover chains: The canonical ensemble via continuous dynamics. *The Journal of Chemical Physics*, 97(4), 1992.
- [110] V Nosenko, S Nunomura, and J Goree. Nonlinear compressional pulses in a 2d crystallized dusty plasma. *Physical review letters*, 88(21):215002, 2002.
- [111] V Nosenko, J Goree, ZW Ma, and A Piel. Observation of shear-wave Mach cones in a 2d dusty-plasma crystal. *Physical review letters*, 88(13):135001, 2002.
- [112] J. Pramanik, G. Prasad, A. Sen, and P. K. Kaw. Experimental observations of transverse shear waves in strongly coupled dusty plasmas. *Phys. Rev. Lett.*, 88:175001, Apr 2002.

Bibliography

- [113] P Bandyopadhyay, G Prasad, A Sen, and PK Kaw. Driven transverse shear waves in a strongly coupled dusty plasma. *Physics Letters A*, 372(33):5467–5470, 2008.
- [114] M. A. Berkovsky. *Phys, Lett. A*, 166(3656), 1992.
- [115] Z. Yin, Li Yuan, and Tao Tang. A new parallel strategy for two-dimensional incompressible flow simulations using pseudo-spectral methods. *J. of Computational Physics*, 210(1):325 – 341, 2005.
- [116] Michele Iovieno, Carlo Cavazzoni, and Daniela Tordella. A new technique for a parallel dealiased pseudospectral Navier Stokes code. *Computer Physics Communications*, 141(3):365 – 374, 2001.
- [117] E. A. Coutias, F. R. Hansen, T. Huld, G. Knorr, and J. P. Lynov. Spectral methods in numerical plasma simulation. *Physica Scripta*, 40(3):270, 1989.
- [118] M. K. Verma. *arXiv:nlin/0510069*, 2005.
- [119] S. Chandrasekhar. *Hydrodynamic and Hydromagnetic Stability* (Clarendon, Oxford), 1961.
- [120] Patrick J R Folz and Keiko K Nomura. Interaction of two equal co-rotating viscous vortices in the presence of background shear. *Fluid Dynamics Research*, 46(3):031423, 2014.
- [121] N. D. Sandham. The effect of compressibility on vortex pairing. *Physics of Fluids*, 6(2), 1994.
- [122] H. Iyetomi S. Ichimaru and S. Tanaka. *Phys. Rev. A*, 149(91), 1987.
- [123] T. C. Killian, P. McQuillen, T. M. O’Neil, and J. Castro. Creating and studying ion acoustic waves in ultracold neutral plasmas. *Physics of Plasmas*, 19(5):055701, 2012.

- [124] MS Murillo. Static local field correction description of acoustic waves in strongly coupling dusty plasmas. *Physics of Plasmas*, 5(9):3116–3121, 1998.
- [125] JJ Niemela, L Skrbek, KR Sreenivasan, and RJ Donnelly. The wind in confined thermal convection. *Journal of Fluid Mechanics*, 449:169–178, 2001.
- [126] Harish Charan and Rajaraman Ganesh. Observation of the Rayleigh Benard convection cells in strongly coupled Yukawa liquids. *Physics of Plasmas*, 22(8):083702, 2015.
- [127] Debabrata Banerjee, Janaki Sita Mylavarapu, and Nikhil Chakrabarti. Viscoelastic modes in a strongly coupled, cold, magnetized dusty plasma. *Physics of Plasmas*, 17(11):113708, 2010.
- [128] S. Hamaguchi, R. T. Farouki, and D. H. E. Dubin. Phase diagram of Yukawa systems near the one component plasma limit revisited. *The Journal of Chemical Physics*, 105(17):7641–7647, 1996.
- [129] M. Rosenberg and G. Kalman. Dust acoustic waves in strongly coupled dusty plasmas. *Phys. Rev. E*, 56:7166–7173, Dec 1997.
- [130] Bin Liu and J. Goree. Shear viscosity of two-dimensional Yukawa systems in the liquid state. *Phys. Rev. Lett.*, 94:185002, May 2005.
- [131] W. I. Klazkin. *J. Appl. Math. Mech. (Prikl. Math. Mekh.)*, 36:263, 1972.
- [132] J. S. A. Green. *J. Fluid Mech*, 62:273, 1974.
- [133] V.I. Kliatskin. On the nonlinear theory of stability of periodic flows. *J. Appl. Math and Mech*, 36(2):263 – 271, 1972.
- [134] H. Okamoto and M. Shoji. Bifurcation diagrams in Kolmogorov’s problem of viscous incompressible fluid on 2-d flat tori. *Japan Journal of Industrial and Applied Mathematics*, 10(2):191–218, 1993.
- [135] N. D’Angelo A. Barkan and R. L. Merlino. *Phy.Rev.Lett*, 73(23), 1994.

Bibliography

- [136] H.Ikezi. *Phys.Fluids*, 26(1749), 1986.
- [137] Vikram Singh Dharodi, Sanat Kumar Tiwari, and Amita Das. Visco-elastic fluid simulations of coherent structures in strongly coupled dusty plasma medium. *Physics of Plasmas*, 21(7), 2014.
- [138] Z Donko, G J Kalman, and P Hartmann. Dynamical correlations and collective excitations of Yukawa liquids. *Journal of Physics: Condensed Matter*, 20(41):413101, 2008.
- [139] Yan Feng, J. Goree, and Bin Liu. Observation of temperature peaks due to strong viscous heating in a dusty plasma flow. *Phys. Rev. Lett.*, 109:185002, Oct 2012.
- [140] Ashwin J. and R. Ganesh. *Physics of Plasmas*, 17(10), 2010.
- [141] André Schella, André Melzer, Patrick Ludwig, Hauke Thomsen, and Michael Bonitz. *Introduction to Streaming Complex Plasmas A: Attraction of Like-Charged Particles*, pages 51–71. Springer International Publishing, Cham, 2014.
- [142] Daniel HE Dubin. The phonon wake behind a charge moving relative to a two-dimensional plasma crystal. *Physics of Plasmas*, 7(10):3895–3903, 2000.
- [143] S Nunomura, S Zhdanov, GE Morfill, and J Goree. Nonlinear longitudinal waves in a two-dimensional screened Coulomb crystal. *Physical Review E*, 68(2):026407, 2003.
- [144] S Nunomura, J Goree, S Hu, X Wang, and A Bhattacharjee. Dispersion relations of longitudinal and transverse waves in two-dimensional screened Coulomb crystals. *Physical Review E*, 65(6):066402, 2002.
- [145] Y Li and SIMEN A Ellingsen. Waves in presence of shear current with uniform vorticity. In *Proceedings of MekIT’15-The 8. National conference on Computational Mechanics*, 2015.

- [146] A Piel, V Nosenko, and J Goree. Laser-excited shear waves in solid and liquid two-dimensional dusty plasmas. *Physics of plasmas*, 13(4):042104, 2006.
- [147] Duck J Lee and Sam O Koo. Numerical study of sound generation due to a spinning vortex pair. *AIAA Journal*, 33(1):20–26, 1995.
- [148] José M Carcione, Dan Kosloff, and Ronnie Kosloff. Wave propagation simulation in a linear viscoelastic medium. *Geophysical Journal International*, 95(3):597–611, 1988.
- [149] Chia-Ling Chan and I Lin. Microstructural evolution and irreversibility in the viscoelastic response of mesoscopic dusty-plasma liquids. *Physical review letters*, 98(10):105002, 2007.
- [150] Yan Feng, J Goree, and Bin Liu. Viscoelasticity of 2d liquids quantified in a dusty plasma experiment. *Physical review letters*, 105(2):025002, 2010.
- [151] Z Donkó, J Goree, and P Hartmann. Viscoelastic response of Yukawa liquids. *Physical Review E*, 81(5):056404, 2010.
- [152] P. G. Drazin and W. H. Reid. *Hydrodynamic Stability*. Cambridge Mathematical Library. Cambridge University Press, 2 edition, 2004.